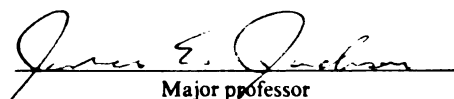This is to certify that the

dissertation entitled

CATALYTIC CONVERSION OF LACTIC ACID AND ITS
DERIVATIVES TO COMMODITY AND SPECIALTY
CHEMICALS: CATALYSTS CHARACTERIZATION AND REACTION
MECHANISM

presented by

RADU CRACIUN

has been accepted towards fulfillment
of the requirements for

Ph. D degree in Chemistry

_____
Major professor

Date July 30. 1997

PLACE IN RETURN BOX
to remove this checkout from your record.
TO AVOID FINES return on or before date due.

DATE DUE	DATE DUE	DATE DUE
JUL 19 2007 JUL 1 1 2009		

CATALYTIC CONVERSION OF LACTIC ACID AND
ITS DERIVATIVES TO COMMODITY AND SPECIALTY CHEMICALS:
CATALYSTS CHARACTERIZATION AND REACTION MECHANISM

By

Radu Craciun

A THESIS

Submitted to
Michigan State University
in partial fulfillment of the requirements
for the degree of

DOCTOR OF PHILOSOPHY

Department of Chemistry

1997

ABSTRACT

CATALYTIC CONVERSION OF LACTIC ACID AND
ITS DERIVATIVES
TO COMMODITY AND SPECIALTY CHEMICALS

By

Radu Craciun

Inexpensive and non-toxic alkali (Na, K, Cs) and alkaline earth metal (Ba)

hydroxides supported on SiO_2 catalysts were successfully used to produce 2,3-

pentanedione (23P) from lactic acid with high yield and selectivity along with other

valuable chemicals (acrylic and propanoic acid). Temperature (280°-350°C), pressure (4-

6 atm), and metal hydroxide loading (0.1 - 3 mmole/g support) on the SiO_2 support were

varied in order to optimize the selectivity to 23P. The yield and selectivity toward 23P

increase in the order Ba <Na < K < Cs with optimized conditions and catalysts giving

23P yields as high as 65% with selectivity up to 80%. Various analytical techniques have

been used to characterize the catalysts before and after exposure to the reaction

conditions. The reaction intermediates formed by the condensation reaction of two lactic

acid molecules to 23P have been evaluated based on product analysis, deuterium labeling

studies, and computational modeling using semi-empirical (PM3) and *ab initio* (STO-3G,

3-21G, and 6-31G* levels) molecular orbital calculations. The latter theoretical

calculations have been used to evaluate variations in energy for each step of the proposed

mechanism. At optimum temperature 23P, H_2O, and CO_2 are continuously removed from

the catalyst surface, so the equilibrium steps in the mechanism are shifted toward product formation.

Several cerium and manganese oxide supported catalysts have been successfully applied to two catalytic oxidative dehydrogenation processes: conversion of methyl lactate to methyl pyruvate and aromatization of 2-ethyl-3-methyl-dihydropyrazine (obtained from condensation of 23P with ethylenediamine) to 2-ethyl-3-methylpyrazine. Bulk and surface characterization techniques were used to characterize the unpromoted and CeO_2-promoted MnO_x/SiO_2 catalysts. Sequential impregnation (cerium followed by manganese), led to mixed Ce-Mn supported oxide catalysts that are active in oxidative dehydrogenations. The $Mn-Ce/SiO_2$ catalytic activity in the above-described reactions are reported in correlation with their structure.

TABLE OF CONTENTS

LIST OF TABLES

LIST OF FIGURES

LIST OF SCHEMES

INTRODUCTION

Among many fascinating phenomena of natural chemistry, enzymatic catalysis is one of the most intriguing processes. Our knowledge of catalysis is far from what nature can do in these enzymatic processes. We have tried to mimic such processes and apply them in many fields of chemical industry, in some cases quite successfully. In recent years, US corn production in excess of food and feed requirements has allowed scientists to develop biocatalytical processes for conversion of biomass materials to specialty chemicals and commodities.

Today, lactic acid is one of the natural products which can be obtained from biofermentation processes in industrial quantities. Lactic acid had been known for many years (first isolation in the 18th century by Scheele), being identified in various micro-organisms as an important component in their metabolism. It was identified in fermented rice water as well as in many other fermented plant liquors. Maybe lactic acid is best known as the source of the sour teste in the milk or as the accumulation in muscle tissues which produces the muscular pain after hard physical exercises. From a chemical point of view, lactic acid, is a bifunctional (hydroxyacid) organic compound, optically active, with a strongly acid taste, and low volatility; when pure and anhydrous, it is a white crystalline solid with low melting point. Generally, lactic acid is available in the form of concentrated (80-90%), viscous, colorless and odorless liquid aqueous solution. Lactic acid can easily undergo intermolecular esterification to form lactoyllactic and higher chain polyesters (oligomers). It exhibits a great variety of chemical reactivity owing to

the presence of the two functional groups in the molecule. To date, several hundred derivatives have been discovered and listed in various books. Holten and coauthors [1] in their review have nicely synthesized a significant amount of information about lactic acid and its derivatives, describing in details its physical properties, preparation, spectra, chemical reactions, optical activity, lactate salts, intermolecular esters, biochemistry, etc.

This work is focused on development of catalytic chemical processes which can add value to lactic acid obtained by biofermentation and open new ways for its industrial utilization. Previous studies on lactic acid's industrial utility have been focused on conversion to acrylic and propanoic acid [2-8]. Catalytic condensation to 2,3-pentanedione (23P) and oxidation to pyruvic acid are two additional interesting and important processes which lactic acid can undergo. Research on catalyst design, structure-activity correlations, structural modification of catalysts during their utilization in the condensation process, mechanistic studies, and reaction parameter optimization for lactic acid catalytic conversion into 23P, are the main topics described in the first two chapters of this dissertation. The interest in the study of the 23P reaction pathway discovered at MSU came from its novelty and unexpected chemical outcome. 23P is a chemical used mostly in the food industry as a flavor agent and food additive in relatively small quantities. It is an important intermediate in many organic syntheses, being able to participate in condensation processes, due to the vicinal carbonyl groups from the molecule. It can easily undergo self-condensation to form duroquinone or intermolecular condensation with various diamines such as ethylenediamine or orthophenylendiamine. Condensation products can be further oxidized to obtain various types of pyrazines. Many food products such as coffee, roasted beef or potatoes contain pyrazines conferring

a nutty roasted flavor. Such pyrazine-based compounds have utility in a large number of biological (herbicide) and drug synthesis applications (additive to various antibiotics).

Cerium and manganese oxides are among the most common solid catalysts used in oxidation reactions. Cerium and manganese catalyst design, novel preparation techniques, catalyst structure characterization using modern analytical techniques, and catalyst activity tests in oxidation of methyl lactate to methyl pyruvate and of 2-ethyl-3-methyl-dihydropyrazine (DHPy), obtained from condensation of 23P with ethylenediamine, to form 2-ethyl-3-methylpyrazine (Py), will be presented in detail in chapters 3-5.

References

1. Holten, C. H.; Muller, A.; Rehbinder, D. *Lactic Acid - Properties and Chemistry of Lactic Acid and Derivatives*, Verlag Chemie, **1971**.
2. Nakel, G. M.; Dirkc, B. M. U.S. Patent 3, **1971**, 579, 353.
3. Holmen, R. E. U.S. Patent **1958**, *2*, 859, 240.
4. Maresca, L. M. U.S. Patent 4, **1986**, 611, 033.
5. Matsumoto, T.; Yamada, E.; Nakachi, O. Komai, T. Japanese Patent 61, **1986**, 243,807 (CA 106:138889k)
6. Paparizos, C.; Dolhyj, S.; Shaw, W. G. U.S. Patent 4, **1988**, 786, 756.
7. Sawicki, R. A. U.S. Patent, **1988**, 729, 978.
8. Moffat, J. B. *Catal. Rev.-Sci. Eng.* **1978**, *19(2)*, 199.
9. Monma, H. *J. Catal.* **1982**, *75*, 200.
10. Mok, W. S. L.; Antal, M. J. Jr.; Jones, M. Jr. *J. Org. Chem.* **1989**, *54*, 4596-4602.
11. Lira, C. T.; McCrackin, P. J. *Ind. Eng. Chem. Res.* **1993**, *32*, 2608.

CHAPTER 1

ALKALI AND ALKALINE EARTH METAL HYDROXIDES CATALYSTS

SUPPORTED ON SiO_2 FOR USE IN LACTIC ACID CONVERSION

1.1 Introduction

Lactic acid (2-hydroxy-propanoic acid) is a bifunctional, optically active molecule traditionally used as food additive or in textile industry. Its production via efficient starch-based fermentation processes, has raised interest in potential applications for its further conversion into other high value specialty and commodity chemicals, as well as its use in production of biodegradable polylactide polymers [1-2]. The decreased cost associated with the application of new biotechnology processes suggests that lactic acid could become a major biomass-based chemical feedstock in the near future. Lactic acid conversion can lead to a variety of products; transformations pertinent to this work are given in Figure 1.1. Reduction to propanoic acid, dehydration to acrylic acid, dehydrogenation to pyruvic acid, and condensation to 2,3-pentanedione (23P) are some of the pathways from lactic acid to valuable chemicals. Decarbonylation/decarboxylation to acetaldehyde is another possible process, which usually is undesired and should be minimized. Direct dehydration of lactic acid to acrylic acid has long been of interest as a potential route to acrylate polymers from biomass; consequently many studies have focused on this pathway. Phosphate salts are known to be good catalysts for the alcohol dehydration reaction [6-7]. However, the highest literature conversion over supported sulfate and phosphate catalysts reached only 58% yield and 65% selectivity to acrylic

acid, at 350°-400°C [3-5]. Lactic acid conversion in supercritical conditions using

phosphate catalysts reached acrylic acid yields of only 23% with 58% selectivity, at 310

bars and 360°C [8-9].
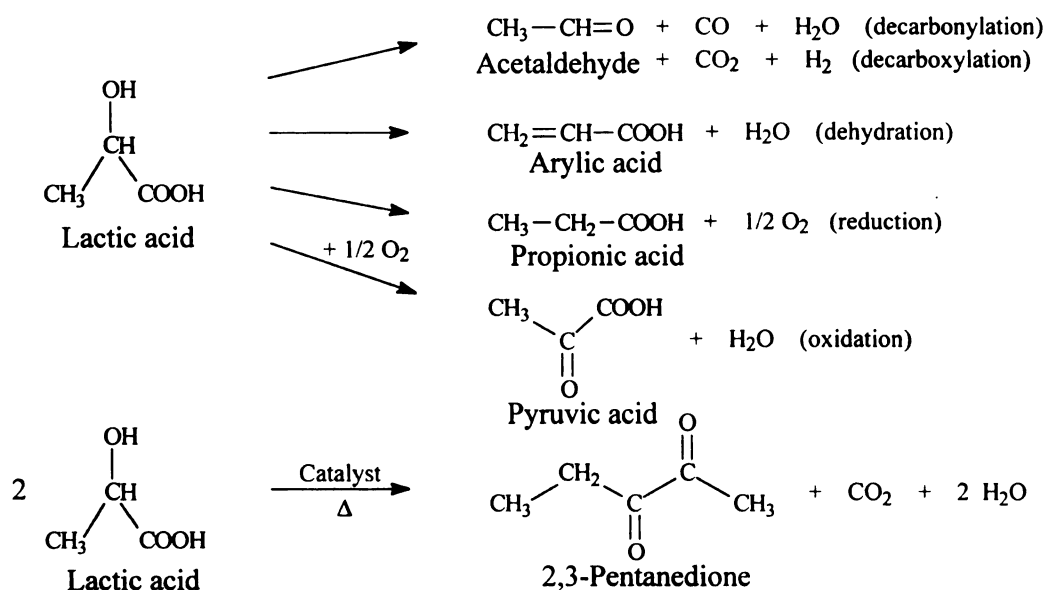
Figure 1.1   Lactic acid conversion pathways toward various chemicals

Previously, our group studied lactic acid conversion using simple phosphates [1]

and other salts [10-11] as catalysts on various type of supports. These studies led to the

discovery of lactic acid catalytic conversion toward 23P at mildly elevated pressures (0.5

MPa) and temperatures (250-350°C). It was found that the yield of 23P is enhanced with

increasing basicity of the salt catalyst, and that low surface-area supports with well

defined porosity are preferred to avoid lactic acid carbonization and catalyst fouling.

Moderately basic catalysts such as sodium phosphates (disodium or trisodium) form

meaningful quantities of 23P and acrylic acid. The Si-Al support alone has almost no activity for 23P and acrylic acid formation. The acid sites from the neat supports provide good catalytic activity toward decarbonylation/decarboxylation to form acetaldehyde and coking of the support as dominant reaction pathways. Simple pyrolysis of lactic acid gives the same products (CO_2, H_2O and actaldehyde). Addition of basic sodium phosphate salts neutralizes these sites and reduces the extent of undesirable reactions.

Alkali and alkaline-earth metals hydroxides are strong bases and have been used as catalysts in various types of base-catalyzed reactions such as alkene isomerization and cumene dehydrogenation on MgO/NaOH [12-13], Claus reaction (H_2S + SO_2) on NaOH/SiO_2 [14], aldol condensation reaction on NaOH/silica-gel [15], Knoevenagel condensation on $AlPO_4$/alumina [16], dehydration of methyl lactate to methyl acrylate on $CaSO_4$ [17], and other organic reactions [18]. A good correlation between the electron-donor properties of silica supported alkali metal hydroxides and catalytic activity have been found in all these reactions [12]. Metal hydroxide loading and reaction temperature played a key role in the optimization of reaction yields, selectivity and the kinetics observed [19].

This work describes a study aimed to elucidate: i) the chemical transformations which occur on sodium phosphate and barium nitrate supported catalysts during preparation and after exposure to the lactic acid feed; ii) correlation of catalyst structure with catalytic activity; iii) the effects of the type of silica used as support for various alkali metal hydroxides catalysts; and iv) the effect of alkali metal hydroxide loadings and reaction temperature on yields and selectivity toward 23P formation.

1.2 Experimental

Materials and Catalyst Preparation. Lactic acid 85% in aqueous solution, crystalline sodium lactate (98%), NaOH, KOH, CsOH, $Ca_{10}(OH)_2(PO_4)_6$, and $NaH_2PO_4xH_2O$, were obtained from Aldrich. Solid $Na_3PO_4x12H_2O$ was obtained from EM Science. Crystalline $Ba(NO_3)_2$, and $Na_5P_3O_{10}$ were obtained from Mallinckrodt. Various Si-based porous materials such as the Si-Al (93% SiO_2, 7% Al_2O_3) with low surface area (5.1 m^2/g, Johnson-Matthey), controlled-pore glass SiO_2 (CPG03000D, 7.2 m^2/g, CPG, Inc.) and SiO_2 high surface area (300 m^2/g) prepared from silica-gel (Davison Chemical Co.) by grinding (240 mesh) and calcining at 500°C were used as supports for the alkali/alkali-earth metal salts. Sodium phosphate catalysts used Si-Al whereas the other salts used SiO_2 as supports (low and high surface area). Two different silica supports, a low surface area, with well controlled pore size distribution ($lSiO_2$, 6.2 m^2/g) and a high surface area ($hSiO_2$, 280 m^2/g), were used for barium nitrate/sodium-methoxide impregnation. The supports were impregnated first with CH_3ONa followed by impregnation with $Ba(NO_3)_2$ aqueous solution. After impregnation the catalysts were dried (125°C) and calcined (400°C). The MOH catalysts were prepared in a similar manner, but the calcination step was necessary. The catalyst loading utilized in the lactic acid conversion varied from 0.1 to 3 mmole of MOH ($M(NO_3)_x$)/g of support (where M is an alkali or alkaline-earth metal). The catalysts were prepared by the incipient wetness impregnation[1] method using an alkali metal salt (MOH) aqueous solution as precursor. After impregnation the catalysts were dried at 125°C and calcined at 500°C, in air. A

---

[1] this methods implies the impregnation with a volume of precursor solution equal with the total pore volume of the support

catalyst deactivation study was performed by analyzing the used and regenerated catalysts

(by calcination at 450°C).

Solid state ^{31}P-MAS-NMR spectroscopy. Magic angle spinning (MAS) - nuclear

magnetic resonance (NMR) spectroscopy has been widely used to characterize inorganic

solids. This spectroscopic technique has proven to be an excellent tool to obtain

information about the structure of various phosphate salts [20-21]. The magic angle can

be explained based on the drawing in Figure 1.2. The nucleus executes a circular motion

about the axis of rotation and if the motion is fast enough, the nucleus can be considered

at the center of the circle (on the axis).

$$H_o$$

$$R_{ij}$$

$$\theta$$

$$(1/R^3_{ij})\ (3\cos^2\theta - 1)$$
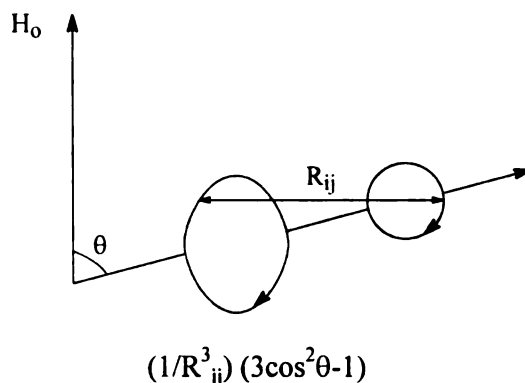
Figure 1.2 Schematic representation of magnetic field (H_o) interaction with the dipolar internuclear vector R_{ij} and below, the equation which describes the process [22].

In liquids, isotropic and rapid tumbling average out direct dipolar coupling and

chemical shift anisotropy by motional narrowing. In solids, these interactions are usually

not completely averaged out due to the absence of molecular tumbling and diffusion and

insufficient motional narrowing. The dipolar interaction between a pair of nuclei i and j

is described by the equation in Figure 1.2, where θ is the angle between R_{ij} and H_o

vectors. The angular dependence term reduces to zero for $\theta = 54.74°$, the so called magic

angle. At this θ value the internuclear vectors are lined up to the maapplied magnetic field, and the dipolar interactions vanish [22]. In most solids, the nuclear magnetic dipole is coupled to those of its neighbors, and only some of the pairs will be near the magic angle. However, when the sample is rotated fast enough, around an axis fixed at the magic angle value, the time average orientation of all the internuclear vectors is parallel to each other and to the rotation axis. When the angle between Ho and the rotation axis is 54.74°, the $3\cos^2\theta - 1$ term is zero [22]. This technique, which minimizes the dipolar interaction in a solid, has found application in pulsed NMR experiments on solid materials [20-26].

Chemical shifts of phosphate atoms can be observed in specific regions as a function of the type of phosphate analyzed (orthophosphates, metaphosphates, or pyrophosphates). Previous studies have correlated factors that influence the ^{31}P chemical shifts from phosphate-based compounds [22-24]. Among these factors can be mentioned the number and the electronegativity of the ligands coordinated to phosphorus atom, the bond angles about phosphorus, the occupation of phosphorus bonding orbitals, the nuclear charge and radius of the phosphate counter-cation. An important aspect from previous studies is that the NMR chemical shifts can differentiate between terminal phosphorus atoms and a chain of phosphate sites. When during analysis complete nuclear spin relaxation for the ^{31}P atom is ensured, quantitative information can be extracted from the data and the evaluation of chain size for a polyphosphate structure is possible [25-27]. Relaxation time experiments have been performed in order to quantify the terminal versus chain phosphorus atom content of phosphate salts present on catalyst surfaces. Several

relaxation times can be defined during an MAS-NMR experiment. The spin-lattice (T_1)

relaxation is defined to be the process of growth toward equilibrium magnetization given

by Curie's law. Placing a sample initially non-magnetized into a magnetic field, the

nuclear moments whose orientations are initially distributed equally between the two

energy states, build up a slight excess of sites aligned parallel to the field according to the

Boltzman equation and to the energy difference $2\mu H$ (μ = magnetic moment, H static

magnetic field) between parallel and antiparallel states. The rate at which magnetization

builds up in a static field depends on the mechanisms available to transfer energy by

translations, rotations, and vibrations (lattice) to the surroundings. The mechanisms of

spin-lattice relaxation influence the value T_1 and the type of equation which describes the

process. The spin-lattice relaxation process is described often by an exponential equation

(in an NMR experiment), when the magnetization $M_{(t)}$ recovers from zero (M_0) after a $\pi/2$

pulse:

$$M_{(t)} = M_0 [1 - \exp(-t/T_1)] \tag{1-1}$$

Besides spin-lattice relaxation with its characteristic time constant T_1, several

other relaxation processes may be encountered such as spin-spin relaxation (T_2), spin-

lattice in the rotating frame time ($T_{1\rho}$), and dipolar spin-lattice relaxation time (T_{1D}).

Among these processes, the spin-spin relaxation may play an important role in the total

spin relaxation value during an NMR experiment. T_2 is defined as the time constant for

decay of x-y component of the magnetization following a disturbance. When molecular

motions are very fast (non-viscous liquids), $T_1 = T_2$, resulting in no additional

information about the system. For solids, $T_1 \gg T_2$, so T_2 may offer more information

about the molecular structure under analysis (see detailed information in reference [25]).

For our purposes, the evaluation of T_1 has proven to be enough to obtain quantitative data about the phosphate-based catalysts. In general, the evaluation of T_1 is time consuming. Among the various strategies to evaluate T_1, the most common method of T_1 determination is to measure $M_{(t)}$ at various values of t and fit them to an exponential decay curve. The error for T_1 evaluation is given by the error to which the value for M_0 is measured (usually not well determined) [25]. Another approach to evaluate T_1, specific to pulse NMR experiments, is the double pulse sequence (inversion and saturation recovery). In this method two pulses are applied, the first pulse (inversion recovery) prepares the nuclear spins in some non-equilibrium configuration and then, after a waiting period during which the spins are allowed to relax, a pulse probes the state of the spins (d_2 from Figure 1.3 a is variable). The inverted spin population recovery is monitored as a function of waiting time and goes from $-M_0$ to M_0, where M_0 is the thermal equilibrium magnetization attainable only after waiting for a time much longer than T_1. A typical NMR signal after a variable waiting time (variable delay time = d_2) during an experiment is presented in Figure 1.3 b. In this experiment, d_2 has values varying from 3.75 s to 900 s. T_1 can be evaluated by fitting the exponential equation which follows the nuclear spin relaxation (dotted line from Figure 1.3 b). Besides the information about how long an NMR experiment should be run in order to ensure complete nuclear spin relation, the T_1 value can be used to identify and assign NMR peaks with very close chemical shifts originating from atoms in different sites, and to provide additional structural information about a given sample (kind and type of atom

13

close to the analyzed one and type of interaction between them) [26-27]. The MAS

technique produces an isotropic band accompanied by spinning sidebands of various

intensities spaced at integer multiples of the spinning frequency on both sides of the main

group of peaks. The symmetry of the spinning bands can provide additional information

about the structure of the phosphorus compound. [28]. Variation in spinning frequency

may help to differentiate between a real peak from the isotropic band and a spinning

sideband [29].

a) Double pulse sequence
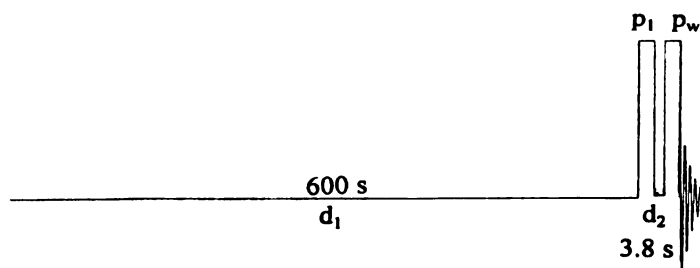
b) NMR signal at various second delay values (relaxation), d_2
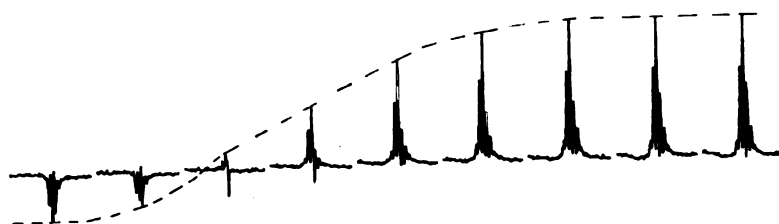
Figure 1.3 Spin-lattice relaxation time (T_1) evaluation from a double-pulse MAS - NMR experiment: a) pulse configuration; b) NMR signal at various delay time array, d_2.

In this study, solid state ^{31}P MAS-NMR spectra were obtained at room

temperature, using a Varian VXR-400S spectrometer with an Oxford cryomagnet

generating a magnetic field of 9.395 T and operated at a Sun workstation network with the

V-NMR operating system Version 4.1. The Fourier transform of free induction decay

(FID) was observed at 161.903 MHz and at spinning rates of 4000 and 6000 ±15 rot/min

(Hz), respectively. A Varian 400VT CP/MAS sample probe of 7 mm diameter and a top

speed of about 8 kHz was used during analysis. The acquisition time was long enough to

ensure full ^{31}P nuclear spin relaxation for accurate quantitative data analysis. Additional

relaxation time experiments were performed in order to assign and evaluate the signals

obtained from analysis.

Table 1.1 Parameters for MAS ^{31}P-NMR Data Acquisition

Instrument Parameters	Numerical values
Transmitter frequency [MHz]	161.903
Spectral width [kHz]	100
Number of data points	16,000
Acquisition time [s]	0.08
Number of scans	> 64
First delay time, d_1 [s]	10.0 or 600.0
Delay time array, d_2 [s]	3.75 - 960
Spinning frequency [kHz]	4 or 6
Pulse width [µs]	4.0

Table 1.1 indicates the operating parameters for data acquisition. About 0.5 g

catalyst powder was introduced into the spectrometer holder for analysis. The

spectrometer was tuned at the start of each session using the tuning band for ^{31}P in the

sample probe. The chemical shifts were evaluated using calcium hydroxyapatite powder

$(Ca_{10}(OH)_2(PO_4)_6$ as standard, which shows a single peak at 2.8±0.2 ppm. For other assignments, the shifts of standard phosphate materials analyzed were typically reproducible within ±0.5 ppm. Bandwidths (FWHM) for the spectra covered a range of 1-18 ppm. The errors in chemical shift values increased for broader bands.

DRIFTS analysis. Diffuse reflectance infrared Fourier transform spectroscopy (DRIFTS) is an IR sampling technique useful for powder sample analysis. The spectra obtained are very similar with those obtained in normal absorption IR analysis, except that on the (y) axis, instead of absorption they are reported as Kubelka Munk units (see below) [30]. In the late 1970's, Fuller and Griffiths [31-32] developed for the first time an efficient optical system together with all the necessary instrumentation which allowed them to perform diffuse reflectance IR spectroscopic measurements on powder materials. After that, many researchers focused their studies on improvements and new directions to develop this IR sampling technique [33-35]. Special *in-situ* DRIFTS cells were developed for catalysis studies [36-39]. Due to its advantages, currently almost all IR studies use the DRIFTS method to investigate heterogeneous catalysis systems. The development of very sensitive detectors, like the mercury-cadmium-telluride (MCT) detector, permit IR analysis even at a low throughput level (less than 5%). This type of detector is the most suitable for DRIFTS studies. The method can be successfully used for quantitative analysis, using the diffuse reflectance beam theory developed by Kubelka and Munk in the early '30s [30]. These units are characteristic for the diffuse reflected beam from the surface of porous or/and powder samples. The DRIFTS spectra

characterize the sample qualitatively and quantitatively. Qualitative analyses are characterized by similar principles as normal absorption spectroscopy.

For powder samples, a DRIFTS spectrum can have a better signal-to-noise (S/N) ratio and more clear IR bands in comparison with a classical absorption spectrum. Quantitative DRIFTS analysis shows good linearity between the intensity of the bands and concentrations for very dilute samples. For concentrated samples, the deviation from linearity becomes significant making the analysis unsuitable for quantitative calculation [37-38]. The lower limit for calibration curve linearity is given by samples with 10^{-5} monolayer surface coverage, whereas the highest limit for linearity is considered to be of several molecular layers (at several monolayers the specific absorption (ε) varies non-linearly [40]). The accuracy and detection limits of the method are in the range for trace analysis, close to electron microscopy and spectroscopy.

In 1964, Kortum and Delfs [41] used a dispersive infrared spectrophotometer operating in a diffuse reflectance mode for surface analysis of solid catalysts. They studied the adsorption of hydrogen cyanide and ethylene on supported metal oxide catalysts. The results showed poor quality, the spectra obtained being hard to interpret due to low resolution. Niwa *et al.* [42] have reported diffuse reflectance IR spectra for simple molecules adsorbed on porous catalysts at high temperatures using the same type of spectrophotometers. With the development of FTIR spectrophotometers, new experiments focused on obtaining diffuse reflectance infrared spectra for solid catalyst materials. DRIFTS became the method of choice in heterogeneous catalysis studies, being continuously improved and developed. One of the main advantages of DRIFTS

analysis is the possibility of obtaining accurate quantitative data at low catalyst surface coverage. The quantitative analysis is based on the Kubelka-Munk function [30] and it is applied in a similar way as Beer's law, which is largely used for quantitative experiments in the UV-VIS domain. The diagram shown in Figure 1.4, illustrates the theory behind this type of quantitative IR analysis.

Incident IR
Flux (I)

Emitted IR
Flux (J)

$x = L$

I

$J + dJ$

dx

$I - dI$

J

K,S

$x = 0$
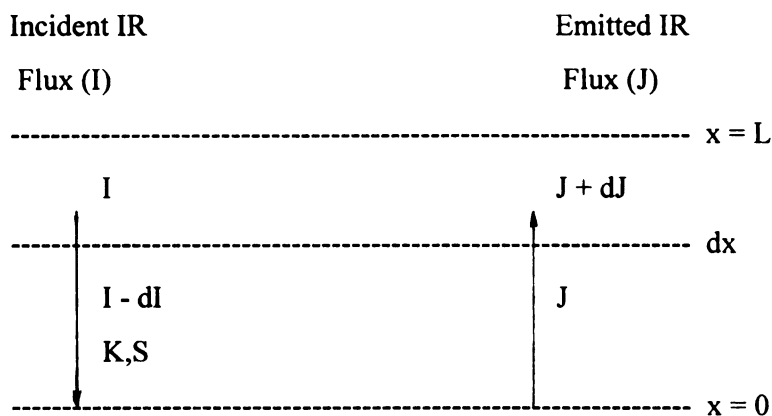
Figure 1.4 Schematic representation of IR beam interaction with the sample.

In Figure 1.4, K stands for the absorption coefficient and S for the scattering coefficient. From the diagram shown above, two different differential equations can be written to describe the variation of the incident and emitted fluxes when they penetrate the surface of a sample:

$$\frac{dI}{dx} = -(K + S)I + SJ \tag{1-2}$$

$$\frac{dJ}{dx} = SI - (K + S)J \tag{1-3}$$

In this case, the following limiting conditions can be considered:

$I = I_0,$ when x = L and

$J = -R_g I$ when x = 0, where R_g is the reflectance at the sample's cup surface.

The reflectance is given by the emitted (J) and incident (I) flux ratio (R = J/I). The expression for these two IR fluxes can be obtained by solving the differential equation system (1-2) and (1-3), respectively; substituting the solutions for I and J yields an expression for reflectance R, given by:

$$R = \frac{J}{I} = \frac{1 - R_g[a - b\coth(bSL)]}{a - R_g + b\coth(bSL)}$$ (1-4)

where : $a = 1 + K/S$, and $b = (a^2 - 1)^{1/2}$ respectively.

As can be observed, the expression for reflectance (R) given in relation (1-4) is very complex, which makes it useless for practical applications. Kubelka and Munk proposed several approximations that can be applied to simplify the relation (1-4). These approximations lead to a function which describes the diffuse reflected beam from an infinitely thick sample surface, called the Kubelka-Munk function.

As was mentioned before, to simplify the relation (1-4) for reflectance (R) several approximations were considered:

I) The incident and emitted fluxes are perpendicular to the sample surface.

II) The sample is considered to be very thick, which implies that (R) will approach zero: $\coth(bSL) \to 1$, when $L \to \infty$.

The expression for reflectance, considered as the reflectance for a sample with infinite thickness (R_∞), is given by relation (1-5) presented below:

$$R_\infty = \{1 + (\frac{K}{S}) - [(\frac{K}{S})^2 + \frac{2K}{S}]^{1/2}\}^{-1}$$ (1-5)

from which can be obtained:

$$\frac{K}{S} = F(R_\infty) = \frac{(1 - R_\infty)^2}{2R_\infty} \tag{1-6}$$

The absorption coefficient is given by the relation (2-6):

$$K = c\,\varepsilon \tag{1-7}$$

where c is the sample concentration and ε is the specific molar absorption.

III) The scattering coefficient is considered to be constant through the sample thickness. In this case, the expression for the Kubelka-Munk function [$F(R_\infty)$] can be obtained from relation (1-6) and has the following form:

$$F(R_\infty) = \frac{\varepsilon c}{S} \tag{1-8}$$

Equation (1-8) represents the relation between the signal collected and recorded in DRIFTS analysis and sample concentration. The spectrum obtained has on the (y) axis $F(R_\infty)$ instead of absorbance. The unique character of this method is given by the utility of this function for quantitative measurements. The practical application of this function depends on the validity of the two approximations described above. Recently, Loyalka and Riggs [43], have reconsidered the general validity of the Kubelka-Munk function for practical meanings due to an overestimation of the (K) constant by a factor of two. However, a redefinition of the expression for (a) from relation (1-4) based on Kubelka and Munk calculations for scattering cross section (S), indicated a correct value. For details regarding this new approach see reference [43].

Because the penetration of the incident beam is very small compared with the sample thickness, and the emitted beam is diffused through the porous surface of the

sample, these approximations (I, II, and III) are reasonable for practical purposes. Experimental data have shown a linear dependence between the DR-signal and sample concentration even at very low concentrations.

Practically, there is no standard which has a perfect diffuse reflectance, so the infinite value of the reflectance will be given by the relation (1-9), presented below:

$$R_\infty = \frac{R_\infty(\text{sample})}{R_\infty(\text{standard})} \qquad (1\text{-}9)$$

The standard considered must present a high diffuse reflectance and should not absorb the incident IR beam in the frequency domain where the sample has specific absorption bands. At high concentrations, the presence of polymolecular layers on the surface of the analyte leads to an increase in the value of molar absorptivity (ε) and consequently to deviation from linearity of the Kubelka-Munk function. On the other hand, when very thin samples are studied (e.g. films), the depth of penetration for the incident beam is dependent on the scattering coefficient (S). In this case, the approximation (L $\rightarrow$ ∞) introduces a significant error to the Kubelka-Munk function evaluation [32]. Different IR beam penetration depths at various points of the sample also can introduce inaccuracies to the measured relative reflectance.

Diffuse Reflectance Accessories. The advantages offered by FTIR spectrometers were the key conditions necessary to develop and continuously improve the DRIFT spectroscopy method. The first step in the development of diffuse reflectance as an IR sampling technique was to design a proper attachment (collector) for the IR beam. The attachment must be placed into the sample compartment on a support, readily adaptable to any type of IR spectrometer. A specific optical arrangement for diffuse reflectance

analysis of porous materials was first successfully used in the UV-VIS region [44]. A spherical mirror proved optimal to collect the diffuse reflectance radiation from the solid surface. Adaptation of this type of mirror to the mid-IR domain introduces some technical problems. In this case, the IR beam collected and focused on the detector is too low in energy (several orders of magnitude) for accurate measurements [45]. The lower sensitivity of detectors used for IR versus UV-VIS spectroscopy exacerbates these difficulties. Cobletz mirrors [46], semi-ellipsoidal mirrors [47] and ellipsoidal mirrors [40,48] were used to optimize the IR beam collection from the irradiated sample surface. Ellipsoidal mirrors proved to be the most efficient and today are the most widely used ones for DRIFT attachments. An optimized optical setup using ellipsoidal mirrors appropriate and very efficient for the collection of diffuse reflected IR beam was described for the first time by Fuller and Griffiths [31]. Another key factor to be considered is the choice of reflective coating material for the inside of the ellipsoidal mirrors. Materials like MgO or $BaSO_4$ have been employed in mirrors for UV-VIS applications; for DRIFTS collectors, MgO or aluminum were successfully used because of their very weak absorption in the IR region (close to zero).

Diffuse reflectance collectors. Two different types of collectors, on-axis and off-axis have been developed for DRIFTS analysis. Figure 1.5 a shows the on-axis collector introduced on the market by Spectra-Tech Inc. [49]. The main components of the collectors are labeled in the figure. The IR beam hits the input ellipsoidal mirror and is dispersed on the sample, placed into a special cup. The blocker placed in the middle of the sample holder helps to eliminate specular distortion produced by radiation reflected without penetration into the sample, which therefore carries no spectral information. The

incident radiation passes into the bulk of the sample and undergoes reflection, refraction and absorption before reemerging at the surface. The diffusely reflected IR beam is collected by the output ellipsoidal mirror and focused onto the detector of the spectrometer. One of the main advantages offered by this type of collector is the high energy output resulting in a spectrum with an excellent signal-to-noise ratio. The collector allows a convenient sample placement from either the top or the front of the accessory and permits operation in unfavorable sampling environments. A build-in micrometer screw adjustment allows rapid and accurate sample positioning and alignment. The collector can be used in three different modes of operation. For neat samples, a pure diffuse reflectance mode allows high quality, transmission-like spectra to be acquired. A combined diffuse/specular reflectance mode provides the highest performance for samples dispersed in a non-absorbing matrix. Finally, the collector can be used to acquire surface reflectance spectra in a specular mode. The disadvantage of this type of collector is given by the high specular reflectance which can interfere and overlap with the signal containing the spectral information from the sample.

The 90° off-axis DRIFTS collector [50], also called the Praying Mantis[R] attachment is shown in Figure 1.5 b. This is the first type of collector introduced on the market by Harrick Scientific Co. in the 1980's and it remains widely used in the field even today. The main components of the collector are similar with those presented in the case of the on-axis collector, except that their arrangement is different. As can be observed from the figure, the IR beam is reflected off-axis before it hits the input ellipsoidal mirror. The output mirror collects and focuses the beam with the spectral

information toward the detector (off axis to the sample). Both ellipsoidal mirrors are tilted forward so that the diffusely reflected radiation is collected at an azimuthal angle of 120°. This deflects the specular reflectance component behind the collection ellipsoid, minimizing the intensity of restrain bands and of the specularly reflected light [50].

a)
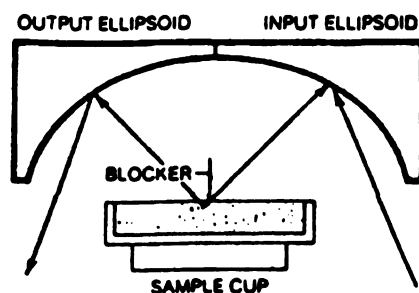
b)
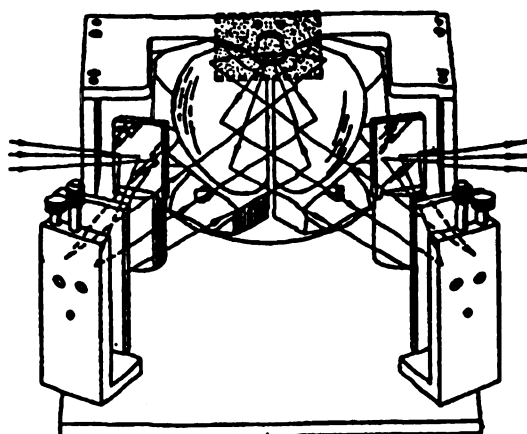
Figure 1.5 Optical attachment (collector): a) on axis (reprinted with permission of *Spectra-Tech Inc.* [49]; b) off axis (reprinted with permission of *Harrick Scientific Co.* [50]), for diffuse reflectance spectra collection.

The optical geometry of the Praying Mantis attachment permits collection of up to 20% of all diffusely reflected radiation and 75% of the open beam at the throughput with the tilted alignment mirror. Due to the lower throughput obtained by using this type of collector, a mercury-cadmium-telluride (MTC) detector is strongly recommended. This type of detector has a higher sensitivity than other type of detectors such as lithium-tantalite (LiTan) or the dimethyl-triglycine sulfate (DTGS). A unique advantage of this type of collector is the ability to rotate the ellipsoidal mirrors (ellipsoids) in the optical plane of the attachment. Thus, with only a minor modification, the ellipsoid can be repositioned from their conventional downward looking mode, expanding the scope of samples that can be analyzed (like large panels or thin layer chromatographic plates). In addition, the collector can be used in a specular reflectance mode at 41.5° incidence angle. A special sample holder is available for this purpose. The attachment can be operated with a precision translation stage for the sample, a viewing microscope, a sample illuminator and micro-sampling cups. The sample stage can be adjusted in all three dimensions, which allows the analysis to be made in either diffuse reflectance mode or specular reflectance mode, as well as a combination of both. The design of the attachment permits a reaction chamber to be attached, for *in-situ* measurements.

Diffuse reflectance in-situ cell. In 1984, Hamadeh *et al.* [36] developed an *in-situ* cell for DRIFTS studies of heterogeneous catalysis processes. The cell allowed good control of temperature and reactant flow rates over the catalyst. Further design improvements resulted in a reliable, adaptable unit with a well controlled environment above the catalyst surface. Figure 1.6 shows a commercially available version of an *in-situ* DRIFTS cell (Harrick Scientific Co.) [50-51]. The free volume above the sample is

not greater than 1.75 cm^3. The hemispherical windows are easily changeable, and may be made of various infrared transparent materials depending on the reaction conditions and spectroscopic range required. For atmospheric pressure, a KBr window can be used with good results. For high vacuum or pressure, more chemical inert windows such as germanium, ZnS or ZnSe windows, should be utilized. For example, with a ZnS window, the reaction chamber can operate at pressure as high as 1.01×10^6 N/m^2 (10 atm).
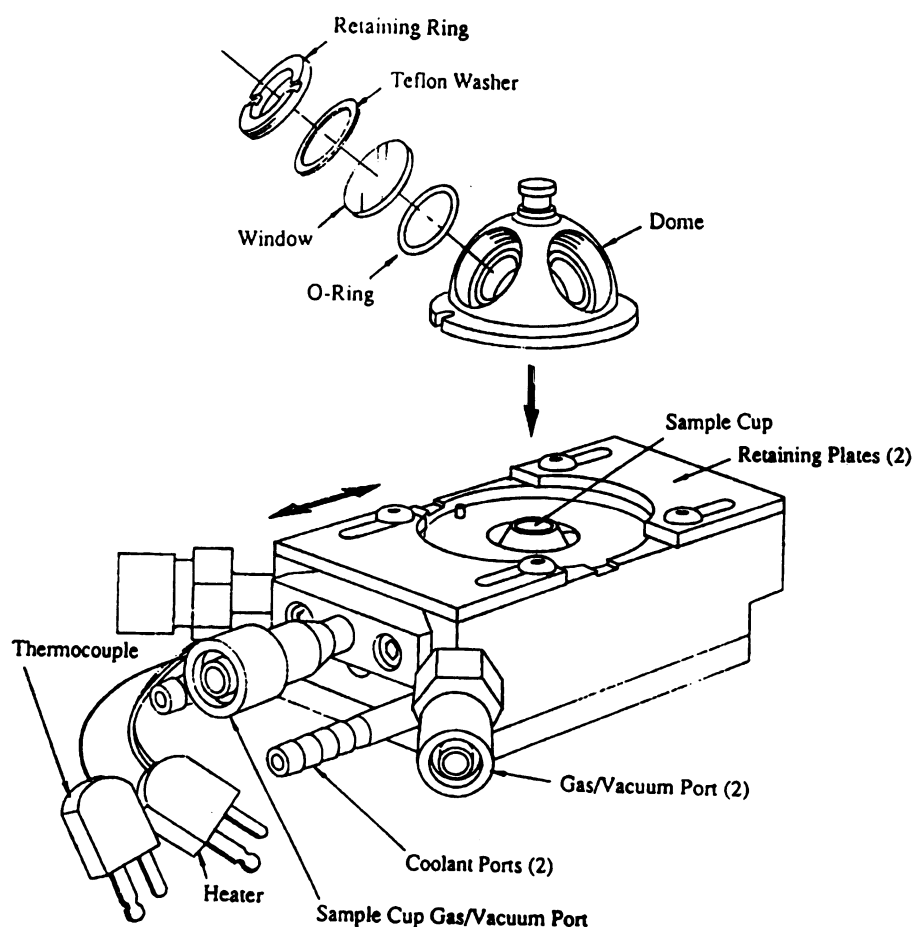
Figure 1.6 *In-situ* DRIFTS cell (*Harrick Scientific Co.* [50]).

The windows of the high pressure cell are very thick, limiting the throughput to 2-5%, leading to a relative low S/N ratio and poor resolution, but these difficulties can be partially reduced by increasing the number of scans and lowering the resolution (8 cm^{-1}). The cell is connected to a vacuum line which allows degassing of the sample or study of reactions under subatmospheric pressures. Temperature is controlled by a thermocouple and the heating of the cell is carried out by an electrical mantel. Reactant and product flow rates are controlled and recorded before and after the gas inlet (sample cup gas/vacuum port) and gas outlet (gas/vacuum port 2). The cell has a cooling system to decrease the noise that might influence the quality of the IR spectra. Leyden *et al.* [52] have modified the collector configuration by introducing a one-dimensional translation stage that allows precise location of the sample at the optimum height. Thermal emission or expansion during heating affects the intensity of the dc-signal from the sample, decreasing the sensitivity of the MCT detector. Lowering or raising the sample height influences the IR band intensity from a DRIFTS spectrum. For absolute quantitative measurements using an *in-situ* DRIFTS cell, optimization of the sample height becomes an important factor. Without this optimization, only relative quantitative measurements are possible. After adjustments (sample height and position) the reproducible variation in the IR band intensities is ± 5-10%. Advantages like quantitative and *in-situ* measurements offered by the instrumentation unique to DRIFTS analysis make this sampling technique attractive for solid catalyst characterization and other studies in the heterogeneous catalysis field.

Advantages and Disadvantages of DRIFTS Compared with other Conventional IR

Techniques. Based on information about the theory and the instrumentation used in DRIFTS analysis provided above, it is now possible to evaluate the advantages and disadvantages offered by this sampling technique over other IR techniques currently used for heterogeneous catalysis studies. The discussion will be focused on conventional transmission/absorption, and emission techniques versus diffuse reflectance. Attenuated total reflectance (ATR) and photoacoustic IR (PAS-IR) spectroscopy are two other major IR sampling techniques, employed in heterogeneous catalysis applications [37, 53], but they are less suitable and/or compatible, as explained below.

Table 1.2 presents comparison data for various IR spectroscopic techniques used for catalyst surface analysis. Transmission IR spectroscopy is a proven and simple technique which uses samples in the form of a thin wafer. The big disadvantage is that the sample must be semi-transparent, sample preparation is laborious, and partial sample oxidation occurs readily [54]. Emission IR spectroscopy has proven to be an effective technique for powder and metal samples. The method is based on the fact that any warm body emits IR radiation proportional with its structure and temperature. Consequently, no IR source is necessary; the sample itself plays the role of source.

Spectra obtained by emission IR include bands with good spatial resolution, but the method has a low S/N ratio and in many cases background radiation becomes an important problem. Sullivan *et al.* [53] in their review, have indicated the main advantages and disadvantages of various IR techniques and their possible applications.

Table 1.2 Comparison of IR techniques for used for catalysts characterization

	Transmission	Emission	Reflection Absorption	Diffuse Reflectance
Samples	Thin Wafers	Powders Metals	Foils Single Crystals	Powders
Advantages	Simple Proven	Sample Versatility Spatial Resolution	Metals	Easy Sampling Improved S/N Surface Sensitive
Disadvantages	Semitransparent Materials Pelleting	Low S/N Background Radiation	Smooth Samples	Reproducibility Dilution

Analyzing the spectra of a zeolite sample acquired using the two different methods, it was observed that the DRIFTS spectrum shows good resolution, with well defined IR bands in 1300-500 cm^{-1} region as compared to the spectra obtained by emission IR. In the case of emission IR spectroscopy, attenuation of some bands, and intense background radiation proportional with temperature, can result in poor resolution of some bands. Reproducibility of emission spectra constitutes another major problem in IR band interpretation. Hence, the analysis of DRIFTS spectra is easier and more accurate than that based on emission data.

Reflection IR spectroscopy is used mostly for smooth metal catalyst surface characterization, when the reflection is close to 100% and the signal is strong enough to provide useful molecular level information about any species adsorbed on a surface [53]. The method fails to provide good quality IR spectra for samples with rough surfaces and low reflection capabilities (not suitable for powders).

Based on the observations presented above and on the summary presented in Table 1.2, the following advantages of DRIFTS analysis can be mentioned: i) easy and non-destructive sample preparation (no pelleting necessary); ii) excellent analysis of opaque powders; iii) avoidance of contact with other materials (like KBr, H_2O) which might interfere with the sample bands or may themselves be catalysts or poisons in the reaction considered; iv) high sensitivity and spectra with well resolved bands compared to those obtained by using other techniques.

In the following work, DRIFTS spectra were acquired using a Perkin-Elmer Spectrum 2000 instrument equipped with the Harrick Inc. diffuse reflectance attachment described above. The catalyst powders (20-25 mg) were put into the sample holder and introduced into the DRIFTS attachment. To simulate the lactic acid conversion process the MOH/SiO_2 catalysts were exposed to lactic acid vapors at temperatures ranging from 25°C to 350°C, using an apparatus designed to direct vapors onto the catalyst surface [11]. The samples were transferred to the IR spectrometer and analyzed via DRIFTS to identify surface species present in the quenched catalyst following reaction, in temperature range between 120°C to 350°C. The spectra are collected and reported in Kubelka-Munk units versus wavenumber. IR spectra were acquired with resolution of 4.0 cm^{-1} over a 400-4000 cm^{-1} wavenumber range.

X-Ray Diffraction (XRD). X-rays, with their wavelength in the Ångstrom range, can penetrate solids and are suitable to probe and provide information about the bulk, crystalline structure. Changes in crystalline phases lead to variations in the X-ray diffraction patterns recorded. Each diffraction pattern can provide information about the

particle size of the solid and the relative proportions of various isomorphous phases. X-rays are produced by bombarding a metal (very often Cu) with high energy electrons. The Cu Kα line (8.04 keV and λ = 0.154 nm) is generated by primary electron ejection from a K shell to leave a core hole, followed by filling of the hole with an electron from the L shell with the emission of an X-ray quantum. This phenomenon is the basis of X-ray sources used in XRD or in other X-ray spectroscopy techniques [X-ray photoelectron (XPS), or fluorescence (XFS) spectroscopies, electron diffraction microscopy, etc.]. X-ray diffraction represents the elastic scattering of X-ray photons by the well organized atoms placed in a crystalline lattice. The scattered monochromatic X-rays yield interference patterns as they scatter off the evenly spaced crystal planes of the lattice. Lattice spacing is given by the Bragg equation (1-10).

$$n\lambda = 2d \sin\theta, \quad n = 1, 2, 3, ... \tag{1-10}$$

where λ is the X-ray wavelength, d is the distance between two lattice planes, θ is the angle of diffraction (X-ray versus normal to the reflecting lattice plane), and the integer n is the reflection order [55] (see Figure 1-7).
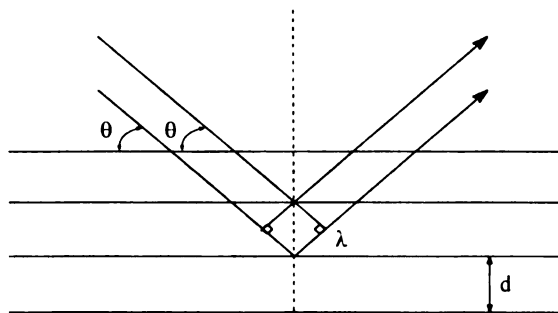
Figure 1.7 Schematic representation of the parameters from the Bragg equation

Measuring the angles, θ, under which the X-ray constructive interference occurs when it leaves the crystal, the Bragg equation (1-10) provides the corresponding lattice spacing, characteristic to a given crystalline solid material [56]. From the XRD diffraction pattern, the mean crystallite size ($\bar{d}$) of a given particle can be determined from line broadening calculations [57], using the Scherrer equation (1-11):

$$\bar{d} = k\lambda/\beta\cos\theta \qquad\qquad (1\text{-}11)$$

where λ is the X-ray wavelength, k is the particle shape factor (1 for spherical particles, or 0.9 for cubic particles), β is the full width at half maximum (FWHM) of the peak at a given 2θ, in radians, and θ is the diffraction angle. The XRD technique has some limitations among which the most important are: i) a clear diffraction pattern can be observed only when the solid material exhibits long range order; ii) crystalline particles less than 2-3 nm are not observable; iii) the method is not suitable for characterization of amorphous materials. This technique can provide clear and unequivocal information about sufficiently large crystalline materials that are used as catalysts, revealing structural modifications that occur during their preparation or after their use in a catalytic process.

In this study, X-ray powder diffraction patterns were obtained with a Rigaku XRD diffractometer employing monochromatic Cu Kα radiation (λ = 1.541838 Å) and operated at 45 kV and 100 mA. Diffraction patterns were obtained using a scan rate of 1 deg/min with 1/2 mm slits. Powdered samples were mounted on glass slides by pressing the powder into an indentation on one side of the slide.

Activity measurements. All reactions were performed in a vertical down-flow packed bed reactor equipped with a quartz insert [1,10]. Figure 1.8 presents the laboratory installation used for catalyst testing and lactic acid conversion studies. The reactor is designed for pressures up to 5 MPa at temperature < 500°C. The catalyst is supported on a quartz frit fused into a quartz tube, inserted into the reactor from the bottom and sealed. An internal thermocouple extends from the reactor flange to the bottom of the support frit. The reactor is electrically heated by a programmable temperature controller. During operation, catalyst temperature is measured by the internal thermocouple, and the reactor set point is adjusted to the desired value. The products of the reaction exit the bottom of the reactor and pass first through a trap placed in an ice bath. The outlet of the reactor was connected to a Riken infrared CO and CO_2 gas analyzer which measured the amounts of these gases produced in the reaction. Typically, products are collected for 30 min during steady-state operation of the reactor. The volume of the liquid product and the flow rate of the gas products are measured during operation in order to compute a mass balance.

Product analyses were performed using a Varian 3700 gas chromatograph equipped with FID detector and a Supelco packed column (4% Carbowax/Carbopack B-DA packed column). The product was mixed with a solution containing 2-propanol as an internal standard and oxalic acid as a column conditioner. Good reproducibility of the lactic acid analysis was achieved by direct injection of 1 μl of condensed product solution mixed with the internal standard. Major products analyzed include 2,3-pentanedione, acrylic acid, propanoic acid, acetaldehyde, and acetol. Minor components identified from

product analysis include ethanol, acetone, acetic acid, pyruvic acid and other unknowns reported as "others".
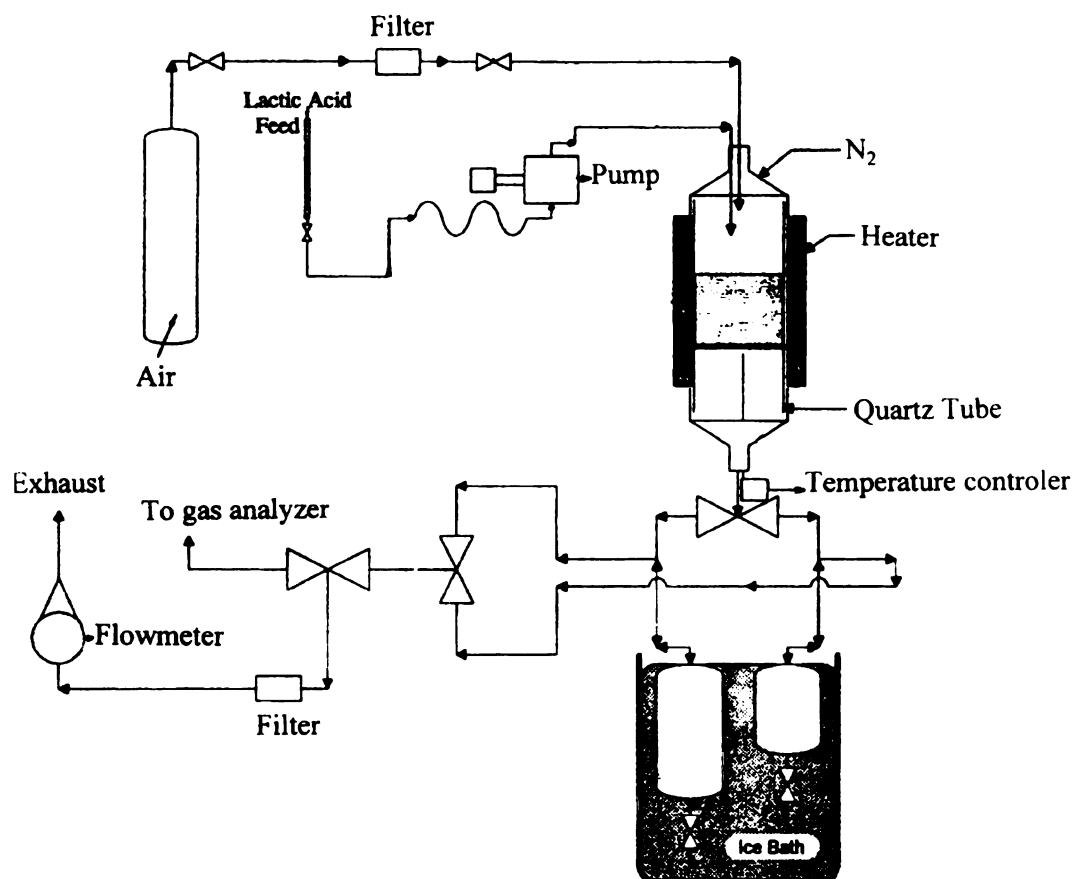
Figure 1.8 Schematic representation of the laboratory setup used for lactic acid conversion studies and catalyst testing.

All product yields are calculated from the ratios of product/internal standard peaks areas and detector response factors. Product component identification was performed by residence time analysis in the GC, by gas chromatography/mass spectrometry (GC/MS) and ^1H and ^{13}C NMR spectroscopy. Product yield was reported as percentage of the theoretical yield based on the lactic acid fed to the reactor; product selectivity is the

percentage of the theoretical yield based on lactic acid consumed in the reaction. The overall carbon balance gives recoveries ranging from 85% to 105%. Each catalyst loaded into the reactor was tested at several temperatures and residence times. The catalyst was heated at the desired temperature under a constant lactic acid flow-rate (0.5 ml/min) and allowed to reach steady state. Table 1.3 presents the experimental reaction conditions used for the catalyst testing.

Table 1.3 Experimental conditions used in lactic acid conversion on MOH/SiO_2 catalysts

Ord.#	Reaction parameters	Experimental value
1	Temperature [C]	200 - 350
2	Pressure [MPa]	0.5
3	Liquid flow rate [ml/min]	0.05 - 0.5
4	Feed composition [mole fraction]	Lactic acid: 0.08 Water vapor: 0.77 Helium: 0.15
5	Catalyst weight [g]	2.0 - 6.0
6	Catalyst bed height [cm]	2.5 -7.6
7	residence time [sec]	0.3 - 5.0

1.3 Results and discussions

Sodium phosphates supported on Si/Al catalysts. Activity data obtained for lactic acid conversion on NaH_2PO_4 and Na_3PO_4 supported on Si/Al catalysts, in comparison with the neat Si/Al support are presented in Table 1.4. The modifications occurring on the sodium phosphate catalyst as a function of temperature were studied using MAS-

NMR and DRIFT spectroscopies, and they were correlated with the differences observed in the catalytic activity. Differences in acidity for the two types of phosphate catalysts which have been chosen in this study, may influence the catalytic behavior. The two protons from NaH_2PO_4 confer on the catalyst a stronger acidity compared with the Na_3PO_4. Temperature plays an important role in the catalyst structure and catalytic activity.

Table 1.4   Yields (selectivities) from lactic acid conversion over sodium phosphate salts supported on Si/Al catalyst, at 300° and 350°C, respectively [10-11]

Product	Si/Al Support [%]		NaH₂PO₄ [%]		Na₃PO₄ [%]	
	300°C	350°C	300°C	350°C	300°C	350°C
L.A. conversion	5.7	17.4	2.5	17.6	19.9	39.9
23P	0.2 (3)	0.3(2)	0.2(11)	1.3(15)	4.3(31)	7.0(22)
Acetaldehyde	1.5(22)	9.0(48)	0.4(22)	2.5(28)	1.9(14)	5.2(16)
Acrylic acid	0.1(1)	0.8(4)	0.1(6)	1.5(17)	2.0(14)	9.8(31)
Propanoic acid	0.5(7)	1.2(6)	0.1(6)	1.7(20)	0.9(6)	1.5(5)
Carbon recovery	100.8	101.2	104.3	91.1	94.2	92.7

L.A. = lactic acid; 23P = 2,3 -pentanedione

The yield and selectivity data shown in Table 1.4 for lactic acid conversion on sodium phosphates supported on Si/Al catalyst indicate the best activity results for Na_3PO_4/Si/Al catalyst (yields of 20% with 30% selectivity, at 300°C). Elevated temperatures favor lactic acid conversion, but selectivity toward 23P formation decreases. Si/Al support shows good selectivity for acetaldehyde formation. This catalytic behavior can be attributed to the presence of surface acid sites (Bronsted and Lewis acid sites) on

Si/Al support structure. The same trend is observed in the case of the Si/Al supported NaH_2PO_4 catalyst, indicating that catalyst acidity favors the acetaldehyde pathway. Na_3PO_4 supported on Si/Al has no acid character. As a consequence, the selectivity for acetaldehyde is much lower than the selectivity for 23P. From these data, it can be concluded that the acid/base character of the catalyst plays an important role in the reaction pathway of lactic acid conversion.

Changes in the temperature may affect the catalyst structure. It is known that the sodium phosphate structure is very sensitive to temperature changes [22-24]. MAS-NMR combined with DRIFT spectroscopy have been used to study the types of phosphate species on the catalyst surface. Figure 1.9 shows the MAS-NMR spectra of pure NaH_2PO_4 salt after calcination at 450°C (19 a) and after aging in air for several days (1.9 b). As can be observed from Figure 1.9, simple water absorption can significantly modify the NMR spectrum of the NaH_2PO_4 salt calcined at 450°C. These spectra are different from that obtained for the NaH_2PO_4 before calcination (not shown), which presents a single isotropic peak at $\delta = 1.8$ ppm, similar with that reported in the literature [11, 22-24]. After calcination at 450°C, five unresolved isotropic peaks, marked with arrows, at -5.4, -15.3, -19.0, -24.0, and -26.2 ppm are observable (Figure 1.9). $^{31}P\{^1H\}$ proton decoupling has no effect on how well the peaks are resolved in the spectrum [11]. Peaks -15.3, -19.0, -24.0, and -26.2 ppm were assigned in the literature to linear sodium polyphosphate $(NaPO_3)_n$ species, in crystalline form [23].
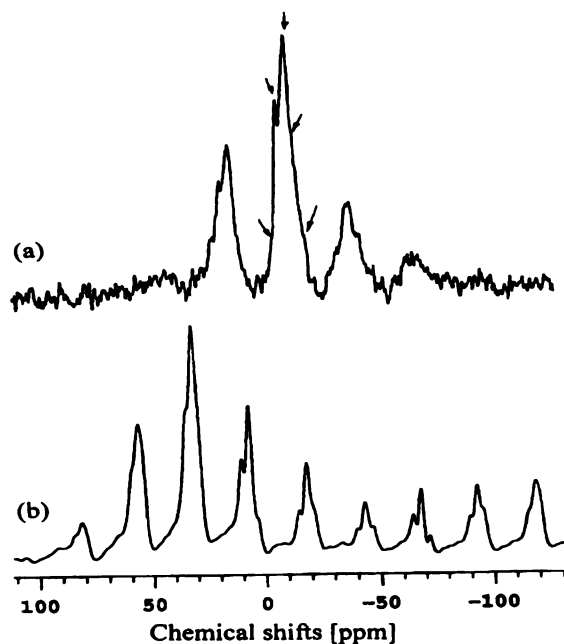
Figure 1.9 MAS-NMR spectra for the NaH_2PO_4 salt, calcined at 450°C (a) and aged (b).

The peak at -5.4 ppm observed can be attributed to an end-chain PO_4 group from a polyphosphate. This peak may also be attributed to the presence of a small quantity of the trimeric ring ($Na_3P_3O_9$). The decrease in the NaH_2PO_4 peak at 1.8 ppm as temperature increases, indicates structural modification of the sodium phosphate salt. These observations suggest that sodium polyphosphate was formed after calcination at 450°C. When supported on Si/Al catalyst and calcined at 450°C, the NMR spectrum of NaH_2PO_4 catalyst obtained (Figure 1.10) is different from that observed for the neat salt (Figure 1.9) with chemical shifts for the isotropic peaks around 11.8 ppm. These chemical shifts indicate that after calcination at 450°C, NaH_2PO_4 is transformed into a different phosphate species, probably polyphosphates (chemical shift analysis [11]). The ^{31}P NMR spectrum for the NaH_2PO_4 supported on Si/Al (Figure 1.10) is less well-

resolved than that of the pure material. Following drying and calcination, peaks specific

to $Na_3P_3O_9$ or other $(NaPO_3)_n$ polymeric amorphous materials are observable [11].
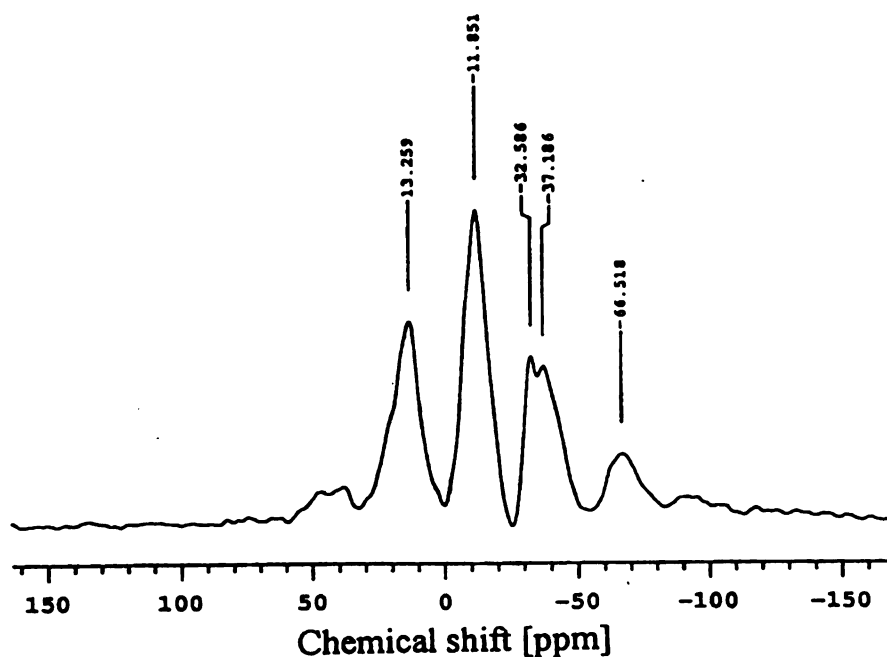
Figure 1.10 ^{31}P-NMR spectrum of Si/Al supported NaH_2PO_4 calcined at 450°C

The peak at 1.8 ppm specific to NaH_2PO_4 is not easily observed in Figure 1.10, indicating

that all the NaH_2PO_4 deposited on Si/Al support was converted into other phosphate

species (as expected based on data from Figure 1.9). Heating at 450°C, a broad isotropic

peak centered at -11.85 ppm is observed. Proton decoupling NMR experiments

suggested that more than one peak is present in this chemical shift region [11]. Peaks -

15.3, -19.0, -24.0, and -26.2 ppm were assigned in the literature to linear sodium

polyphosphate $(NaPO_3)_n$ species in crystalline form [23]. Any shift in these values may

indicate the formation of amorphous sodium polyphosphate species. Peaks with chemical

shifts close to these values can be observed in the spectrum presented in Figure 1.10, as well. A peak at -5.4 ppm, observed as a shoulder in Figure 1.10 can be attributed to end-chain PO_4 groups, based on literature data [11]. From these observations, it can be concluded that sodium polyphosphate was formed after calcination at 450°C, on Si/Al support. The extent of phosphate polymerization can be calculated from the intensity ratio of the end-chain to intra-chain PO_4 NMR peaks.

In order to find the degree of phosphate polymerization and to identify other possible sodium phosphate species formed, T_1 values were measured and full relaxation of the ^{31}P nucleus was ensured during analysis. Spin-lattice relaxation time (T_1) values were evaluated for each peak from the NMR spectrum presented in Figure 1.10, based on the exponential dependence of magnetization versus T_1 (see relation 1-1) shown in Figure 1.11, are reported in Table 1.5. Due to the fact that the isotropic peaks are not the most intense peaks in the spectrum, all the peaks in the 0-100 ppm were considered in the relaxation time experiments. Peaks indicating similar T_1 values correspond to the same species, so that T_1 can be used to identify various phosphate species formed on Si/Al supports. T_1 values presented in Table 1.5 indicate that at least three different phosphate atoms are present on the catalyst surface. The error in the value for T_1 was less that 10%. The presence of less intense peaks which overlap with some of these peaks can't be excluded. The peak at -32.59 ppm shows the longest T_1 value. A longer T_1 value corresponds to a longer relaxation due to a stronger coupling between the nuclear spin and the neighbors spins from the lattice [26]. As a consequence, this peak can be

attributed to a different phosphate species, maybe a cross-linked polyphosphate species

formed during thermal treatment of the catalyst.
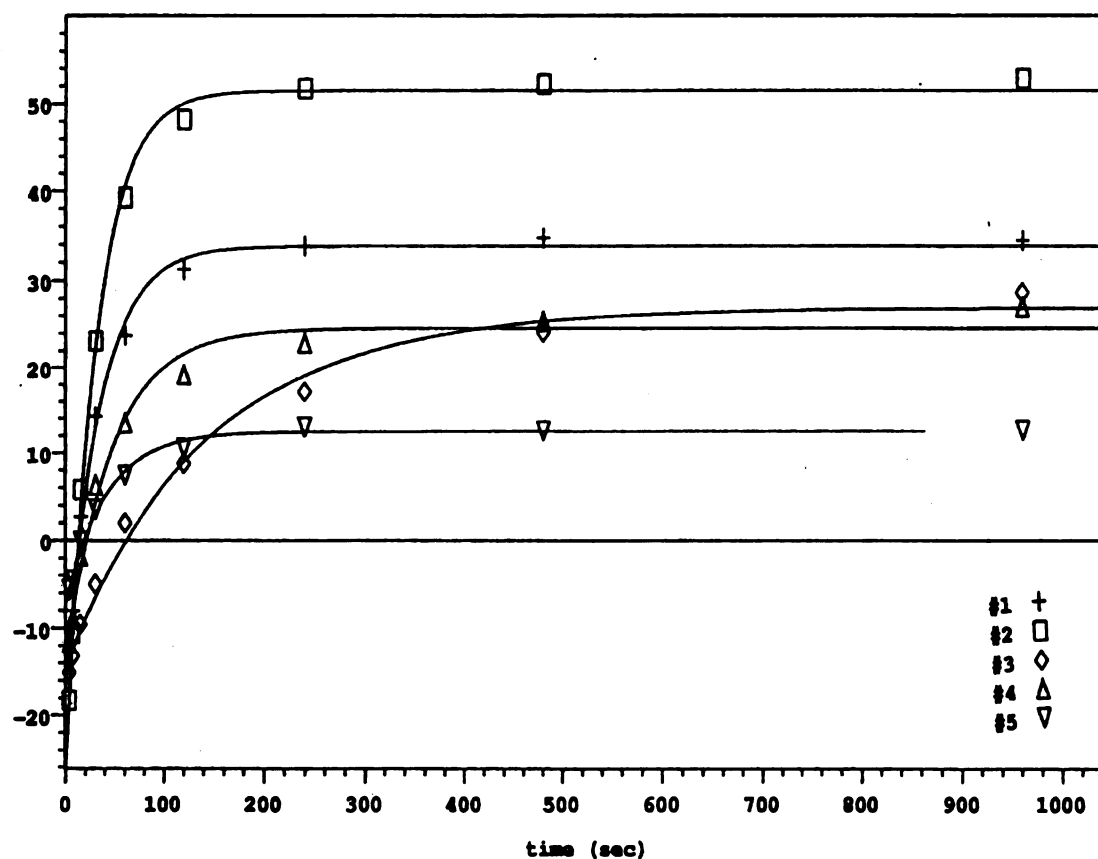
Figure 1.11 ^{31}P-NMR intensity versus time [s], for the peaks specific to the Si/Al supported NaH_2PO_4 catalyst, calcined at 450°C, where #1 = 13.26 ppm, #2 = -11.85 ppm, #3 = -32.59 ppm, #4 = -37.19 ppm, #5 = -66.52 ppm.

Table 1.5 Spin-lattice relaxation time (T_1) values for Si/Al supported NaH_2PO_4 catalyst, calcined at 450°C, evaluated from the exponential dependences in Figure 1.11.

Peak #	Peak's chemical shift [ppm]	Relaxation time [seconds]	Error [seconds]
1	-13.26	33.5	2.4
2	-11.85	30.1	1.6
3	-32.59	144	18.3
4	-37.19	47.1	6.5
5	-66.52	45.3	5.7

Summarizing all the information from the NMR spectra (Figures 1. 9-11) and from the T_1 calculations, it can be concluded that amorphous, short chain (3<n<6) sodium polyphosphate species are formed on Si/Al support after calcination at 450°C [11]. This observation is reasonable considering the fact that on the support, NaH_2PO_4 is likely to be in a more dispersed phase that in the neat salt, so smaller condensation products such as trimetaphosphate (trimer) are favored over polyphosphate (liner polymer). Phosphate anions may also interact with the surface acidic sites of the Si/Al catalyst, inhibiting formation of long polyphosphate chains [10].

Considering the low structural stability of the NaH_2PO_4 catalyst (formation of sodium pyrophosphate or triphosphate) and the relatively high acidity of the sodium salt formed at elevated temperatures (competitive with lactic acid's acidity) the observed high selectivity to acetaldehyde can be explained (see Table 1.4). The small modifications observed in the structure of the Na_3PO_4 salt and Na_3PO_4 supported on Si/Al catalysts with

temperature are well reflected by the NMR spectra obtained for these compounds and presented in Figure 1.12 a-d.
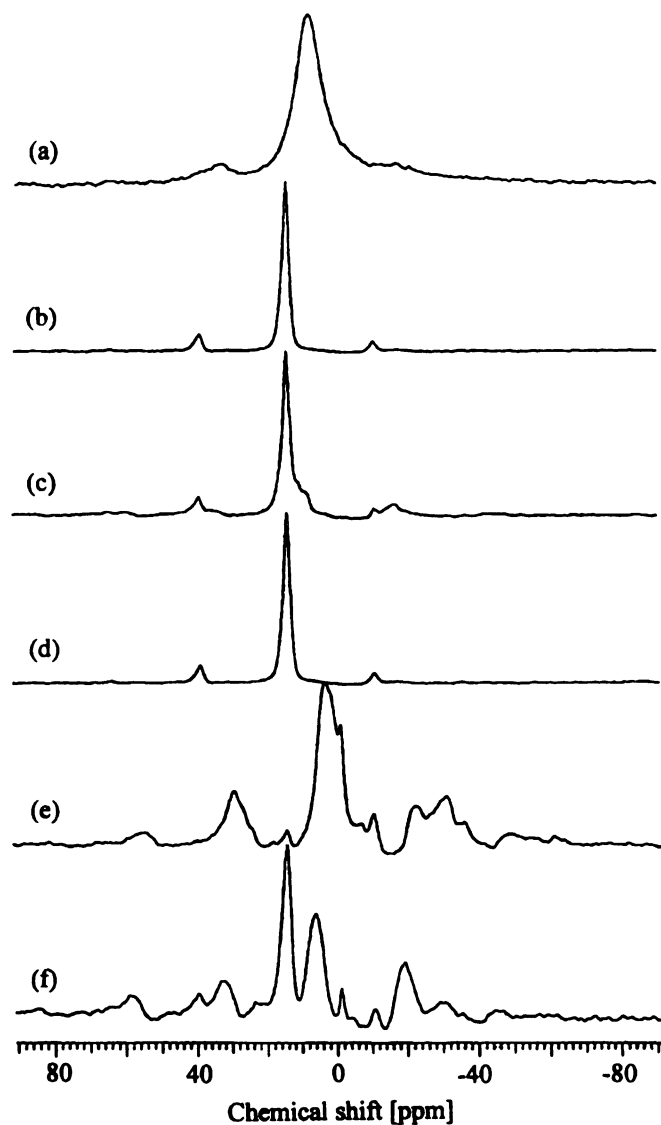
Figure 1.12 ^{31}P-NMR of Na_3PO_4 salt and Na_3PO_4 supported on Si/Al catalysts: a) $Na_3PO_4x12H_2O$; b) Na_3PO_4 calcined at 450°C; c) Na_3PO_4/Si/Al catalyst dried at 100°C; d) Na_3PO_4/Si/Al catalyst dried at 450°C; e) used Na_3PO_4/Si/Al catalyst in lactic acid conversion; f) regenerated Na_3PO_4/Si/Al catalyst by calcination at 450°C.

However, significant changes in catalyst structures were observed after its utilization in lactic acid conversion or regeneration by recalcination (Figure 1.12 e-f).

The NMR spectrum of $Na_3PO_4 \times 12H_2O$ presented in Figure 1.12 a shows one isotropic peak at -7.5 ppm, in good agreement with the literature [22-24]. Calcination at 450°C led to dehydration, resulting in a narrowing of the isotropic peak and a shift to -14.2 ppm (Figure 1.12 b). Supporting the Na_3PO_4 salt on a Si/Al catalyst and drying at 100°C led to a phosphate catalyst with a spectrum having peaks specific to hydrated and dehydrated Na_3PO_4 species (Figure 1.12 c). The spectrum of the Na_3PO_4/Si/Al catalyst dried at 450°C shown in Figure 1.12 d looks similar with that of the dehydrated Na_3PO_4 salt spectrum (Figure 1.12 b). As can be observed, simple thermal treatment of the Na_3PO_4 catalyst led to very minor structural changes compared to the NaH_2PO_4 catalyst. Utilization of the Na_3PO_4 catalyst in the lactic acid conversion led to significant modification in the catalyst structure as can be observed in Figure 1.12 e. Regeneration of the catalyst, by recalcination at 450°C occurs only partially, as observed from the ^{31}P NMR spectrum (Figure 1.12 f). To improve peak assignments, samples were analyzed at two different spinning frequencies. Variation in the spinning rate alters the positions of the spinning side-peaks band, leaving the chemical shift of the isotropic band unchanged. Thus, variation of the spinning rate allows separation and identification of the isotropic bands in the spectrum. Figure 1.13 shows the ^{31}P NMR spectra of the used and regenerated Na_3PO_4 supported on Si/Al catalyst, at 4 kHz and 6 kHz, respectively.
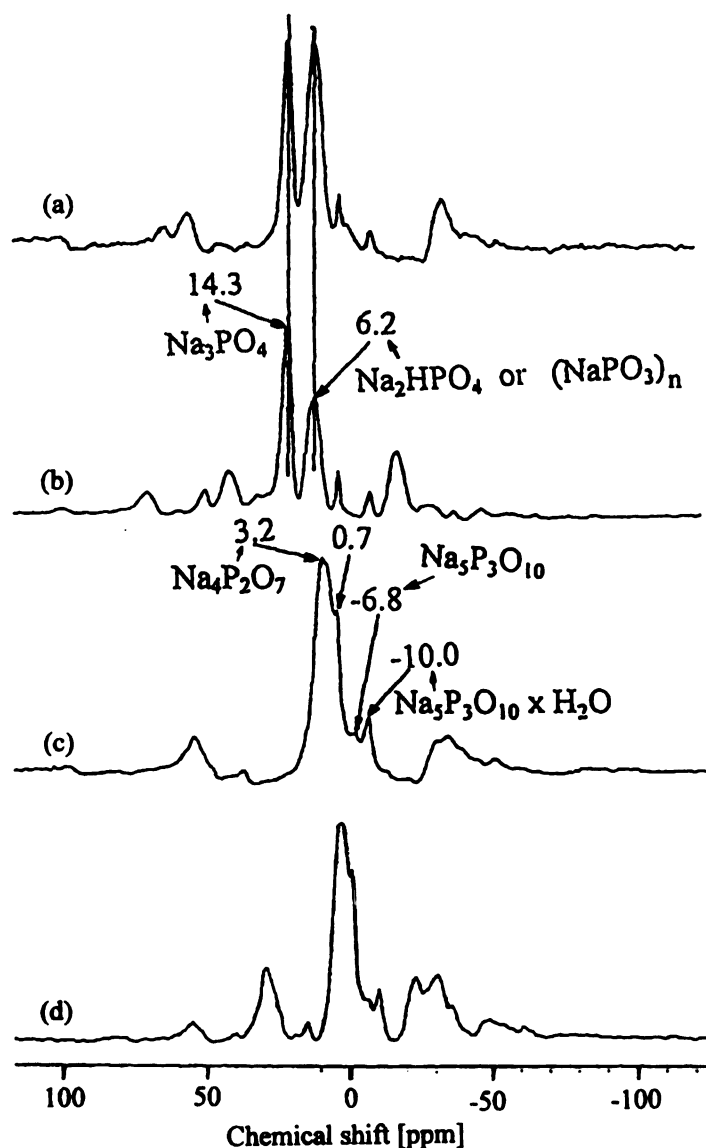
Figure 1.13 ^{31}P-NMR of Na$_3$PO$_4$ supported on Si/Al catalysts: a) regenerated at 6 kHz; b) regenerated at 4 kHz; c) used at 6 kHz; d) used at 4 kHz

The ^{31}P NMR spectrum of the used Si/Al supported Na$_3$PO$_4$ catalyst presented in

Figure 1.13 c obtained at 6 kHz shows a better separation of the isotropic band from the

spinning bands, consequently it was used to identify the phosphate species formed during

its utilization in the lactic acid conversion. The spectrum shows five isotropic peaks at

3.2, 0.7, -0.6, -6.8, and -10.0 ppm. The primary species present are the anhydrous

$Na_4P_2O_7$ (3.2 ppm) and $Na_4P_2O_7 \times 10H_2O$ (-0.6 ppm), as indicated on the figure. The peaks for these species are shifted slightly from the standard value but are within the ranges reported in the literature [11, 24]. The peaks at 0.7 ppm and -6.8 ppm are assigned to anhydrous sodium triphosphate ($Na_5P_3O_{10}$) and the peak at -10 ppm to a hydrated triphosphate ($Na_5P_3O_{10} \times H_2O$). The linear triphosphate is believed to form by condensation of the $Na_3HP_2O_7$ and Na_2HPO_4 (proton exchange products). The loss in catalytic activity can be attributed to the formation of this type of polyphosphate species. It is known that in water, the extent of sodium dissociation from phosphate anions, while over 90% for orthophosphates, decreases with increasing chain length for condensed phosphates [58].

As can be observed from Figure 1.13 a,b, calcination at 450°C of the used catalyst only partially regenerates the active Na_3PO_4 species (reappearance of the peak at 14.3 ppm). The extra peaks from the NMR spectrum of the regenerated catalysts, at 6.2, 0.7, -6.8, -10 ppm, can be attributed to various types of polyphosphate species $(NaPO_3)_n$ or of Na_2HPO_4 which maybe formed at elevated temperature from $Na_4P_2O_7$ and $Na_5P_3O_{10}$ in the used catalyst (see Figure 1.13).

Additional information about chemical transformations that occurred on the Si/Al supported Na_3PO_4 catalyst during lactic acid conversion were obtained from DRIFTS analysis. The DRIFTS spectra for the Na_3PO_4 catalysts are presented in Figure 1.14.
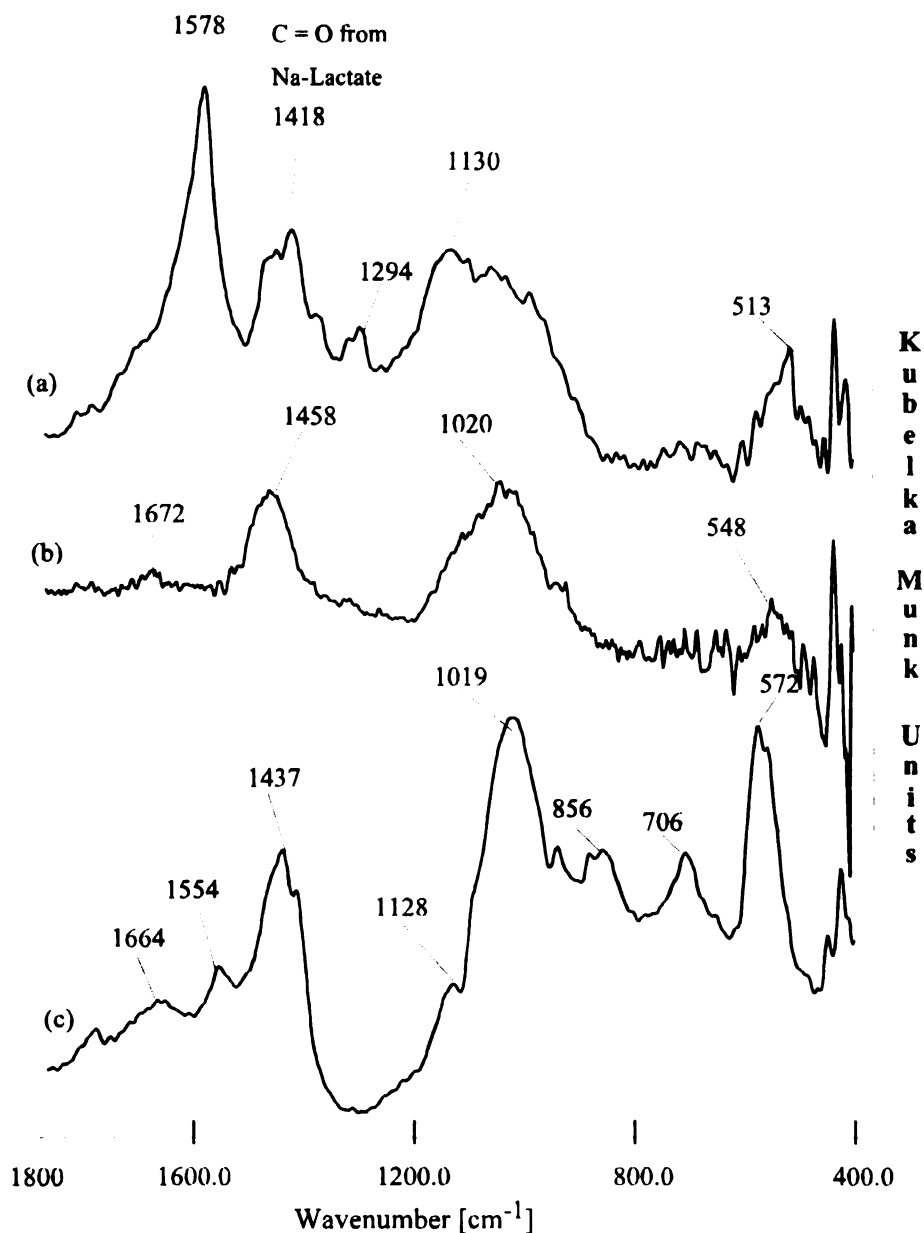
Figure 1.14. DRIFTS spectra for Si/Al supported Na_3PO_4 catalysts: a) following lactic acid exposure at 320°C and b) fresh, compared with c) pure Na_3PO_4 salt.

The presence of IR bands specific to tetrasodium pyrophosphate (1120 cm^{-1}) on the supported catalyst exposed to lactic acid vapors at 320°C (see Figure 1.14 a) is in good agreement with the results from ^{31}P NMR. The DRIFTS spectra of Na_3PO_4 on Si/Al (Figure 1.14 b) and neat Na_3PO_4 salt (Figure 1.14 c) confirm the lack of change in

the catalyst structure observed by NMR. Proton transfer from lactic acid to Na_3PO_4 (and to a lower extent at NaH_2PO_4, $Na_4P_2O_7$ or other polyphosphate species) was implied by the observation of sodium lactate as a stable species on the catalyst surface, during reaction [11]. The large quantity of sodium lactate on the Na_3PO_4 catalyst surface may explain the higher activity relative to NaH_2PO_4, at lower temperature (see table 1.4). Conversion at high temperatures is affected by something other than quantity of the sodium lactate present on the catalyst surface. This information may be useful to understand and optimize the catalyst's activity and to elucidate the mechanism of lactic acid conversion to 23P (see details in Chapter 2).

Ba/Na/SiO₂ catalysts; influence of SiO₂ support configuration on lactic acid conversion. The interest in this study came from the fact that a simple high surface area silica support ($hSiO_2$) has a much lower price in comparison with a silica with low surface area but well controlled pore size distribution ($lSiO_2$) used in previous studies [64-66]). Barium is known to be a useful additive to high surface area catalysts (Al_2O_3, TiO_2) conferring good thermal stability on the porous material [59]. Inexpensive and non-toxic alkali and alkaline-earth metal hydroxides and nitrates [NaOH, $Ba(NO_3)_2$] supported on SiO_2 with various surface areas, have also been successfully used to produce 23P together with other valuable chemicals (acrylic acid or propanoic acid) with high conversion and selectivity. Supported Ba/Na and NaOH on $lSiO_2$, and $hSiO_2$ catalysts, prepared as described previously, were characterized by DRIFTS spectroscopy and X-ray diffraction (XRD) and used in lactic acid conversion.

In order to understand the catalytic activity for a given solid material it is essential to obtain information about its surface configuration and structure. Following the

preparation steps by IR spectroscopy reveals the molecular level structural changes of the catalysts during the process. Figures 1.15 and 1.16 show series of DRIFTS spectra for hSiO$_2$ and lSiO$_2$ catalysts, respectively. Figures 1.15 a and Figure 1.16 a show spectra of the supports. Specific to hSiO$_2$ are the band at 3738 cm^{-1}, attributed to the O-H stretching mode of free hydroxyl groups, and at 1630 cm^{-1} and 1291-969 cm^{-1}, attributed to bending mode of bond vibrations. The spectrum for lSiO$_2$ is very similar with that for hSiO$_2$ but the -OH groups appear more as broad bands specific to hydrogen bonded hydroxyl groups (see bands in the 3000-3600 cm^{-1} region).

Before impregnation, the silica supports were treated with a sodium-methoxide/ methanol (CH$_3$ONa/CH$_3$OH) solution to annihilate any acid sites (Brönsted acid sites) from the surface. After drying, DRIFTS spectra were acquired. Figures 1.15 b and Figure 1.16 b show spectra of the silica supports impregnated with CH$_3$ONa solution. From these figures, it can be observed how the bands at 3738 cm^{-1} and 3000-3600 cm^{-1}, corresponding to the surface hydroxyl groups disappeared, and a new band at 778 cm^{-1} (860 cm^{-1}) appears. Morrow and McFarlan [60] have indicated an upward shift of bands from the 900-750 cm^{-1} IR region[2] where bands specific to Si-O- stretch from a Si-O-H group are observable when hydrogen was replaced by deuterium. Consequently, the band observed at 778 cm^{-1} (860 cm^{-1}) from Figure 1.15 (or Figure 1.16) can be attributed to a - Si-O- vibration when -Si-O-Na is formed [61].

---

[2] firmly established in the literature as Si-O deformation and stretching modes of bond vibration [59-62].
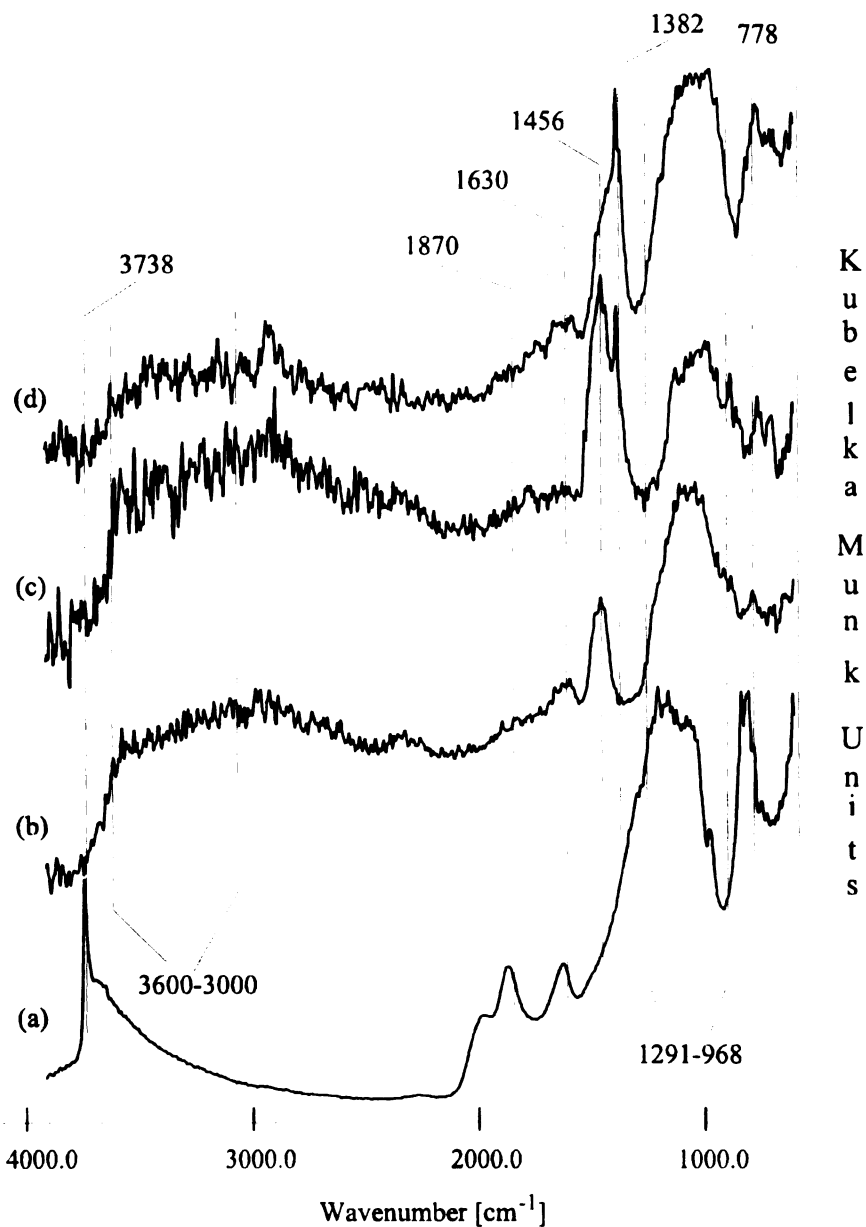
Figure 1.15 DRIFTS spectra for Ba/Na/hSiO₂ catalyst acquired at different times during preparation: (a) pure hSiO₂ catalyst ; (b) hSiO₂ treated with CH₃-ONa ; (c) Ba(NO₃)₂/NaOH on hSiO₂ catalyst dried at 125°C ; (d) Ba/Na/hSiO₂ catalyst calcined at 400°C.
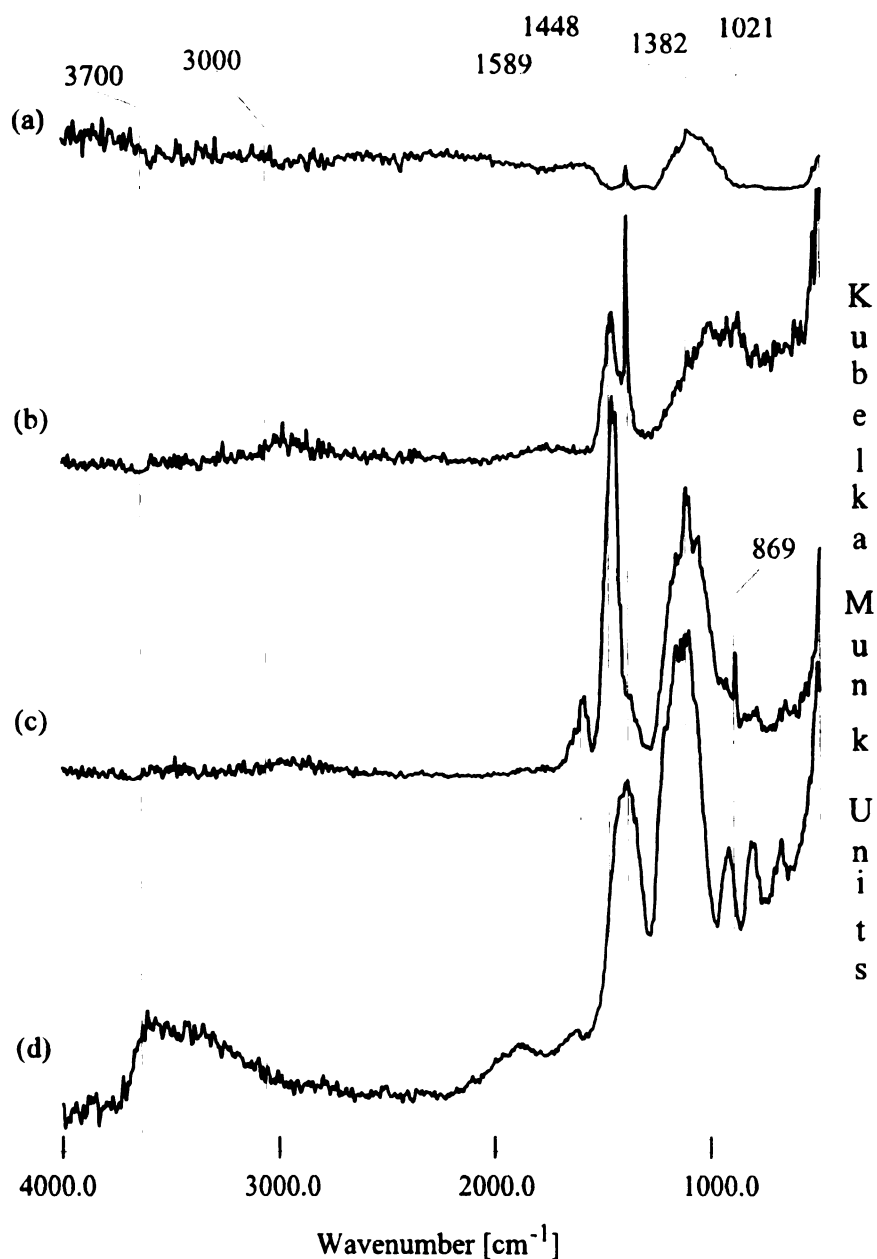
Figure 1.16 DRIFTS spectra for Ba/Na/lSiO$_2$ catalyst acquired at different times during preparation: (a) pure lSiO$_2$ catalyst; (b) lSiO$_2$ treated with CH$_3$-ONa; (c) Ba(NO$_3$)$_2$/NaO-lSiO$_2$ catalyst dried at 125°C; (d) Ba/Na/lSiO$_2$ catalyst calcined at 400°C.

Aqueous Ba(NO$_3$)$_2$ was then used as precursor for wet impregnation of the silica supports. After drying at 125°C and calcination at 400°C, the catalysts were characterized using DRIFTS and XRD. Figures 1.15 c and 1.16 c show the DRIFTS

spectra of the dried catalysts and Figures 1.15 d and 1.16 d the spectra of the calcined catalysts. In the case of dried catalyst, a band at 1382 cm^{-1} attributed to NO_3^- vibration [62] appeared as a new feature in the spectrum, for both types of catalysts. After calcination, this band is diminished due to the elimination of the nitrate from the system. This process is more pronounced in the case of the $Ba/Na/lSiO_2$ catalyst due to the low surface area which makes the elimination of nitrate gases easier.

The information obtained from the XRD spectra of the Ba/Na supported on $hSiO_2$ (Figure 1.17 a-d) and on $lSiO_2$ (Figure 1.18 a-d), are in good agreement with those from DRIFTS analysis. In addition, it was found that after drying at 100°C, $Ba(NO_3)_2$ starts to decompose and form $Ba(OH)_2$. XRD patterns specific to $Ba(OH)_2$ are observable in Figure 1.17 c and 1.18 c, respectively. No patterns of crystalline $Ba(NO_3)_2$ are observed after calcination at 400°C. On the $hSiO_2$ support, calcination of barium nitrate favored the formation of γ-$Ba(OH)_2$ whereas on $lSiO_2$ support, the β-$Ba(OH)_2$ forms [63]. As expected, no crystalline phases are formed or observed on the NaOH catalyst supported on SiO_2 and calcined at 400°C. Knowledge about catalyst structure allow us to explain the catalytic activity observed for these solid materials (see Table 1.6).

There are differences in catalytic activity between the Ba/Na and NaOH supported catalysts as well as between the catalysts supported on low and high surface area SiO_2. The neat SiO_2 supports show little catalytic activity (lactic acid conversion is below 30 %). The $hSiO_2$ support is more active, but toward acetaldehyde formation. This fact can be attributed to higher number of acid sites on the $hSiO_2$ than on the $lSiO_2$ support, favoring the acetaldehyde pathway (see Figure 1.1).
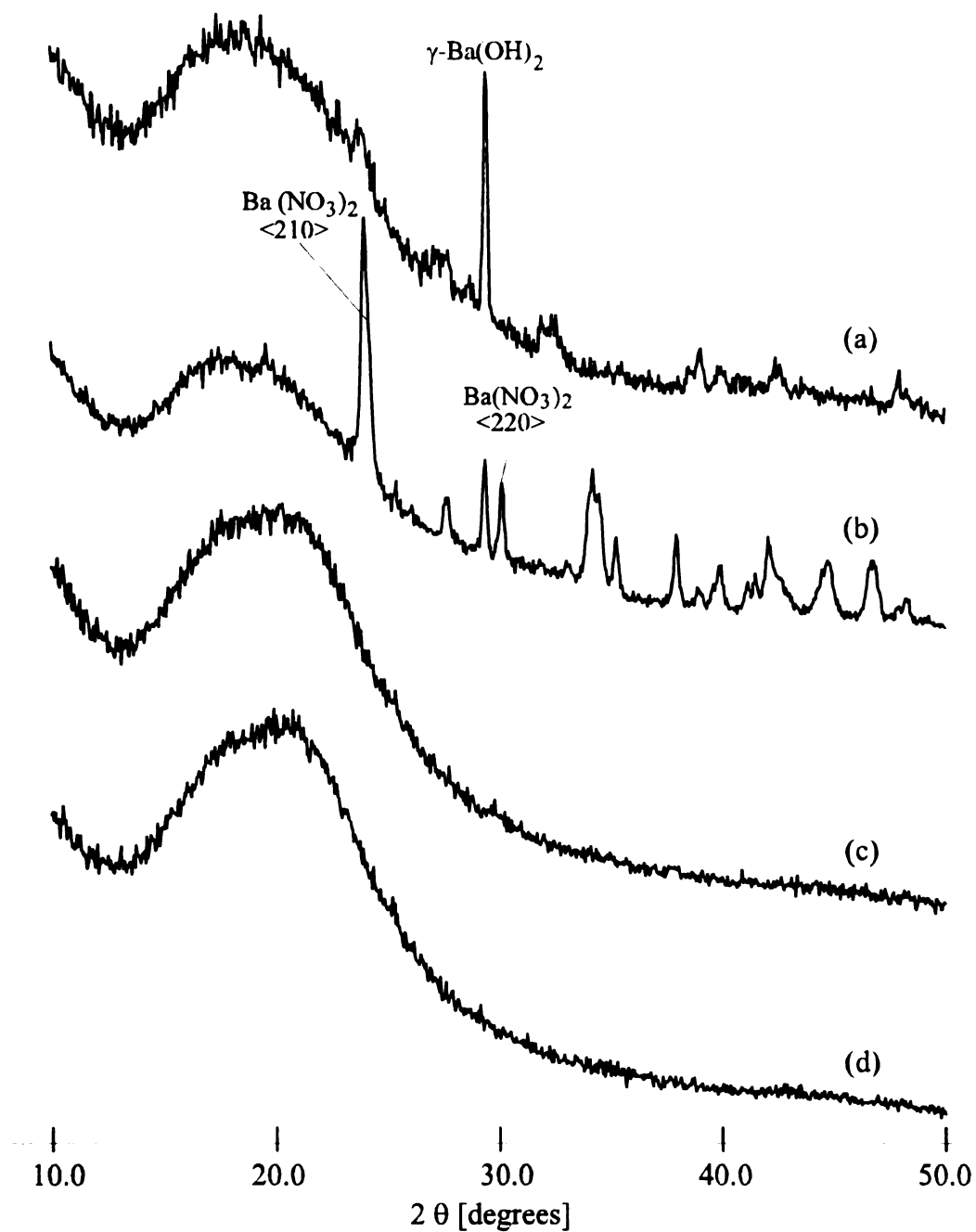
Figure 1.17   XRD spectra for hSiO₂ supported Ba/Na and NaOH catalysts: a) Ba/Na calcined at 400°C; b) Ba/Na dried at 100°C; c) NaOH calcined at 400°C; d) pure hSiO₂ support.
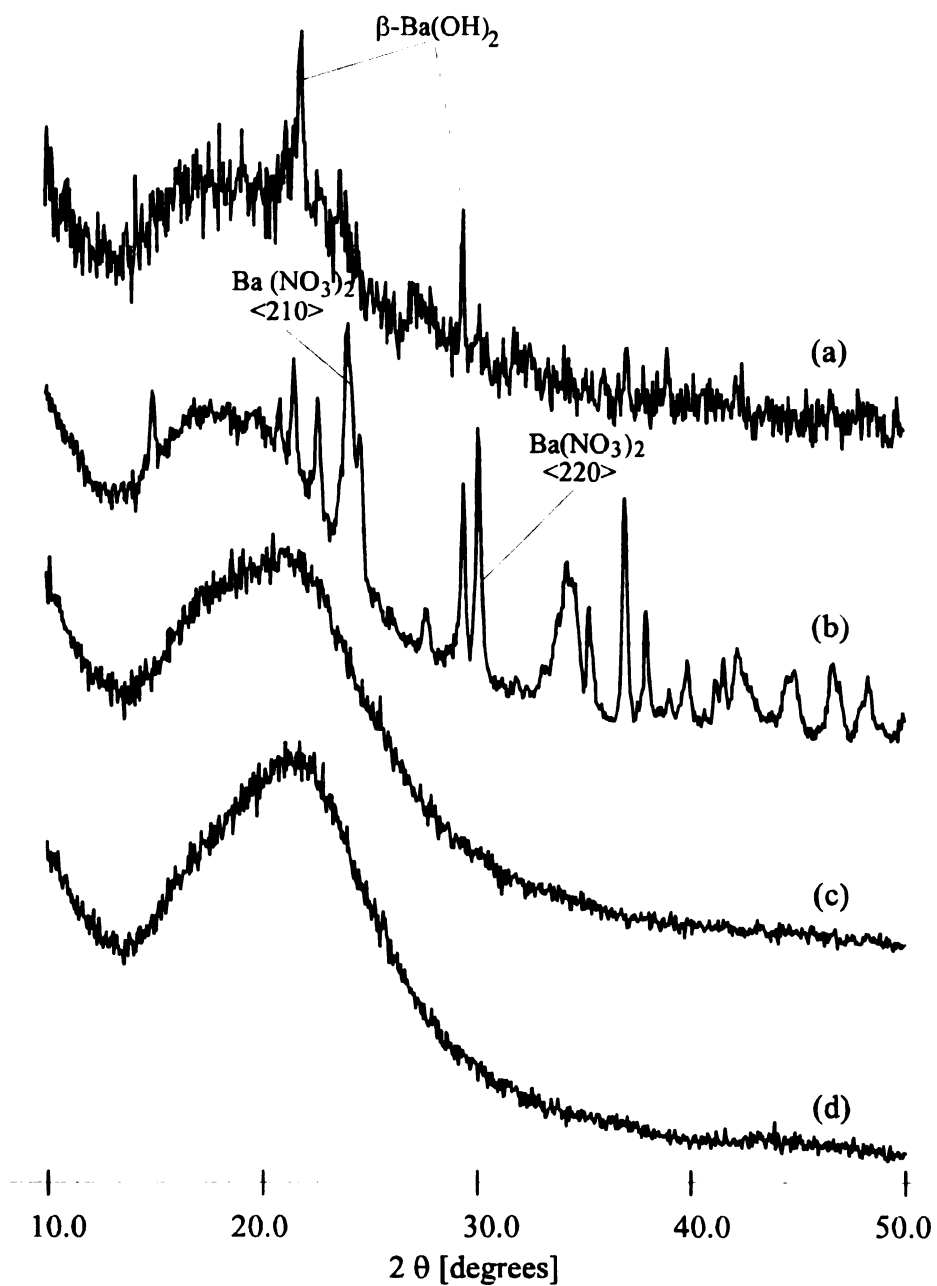
Figure 1.18   XRD spectra for $lSiO_2$ supported Ba/Na and NaOH catalysts: a) Ba/Na calcined at 400°C; b) Ba/Na dried at 100°C; c) NaOH calcined at 400°C; d) pure $lSiO_2$ support.

Table 1.6 Yields and selectivities from lactic acid conversion over Ba(OH)₂ and NaOH supported on SiO_2, at 280°C, with 1 mmole MOH/g SiO_2 loading

Products	Low SiO_2	High SiO_2	Ba/Na on lSiO_2	Ba/Na on hSiO_2	NaOH/ lSiO_2	NaOH/ hSiO_2
Yield in						
23P	0.1	1.2	30.3	12.3	15.3	16.7
Acrylic Acid	0.4	0.5	7.8	0.0	3.7	2.9
Propanoic Acid	0.2	0.0	0.7	2.1	0.0	0.7
Acetaldehyde	1.5	18.4	9.6	37.1	2.5	5.1
Selectivity						
23P	3.5	6.0	59.9	23.6	64.6	66.0
Propanoic Acid	9.8	0.0	1.4	3.9	0.0	2.6
Acetaldehyde	66.8	91.2	18.9	70.9	10.4	20.1

Lactic acid conversion on the Ba/Na catalysts is much higher (reaching 97% on hSiO_2 support) than on the NaOH catalyst, at the same reaction conditions. This activity is probable due to the presence of both Ba and Na hydroxide on the catalysts surface, as observed from DRIFTS and XRD data. However, the XRD pattern shows narrow peaks which correspond to large crystalline particles (low dispersion), specific to β- and γ-Ba(OH)₂ phases on the SiO_2 support. Lower Ba dispersions result in higher yield and selectivity toward acetaldehyde, as observed in the case of the neat SiO_2 support. As a consequence, on untreated supports, yield and selectivity to 23P are relatively low, and decrease in the case of the Ba/Na catalyst supported on hSiO_2. The NaOH catalysts show high yield and selectivity in 23P with small difference between the catalyst supported on lSiO_2 and hSiO_2. This may suggest that NaOH is well dispersed on the SiO_2, neutralizing

the surface acidity of the catalysts and minimizing acetaldehyde formation. Lactic acid conversion however, reaches only 40%, much lower than in the case of Ba/Na supported catalysts.

MOH/SiO$_2$ catalysts- Influence of MOH loading on lactic acid conversion (M = Na, K, Cs). A basic conclusion from the work previously presented is that the yield and selectivity toward 23P formation is favored by the basicity of the catalyst and the configuration of the surface acidity of the support. A comparison study of several sodium salts supported on various type of supports have indicated that the hydroxide may act as an optimum catalyst for conversion of lactic acid to 23P [1, 10, 64].

This part of the study explores the importance of the basic character of the catalyst for 23P formation and tries to optimize the reaction temperature and alkali metal cation hydroxide type and loading on the hSiO$_2$. Figure 1.19 shows the temperature dependence of the yields and selectivities for lactic acid conversion to 23P, in the 250°-380°C range, on various types of hSiO$_2$ supported alkali metal (M = Na, K, Cs) hydroxide (1 mmole/g support) catalysts. As observed, the optimum temperature range is around 300°C, for CsOH and KOH supported catalyst, and slightly higher for NaOH. Yields of 40% with selectivities of 80% in 23P were obtained for the CsOH/hSiO$_2$ catalyst. Lower temperature favors lower conversion but higher selectivity toward 23P. Pure hSiO$_2$ support has little catalytic activity (yields and selectivity to 23P do not exceed 10%, at temperatures lower than 350°C). In contrast, acetaldehyde formation is favored by high temperatures and by the neat hSiO$_2$ support, as observed in Figure 1.20. The trend of catalytic activity is similar for all MOH supported catalysts.

There are significant variations in the catalytic activity toward 23P formation as a function of MOH loading. As observed in Figure 1.21 a, the yield in 23P increases with the MOH loading, reaching a maximum at 2 mmole MOH/g $hSiO_2$ support. The difference between 2 mmole and 1 mmole MOH is not significant. It appears that above 2 mmole MOH/g support there is a saturation effect, which may be attributed to either a limited access of the lactic acid to the MOH to form lactate or to the formation of an non-optimum lactate/lactic acid ratio (pH value of the buffer), at the contact time used in the experiment. At very high MOH loading (9 mmole/g, not shown) the yield and selectivity to 23P is very low. The trend is very similar for the selectivity in 23P, as observed in Figure 1.21 b. The best yield (42%) and selectivity (80%) was obtained in the case of the 2 mmole KOH/g catalyst.

The catalysts behavior toward acetaldehyde is opposite from that observed in the case of 23P; at low MOH loading the lactic acid conversion is higher than in the case of high loading. This can be attributed to the catalytic effect of the support which can be accessed by the lactic acid feed due to low MOH coverage. Compared with previous studies on same type of catalysts, but using a $lSiO_2$ support with well controlled pore size distribution [10, 64], the 23P yield and selectivity results are comparable (lower by ≈ 3-5%) with those presented here, in the case of a $hSiO_2$ support. As a consequence, in this case it appears that the support porosity plays a minor role in the 23P reaction pathway (Figure 1.1).

a)
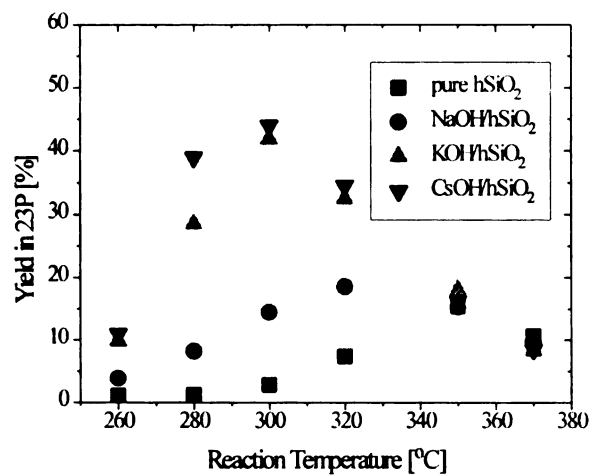
b)
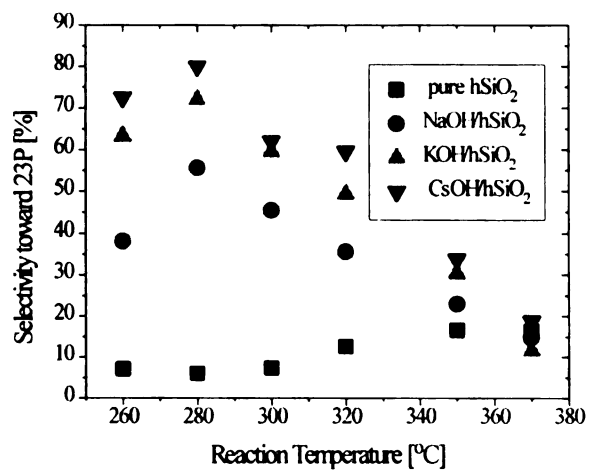
Figure 1.19 Conversion of lactic acid to 23P as a function of temperature, for hSiO₂ supported MOH (M = Na, K, Cs) catalysts: a) yields; b) selectivities.

a)
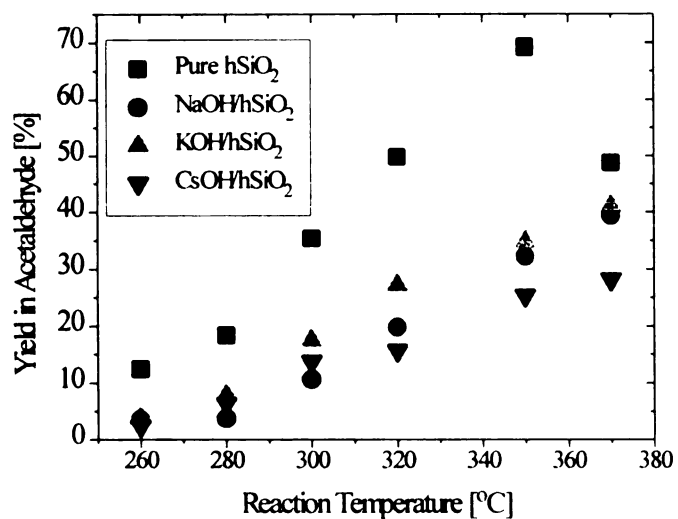
b)
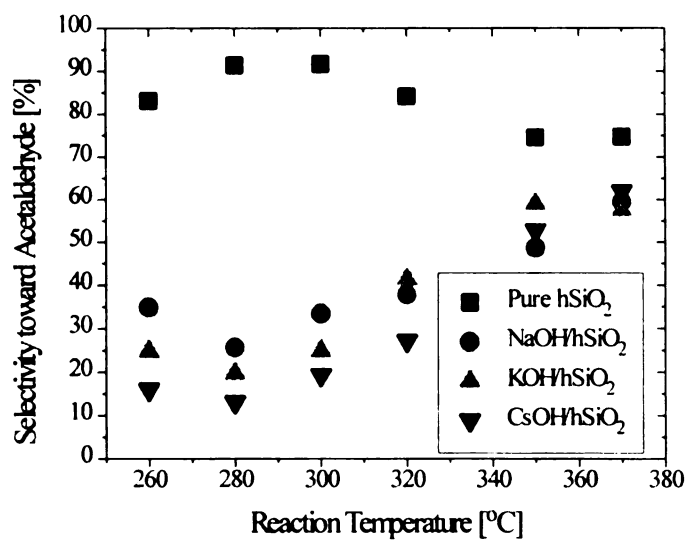
Figure 1.20 Temperature dependence of lactic acid conversion to acetaldehyde for $hSiO_2$ supported MOH (M = Na, K, Cs) catalysts: a) yields, b) selectivities.

a)
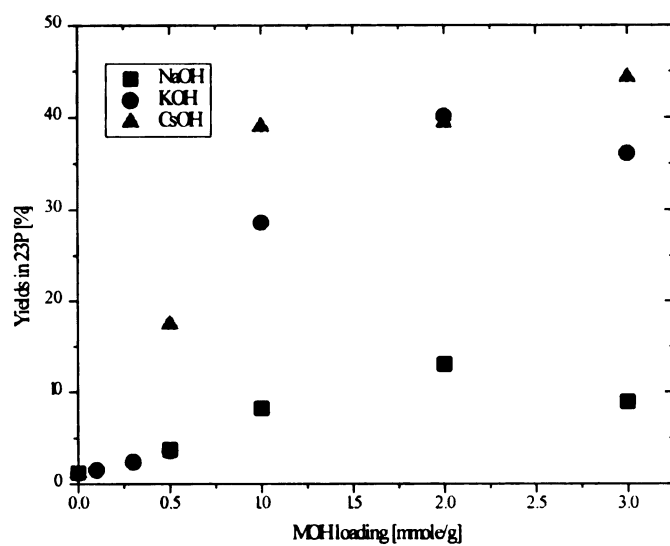
b)
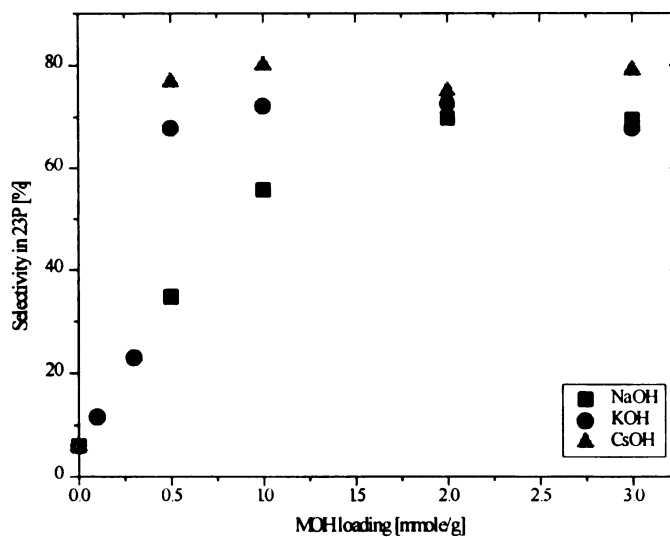
Figure 1.21 Activity data for lactic acid to 23P conversion on $hSiO_2$ supported MOH (M = Na, K, Cs) catalysts, as a function of MOH loading: a) yields, b) selectivities.

Compared with previous studies on same type of catalysts, but using a $lSiO_2$ support with well controlled pore size distribution [10, 64], the 23P yield and selectivity results are comparable (lower by $\approx$3-5%) with those presented here, in the case of a $hSiO_2$ support. As a consequence, in this case it appears that the support porosity plays a minor role in the 23P reaction pathway (Figure 1.1). A high surface area favors the acetaldehyde pathway (Figure 1.1) due to the higher number of surface acid sites. However, this acidity is easily neutralized by the strong basicity of the alkali metal hydroxides supported on the $hSiO_2$, and the reaction pathway is directed more toward 23P formation, a process favored by a base catalyst. Lactic acid conversion on a 2 mmole $CsOH/g\ hSiO_2$ catalyst has proven to be optimum for 23P pathway. The easy access of lactic acid to a Cs ion characterized by a large ionic radius, small hydration sphere and mobility, low Lewis acidity allows the lactate/lactic buffer formation, with a pH optimum for the process. The differences between KOH and CsOH are very small, so the former may be more attractive from catalyst preparation and economic points of view.

1.4 Conclusions

From the data presented above, several sets of conclusions can be outlined: 1) the yield and selectivity of phosphate-catalyzed lactic acid conversion to 23P is a function of the sodium phosphate species from the Si/Al support; conversion up to 20% in lactic acid with selectivity of 30% in 23P was obtained on Na_3PO_4 supported on Si/Al catalyst; lower yields and selectivity in 23P were obtained in the case of NaH_2PO_4/Si/Al catalysts; this fact was attributed to acidity of the catalyst, reflected by high yield and selectivity in acetaldehyde; sodium polyphosphates are formed on the catalysts' surface after exposure

to the reaction feed; ^{31}P-NMR relaxation time experiments help to differentiate various type of sodium phosphate species present on the Si/Al support and to evaluate the extent of sodium phosphate polymerization; regeneration of the active sodium phosphate species, by recalcination at 450°C can be done only partially; 2) DRIFT spectroscopy has identified the formation of sodium lactate on the catalyst surface; this intermediate may play an important role in the mechanism of catalytic lactic acid conversion to 23P; 3) the presence of $Ba(OH)_2$ on the SiO_2 surface may improve thermal resistance to the NaOH supported catalyst but negatively affects the selectivity of 23P formation from lactic acid; 4) a small decrease in the selectivity towards 23P with a slight increase in the selectivity towards acetaldehyde is observed for the high surface area SiO_2 support in comparison to the low surface area, SiO_2; this was attributed to a higher surface acidity for the former support; 5) the yields and selectivities of lactic acid conversion toward 23P is a function of the loading and type of the alkali metal salt used to prepare the MOH supported catalysts; the yield and selectivity toward 23P increase in the order Ba < Na < K < Cs. Optimized conditions (300°C, 0.5 MPa, 1-2 mmole MOH/g SiO_2, etc) and catalysts give 23P yields as high as 42% with selectivity up to 80%.

1.5 References

1.   Gunter, G. C.; Miller, D. J.; Jackson, J. E. *J. Catal.* **1994**, *148*, 252-260.
2.   Lipinsky, E. S.; Sinclair, R. G. *Chem. Eng. Prog.* **1986**, *82(8)*, 25-.
3.   Holmen, R. E. U.S. Patent **1958**, *2*, 859, 240.
4.   Paparizos, C.; Dolhyj, S.; Shaw, W. G. U.S. Patent 4, **1988**, 786, 756.
5.   Sawicki, R. A. U.S. Patent, **1988**, 729, 978.
6.   Moffat, J. B. *Catal. Rev.-Sci. Eng.* **1978**, *19(2)*, 199-258.
7.   Monma, H. *J. Catal.* **1982**, *75*, 200-203.
8.   Mok, W. S. L.; Antal, M. J. Jr.; Jones, M. Jr. *J. Org. Chem.* **1989**, *54*, 4596-4602.
9.   Lira, C. T.; McCrackin, P. J. *Ind. Eng. Chem. Res.* **1993**, *32*, 2608-.
10. Gunter, G. C.; Langford, R. H.; Jackson, J. E.; Miller, D. J. *Ind. Eng. Chem. Res.* **1995**, *34*, 974-980.
11. Gunter, G. C.; Craciun, R.; Tam, M. S.; Miller, D. J.; Jackson, J. E., *J. Catal.* **1996**, *164*, 207-219.
12. Matsuda, T.; Tanabe, J.; Hayashi, N.; Sasaki, Y.; Miura, H.; Sugiyama, K. *Bull. Chem. Soc. Jpn.* **1982**, *55*, 990-994.
13. Kijenski, J.; Malinowski, S. *J. Chem. Soc. Faraday I*, **1978**, *174*, 250-261.
14. Dudzik, Z.; George, Z. M. *J. Catal.* **1980**, *63*, 72-82.
15. Klaassen, A. W.; Hill, Jr. C. G. *J. Catal.* **1981**, *69*, 299-311.
16. Holten, C. H.; Muller, A.; Rehbinder, D. *Lactic Acid - Properties and Chemistry of Lactic Acid and Derivatives*, Verlag Chemie, **1971**.
17. Clark, J. H. *Catalysis of Organic Reaction by Supported Inorganic Reagents*, VCH Publishers, Inc. New York, **1994**.
18. Walkup, P. C.; Rohrmann, C. A.; Hallen, R. T.; Eahin, D. E. PRAI U.S. Pattent Nr. 90-468704, **1991**.
19. Malinowski, S.; Basinski, S. *J. Catal.* **1963**, *2*, 203-207.
20. Andrew, E. R.; Bryant, D. J.; Cashell, E. M.; Dunell, B. A. *Chem. Phys. Lett.* **1981**, *77(3)*, 614.
21. Tuner, G. L.; Smith, K. A.; Kirkpatrick, R. J.; Oldfield, E. *J. Magn. Res.* **1986**, *70*, 408.
22. Hiyashi, S.; Hayamizu, K. *Bull. Chem. Soc. Jpn.* **1989**, *62*, 3061-3068.
23. Prabhakar, S.; Rao, K. J.; Rao, C. N. R. *Chem. Phys. Lett.* **1987**, *139(1)*, 96-102.
24. Duncan, T. M.; Douglass, D. C. *Chem. Phys.* **1984**, *87*, 339-349.
25. Diehl, P.; Fluck, E.; Gunther, H.; Kosfeld, R.; Seelig, J. *NMR Basic Principles and Progress*, Springer-Verlag Berlin Heidelberg, **1994**, Vol. 30, p. 3-27.
26. Fukushima, E.; Roeder, S. B. W. *Experimental Pulse NMR - A Nuts and Bolds Approach*, Addison-Wesley Inc. **1981**, p. 125-295.
27. Fierro, J. L. G. *Spectroscopic Characterization of Heterogeneous Catalysts, Part A: Methods of Surface Analysis*, Elsevier, Amsterdam, **1990**, p. A18-A28.
28. Herzfeld, J.; Berger, A. E. *J. Chem. Phys.* **1980**, *73(12)*, 6021-6030.
29. Un, S.; Klein, M. P. *J. Am. Chem. Soc.* **1989**, *111*, 5119-5124.
30. Kubelka, P.; Munk, F. *Z. Tech. Phys.* **1931**, *12*, 593-598.
31. Fuller, M. P.; Griffiths, P. R. *Anal. Chem.* **1978**, *50*(13), 1906-1910.
32. Fuller, M. P.; Griffiths, P. R. *Appl. Spectrosc.* **1980**, *34(5)*, 533-539.

33. Fraser, D. J. J.; Griffiths, P. R. *Appl. Spectrosc.***1990**, *44(2)*, 193-199.

34. Hembree, D. M. Jr.; Smyrl, H. R. *Appl. Spectrosc.* **1989**, *43(2)*, 267-274.

35. Yeboah, S. A.; Wang, S. H.; Griffiths, P. R. *Appl. Spectrosc.* **1984**, *38(2)*, 259.

36. Hamadeh, I. M.; King, D.; Griffiths, P. R. *J. Catal.* **1984**, *88*, 264-272.

37. Bell, A.T. in *Vibrational Spectroscopy of Molecules on Surfaces*, edit by Yate, J. T. Wiley, New-York, **1987.**

38. Venter, J. J.; Vamrice, M. A. *Appl. Spectrosc.* **1988**, *42(6)*, 1096-1102.

39. Miller, M. P. *Appl. Spectrosc. Rev.* **1987**, *23*, 329-345.

40. VanEvery, K. W.; Griffiths, P. R. *Appl. Spectrosc.* **1991**, *45*, 347-359.

41. Kortum, G.; Delfs, H. *Spectrochim. Acta,* **1964**, *20*, 405-413.

42. Niwa, M.; Hattori, T.; Takahashi, M.; Shirai, K.; Watanabe, M.; Murakami, *Anal. Chem.* **1979**, *51*, 46-52.

43. Loyalka, S. K.; Riggs, C. A. *Appl. Spectrosc.* **1995**, *49(8)*, 1107-1110.

44. Frei, R. W.; MacNeil, J. D. *Diffuse Reflectance Spectroscopy in Environmental Problem-Solving*, CRC Press, Cleveland, USA, **1973**.

45. White, R. L. *Appl. Spectrosc.* **1976**, *30*, 593-596.

46. Coblentz, W. W.; *Natl. Bur. Stand. (US) Bull.* **1913**, *9*, 283.

47. Wood, B. E.; Pipes, J. G.; Smith, A. M.; Roux, J.A. *Appl. Opt.* **1976**, *15*, 940-945.

48. Blevin, W. R.; Brown, W. J. *J. Sci. Instrum.* **1965**, *42*, 385-392.

49. Spectra-Tech Inc. *Product Brochure*, **1995.**

50. Harrick, N. D. *Optical Spectroscopy: Sampling Techniques Manual*, Harrick Scientific Co. Ossining, New York, **1987**.

51. Bernitez, J. J.; Carrizosa, I.; Odriozola, J. A. *Appl. Spectrosc.* **1993**, *47(11)*, 1760-1766.

52. Leyden, D. E.; Murthy, R. S. S. *Trends in Anal. Chem.* **1988**, *7(5)*, 164-168.

53. Sullivan, D. H., Conner, C. W., Harold, M. P. *Appl. Spectrosc.* **1992**, *46*, 811-818.

54. Craciun, R.; Craciun, L. *Studia*, **1997**, in press.

55. Beeston, B. E. P.; Horne, R. W.; Markham, R. *Electron Diffraction and Optical Diffraction Techniques*, American Elsevier Publishing Company, Inc. New York, **1973**, p. 223-316

56. Niemantsverdriet, J. W. *Spectroscopy in Catalysis*, VCH, Weinheim, **1993,** p. 293-317.

57. H. P. Klug, and L. E. Alexander, *X-ray Diffraction Procedures for Polycrystalline and Amorphous Materials, 1-st Ed.* Wiley, New York, **1954**.

58. Wall, F. T.; Doremus, R. H. *J. Am. Chem. Soc.* **1954**, *76*, 868-870.

59. Groppi, G.; Belloto, M.; Cristiani, C.; Forzatti, P.; Villa, P. L. *Appl. Catal.* **1993**, *104*, 101-108.

60. Morrow, B. A.; McFarlan, A. J. *J. Phys. Chem.* **1992**, *96*, 1395-1400.

61. Kustov, L. M.; Borovkov, V. Yu.; Kazanskii, V. B.; *Russ. J. Phys. Chem. (Engl. Transl.)*, **1985**, *59*, 1314-1318.

62. Nakamoto, K. *Infrared and Raman Spectra of Inorganic and Coordination Compounds, 3-rd Edition*, Wiley & Sons Inc. New York, **1978**, p. 105-401.

63. McClune, W. F. *Powder Diffraction File: Inorganic phases*, Swarthmore, **1983.**

64. Wadley, D. C.; Tam, M. S.; Kokitkar, P. B.; Jackson, J. E.; Miller, D. J. *J. Catal.* **1997**, *165*, 162-171.

CHAPTER 2

THE MECHANISM OF CATALYTIC LACTIC ACID CONVERSION TO 2,3-

PENTANEDIONE: CORRELATION OF EXPERIMENTAL

AND MOLECULAR MODELING DATA

2.1. Introduction

Lactic acid obtained from corn-based fermentation processes represents a new resource for the chemical and food industries. Conversions of this renewable biomass-derived feedstock to acrylic acid or propanoic acid have been explored under heterogeneous catalysis [1,2] and supercritical conditions [3,4]. Previous studies in our laboratory have shown that, unexpectedly, aqueous lactic acid (typically 30% in H_2O) can be converted to 2,3-pentanedione (23P) along with acrylic and propanoic acid byproducts. The reaction takes place over inexpensive and non-toxic alkali metal phosphates, nitrates, and hydroxides supported on Si or Si/Al oxides of various surface areas [5-7]. More recently it has become clear that the same conversion can occur in heated aqueous lactic acid/alkali metal lactate solutions [9-10]. Optimized temperature, pressure and alkali metal loadings have led to yields as high as 60% with 80% selectivity toward 2,3-pentanedione formation [10-11]. Used primarily as a flavor agent and food additive, 2,3-pentanedione has a relative small market (5,000 kg/year). Our discovery of this new low cost route (<$15/kg compared with previous methods at $120/kg) has led us to seek new applications for this diketone and its various valuable derivatives [12]. In

previous reports, however, we have only speculated on the mechanism of 2,3-pentanedione formation [5-11].

This paper analyzes the mechanism of lactic acid conversion to 2,3-pentanedione, in the presence of supported base catalysts (MOH/SiO_2, where M = Na, K, Cs). Possible reaction intermediates are suggested by product analysis, variable-temperature-mass spectrometry (VT-MS), post-reaction diffuse reflectance infrared Fourier transform (DRIFT) spectroscopy, deuterium labeling studies, and computational modeling using semi-empirical and *ab initio* molecular orbital calculations. These approaches may be extended to the general understanding of any Claisen condensation process occurring in a base catalytic system.

Experimental

Post-reaction DRIFTS. Diffuse reflectance infrared Fourier transform (DRIFTS) spectra were acquired using a Perkin-Elmer Spectrum 2000 instrument equipped with a diffuse reflectance attachment, an environmental *in-situ* reactor from Harrick Scientific Co. and a mercury-cadmium-telluride (MCT) detector. The catalyst powder (20-25 mg) was exposed to lactic acid vapor at various temperatures (25°-350°C) and analyzed by DRIFTS. The resulting spectra are presented in Kubelka-Munk units (see Chapter 1). For the isotopic labeling experiments, samples were analyzed using traditional FTIR using the same IR spectrophotometer. Thin layers of liquid sample deposited on a silica window were used to examine C-H versus C-D bands in the transmission mode utilizing a dimethyl-triglycine sulfate (DTGS) detector. In both operational modes, spectra were acquired with 4.0 cm^{-1} resolution over 400-4000 cm^{-1} range.

Molecular modeling. The Spartan software developed by Hehre *et al.* [13] and running on a Silicon Graphics Indigo 2 computer system was used for molecular orbital and solvation calculations. Previous evaluations of various semiempirical molecular modeling programs such as MNDO [14], AM1 [15], and PM3 [16, 17] have indicated that the PM3 model performs the best in describing carboxylic acids and their acidities [18]. Table 2.1 shows such ΔH°_f values calculated using various semiempirical molecular modeling programs in comparison in comparison with the experimental value for several organic molecules with structures similar to that of lactic acid.

Table 2.1 Experimental and calculated enthalpies of formation (ΔH°_f) for various carboxylic acids [17]

Ord #	Carboxylic Acid	Enthalpy of Formation, ΔH°_f [kcal/mol]			
		Experim.	AM1	MNDO	PM3
1	Methanoic	-378.7	-407	-387	-395
2	Ethanoic	-432.8	-431	-423	-426
3	Propanoic	-453.5	-456	-444	-444
4	Butanoic	-475.8	-485	-464	-467
5	Pentanoic	-491.9	-513	-480	-490
6	Hexanoic	-511.9	-542	-500	-512
7	1,6-Hexanedioic	-865.1	-895	-836	-857
8	Lactic acid	-149.5	-153	-147	-147

Consequently, PM3 was used as a starting point to calculate heats of formation for each intermediate considered in the mechanism. Analogous *ab initio* calculations were performed at STO-3G, 3-21G, and 6-31G* levels, models which improve the PM3 model

in more accurately describing hydrogen bonding and dipole-dipole interactions. This type of mechanistic approach has been successfully applied to another unrelated catalytic reaction mechanisms [19]. Because the reaction is thought to occur in a highly polar condensed phase (catalyst surface or liquid film), solvation calculations were performed using the Cramer/Truhlar SM3 model for water [20]. Ionic species of varying sizes play key roles in the mechanism, and we expect solvation to substantially perturb the reaction.

α-H/D Isotopic labeling experiment. Lactic acid 85 % solution (Aldrich) was dried under vacuum and by benzene-water azeotropic extraction, to remove as much of the water as possible from the feed. Dried lactic acid was used to prepare a feed of 35% (by weight) concentration in D_2O. H/D exchange reactions were performed by passing this feed over a 0.5 mmole KOH/g SiO_2 catalyst, at 200°C and 250°C, temperatures favoring the H/D exchange reaction but below the range where a significant conversion to products occurs. The dried lactic acid, the feed and the product were analyzed by ^{1}H and ^{2}H-NMR, FTIR, and GC-MS methods.

Gas chromatography-Mass spectrometry (GC-MS). GC-MS analyses were carried out on a JEOL AX-505H double-focusing mass spectrometer coupled to a Hewlett-Packard 5890J gas chromatograph via heated interface. GC separation employed a DBWax fused-silica capillary column of 30m length x 0.25 mm I.D. with a 0.25 μm film coating (J&W Scientific Co). Direct (splitless) injection was used. Helium gas flow was 1 ml/min. The GC temperature program was initiated at 50°C, with a ramp rate of 10°C/min.

Variable temperature-mass spectrometry (VT-MS). In order to mimic the reaction

conditions and collect *in-situ* data, VT-MS experiments were performed. Figure 2.1

shows the instrumental setup for this type of experiments. Samples for VT-MS were

capillary tubes containing a 2 mmole KOH/g SiO_2 catalyst (280 mesh, 1-2 mg) and lactic

acid feed (1-2 μL); control experiments omitting the KOH catalyst or using sodium

lactate and dilactide feed were also performed These samples closely approximate the

real catalytic system and yield significant insight into the mechanism operating therein.
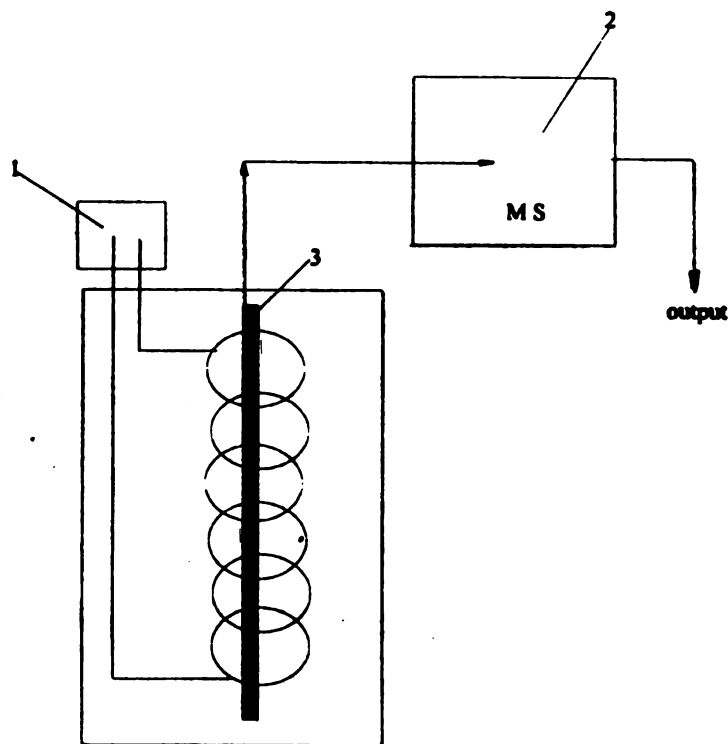
Figure 2.1 Experimental setup for VT-MS experiments: 1) temperature regulator; 2) mass spectrometer; 3) capillary holder.

Capillaries were placed in the temperature-controlled block heater of the mass spectrometer. The vaporized products from a sample of catalyst mixed with lactic acid reaction feed were analyzed via mass spectrometry as the temperature in the sample probe was raised from 25°C to 350°C, at ramp rates of 8°C or 16°C/min. Conditions in the MS were as follows: interface and ion source temperatures of 240°C, electron energy of 70 eV, mass spectrometer scan rate of 1 scan/s over the m/z range 0-400 amu.

Results and Discussion

Our prior optimization studies of lactic acid conversion to 2,3-pentanedione have uncovered the following mechanistic elements: i) the reaction is catalyzed by bases, including alkali metal lactates themselves; little or no 23P is obtained from pyrolyses of either lactic acid or alkali metal lactates alone [21-23]; ii) kinetic analysis points to a process that is second order in lactic acid and first order in catalyst, as expected for a condensation process; an approximate Arrhenius activation energy (E_a) of 32.3-32.7 kcal/mol is obtained for a 2 mmole KOH/g SiO_2 catalyst, though its exact interpretation is shadowed by the complexity of the continuous-flow, heterogeneous reaction conditions [24]; iii) studies of lactic acid feeds containing ammonium lactate (as a potential impurity found in fermentation broth) show reversible poisoning of the reaction by ammonia; full recovery of catalytic function is seen on returning to the unadulterated feed. Formation of 23P is favored by basic catalysts, suggesting that enolization might be a key intermediate. Scheme 2.1 displays the proposed molecular mechanism, in which a Claisen condensation is the critical step for C-C bond-forming reaction [25].

Scheme 2.1   The proposed mechanism of lactic acid conversion to 23P

Step 1

2   Lactic Acid   +   Lactate I
                        (M⁺ = H⁺, Na⁺, K⁺, Cs⁺)

nucleophilic attack

Step 2

Lactic Acid   +   Enol
                    (+ Lactate I)

Step 3

Intermediate-H I
(+ Lactate I)

- H₂O

Step 4

Intermediate-H II
(+ Lactate I + H₂O)

- CO₂

Intermediate-H III
(+ Lactate I + CO₂ + H₂O

Step 5

- H₂O

Step 6

2,3-Pentanedione-enol
(+ CO₂ + 2 H₂O + Lactate I)

2,3-Pentanedione
(+ CO₂ + 2 H₂O + Lactate I)
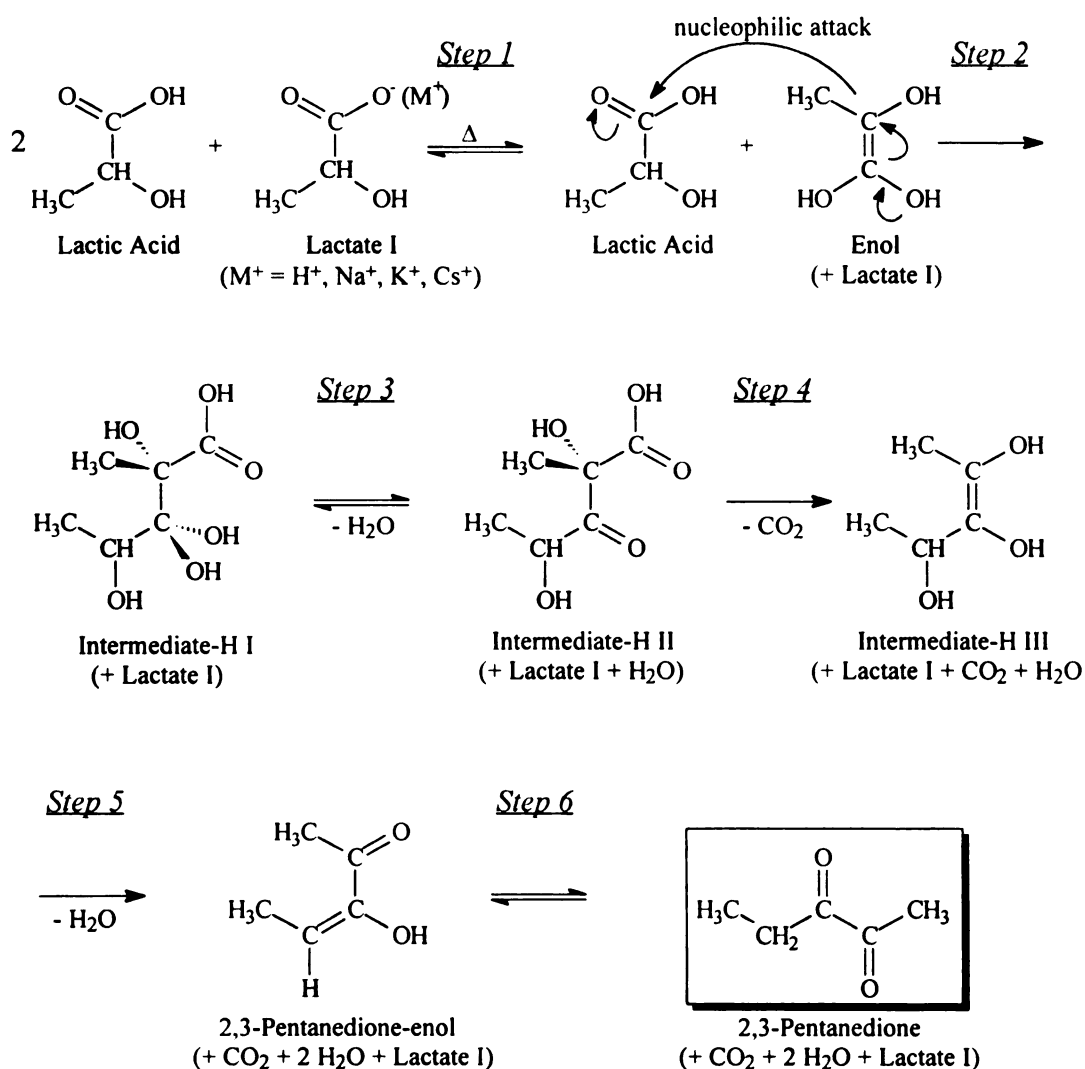
Under high temperature and buffered lactic acid/alkali lactate conditions, hydrogen bonds and ion pairing may stabilize the enolate or enol forms of lactic acid which then may attack a molecule of lactic acid at the carbonyl. After loss of water, the six-carbon dihydroxy-ketocarboxylate (Intermediate I) loses CO_2 to form Intermediate II. Loss of hydroxide leads via Intermediate III and subsequent ketonization, to 23P, in the same way that dihydroxyacetone isomerizes under enolizing conditions to pyruvaldehyde [25]. In

the following discussion, we present new evidence for this reaction sequence and show how it explains the early findings describes above.

Molecular orbital calculations. Data from PM3, PM3-SM3, and *ab initio* calculations at the STO-3G, 3-21G, and 6-31G* levels performed for the reactants, possible intermediates, and products are presented in Table 2.2. In the proposed pathway, most of the intermediates are stabilized by intramolecular hydrogen bonding. By exploring various states of protonation/deprotonation relative to lactic acid/lactate, we considered the most "relaxed" forms (with respect to proton exchange with the medium) at each reaction stage. Though the condensation step (step 2) is entropically unfavorable, the process is aided by the low enthalpies of formation of the resulting intermediates, while subsequent fragmentations releasing volatile H_2O and CO_2 are favored entropically.

The differences between PM3 and PM3-SM3 calculated energies for each component involved in the proposed mechanism are presented in a separate column of Table 2.2 as well. These "hydration enthalpy" values were combined with the *ab initio* results to further explore the effects of solvation. Based on these calculations, the energy variations for each step of the mechanism has been evaluated and are presented in Table 2.3. The energies vary over 20 kcal/mol range both in the gas phase and aquated models. At the process temperatures, such energy variations are easily accessible.

Table 2.2 PM3 and *ab initio* data for reactants, intermediates and products involved in the mechanism of lactic acid conversion to 2,3-pentanedione

Interm. of the 23P mechanism	Enthalpy-PM3 [kcal/mol]			Ab initio [hartrees]		
	Gas phase	SM3)	Δ[a]	STO-3G	3-21G	6-31G*
Lactic Acid	-147.3[b]	-159.1	-11.8	-337.21908	-339.79087	-341.69662
Lactate I	-174.8	-246.9	-72.1	-336.49629	-339.21895	-341.13419
Lactate II	-157.4	-226.9	-69.6	-336.43235	-339.14697	-341.05096
Lactic Acid Enol	-132.3	-143.2	-10.9	-337.18294	-339.75112	-341.64003
Interm.-H I	-284.5	-298.3	-13.8	-674.46588	-679.59049	-683.36488
Interm.-H II	-223.5	-240.6	-17.1	-599.43273	-603.96437	-607.34283
Interm.-H III	-138.6	-149.7	-11.1	-414.33918	-417.38976	-419.70962
Enol form 23P	-80.5	-88.4	-7.9	-339.32205	-341.79054	-343.70703
23P	-87.7	-95.2[c]	-7.6	-339.34396	-341.80219	-343.72497
CO$_2$	-85.1	-91.9[d]	-6.8	-185.06839	-186.56126	-187.63418
H$_2$O	-53.4	-59.7[e]	-6.1	-74.96590	-75.58596	-76.01075

Δ = energy difference between the PM3 and PM3-SM3 calculations; experimental enthalpies of formation [kcal/mol]: b = -149.5±1.5; c = -83.5±0.5; d = -94.1; e = -57.8.

$$2\ CH_3CHOHCOOH \rightarrow CH_3C(O)C(O)CH_2CH_3 + CO_2 + 2\ H_2O \qquad (2\text{-}1)$$
Lactic acid   23P
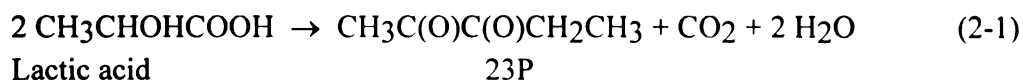
The experimental gas phase enthalpy of reaction for lactic acid to 2,3-pentanedione (reaction 2-1, given above) was evaluated from literature data to be ΔH_r = +5.4 kcal/mole [26]. With the PM3 model, the overall reaction enthalpy was also calculated to be endothermic, with ΔH_r = +15.0 kcal/mol (gas phase) and ΔH_r = +11.7 kcal/mol (aquated) in qualitative agreement with the experimental value. The excess endothermicity is largely due to PM3's 9 kcal/mol underestimation of the stability of

CO_2. The *ab initio* results can be interpreted in a similar manner, as shown in Tables 2.2

and 2.3. The energies of each proposed mechanistic stage, calculated from *ab initio* data

and the solvation model, are presented in Table 2.3 as well.

Table 2.3 Relative energies calculated in gas phase and solvated models from PM3 and *ab initio* methods for $C_6H_{13}O_7^-$ species[a] at each step of the proposed mechanism, normalized to the energy of the starting materials

Steps [a]	PM3 [kcal/mol]		*Ab initio* STO-3G [kcal/mol]		*Ab initio* 3-21G [kcal/mol]		*Ab initio* 6-31G* [kcal/mol]	
	Gas ph.	SM3	Gas	solvated[b]	Gas	solvated[b]	Gas	solvated[b]
feed	0	0	0	0	0	0	0	0
1	+15.0	+15.9	+22.8	+23.6	+24.9	+25.9	+35.5	+36.5
2	+10.1	+19.9	-17.4	-7.5	-5.5	+4.4	+17.8	+27.6
3	+17.7	+17.9	+24.8	+16.3	+19.7	+20.2	+24.9	+25.3
4	+17.5	+16.9	+40.6	+40.3	+28.0	+27.7	+24.3	+23.9
5	+22.2	+18.5	+72.8	+69.5	+36.3	+33.1	+19.2	+15.9
6	+15.0	+11.7	+59.0	+56.3	+29.1	+26.1	+7.9	+4.9

a - the components considered in our calculations for each step are presented in Scheme 2.1; b - calculated values were corrected with the solvation energies obtained from PM3-SM3 calculations

As with PM3, there is a leveling effect when the SM3 solvation model is used to correct

the *ab initio* gas phase values. The 6-31G*-SM3 data gave values for the energies

following the reaction pathway closer to the PM3 model (not greater than 25 kcal/mol

variation) and $\Delta E_r = 7.9$ kcal/mole in the gas phase ($\Delta H_r = 4.9$ kcal/mol solvated) in

reasonable agreement with the experimental ΔH_r value. Considering the crudeness of the

methods empployed, the highest energy points found along the reaction path (19.9

kcal/mol and 36.5 kcal/mol at PM3-SM3 and HF/6-31G*-PM3 levels) are in rather good agreement with the experimental measured 32-33 kcal/mol activation energy (E_a) value.

Additional experiments using DRIFTS analysis, H/D exchange and VT-MS have been performed to probe further the 23P formation mechanism outlined in Scheme 2.1.

DRIFTS data. Figure 2.2 displays DRIFTS spectra of a 2 mmole KOH/g SiO_2 catalyst before and after exposure to lactic acid vapors at various temperatures (in the range 150-350°C) in an *in-situ* DRIFTS reactor. At room temperature, only the bands attributed to Si-O vibrations from SiO_2 at around 800 cm^{-1} and 1000-1200 cm^{-1} are observable [27]. After exposure to lactic acid vapors, the strong carbonyl stretching bands characteristic of -COOH and -COO⁻ at 1721 cm^{-1} and 1597 cm^{-1}, respectively [6-8], together with the less intense bands specific to these species, start to appear and become well defined at temperatures higher than 150°C. At temperatures above 300°C, the band at 1597 cm^{-1} is shifted to lower frequency, indicating the formation of another type of carboxylate, identified to be potassium propanoate; this species can remain on the catalyst surface at very high temperature (350°C) in the absence of a continuous flux of lactic acid [28]. The low S/N ratio observed for the DRIFTS spectra of Figure 2.2 is due to the low light throughput of the *in-situ* cell. In these conditions, even the very sensitive MCT detector does not yield very good IR spectra, but it does provide information directly about the catalyst surface modifications under conditions closely approximating the continuous flow reactor.
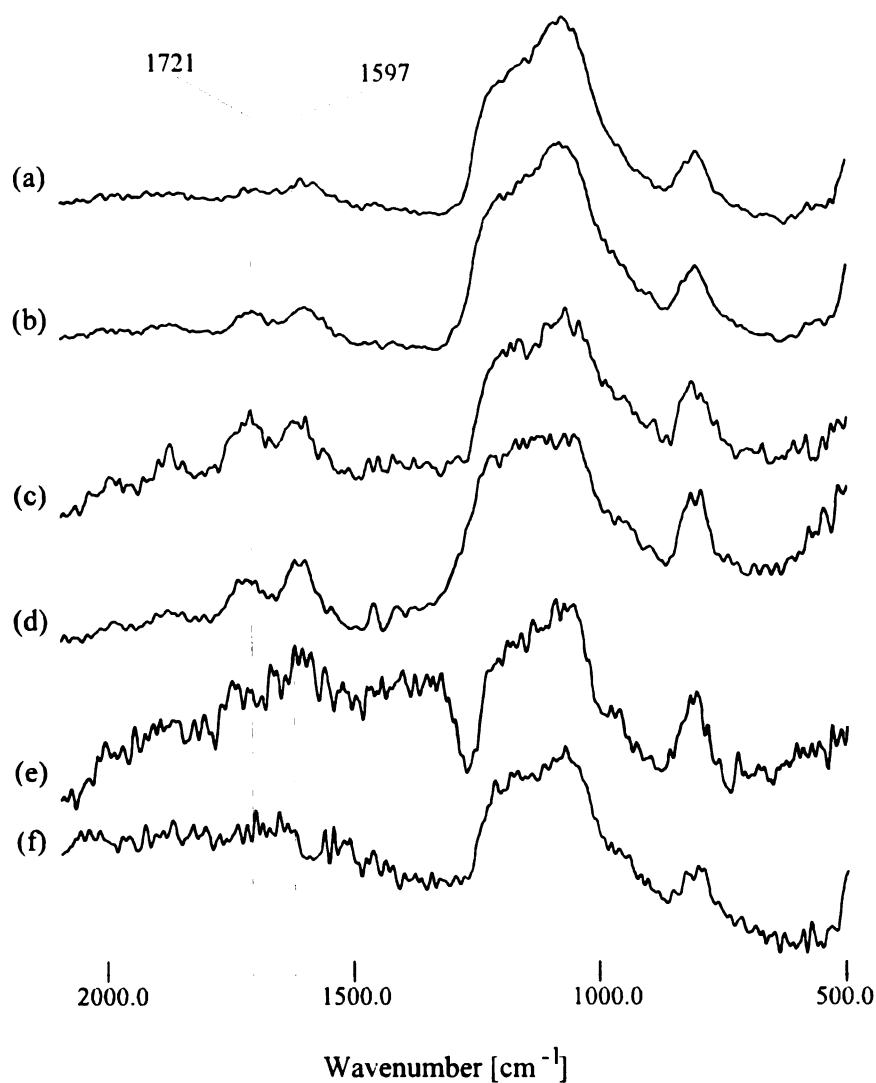
Figure 2.2 DRIFTS spectra of KOH/SiO₂ catalysts after exposure to lactic acid vapor at various temperature: a) 350°C; b) 300°C; c) 250°C; d) 200°C; e) 150°C; and before exposure at f) 25°C.

We have previously reported the observation of lactic acid and lactate bands on silica surfaces using transmission IR, a method that is more sensitive, but less directly comparable to our reactor conditions [6].

Potassium lactate observed on the catalyst surface after exposure to lactic acid vapor is one of the intermediates in the mechanism of Scheme 2.1. Indeed, an effective catalyst can be formed by simply loading potassium lactate on silica or silica/alumina.

However, pyrolysis of potassium lactate alone does not form 23P; addition of fresh lactic acid to the system is necessary for the reaction to occur [7-10, 28].

α-H/D exchange in lactic acid. Based on the mechanism presented in Scheme 2.2, base-catalyzed H/D exchange at the α-hydrogen site is expected; the enol intermediate or enolate of lactic acid then provides the nucleophilic center to attack another lactic acid molecule in the condensation process. The H/D exchange process could also be acid catalyzed, but such a path would presumably require stronger acids than are available in our catalytic system and it is established that acid catalysts cleave lactic acid to acetaldehyde, CO, and H_2O [29]. The closely related mandelic acid system in which the CH3 of the lactic acid is replaced by a phenyl group, undergoes analogous proton exchange with racemization; the details of this enzyme-catalyzed process are a topic of recent investigations [30].

The gas chromatography-mass spectrometry (GC-MS) method has been used to observe the H/D exchange process, by analyzing the lactic acid GC peak in a lactic acid/D_2O feed mixture, before and after passage through the catalyst at various temperatures. Standard MS spectra for lactic acid and dilactide are presented in Figure 2.3. Table 2.4 presents the abundance of the main ion at m/z = 45 amu for four samples: the plain lactic acid in H_2O; lactic acid dried and rediluted in D_2O; and samples of the lactic acid in D_2O after passing over the KOH catalyst at 200°C and at 250°C. The peak at m/z = 45 amu was attributed to either $-^+COOH$ or CH_3-CH^+-OH ions formed during the fragmentation of lactic acid in the MS chamber [31-32].

a)
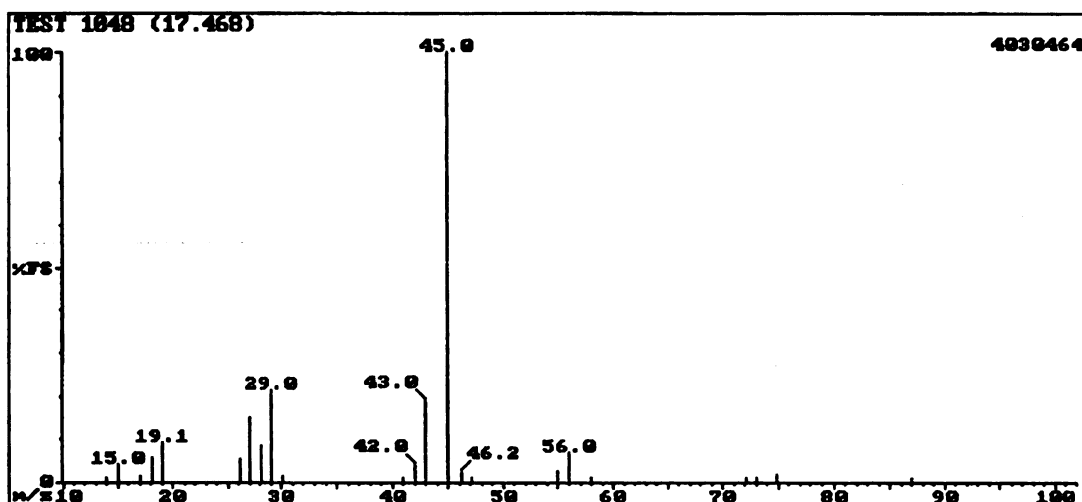
b)
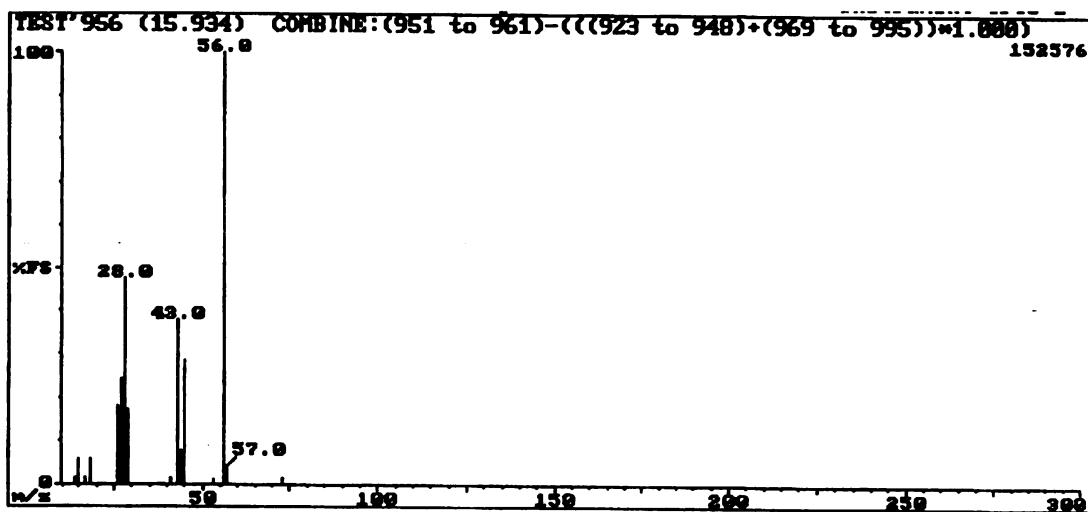
Figure 2.3 Mass spectra of standards: a) lactic acid and b) dilactide

For both ions, one D-incorporation would lead to formation of a m/z = 46 amu ion, but only the CH_3-CH^+-OH has the ability to exchange more protons, including the one from the α-position of lactic acid, leading to the formation of a m/z = 47 amu ion. There is no molecular peak observed or reported in the mass spectrum of the lactic acid when the

electron impact MS technique was used for analysis [31, 35]. However, peaks with the masses of the lactic acid molecular ion (M) m/z = 90 and m/z = 91 (M+1) were observed in the dilactide GC peak that appeared when a concentrated solution of lactic acid was injected into the GC or in previously reported work when direct probe/chemical ionization (CI) or field desorption (FD) techniques were used. In all these techniques, the mass spectrum of lactic acid reveals the formation of the $[M+1]^+$ ion followed by $[2M+1]^+$ and $[M-1]^+$ ions. These large ions must be formed in the MS chamber at high concentration and pressure due to gas phase reactions [32-35]. The presence of ions that simulate the molecular ions in these spectra caused some initial confusion in our work which was clarified by reference to the literature and GC-MS experiments with sample dilution and injection size. MS-MS experiment would provide more inside about the structure of these molecular-type of ions observed ion these experiments.

Scheme 2.2 Proposed mechanism for α-H/D exchange from lactic acid molecule

a) Trivial H-D exchange on carboxyl and hydroxyl hydrogen

$$CH_3-\underset{\underset{OH}{|}}{CH}-COOH \ + \ 2\,D_2O \ \rightleftharpoons \ CH_3-\underset{\underset{OD}{|}}{CH}-COOD \ + \ 2HDO$$
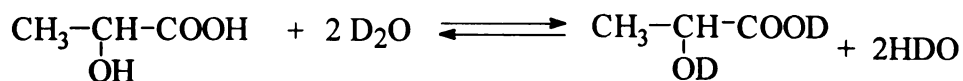
b) α H-D exchange in lactic acid - base catalysis
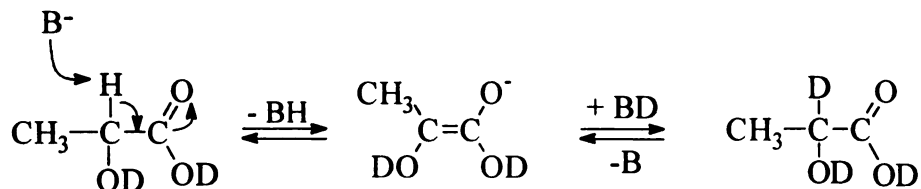
As mentioned above, the main fragment ion from lactic acid corresponds to m/z = 45 amu [CH_3-CH^+(OH) and $COOH^+$, though the latter may contribute little or nothing] [32]. For the D_2O treated material, the peak at m/z = 46 amu, attributable to either CH_3-CH^+-OD and $COOD^+$ ions, is enhanced compared with the undeuterated case. The relative intensity of the peak at m/z = 47 amu, assigned to CH_3-CD^+-OD ion, has significantly increased in the case of the converted lactic acid (see Table 2.4 given below) and , as expected, is more enhanced in the sample run at higher temperature. In addition, from the GC peak corresponding to the small amount of acrylic acid obtained in these low conversion runs via lactic acid dehydration, the mass spectra contain the molecular ion peak at m/z = 72 amu. Increases in the relative intensities of the molecular peaks at m/z = 73 amu and most importantly the peak at m/z = 74 amu, corresponding to one ($CH_2CHCOOD$) or two ($CH_2CDCOOD$) deuterium incorporated into acrylic acid in comparison with the peak at m/z = 72 amu offer additional evidence of the α-H/D exchange process.

Table 2.4 α-Deuterium incorporation into lactic acid (GC-MS data)

Sample	Lactic acid feed	Lactic acid in D_2O	Lactic acid after H/D exchange at	
			200°C	250°C
m/z	Ion relative intensity [%]	Ion relative intensity [%]	Ion relative intensity [%]	
45	93.3	16.6	14.2	11.3
46	6.7	83.8	76.7	50.4
47	---	---	9.1	38.3

To further confirm the α-H/D-exchange, additional information was obtained by analyzing the D_2O/lactic acid system, before and after passage through a 1 mmole KOH/g SiO_2 catalyst, by FTIR and ^{2}H-NMR spectroscopy. Figure 2.4 shows the FTIR spectra of the dried lactic acid (c) from a 35% feed in D_2O, before (b) and after (a) passing over a KOH/SiO_2 catalyst at 250°C. The IR spectra (3700-200 cm^{-1} region) of the dried lactic acid before H/D exchange or dissolved in D_2O show only bands characteristic of -OH at 3600 cm^{-1}, the -OD at 2150 cm^{-1}, methyl and methine C-H stretches at 2994 cm^{-1}, 2944 cm^{-1}, and 2886 cm^{-1} for lactic acid [33].

The IR spectrum of the lactic acid after passing over the catalyst bed at high temperature shows a new band in the -CD stretch region, at 2317 cm^{-1}, supporting our assertion that α-H/D exchange has occurred. Some acrylic acid is formed at the reaction temperature (250°C) and was identified in the product mixture by MS. An additional C-D band observed around 2370 cm^{-1} might be due to trace amounts of acrylic acid with D incorporated in the α-position, as well[3]. As observed from Table 2.5, calculated vibrational frequencies for the C-H and C-D stretch bands do not agree with the experimental value.

---

[3] Frequency calculations based on PM3 data predict an α C-D stretch at 2140 cm^{-1}, in relatively poor agreement with the observations
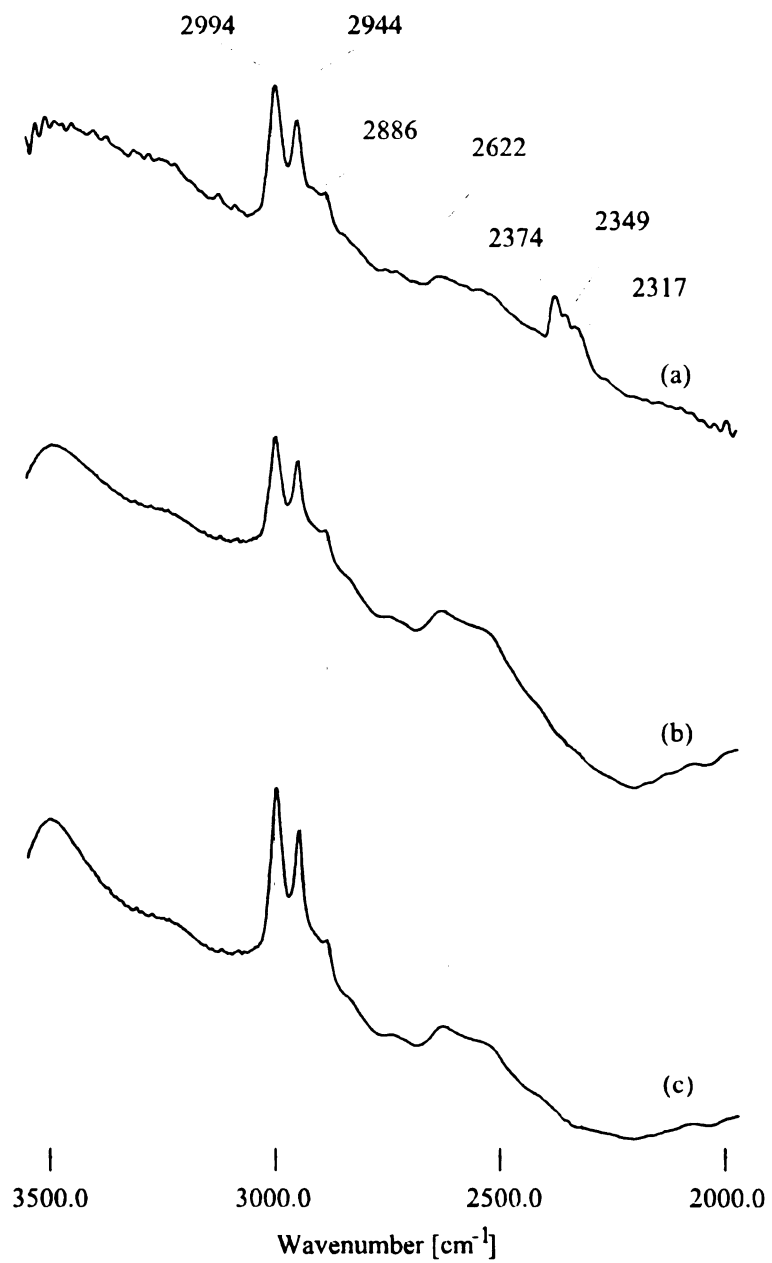
Figure 2.4 IR spectra of the lactic acid after (a) and before (b) passing over a KOH/SiO₂ catalyst, in comparison with the dried lactic acid (c).

Table 2.5 Calculated vibrational frequencies for C-H and C-D stretch bands in α-position of isopropanol molecules from PM3 and *ab initio* 6-31G* data in comparison with the experimental values

Molecules	α-C-H stretch frequency [cm^{-1}]			α-C-D stretch frequency [cm^{-1}]		
	experimental	PM3	*ab initio*[b]	experimental	PM3	*ab initio*
Lactic acid	2886	2914	3238	2318	2144	2388
K-lactate	2895	2890	3152	a	2126	2324
isopropanol	2878	2917	3239	a	2146	2400

a - value not available; b - these values could be corrected by dividing with 1.12

^{2}H-NMR analysis of product obtained from lactic acid in D_2O solution before and after passing over a KOH/SiO_2 catalyst are presented in Figure 2.5 a-c. For the converted lactic acid at 200°C (2.5 a) and 250°C (2.5 b) compared with the spectrum of lactic acid just mixed with D_2O (2.5 c), ^{2}H-NMR spectra indicate the presence of a new peak with chemical shift corresponding to the α-methine site.
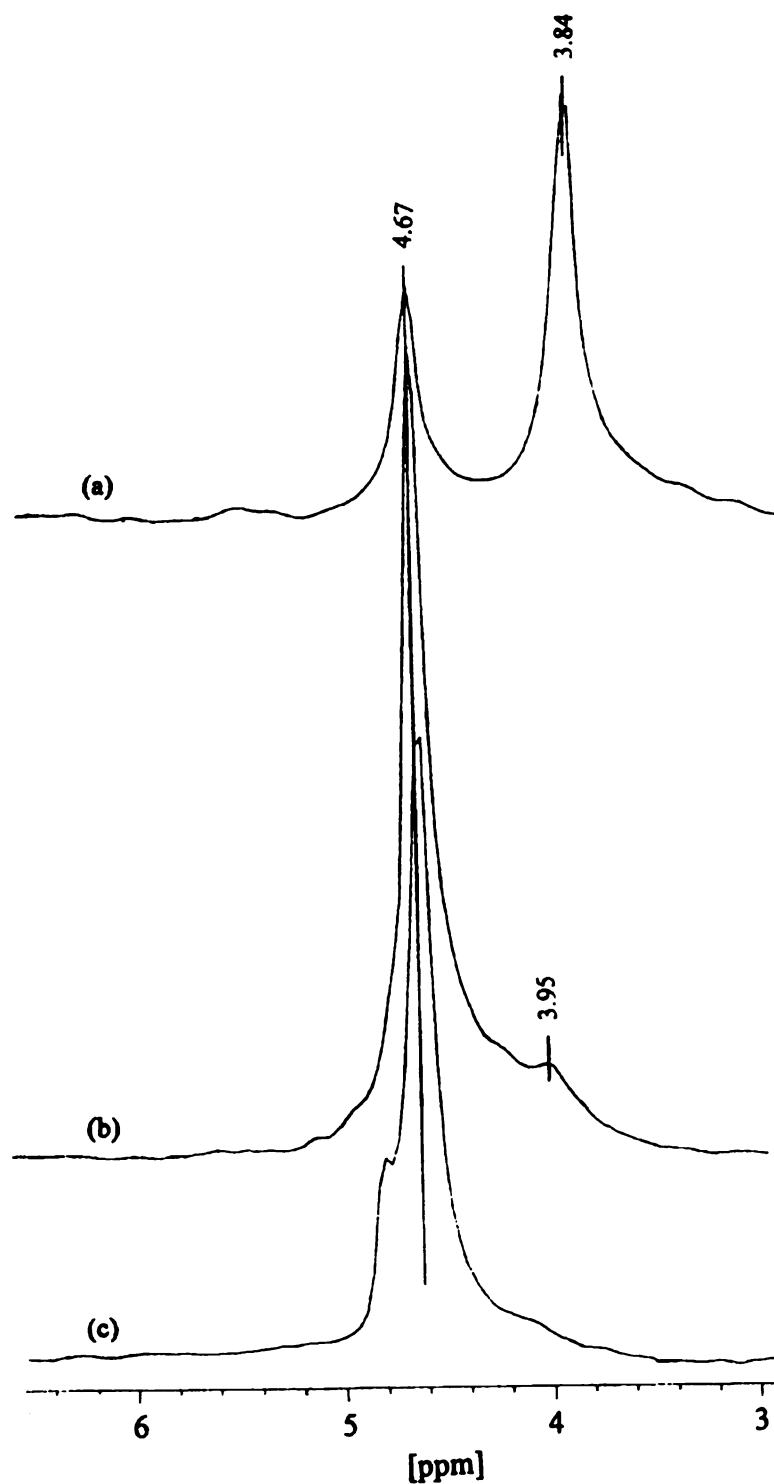
Figure 2.5 ^{2}H-NMR spectra of dried lactic acid after H/D exchange process (passing over a KOH/SiO$_2$ catalyst) at a) 250°C and b) 200°C in comparison with c) the lactic acid just diluted in D$_2$O and dried

Considered together with the GC-MS results, these additional spectroscopic data point clearly to incorporation of deuterium at the α-site of lactic acid. Most importantly, no ^{2}H-NMR peaks appear at the chemical shift of the β-methyl group.

VT-MS data. An attempt was made to analyze the reaction of lactic acid deposited on KOH/SiO_2 catalyst by VT-MS. These types of experiments may yield *in situ* chemical and structural information about intermediates in a catalytic reaction. However, the method can be used to analyze mostly pure compounds; analysis of mixtures generates mass spectra that are hard to interpret, unless the compounds under study have clearly distinguishable fragmentation patterns [36]. Application of the method to a reacting system is even more complex, as the suite of compounds of varying masses and volatilities, is itself changing with time over the heated catalyst. Finally, for a condensation reaction, the relatively volatile starting material (lowest molecular weight species of interest) must be available in large enough quantity to undergo bimolecular reaction on the catalyst once an adequate temperature is reached. Despite these challenges, the promise of observing the sequence of reaction intermediates and the simplicity of the experiments led us to search for mechanistic insight using this tool.

Figure 2.6 shows the mass spectra at several temperatures of the products evolved during heating of lactic acid on a 2 mmole KOH/g SiO_2 catalyst, at a 16°C/min temperature ramp-rate, with the initial temperature set at 30°C. At low temperatures (<100°C), the mass spectra indicate only the presence of ions with m/z = 91 amu, similar with the M+1 ion of lactic acid and the corresponding secondary ions formed in the MS chamber observed in the case of ion source saturation from a GC-MS experiment. The

presence of the $[M+1]^+$ ion together with the $[2M+1]^+$ and $[2M-H_2O+1]^+$ ions, indicate gas phase reactions in the ion source from the mass spectrometer, due to the high gas phase concentration of lactic acid. After 1.5 minutes (Figure 2.6 a), new, new peaks begin to appear at m/z = 181, m/z = 163, m/z = 145, m/z = 144, m/z = 135, m/z = 117 (118), and m/z = 100 amu. Of these, only the resonances at m/z = 100 amu (2,3-pentanedione) and m/z= 144 amu (dilactide) are seen in the product mixture from a regular catalytic conversion experiment. The presence of the $[M+1]^+$ ion together with the $[2M+1]^+$, $[2M-COOH]^+$, and $[2M-H_2O]^+$ ions, points to gas phase reactions in the MS analysis chamber. The other peaks in Figures 2.6 a-c can be attributed to fragments formed in the MS chamber from the molecular ion corresponding to the $[2M+1]^+$ with m/z = 181 amu [37-38]. It appears that after a short time corresponding to a relatively low temperature ($\approx$60°C), lactic acid evolves from the catalyst surface in large quantities and the ions abundantly formed in the MS chamber start to react and form various type of product ions (see Figure 2.6 a-c). Due to these gas phase reactions from the analysis chamber, it was not possible to obtain unambiguous information about lactic acid/lactate catalytic system from this experiment. Although the ions seen have m/z values appropriate to the intermediates from the proposed mechanism (see Scheme 2.1), the gas phase dimerization from m/z = 91 amu ($[M+1]^+$) to m/z = 181 amu ($[2M+1]^+$) and the subsequent fragmentations via losses of H_2O and CO_2 closely mirror the proposed solution pathway.
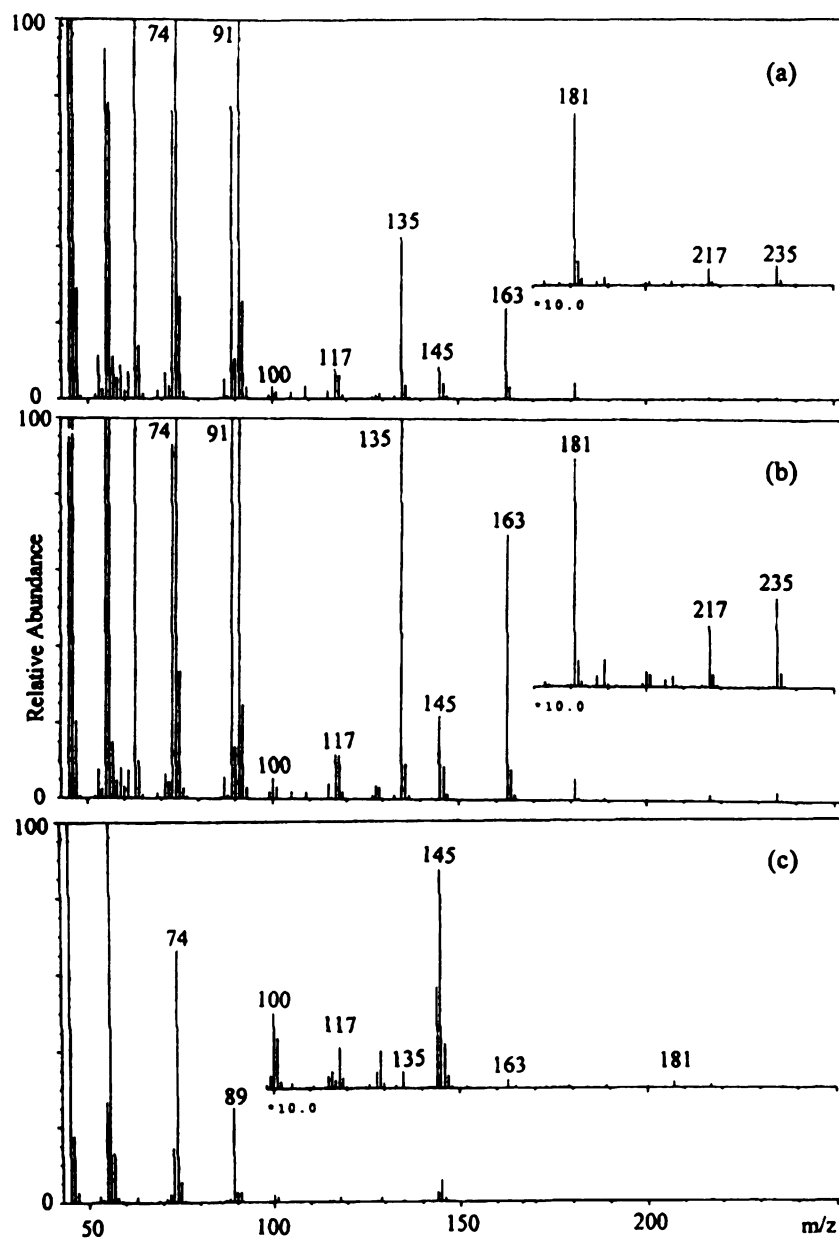
Figure 2.6 Mass spectra of products obtained on a 2 mmole KOH/g SiO$_2$ catalyst
by VT-MS analysis after: a) 1.5 min.; b) 2.5 min.; c) 5.2 min of heating

At high desorption temperature, the only peaks observable are at m/z = 144 amu

(dilactide) or at low m/z values such as m/z = 56, and 45 amu, etc. which correspond to

the fragment ions from a standard MS spectrum for dilactide (see Figure 2.3 b). The persistent presence of the peak at m/z = 144 indicates that dilactide is formed but it was found that plain compound does not participate in further chemical transformations on the catalyst nor play a significant role in the pathway to 2,3-pentanedione.

Figure 2.7 presents the total ion current (TIC) and VT profiles, respectively, for several m/z ions (2.7 a) as well as a mass spectrum recorded after 2.13 minutes (2.7 b) during the VT experiment when a 2 mmole KOH/g SiO_2 catalyst impregnated with lactic acid, at 16°C/min temperature ramp rate with the initial temperature set at 30°C was used. Most of the lactic acid is desorbed in less than 2 minutes from the catalyst surface. As explained above, due to a saturation effect it is hard to differentiate between peaks specific to species formed on the catalyst surface or in the MS analysis chamber. Similar VT-MS experiments were performed at a slower temperature ramp-rate (8°C/min), in an attempt to ensure lower gas pressure in the ion source of the mass spectrometer and to allow time to reach higher temperature before all the lactic acid has been desorbed from the catalyst surface. Figure 2.8 shows the VT profiles of several ions observed during the experiment (2.8 a) and the mass spectrum after 2.09 minutes (2.8 b). In this case the lactic acid desorbtion is slower than in the previous case (see Figure 2.7 a), however most of the lactic acid was removed after less than 3 minutes. The mass spectra from Figure 2.8 b looks very similar with that from Figure 2.7 b, but even peaks such as m/z = 117, m/z = 163 and m/z = 181 amu, which were less abundant, are now completely saturated. Consequently, the only different observed is in the rate of lactic acid desorption.

In order to try to differentiate between reaction on the catalyst and in the gas phase from the ion source, reference experiments using pure dilactide, sodium lactate on 2 mmole KOH/g SiO_2 catalyst and lactic acid on plain support have been performed, with a temperature ramp rate of 8°C/min and initial temperature of 30°C. Figure 2.9 shows the VT profiles for several ions (2.9 a) and a mass spectrum collected after 1.43 minutes (2.9 b), when the dilactide was impregnated on the catalyst. As observed in Figure 2.9 a, after several minutes, most of dilactide was desorbed from the catalyst. The mass spectrum presented in Figure 2.9 b looks similar with that of the standard dilactide, presented in Figure 2.1 b. Figure 2.10 shows the VT profiles for the same ions considered in the previous experiments (2.10 a) and the mass spectrum (2.10 b) collected after 0.5 minutes, when the catalyst was impregnated with sodium lactate. As observed from Figure 2.10 a, little material is desorbed slowly from the catalyst surface, most of the signal being in the noise level. The mass spectrum of the desorbed material presented in Figure 2.10 b is similar with that obtained for dilactide. It seems that some dilactide is formed during heating and desorbs slowly from the catalyst surface. Figure 2.11 shows the FID (2.11 a) and a mass spectrum collected after 3 minutes in the case of a control experiment with lactic acid but no catalyst (just SiO_2 support). The VT profiles look similar to that obtained when catalyst was used, but the abundances of the main ions (m/z = 100, m/z = 117, m/z = 135, m/z = 145, m/z = 163, and m/z 181 amu) are significantly reduced. As observed in Figure 2.11 b, the mass spectrum shows the presence of all main peaks observed previously when the impregnated catalyst with lactic acid was used in the VT-MS (see Figure 2.7 b).

a)
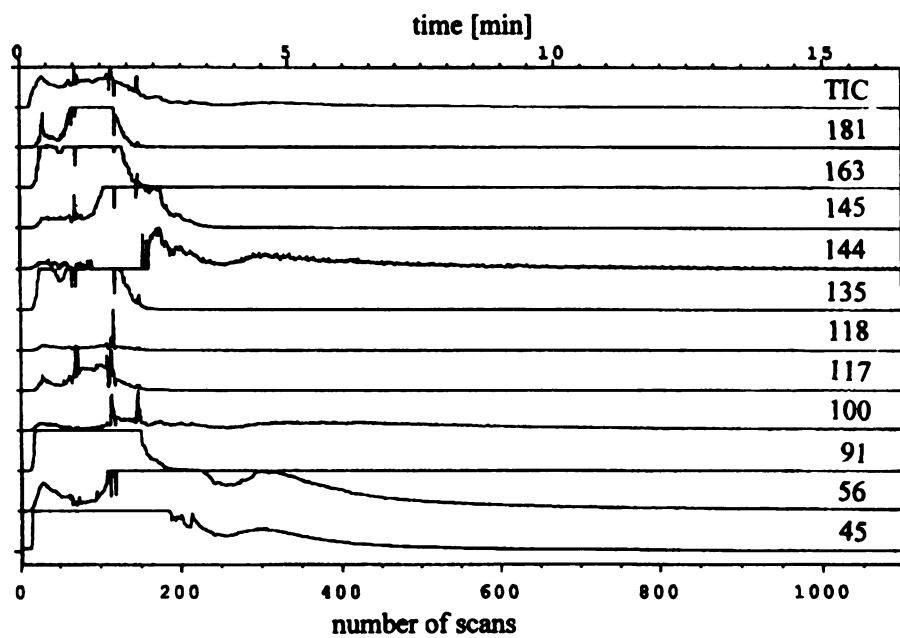
b)
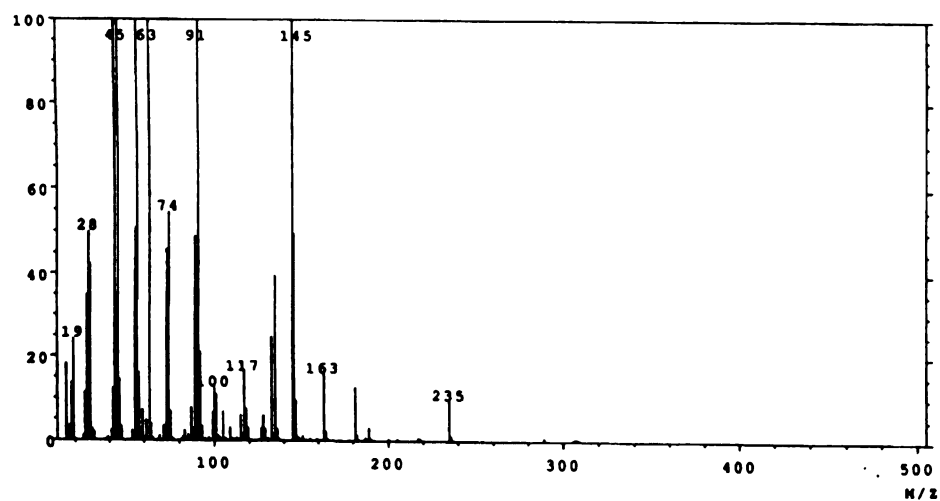
Figure 2.7 VT-MS data (16°C/min ramp rate) using a 2 mmoles KOH/g SiO₂ catalyst impregnated with lactic acid: a) abundance variations versus time for ions of interest; b) mass spectrum obtained after 2.13 minutes.

a)
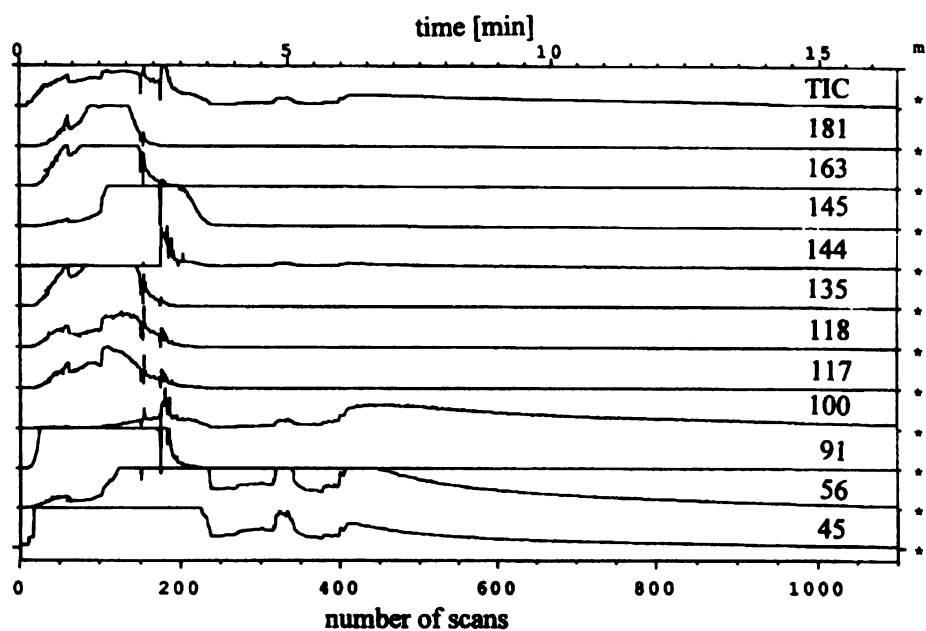
b)
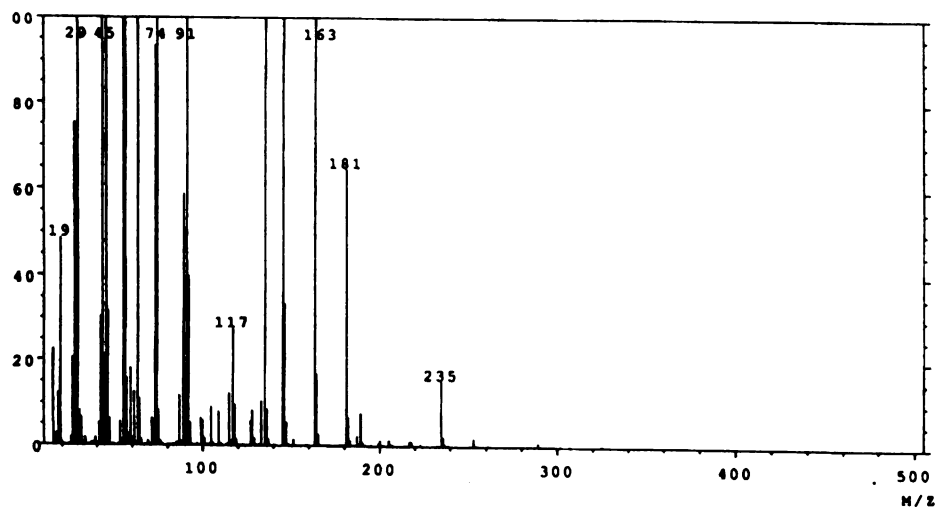
Figure 2.8 VT-MS data (8°C/min ramp rate) using a 2 mmoles KOH/g SiO_2 catalyst impregnated with lactic acid: a) abundance variations versus time for ions of interest; b) mass spectrum obtained after 2.09 minutes.

a)
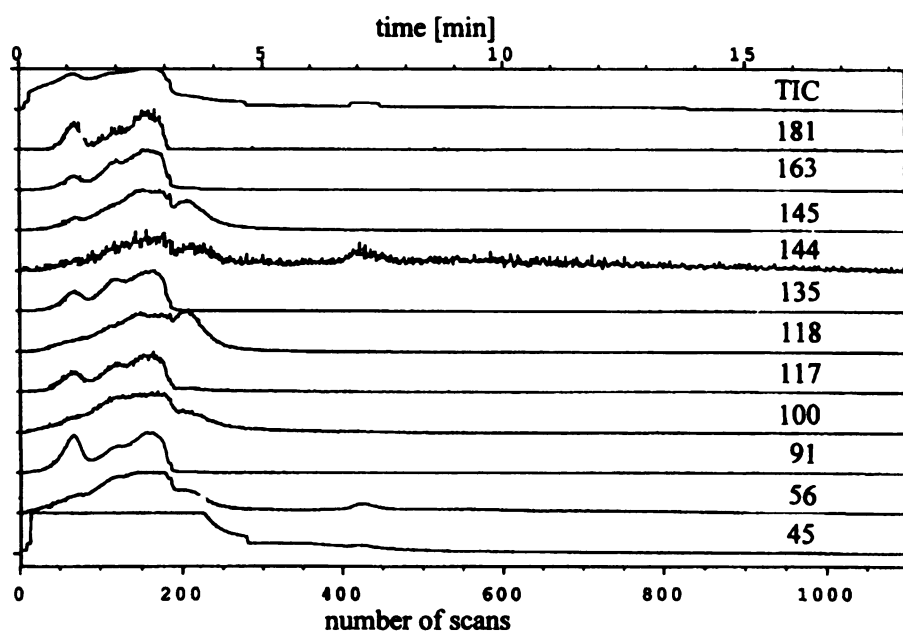
b)
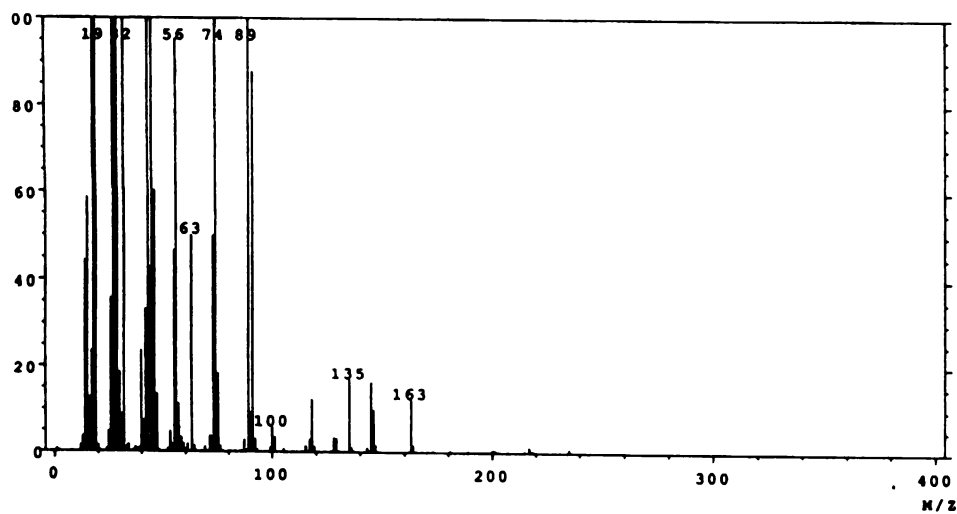
Figure 2.9   VT-MS data (8°C/min ramp rate) using SiO$_2$ support impregnated with lactic acid: a) abundance variations versus time for ions of interest; b) mass spectrum obtained after 2.48 minutes.

a)
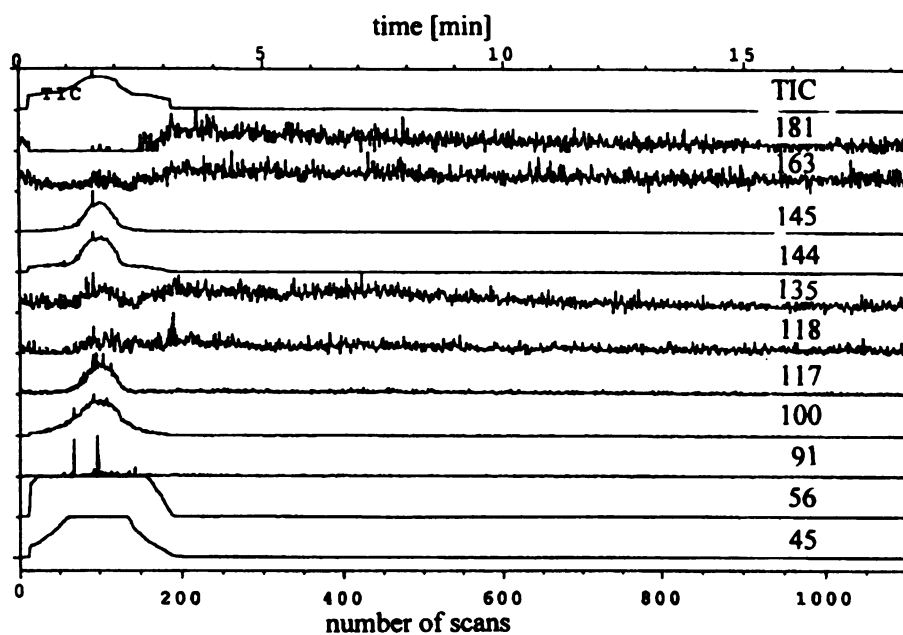
b)
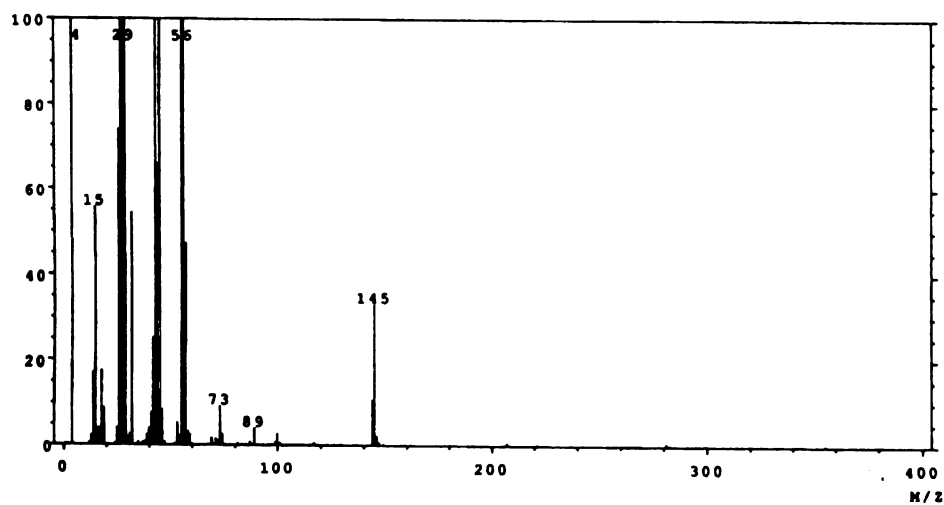
Figure 2.10 VT-MS data (8°C/min ramp rate) using a 2 mmoles KOH/g SiO_2 catalyst impregnated with dilactide: a) abundance variations versus time for ions of interest; b) mass spectrum obtained after 1.43 minutes.

a)
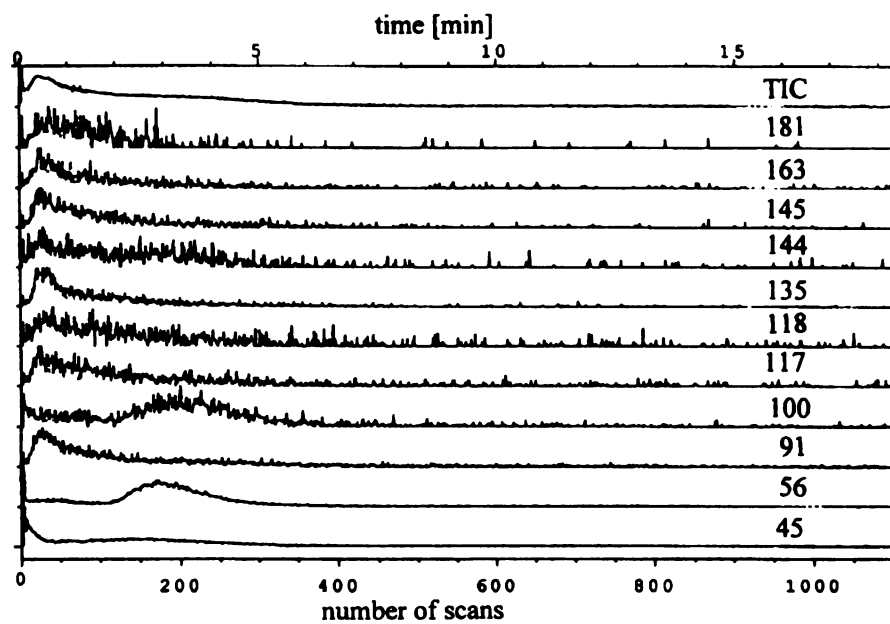
b)
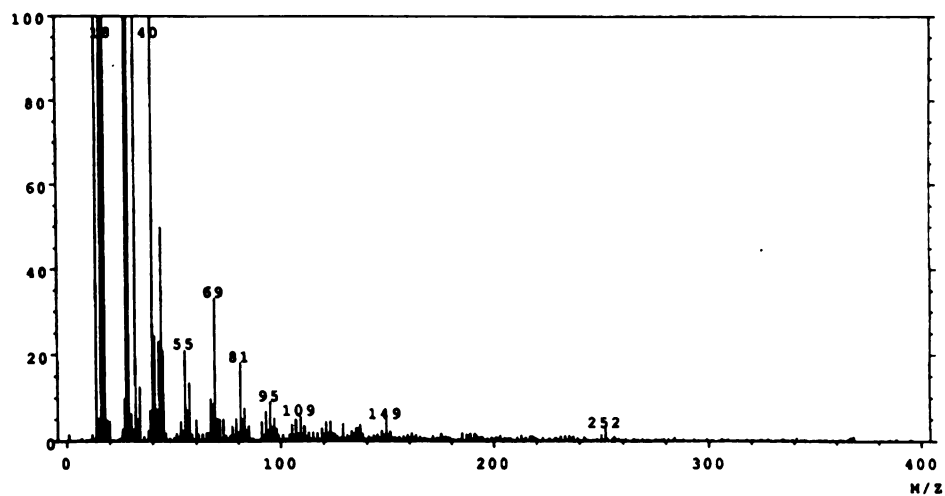
Figure 2.11   VT-MS data (8°C/min ramp rate) using a 2 mmoles KOH/g SiO_2 catalyst impregnated with sodium lactate: a) abundance variations versus time for ions of interest; b) mass spectrum obtained after 0.5 minutes.

From all these data, it is still not possible to conclude that the main peaks observed in the mass spectra are correlated with the catalysis process from the catalyst surface. The fast lactic acid desorption from the catalyst surface before the temperature reaches 100°C, as well as the clear presence of characteristic ions from well-known gas-phase processes, preclude a clear assignment of any differences seen among these experiments to chemistry on the catalyst surface, even though many of the peaks observed correlate well with the masses of the intermediates proposed and presented in Scheme 2.1. The high masses of the proposed intermediates and their low volatility may be an important barrier for electron impact-MS data acquisition. However, because the highest barrier observed from theoretical calculations was related to the lactic acid enolization (step 2, Scheme 2.1) and its downhill trend afterward, together with all chemical reasoning presented before, support the proposed mechanism of lactic acid conversion to 2,3-pentanedione presented in Scheme 2.1.

Conclusions

Based on experimental results, analyzed in the light of theoretical calculations, we have outlined and explored a detailed pathway for lactic acid condensation to 2,3-pentanedione. Lactate salts have been identified via DRIFTS on catalyst surfaces that have been exposed to lactic acid vapor. H/D exchange in the α-position of the lactic acid molecule has been observed by FTIR, D-NMR, and GC-MS, confirming the possibility of lactate enolization under these relative mild (buffered) conditions. This process leads to the key carbon nucleophile required for the condensation mechanism. PM3 and *ab initio* calculations, augmented by the SM3 solvation model, have been used to evaluate energy

variations and protonation state along the reaction sequence; for the condensed-phase situation, all energy changes were within accessible range at the reaction temperatures; the maximum barrier is also in good agreement with the experimentally observed activation energy for this process. Since most reaction steps involve simple proton transfer or other common processes (dehydration, decarboxylation), the activation barriers between intermediates are also unlikely to be abnormally high. The actual bond making and breaking steps in this sequence will be examined in a separate *ab initio* study. Thus, the proposed pathway is energetically plausible and consistent with all observations. Its one surprising feature - a Claisen condensation of a free carboxylic acid under buffered conditions - appears to be energetically feasible based on the calculated energetics of lactate and its enolized form. Though specifically focused on the multistep mechanism of lactic acid condensation to 2,3-pentanedione, this work more generally illustrates the way in which theory and experiment can begin to dissect complex processes such as catalysis and condensed phase reactivity. Via such detailed mechanistic analyses of catalytic conversions, we hope to evolve toward a day when rational design will vastly accelerate discovery of novel catalysts and reaction paths.

References

1. Paparizos, C.; Dolhyj, S.; Shaw, W. G. U.S. Patent 4, **1988**, 786, 756.
2. Sawicki, R. A. U.S. Patent, **1988**, 729, 978.
3. Mok, W. S. L.; Antal, M. J. Jr.; Jones, M. Jr. *J. Org. Chem.* **1989**, *54*, 4596-4602.
4. Lira, C. T.; McCrackin, P. J. *Ind. Eng. Chem. Res.* **1993**, *32*, 2608.
5. Gunter, G. C.; Miller, D. J.; Jackson, J. E. *J. Catal.* **1994**, *148*, 252-260.
6. Gunter, G. C.; Langford, R. H.; Jackson, J. E.; Miller, D. J. *Ind. Eng. Chem. Res.* **1995**, *34*, 974-980.
7. Gunter, G. C.; Craciun, R.; Tam, M. S.; Miller, D. J.; Jackson, J. E., *J. Catal.* **1996**, *164*, 207-219.
8. Craciun, R.; Tam, M. S.; Perry, S. M.;Thiel, M. A.; Jackson, J. E.; Miller, D. J. in *Book of Abstracts* at 8th SHHC Meeting, **1995**, Balatonfured, Hungary, p104.
9. Craciun, R.; Tam, M. S.; Miller, D. J.; Jackson, J. E. in *Book of Abstracts* at 4th HCFC Symposium, **1996**, Basel, Switzerland, p 268-269.
10. Craciun, R.; Tam, M. S.; Kokitkar, P. B.; Perry, S. M.; O'Donnell, M. A.; Jackson, J. E.; Miller, D. J. in *Book of Abstracts* at 11th Congress on Catalysis, **1996**, Baltimore, USA, p 010.
11. Wadley, D. C.; Tam, M. S.; Kokitkar, P. B.; Miller, D. J.; Jackson, J. E. *J. Catal.* **1997**, *165*, 162-171.
12. Evaluation made by discussions with experts from various companies involved in flavor and food industry.
13. Hehre, W. J.; Burke, L. D.; Shusterman A. J.; Pietro, W.J. *Experiments in Computational Organic Chemistry: Spartan User Guide*, Wavefunction, Inc. Irvine, USA, 1994 p 44-77.
14. Dewar, M. J. S.; Thiel, W. *J. Am. Chem. Soc.* **1977**, *99*, 4899-4906.
15. Dewar, M. J. S.; Zeobisch, E. G. Healy, E. F.; Stewart, J. J. P. *J. Am. Chem. Soc.* **1985**, *107*, 3902-3909.
16. Stewart, J. J. P. *J. Comput. Chem.* **1989**, *10(2)*, 209-220.
17. Stewart, J. J. P. *J. Comput. Chem.* **1989**, *10(2)*, 221-264.
18. Aakeroy, C. B. *J. Mol. Struct. (Theochem)*, **1993**, *281*, 259-267.
19. (a) Jackson, J. E.; Bertsch, F. M. *J. Am. Chem. Soc.* **1990**, *112*, 9085-9092; (b) Mohamad, Master thesis, Michigan State University, East Lansing, USA, **1995**.
20. (a) Cramer, C. J.; Truhlar, D. G. *J. Am. Chem. Soc.* **1991**, *113*, 8305; (b) Cramer C. J.; Truhlar, D. G.; *Science*, **1992**, *256*, 213; Cramer, C. J.; Truhlar, D. G. *J. Comp. Aid. Mol. Des.* **1992**, *6*, 69.
21. Chuchani, G.; Martin, I.; Rotinov, A.; Dominguez, R. A. *J. Phys. Org. Chem.* **1993**, *6*, 54-58.
22. Chuchani, G.; Martin, I.; Rotinov, A. *Int. J. Chem. Kinet.* **1995**, *27*, 849-853.
23. Chuchani, G.; Rotinov, A.; Dominguez, R. A.; Martin, I. *J. Phys. Org. Chem.* **1996**, *9*, 348-354.
24. Tam, M. W.; Craciun, R.; Jackson, J. E.; Miller, D. J. **1997**, in preparation.
25. March, J. *Advanced Organic Chemistry-Reactions, Mechanisms and Structures*, 4th ed.; Wiley&Sons: New York, **1992**, p 491-493.

26. Keeffe, J. R.; Kresge, A. J. *J. Phys. Org. Chem.* **1992**, *5*, 575-580.

27. White, R. L.; Nair, A. *Appl. Spectrosc.* **1990**, *44(10)*, 69-75.

28. Tam, M. S.; Craciun, R.; Miller, D. J.; Jackson, J. E. *Ind. Eng. Chem. Res.* **1997**, in press.

29. Thomas, A. F. *Deuterium Labeling in Organic Chemistry*, Appleton Century Crofts: New York, **1991.**

30. Schafer, S. L.; Barrett, W. C.; Kallarakal, A. T.; Mitra, B.; Kozarich, J. W.; Gerlt, J. A. *Biochemistry*, **1996**, *35*, 5662-5669.

31. Stenhagen, E.; Abrahamsson, S.; McLafferty, F. W. *Registry of Mass Spectral Data*, Vol. 1, John Woley & Sons, 19, p. 62.

32. Wood, G. W.; Oldenburg, E. J.; Lau, P. ; Wade, D. L. *Can. J. Chem.* **1978**, *56*, 1372-1377.

33. Li, Z.; Kruger, T. L.; Cooks, R. G. *Org. Mass Spectrom.***1982**, *17(10)*, 519-523.

34. Harrison, A. G.; Kallury, R. K. M. R. *J. Org. Chem.* **1984**, *49*, 4993-4995.

35. Konopski, L. *Org. Mass Spectrom.* **1990**, *25*, 537-539.

36. Watson, J. T. *Introduction to Mass Spectrometry*, Lippin-Raven, Philadelphia, **1997**, p. 37-41.

37. McLafferty, F. W.; Turecek, F. *Interpretation of Mass Spectra*, 4th Ed. University Science Books, Mill Valey, **1990**.

38. Goulden, J. D. S.; Millard, B. J. *Org. Mass Spectrom.* **1969**, *2*, 893-900.

CHAPTER 3

DESIGN OF UNPROMOTED AND RARE EARTH PROMOTED MnO_x/SiO_2

CATALYSTS USED IN OXIDATIVE DEHYDROGENATION REACTIONS

The design of cerium and manganese oxide catalysts supported on SiO_2 catalysts for use in the oxidative dehydrogenation of methyl lactate to methyl pyruvate and of 2-ethyl-3-methyl-dihydropyrazine (obtained from 23P and ethylenediamine) to 2-ethyl-3-methyl-pyrazine was studied. The Ce (Mn) precursor solution used for support impregnation and the conditions during catalyst preparation determine the bulk and surface structure of the catalysts. Catalyst structure configuration strongly influences the catalytic activity. The great interest for the study of a MnO_x-based catalyst is an indication of their importance in chemical industry, particularly selective oxidation or oxidative dehydrogenation of fine chemicals and more recently in emission control processes (environmental protection technologies). Despite the considerable amount of effort devoted to the study of Mn catalysts, the active sites of these catalysts, the role of promoters, the mixed effect of single oxides, and the nature of any surface phases are still the subject of intense investigations. In an effort to better understand the relation between the structure of a solid material and its catalytic activity, the unpromoted and Ce-promoted MnO_x/SiO_2 catalytic system have been investigated. The purpose of this research is to design a new class of $Mn/Ce/SiO_2$ catalysts with high catalytic activity and selectivity in oxidative dehydrogenation processes applicable in the fine chemical

98

industry. The Mn/Ce/SiO$_2$ catalysts under study are characterized using various analysis techniques. XRD is used to determine the chemical and physical nature of the species on catalyst surfaces, identifying the crystalline phases in the catalysts by means of lattice structural parameters and obtaining data regarding the particle size. Additional information about the structure morphology and crystallography of the supported species can be provided by electron microscopy. Analysis by transmission electron microscopy (TEM) equipped with energy dispersive X-ray (EDX) analysis reveals information about the composition and internal structure of the particle. Transmission electron microscopy (TEM) is used in this work to provide a measure for crystalline phase(s) and to characterize the amorphous or the highly dispersed surface phases that can not be detected by XRD. Manganese or cerium are elements very labile to oxidation state changes. X-ray photoelectron spectroscopy (XPS) is used to obtain information about the chemical state of supported phases on the catalysts surface. Temperature programmed reduction (TPR) gives additional information about the oxidation state changes on catalyst surface and structure. The presence of paramagnetic species such as Ce^{3+} or Mn^{2+} oxides detectable by EPR allow us to further probe the catalysts structure. Two probe-reactions were used in this study: oxidative dehydrogenation of methyl-lactate to methyl-pyruvate, and 2-ethyl-3-methyl-dihydropyrazine to 2-ethyl-3-methyl-pyrazine. Catalyst structure and reaction conditions were optimized in order to obtain high yield and selectivity in the desired product.

3.1. Rare earth promoted catalysts

The demand for various chemicals required by industry and the great technical developments in analysis techniques and apparatus have allowed the introduction of a wide variety of catalysts for total or selective oxidation and combustion reactions. The main advantages offered by catalytic total oxidation are the wide range of fuel concentration used in the process and the low temperature at which the reactions can occur compared with the uncatalyzed ones (incineration). Among the advantages offered by selective catalytic oxidation processes are high conversion into useful (desirable) products and reduced waste generation. Catalytic exhaust gas treatments, especially for automobiles, operate in a temperature range of 600-800°C. At high temperature nitrogen oxides (NO_x) are formed from nitrogen and oxygen in the air. The presence of NO_x in exhaust gases is undesirable from a pollution control point of view. Control of the reaction at these high temperatures is difficult due to the limited flexibility in the fuel concentration. The use of total oxidation catalysts for high-temperature processes (>1000°C) is difficult because catalysts such as supported noble metals or transition metal oxides are not resistant to such conditions. Therefore, is necessary to develop new materials which may be used as catalysts or supports for these types of processes.

The development of advanced heterogeneous catalysts involves several important activities. These include the development of sophisticated preparation procedures that can be used to design specific surface structures, guided by examination of the active sites as well as promoter/support and promoter/transition metal oxide interactions in the active catalytic phases. Mixed metal oxides are important catalysts that are used widely

for selective oxidation of fine chemicals. The surface of the mixed metal oxide exhibits two metal ions in addition to O^{2-} ions or -OH groups present at the surface. The oxidation process which takes place on the active site of the catalyst surface is schematically presented in Figure 3.1 [3].

When the metal oxide catalysts consist of only one metal species, the oxidation process is represented as one side of the cycle represented in Figure 3-1. When two metal oxide species are present on the catalyst surface, the process is represented by the entire cycle from the figure. The oxidation process occurs at the surface where the oxygen atoms have limited reactivity (related to metal M_1).
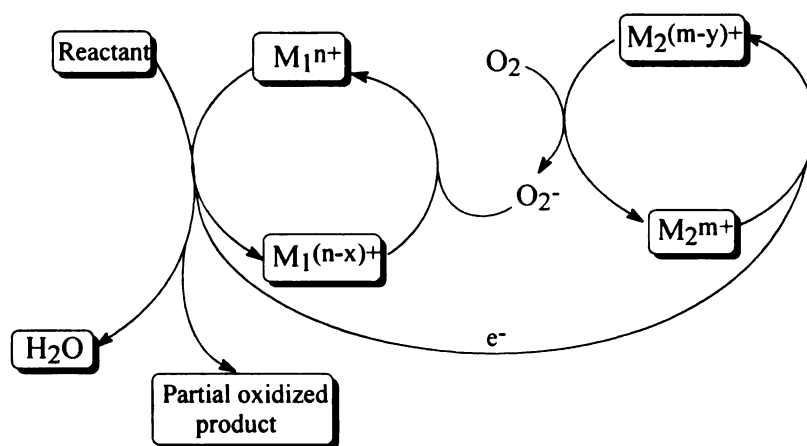
Figure 3.1   Schematic representation of the catalytic cycle for a selective oxidation process which occurs on a mixed metal oxide catalyst surface; M_1 and M_2 are two different transition metals (x,y = number of the electrons exchanges in the redox process by the M_1 and M_2, and n and m are the oxidation numbers for the M_1 and M_2) [3].

Activated by the metal ions, the oxygen ions react with the reactants to give water and the partially oxidized product rather than the total oxidation process. The surface sites involved in the process are reoxidized indirectly and not by O_2 from the gas phase. The

O_2 reacts instead with the surface site associated with the second metal, M_2, and thus, oxygen is transported as ions through the bulk of the catalyst from the second site to the first to deoxidize the surface, with the electron compensation to complete the cycle [3].

At present, the catalyst systems used in these processes are based on noble metals which are expensive and susceptible to poisoning. Transition metal oxide catalysts have been suggested as suitable substitutes for noble metals even though they are not as active and are also subject to poisoning. However, some industrial catalytic processes have been designed and exploited successfully using transition metal oxides as catalysts rather than noble metal (e.g. Wacker oxidation using Pt/V_2O_5 catalyst [3]). The advantages of transition metal oxides are their low cost and better resistance to chlorine poisoning. By improving their stability, selectivity and activity using suitable promoters, transition metal oxides may become good replacements for noble metal-based catalysts [1-3].

Noble Metals. Noble metals typically catalyze total oxidation processes. Catalytic incineration over noble metal catalysts has been widely used for decades. The advantages of these catalysts are given by the high catalytic activity and selectivity. Platinum, palladium and rhodium are the most commonly used active phases for catalytic combustion applications [4-6]. A desirable characteristic of the noble metal catalysts is their high resistance to sulfur poisoning compared with the transition metal oxide catalysts [7]. Highly dispersed Pt and Pd catalysts are easily prepared using a number of support materials like silica or alumina.

Oxidation over noble metals is considered to be a structure sensitive reaction in which the surface configuration of the catalyst strongly influences the activity, selectivity, reaction pathway and rate [8-12]. Briot *et al.* [8-9] have attributed the activity of

supported platinum and palladium catalysts to the high specificity of surface oxygen on large crystallites. For these types of catalysts, an activity enhancement was observed at low temperature, close to the catalyst ignition temperature. Catalysts with high noble metal dispersion (small crystallites) exhibit high catalytic activity [10]. No oxygen pressure dependence on the reaction rate was found. In the case of methane oxidation, the reaction order was found to be around one in methane with little influence of oxygen concentration on the reaction rate. The dissociation of the methane or oxygen-methane complexes at the catalyst surface was proposed to be the rate-limiting step in the mechanism [12].

Transition Metal Oxides. Oxidation over solid metal oxide catalysts has been widely studied during the last years. The main advantage over noble metal catalysts is the low cost of the raw material. By choosing a well defined composition of the metal oxide in the catalyst, an oxidation activity close to that of the noble metal catalysts can be obtained. It was found that the formation of nitrogen oxides can be avoided using metal oxide catalysts [13].

Oxygen can be activated by interaction with the catalyst surface. Coordination or incorporation of oxygen into the oxide lattice may be an important step in catalyst activation. Lattice incorporation leads to a more strongly bound oxygen than in the case of simple physical adsorption. The lattice oxygen was found to be more active in the case of selective oxidation processes whereas the surface oxygen was more important in complete oxidation reactions [14]. Participation of lattice oxygen in complete oxidation reactions increases with temperature. Wise *et al.* [15] observed that the ratio of the rate constants corresponding to the reactions of lattice oxygen and adsorbed oxygen increases

with temperature from 0 at 500°C to 0.3 at 800°C for methane oxidation on a $LaFeO_3$ catalyst. At higher temperatures lattice oxygen interactions dominate the oxidation process. Many studies have been focused on the suitability of different types of metal oxides for catalytic incineration, trying to rationalize their catalytic activity. Comparison studies of the catalytic activities in terms of conversion for a variety of oxides such as Cr_2O_3, Co_2O_3 [16], Mn_2O_3 [17] V_2O_5 [18], or CuO [19] led to the conclusion that many of these oxides are potentially good catalysts for total oxidations.

Mixed oxides with perovskite structures XYO_3, (where X and Y are different transition metals), have revealed high activity in total oxidation reactions [20]. Their use as catalysts was first reported in 1970, by Meadowcroft [21]. Their well defined and stable structures make them suitable for oxidation catalysts. Perovskite electronic structures are comparable with those of the transition metals. Seiyama [20] summarized in a review article the important aspects of total catalytic oxidation reactions on various perovskite oxides, like sorption and desorption of oxygen, H_2 oxidation and total oxidation of hydrocarbons. Many of the pervoskite structures incorporated lanthanides (La, Ce, Pr) and/or alkaline earth metals (Ba, Sr, Ca) in combination with transition or noble metals. Structures like $La_{1-x}Sr_xBO_3$, $La_{1-x}Sr_xMnO_3$, and $La_{1-x}Sr_xCoO_3$ [22-24] are some of the most recent perovskite-type catalysts prepared and used successfully in total oxidation reactions.

From the material presented above we can conclude that a great number of high-temperature-stable, complex oxide materials are promising catalysts for catalytic oxidation processes applicable in the large scale chemical industry.

Supports. Another important element in the structure and composition of a catalyst is the support. The chemical nature of supports may play an important role in catalyst's activity. Supports are mostly used to improve thermal and chemical stability while decreasing the amount of the expensive active component required to make a catalyst. The surface area and chemical nature of the support play major roles in the behavior of the catalysts. The most commonly used supports are based on silicates and aluminates, but often less resistant, low surface area materials such as MgO or TiO_2 are used to improve the selectivity of a catalyst or as a catalyst site itself. The geometry and the dimension of the particle used as support are very important factors in the catalyst activity. The characteristics needed for a support to be used in high-temperature reactions such as combustion can be summarized as follows: i) high thermal stability and mechanical strength; ii) no chemical reaction between support and the catalytic component; iii) high volume throughput [25]. It is hard to find an ideal material that meets all the requirements for an excellent support. Many times, additives or promoters are used to improve the properties of the supports used for catalyst preparation. Silica is one of the most commonly used support materials; at high temperature and in the presence of oxygen, silica exhibits sintering phenomena. γ-Al_2O_3 is another support that shows resistance to the sintering process compared to silica. However, at very high temperature ($1000^\circ C$) the γ-Al_2O_3 phase is transformed into α-Al_2O_3 which has a lower surface area [26]. Many studies on alumina based catalysts show loss in surface area due to sintering of particles by solid-state diffusion. Consequently, the thermal treatment used for the support material also affects a catalyst's properties [27].

Addition of a promoter may stabilize the support by inhibiting the sintering process. Promoters can be divided into two different classes: structural and textural. Structural promoters lead to a transformation of the catalysts surface configuration which affects catalyst activity. Textural promoters have less influence on the structure of the catalyst but improve the textural properties of the catalyst like surface area, pore volume size, and mechanical resistance of the catalyst surface. Alkaline earth metals (Ba, Ca, Sr) are well known as additives with consequences on the textural properties as well as mechanical resistance of the catalysts. Lanthanide oxides are known to be used as both textural and structural promoters, influencing the thermal resistance and the surface configuration of the catalyst. Another way to promote a catalyst is to introduce lattice flaws into the structure. These kinds of promoters are called electronic promoters, substances with semiconductor character. These materials will accept or lose electrons from conduction band. Impurities in the lattice of the catalyst can thus increase its catalytic activity.

Dispersion of the active component, loading and surface structure are important parameters in designing a proper catalyst. The main chemical effect of a catalyst in total or selective oxidation reactions is to force them to completion, yielding water, carbon dioxide and nitrogen as final products (assuming only C, O, H, N are in the feed) and the main product, respectively. Metal oxide based catalysts are of particular interest for these types of processes. Procedures such as temperature treatment, or additives such as promoters or activators may strongly influence the surface structure of the catalyst and its catalytic activity. Manipulation of these factors during catalyst preparation offers control over activity, selectivity and resistance of the catalyst to various poisons or inhibitors.

Tailoring a catalyst surface by controlling the dispersion and/or particle size of the active phase, crystalline structure and oxidation state of the metals on the surface, ultimately gives control over the catalytic process.

Promoter effect. Rare earth additives have been employed extensively as textural and structural promoters in supported metal catalysts [28-30]. Cerium oxide in particular has been widely used for these purposes [31-39]; its promoter effect is given by the nonstoichiometric crystal structure [40-41], oxygen storage capabilities [42-45], redox properties [46] and very good thermal resistance [47-53]. Cerium promotion enhances the catalytic activity of transition metals and/or transition metal oxide-supported catalysts for CO oxidation and NO_x reduction because of its ability to form oxygen-deficient oxides under reducing conditions [49,40]. Due to their importance in a variety of catalytic applications, the structures of supported cerium catalysts have been the focus of many investigations [29-59]. Miki *et al.* [42] have used XRD to examine the structure of a 20 wt.% CeO_2/Al_2O_3 catalyst oxidized and reduced at high temperature (900°C). High temperature reduction of the catalysts led to $CeAlO_3$. Reoxidation of the reduced catalysts had no effect on $LaAlO_3$ whereas $CeAlO_3$ was reoxidized to CeO_2. Shyu *et al.* [57] reported XPS, Raman spectroscopy, and TPR results for a series of Ce/Al_2O_3 catalysts. They concluded that Ce existed as a $CeAlO_3$ precursor, small CeO_2 crystallites, and large CeO_2 particles on Ce/Al_2O_3 catalysts. Graham *et al.* [35] reported that lanthanum promotion increases the dispersion and the range of reversible reducibility of alumina supported CeO_2. High temperature led to a loss of support surface area. The presence of promoter such as CeO_2 or mixed Ce-Zr oxides considerably reduces this effect, but it can't be totally avoided. During this process, noble metals deposited on

these supports are encapsulated by support materials leading to loss in catalytic activity. Recently, it was shown using X-ray diffraction analysis that a substantial fraction (25%) of Pd (Pt) becomes unavailable for catalysis as a result of encapsulation [60].

Spectroscopic measurements combined with *ab initio* calculations have shown that in the case of supported rare earth oxides on alumina, modification of the electronic structure of the lanthanide cation occurs, affecting the catalytic properties of the catalyst. Charge redistribution over an alumina surface implies a modification of the acid-base characteristics of the active sites [61]. Lanthanide cations are known to have strong interactions with the support which results in an electronic density redistribution. Metal-support interactions influence both the electronic state of the metal and the surface morphology. The Al_2O_3 support provides a weak ligand field, favoring the high-spin state of the metal and a change in the oxidation state [62].

The crystallographic and solid-state properties of the lanthanide oxides are largely limited to the so-called sesquioxide stoichiometry (M_2O_3), the only stable composition ordinarily observed for these materials. Exceptions from this structure have been observed in the cases of EuO_x and SmO_x. Dioxides having a face-centered cubic structure (fluorite type structure) are known in the case of Ce, Pm and Tb but only the cerium stoichiometry is more stable than the corresponding sesquioxide structure, mostly due to the stability of the Ce^{4+} oxidation state. Ce_2O_3 can be prepared only with difficulty, by extended reduction of CeO_2 at high temperature or by vacuum decomposition of certain salts. Ce_2O_3 oxidizes easily in air to the dioxide. In addition, the oxide system of Ce and Tb contain LnO_x with $1.5 < x < 2.0$. In all three systems mentioned above as characteristic for lanthanide oxides, the stable phases show variable

Ln^{3+}/Ln^{4+} ratios together with the appropriate number of O^{2-} ions needed to achieve electrical neutrality. Rare earth sesquioxides exhibit characteristic polymorphism and can exist in one or more distinct crystalline modifications, depending on the radius of the tetravalent metal ion and the temperature for oxide preparation and quenching. Pertinent parameters of the rare earth cations and stable rare earth oxide phases are available in the literature [63]. X-ray diffraction patterns of most of these materials are also available for comparative purposes [64]. Various oxide modifications may be further distinguished by analysis of IR bands from 200-700 cm^{-1} range. All anhydrous rare earth oxides are ≈75% ionic having a strong basic character (important property for catalytic purposes).

Lanthanide oxides undergo dehydration/rehydration processes. This cyclic process was used to prepare Ln_2O_3 having highly reproducible catalytic activities for alcohol dehydrogenation/dehydration and for double bond isomerizations of olefins [65]. For some reactions, catalytic activities are independent of electronic or magnetic properties of the oxides and are determined by relative acid-base properties or by the surface structure of the catalysts whereas for other types of reactions the paramagnetic nature, lattice oxygen mobility and cation variable valence play important roles, governing the catalytic behavior. For instance, paramagnetic rare earth oxides have been shown in several studies to be effective catalysts for ortho-para hydrogen conversion [66]. The rate is strongly influenced by temperature which affects the paramagnetic properties of the catalyst materials. Diamagnetic oxides such as Y_2O_3 or Lu_2O_3 can be activated by thermal treatment which apparently generates the paramagnetic ions Y^{2+} and Lu^{2+} [67].

Preparation methods. The precursors and/or methods used for preparation can strongly influence the surface structure of a catalyst and consequently its catalytic activity and selectivity. The most widely used precursor for cerium impregnation is the Ce^{3+}-nitrate solution utilized often for preparation of three-way catalysts for automotive exhaust systems [68]. After calcination, a well dispersed cerium phase is observed on the Al_2O_3 support, at low cerium loading [69-70]. Miki *et al.* [42] prepared a cerium catalyst by incipient wetness impregnation and compared its surface structure with a cerium catalyst prepared by the sol-gel technique, which uses Ce^{3+}-nitrate dissolved in ethylene glycol and aluminum tri-isopropoxide. Different CeO_x surface structures were obtained which led to modified catalytic behavior.

Ion exchange is an alternative method used for preparation of catalysts [70-71]. The method is based on the electrostatic adsorption of the ions at a pH lower than the isoelectric point (IEP) characteristic for each support when the surface is positively charged and anion adsorption can occur. Positive and negative charged support surfaces can adsorb oppositely charged ions from the solution. The exact chemistry depends on support, pH and species in solution. The pH value of the solution will act as a surface charge selection switch, favoring the deposition of a given ion. Using this method, molybdenum was successfully well dispersed on TiO_2 [72] and Al_2O_3 [73] supports. Difficulties in controlling the equilibrium of ionic species present in the precursor solutions at various pH values preclude the general utilization of this technique.

For metal impregnation, Kummer *et al.* [74] proposed a method which involves thermal transport from the bulk phase of a metal foil to a dispersed phase on the support surface. The metal concentration on such catalysts is low but highly dispersed. In this

way, cerium was deposited on the support by incipient wetness impregnation using Ce^{3+}-nitrate solution, before the transition metal impregnation. Such catalysts used CeO_2 as an additive favoring the metal transport (in this case, Pt) and dispersion, leading to a very complex CeO_2-metal surface structure.

Dufour *et al.* [75] used organometallic compounds for rhodium impregnation of a silica support. The interaction mode of the $Rh(\eta^3\text{-}C_3H_5)$ with the oxide support varies according to the nature and the degree of hydroxylation of the support. Different grafted rhodium species were found on the support surface after impregnation. Didillon *et al.* [76] extended the use of organometallics for other transition metals (group VIII-metals) and found that highly dispersed metal phases can be successfully anchored onto low-surface area Al_2O_3. Usmen *et al.* [77] used a La^{3+} pretreated alumina as a support to form a well dispersed cerium phase during impregnation. They found that well dispersed La^{3+}-phases interact with CeO_2 leading to a better cerium and platinum dispersion. Higher cerium dispersion leads to the retention of more reducible oxides such as $CeAlO_3$ with consequences on the oxygen storage capacity of the catalyst [57].

Van Hengstum *et al.* [78] and later Baiker *et al.* [18] have developed a synthetic method for catalyst preparation that involves alkoxide grafting using a metal-organic compound. Generally, an alkoxide grafting reaction may be written as follows:

$$\text{Support-OH} + \text{M-(OR)}_x \rightarrow \text{Support-O-M(OR)}_{x-1} + \text{R-OH} \qquad (3\text{-}1)$$
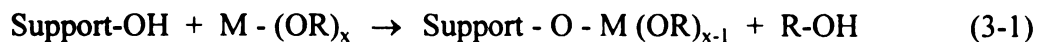
The chemistry of this method involves the formation of a covalent bond between the metal center and the support surface, followed by the elimination of an alkoxide ligand from the metal center (M) as an alcohol. Excellent dispersion was obtained for

vanadium impregnation on different supports (SiO_2, Al_2O_3 or TiO_2), when vanadium tetra-isobutoxide solution was used as a precursor.

For example, silica-supported cerium oxide catalysts of various contents (less than 11% Ce) were prepared by anchoring cerium acetylacetonate in organic media and studying their surface structure. The resulting CeO_2 particles were 1-3 nm in diameter after calcination in oxygen at 673 K. The highly dispersed cerium oxide obtained by using the cerium acetylacetonate precursor shows a shift to higher XPS binding energies for Ce_{3d} and O_{1s}, increased CO stretching in CO-Ce^{4+} terminal groups, and a blue shift of the band gap measured by diffuse reflectance in comparison with catalysts prepared using the classical preparation by incipient wetness using cerium nitrate [79].

The use of a "hot grafting" technique refers to a grafting process using a metal-alkoxide precursor under reflux condition and elevated temperature. This technique can be an alternative way to improve the interaction between the precursor and support surface [80]. The high cost as well as the sensitivity to air and water of these metal-organic compounds [81], confer to the grafting method a disadvantage for large scale catalyst impregnation. It was found that in some cases, the presence of ethanol in the system as an exchange ligand influences the reactivity of cerium alkoxide toward grafting with the hydroxyl groups from the support surface [82].

Recently, lanthanide alkoxide catalysts were successfully used in such organic reactions as synthesis of vitamins and steroids [83-84], being promising catalysts for heterogeneous catalysis processes applied in organic synthesis. If these alkoxides are prepared from chiral alcohols, the catalysts obtained may be used to perform asymmetric synthesis, largely applied in the drug industry [85]. A monolayer dispersion of the

impregnated lanthanide-alkoxide, fixed on a solid support, may confer on the catalysts increased selectivity and activity in these types of organic synthesis.

3.2 Supported MnO_x catalysts used in oxidative dehydrogenation reactions

One of the goals in this study has been to develop new synthetic methods that allow good control over the structure of the catalytically active element, in this case a metal oxide material. As mentioned above, variation in the unpromoted or promoted metal oxide bulk and surface structure would be reflected in the catalysts' properties such as stability, activity and selectivity. A heterogeneous catalytic process takes place by adsorption of the reactants on the active site of catalyst surface, where the bonds in the molecule are weakened and broken followed by the reorganization of the molecule by forming a different bonding scheme, leading thus to product. The function of the solid catalyst is to provide an energetically favorable pathway, with low activation energy, for the formation of the desired product. Consequently, a catalyst should consist of small particles acting as active sites, with high dispersion on a high surface, porous material. In many cases, metal oxides play the role of the active site in a catalyst, being able to disperse well on inert supports and act selectively in the catalytic process.

Manganese oxides have been successfully used as the active catalyst phase mostly in oxidation processes. This catalytic activity was attributed to manganese's capability of forming oxides having different oxidation states (MnO_2, Mn_2O_3, Mn_3O_4, or MnO) and storing oxygen in its crystalline lattice. Unsupported or supported MnO_x was found to be an active catalyst in several oxidation processes such as CO [86-89], ethylene [90], methanol [91] oxidation, NO_x [92-93], H_2O_2 [94], O_3 [95] decomposition, oxidative coupling of methane [96-98], selective catalytic oxidation of NH_3 [99-101], ethylbenzene

[102], hydropyrazine to pyrazine oxidative dehydrogenation [103], selective catalytic reduction of NO with NH_3 [99-101, 104-105], CO [106] and C_2H_4 [91] hydrogenation, H_2S/H_2 sulfidation [107], and Hg waste removal [108]. As observed from the literature search, a wide variety of catalytic reactions have been tested on MnO_x-based catalysts. Due to its labile oxidation state, manganese is capable of performing either as an oxidation agent being reduced (relation 3-2) or as a reducing agent being oxidized (relation 3-3) acting as the active component in the redox process.

$$Mn^{4+} + e^- \rightarrow Mn^{3+} + e^- \rightarrow Mn^{2+} \qquad (3-2)$$

$$Mn^{2+} - e^- \rightarrow Mn^{3+} - e^- \rightarrow Mn^{4+} \qquad (3-3)$$

Structural characterization of unsupported or supported MnO_x catalysts identify the presence of MnO_2 or mixed MnO_2/Mn_2O_3 phases as active components [105, 107, 109]. The ratio between the MnO_2 and Mn_2O_3 phases is a function of manganese loading and calcination temperature of the catalyst during preparation [107, 109]. Manganese interaction with the support or other components present on the catalyst significantly influences its oxidation state. Thus, the Mn_{2p} XPS binding energy showed a 0.57 ±0.04 eV shift when manganese interacted with copper and formed a mixed spinel structure of $Cu_{1+x}Mn_{2-x}O_4$ [101]. The presence of promoter such as lanthanum influences the MnO_x structure and dispersion. It was found that lanthanum interacts with manganese during thermal treatment of the catalyst to form mixed Mn-La oxides, leading to a better MnO_x dispersion than in the case of the unpromoted catalyst. Lanthanum promotion led to a more robust MnO_x catalyst, which minimized the formation of catalytically less active Mn_3O_4 species [102]. In some cases, the unsupported MnO_x catalyst was more active

than the supported one, due to the absence of manganese interaction with the support and availability to the reaction [87, 103]. For unsupported MnO_x catalyst it was observed that for NO catalytic decomposition, high reaction temperatures are required in order to get significant reaction rates (> 500°C). At high calcination temperatures (above 600°C), Mn_2O_3 releases more oxygen than Mn_3O_4 phase, being more catalytically active. Because these reactions occur at high temperatures and the reaction pathway is temperature dependent (NO can be converted either to N_2O or to NO_2), the structural modification of MnO_x should be carefully examined. MnO_x loading and dispersion of supported catalysts influence the catalytic activity as well. Previous data for CO oxidation have shown that the specific activity increases with decreasing concentration of the MnO_x, except for very low concentration (loadings) in which activity decreases anyhow. Increased dispersion of the oxide on the support surface led to a significant increase in the activity, a fact attributed to the increased quantity exposed to the reaction feed [86, 105]. MnO_x dispersion was found to be a function of manganese precursor and loading, preparation method, and post-preparation thermal treatment. It was found that compared with Mn-nitrate, a Mn-acetate precursor led to a highly dispersed Mn_2O_3 phase on a γ-Al_2O_3 support [109]. This was attributed to ionic interactions with acidic and basic surface -OH groups from alumina. Mn-nitrate yields comparable dispersion with that obtained from Mn-acetate precursor, for loading below 1 wt% Mn. Large manganese oxide crystals are formed at higher loadings. Multiple step treatment with low concentration Mn-nitrate solution does lead to a better MnO_x dispersion. In the case of a supported MnO_x catalyst prepared with Mn-nitrate, higher loading of Mn is

recommended, in order to observed the influence of the calcination temperature during preparation process. Structural transformations of MnO_x were observed as a function of calcination temperature. Thus, for a series of MnO_x supported on γ-Al_2O_3 catalysts with various Mn-loadings, the β-MnO_2 phase was predominant for low Mn-loading and calcination temperature during preparation. At high loadings and calcination temperatures, the α-Mn_2O_3 phase is dominant [105, 107].

The ability of manganese to form MnO or $Mn(OH)_2$ species makes it a useful catalyst in hydrogenation reactions as well [91, 106]. MnO can be formed only after calcination at very high temperatures (above 900°C), when XRD patterns start to be observable [110]. Its catalytic activity is a function of the support and dispersion. The MnO phase was found to act as a promoter, prohibiting the hydrogenation of C_2H_4 and C_3H_6 to C_2H_6 and C_3H_8, respectively, in CO hydrogenation processes [106].

As suggested by many previous experiments, MnO_x catalysts can be used in combination with other transition metals which can form either mixed oxides (spinel type or pervoskite) or oxides acting as promoters for manganese (such as lanthanum, yttrium, cerium, etc.). From previous studies, it is known that manganese can interact to form spinel-type structures with copper [101], or with WO_3 [98], TiO_2, Al_2O_3, [111], CeO_2 [111, 112], or pervoskite-type structures with La, Sm and Ba [113-114]. Manganese has an excellent oxygen storage capability, so if it is combined with cerium, the unit cell parameters increase with the presence of mixed $MnCeO_x$ phase, forming a catalyst with "superstoichiometric" oxygen concentration [115]. EPR characterization of these MnO_x catalysts supported on CeO_2 and Al_2O_3 have shown a high degree of ionicity of the well-

dispersed MnO_x layer, with well defined sites on CeO_2 and isolated sites on Al_2O_3 (poor MnO_x dispersion). Integration of the EPR signals corresponding to paramagnetic O_2^- lattice species from mixed $MnCeO_x$ oxide allowed an evaluation of its oxygen storage capacity [116]. Another important aspect in catalysts structure characterization of materials with catalytic activity in oxidation processes is the mobility of lattice oxygen. Migration of oxygen on the surface is important due to the repeated oxidation-reduction cycles of the catalyst. Combination of two element interacting with each other, deposited on a given support and used as catalyst in catalytic oxidation processes exhibits different oxygen mobility in comparison with a single component catalyst. Manganese oxides are typical berthollide compounds with very labile lattice oxygen. It was found that placed in the proximity of CeO_2, the oxygen mobility from the MnO_x structure is strongly affected. In a Mn-Ce mixed oxide, Ce provides oxygen to Mn at low temperature and, contrarily, withdraws oxygen at elevated temperatures (> 500°C). Thus, cerium improves the activity of MnO_x in oxidation processes at lower temperature and decreases its activity at high temperature, the active component in this case being CeO_2 which takes oxygen from MnO_x [117]. Having all this information in mind, the following research objectives have been suggested.

3.3 References

1. Moffat, J. B. *Theoretical aspects of heterogeneous catalysis*, Van Nostrand Reinhold, New York, **1990**, p. 256-426

2. Thomas, J. M. *Angew. Chem. Int. Ed. Engl.* **1994**, *33*, 913-937.

3. Gates, B. C. *Catalytic Chemistry*, John Wiley & Sons, Inc. New York, **1992**, p. 310-421.

4. Hicks, R. F. *Chem. Eng. Sci.* **1990**, *45(3)*, 2647-2651.

5. Worley, S. D.; Rice, C. A.; Mattson, G. A.; Curtis, C. W.; Guin, J. A. *J. Chem. Phys.* **1982**, *76*, 20-24.

6. Taylor, K. C. in *Catalysis and Automotive Pollution Control* by Crucq, A.; Fressnet, A. **1987**, Elsevier, Amsterdam.

7. Johnson, D. W. Jr. *J. Catal.* **1977**, *48*, 87-97.

8. Briot, P. *Appl. Catal.* **1990**, *59*, 141-152.

9. Briot, P.; Primet, M. *Appl. Catal. 1991*, *68*, 301-314.

10. Hick, R. F. *J. Catal.* **1990**, *122*, 295-306.

11. Baldwin, T. R.; Burch, R. *Appl. Catal.* **1990**, *66*, 359-381.

12. Otto, K. *Langmuir*, **1989**, *5*, 1364-1369.

13. Ismagilov, Z. R.; Kerzhentsev, M. A. *Catal. Rev.-Sci. Eng.* **1990**, *32(1,2)*, 51-103.

14. Arakawa, T.; Tsuchi, Y. S.; Shiokawa, J. *J. Catal.* **1982**, *74*, 317-322.

15. Wise, H.; McCarty, J. G. *Catal. Today*, **1990**, *8*, 231-248.

16. Prasad, R.; Kennedy, L. A.; Ruckenstein, E. *Combust. Sci. Technol.* **1980**, *22*, 271-275.

17. Dwyer, F. G. *Catal. Rev.* **1972**, *6(2)*, 261-291.

18. Kifenski, J.; Baiker, A.; Glinski, M.; Dollenmeier, P.; Wokaun, A. *J. Catal.* **1986**, *101*, 1-11.

19. Stubenrauch, J. ; Vohs, J. M. *J. Catal.* **1996**, *159*, 50-57.

20. Seiyama, T. *Catal. Rev. - Sci. Eng.* **1992**, *34(4)*, 281-300.

21. Fornasiero, P.; Balducci, G.; DiMonte, R.; Kaspar, J.; Sergo, V.; Gubitosa, G.; Ferrero, A.; Graziani, M. *J. Catal.* **1996**, *164*, 173-183..

22. Jaecnicke, S.; Chuah, G. K. *Ber. Bunsenges. Phys. Chem.* **1992**, *96(1)*, 1-9.

23. Arai, H. *Appl. Catal.* **1986**, *26*, 265-276.

24. Zhang, H. M.; Teraoka, Y.; Yamazoe, N. *Appl. Catal.* **1989**, *6(1,2)*, 155-162.

25. Zwinkels, M. F. M.; Jaras, S. G.; Menon, P. G.; Griffin, T. A. *Catal. Rev. - Sci. Eng.* **1993**, *35(3)*, 319-358

26. Beguin, B.; Garbowski, E.; Primet, M. *J. Catal.* **1991**, *127*, 595-604.

27. Tijburg, I. I. M.; Geus, J. W.; Zandbergen, H. W. *J. Mater. Sci.* **1991**, *26*, 6479-6486.

28. Alvero, R.; Bernal, A.; Carrizosa, I.; Odriozola, J. A. *Inorg. Chim. Acta*, **1987**, *140*, 45-48.

29. Xie, Y. C.; Qian, M. X.; Tang, Y. Q. *China-Japan-U.S. Symposium on Heterogenous Catalysis Related to Energy Problem*, **1982**, *B.10C*, China.

30. Yang, J. Y.; Swartz, W. E. *Spectrosc. Lett.* **1984**, *17*, 331-332.

31. Baiker, B. G.; Clark, N. J. in *Studies in Surface Science and Catalysis*, Delmon, B. Grange, P. Jacobs, P. A. Poncelet, G. Elsevier, Amsterdam, **1987**, *31*, 455-62.

32. Kieffer, R.; Kiennemann, A.; Rodriquez, M.; Bernal, S.; Rodriquez-Izquierdo, J. M. *Appl. Catal.* **1988**, *42*, 77-86.

33. Shyu, J. Z.; Otto, K.; Watkins, W. L. H.; Graham, G. W.; Belitz, R. K.; Gandhi, H. S. *J. Catal.*, **1988**, *114*, 23-28.

34. Hay, C. M.; Jennings, J. R.; Lambert, R. M.; Nix, R. M.; Owen, G.; Rayment, T. *Appl. Catal.* **1988**, *37*, 291-304.

35. Graham, G. W.; Schmitz, P. J.; Usmen, R. K.; McCabe, R. W. *Cat. Lett.* **1993**, *17*, 175-184.

36. Masuda, K.; Kawai, M.; Kuna, K.; Kachi, N.; Mizukami, F. in *Preparation of Catalysts V Ed.* Poncelet, G.; Jacobs, P. A.; Grange, P.; Delmon, B.; Elsevier, Amsterdam, **1991**, 229-238.

37. Sugiyama, S.; Matsumura, Y.; Moffat, J. B. *J. Catal.* **1993**, *139*, 338-350.

38. Bunluesin, T.; Cordatos, H.; Gorte, R. J. *J. Catal.* **1995**, *157*, 222-226.

39   Dulamita, N. *Rev. Rom. Chim.* **1985**, *36(11)*, 1050-1051.

40. Steinberg, M. *Anal. Appl. Rare Earth Mater. Nato Adv. Study Inst.* **1972**, 263-270.

41. Perrichon, V.; Laachir, A.; Bergeret, G.; Frety, R.; Tournayan, L.; Touret, O.; *J. Chem. Soc. Faraday Trans.* **1994**, *90(5)*, 773-781.

42. Miki, T.; Ogawa, T.; Haneda, M.; Kakuta, N.; Ueno, A.; Tateishi, S.; Matsuura, S.; Sato, M. *J. Chem. Phys.* **1990**, *94*, 6464-6467.

43. Yao, H. C.; Yao yu, Y. F. *J. Catal.* **1984**, *86*, 254-265.

44. Su, E. C.; Montreuil, C. N.; Rothschild, W. G. *Appl. Catal.* **1985**, *17*, 75-86.

45. Loof, P.; Kasemo, B.; Keck, K. E. *J. Catal.* **1989**, *118*, 339-348.

46. Haneda, M.; Mizushima, T.; Kakuta, N.; Ueno, A.; Sato, Y.; Matsuura, S.; Kasahara, K.; Sato, M. *Bull. Chem. Soc. Jpn.* **1993**, *66*, 1279-1288.

47. Schaper, H.; Doesburg, E. B. M.; VanReijen, L. L. *Appl. Catal.* **1983**, *7*, 211-220.

48. Cordatos, H.; Bunluesin, T.; Stubenrauch, J. ; Vohs, J. M.; Gorte, R. J. *J. Phys. Chem.* **1996**, *100*, 785-789.

49. Yu-Yao, Y.F.; Kummer, J.T. *J. Catal.* **1987**, *106*, 307-312.

50. Chojnacki, T.; Krause, K.; Schmidt, L.D. *J. Catal.* **1991**, *128(1)*, 161-185.

51. Oudet, F.; Courtine, P.; Vejux, A.J. *J. Catal.* **1988**, *114*, 112-120.

52. Yang, J.K.; Swartz, W.E. *Spectrosc. Lett.* **1984**, *17*, 331-335.

53. Cordatos, H.; Ford, D.; Gorte, R. J. *J. Phys. Chem.* **1996**, *100*, 18128-18132.

54. Zafiris, G. S.; Gorte, R. J. *J. Catal.* **1993**, *143*, 86-91.

55. Yamaguchi, T.; Ikeda, N.; Hattony, H.; Tanabe, K. *J. Catal.* **1981**, *67*, 324-330.

56. Zafiris, G. S.; Gorte, R. J. *J. Catal.* **1993**, *139*, 561-567.

57. Shyu, J. Z.; Weber, W. H.; Gandhi, H. S. *J. Phys. Chem.* **1988**, *92*, 4964-4970.

58. Ledford, J. S.; Houalla, M.; Proctor, A.; Hercules, D. M. *J. Phys. Chem.* **1989**, *93*, 6770-6777.

59. Dulamita, N.; Pop, A.; Corbeanu, V. *Studia*, **1984**, *29*, 3-11.

60. Graham, G. W.; Jen, H.-W.; Chun, W.; McCabe, R. W. *Catal. Lett.* **1997**, *44*, 185-187.

61. Capitan, M. J.; Centeno, M. A.; Malet, P.; Carrizosa, I.; Odriozola, J. A. *J. Phys. Chem.* **1995**, *99*, 4655-4660.

62. Tauster, S. J.; Fung, S. C.; Garten, R. L. *J. Am. Chem. Soc.* **1978**, *100*, 170-175.

63. Korner, R.; Ricken, M.; Nolting, J. *J. Solid State Chem.* **1989**, *78*, 136-147.

64. *Powder Diffraction File*, Inorganic Phases, JCPDS, **1983**, p. 18, 91, 346, 534

65. Rosynek, M. P.; *Cat. Rev. - Sci. Eng.* **1977**, *16(1)*, 111-154.

66. Baron, K.; Selwood, P. W. *J. Catal.* **1973**, *28*, 422-426.

67. Aries, J. A.; Selwood, P. W. *J. Catal.* **1974**, *33*, 284-288.

68. Kubsh, J. E.; Rieck, J. S.; Spencer, N. D. in *Catalysis and Automotive Pollution Control II*, ed. Crucq, A. Elsevier, Amsterdam, **1991**, 125-138.

69. Diwell, A. F.; Rajaram, R. R.; Shaw, H. A.; Truex, T. J. *in Catalysis and Automotive Pollution Control II*, ed. Crucq, A. Elsevier, Amsterdam, **1991**, 139-152.

70. Burch, R.; Flambard, A. R. in *Preparation of Catalysts III* by Poncelet, G.; Grange, P.; Jacobs, P. A. Els. Sci. Publ. Amsterdam, **1983**, 311-320.

71. Brunelle, J. P. *Pure Appl. Chem.*, **1978**, *50(9,10)*, 1211-1229.

72. Luthra, N. P.; Cheng, W. C. *J. Catal.* **1987**, *107*, 154-160.

73. VanVeen, J. A. R.; deWitt, H.; Emeis, C. A.; Hendriks, P. A. J. M. *J. Catal.* **1987**, *107*, 579-582.

74. Kummer, J. T.; Yu-Yao, Y. F. *J. Catal.* **1987**, *106*, 307-312.

75. Dufour, P.; Houtman, C.; Santini, C. C.; Basset, J. M.; Hsu, L. Y.; Shore, S. G. *J. Am. Chem. Soc.* **1992**, *114*, 4248-4257.

76. Didillon, B.; El Mansour, A.; Candy, J. P.; Basset, J. M.; Le Peltier, F.; Bournonville, J. P. in *Preparation of Catalysts V* ed. Poncelet, G.; Jacobs, P. A.; Grange, P.; Delmon, B. Elsevier, Amsterdam, **1991**, 717-723.

77. Usmen, R. K.; Graham, G. W.; Watkins, W. L. H.; McCabe, R. W. *Catal. Lett.* **1995**, *30*, 53-63.

78. Van Hengstum, A. J.; Van Ommen, J. G.; Bosch, H.; Gellings, P. J. *Appl. Catal.* **1983**, *5*, 207-217.

79. Bensalem, A.; Bozon-Verduraz, F.; Delamar, M.; Bugli, G. *Appl. Catal.* **1995**, *121*, 81-93.

80. Smith, P. D.; Klendworth, D. D.; McDaniel, M. P. *J. Catal.* **1987**, *105*, 187-193.

81. Namy, J. L.; Souppe, J.; Kagan, H. B. *J. Org. Chem.* **1984**, *49*, 2045-2049.

82. Mehrotra, R. C.; Kapoor, P. N.; Botsoara, J. M. *Coord. Chem. Rev.* **1980**, *31*, 67-91.

83. Kirk, D. N.; Slade, C. J. *J. Chem. Soc. Perkin Trans*, **1980**, 1, 2591-2569.

84. Evans, D. A.; Hoveyda, A. H, *J. Am. Chem. Soc.* **1990**, *112*, 6447-6449.

85. LeBrun, A.; Namy, J. L.; Kagan, H. B. *Tetrahedron Letters*, **1991**, *32(21)*, 2355-2358.

86. Mooi, J.; Selwood, P. W. *J. Am. Chem. Soc.* **1952**, *74*, 2461-2464.

87. Nohman, A. K. H.; Duprez, D.; Kappenstein, C.; Mansour, S. A. A.; Zaki, M. I. in *Preparation of catalyts V*, ed. Delmon, B.; Jacobs, P. A.; Poncelet, G. Elsevier, Amsterdam, **1991**, p. 617-626.

88. Katz, K. *Adv. Catal.* **1953**, *5*, 177-183.

89. Boreskov, G. K. *Adv. Catal.* **1964**, *15*, 285-294.

90. Dmuchovsky, B.; Freeks, M. C.; Zienty, F. B. *J. Catal.* **1965**, *4*, 577-.

91. Baltanas, M. A.; Stiles, A. B.; Katzer, J. R. *Appl. Catal.* **1986**, *28*, 13-33.

92. Karlsson, H. T.; Rosenberg, H. S. *Ind. Eng. Chem. Process Des. Dev.* **1984**, *23*, 808-815.

93. Yamashita, T.; Vannice, A. *J. Catal.* **1996**, *163*, 158-168.

94. Kanungo, S. B. *J. Catal.* **1979**, *58*, 419-435.

95. Nishino, A. *Catal. Today*, **1991**, *10*, 107-112.

96. Moggridge, G. D.; Rayment, T.; Lambert, R. M. *J. Catal.* **1992**, *134*, 242-252.

97. Burch, R.; Chalker, S.; Squire, G. D.; Tsang, S. C. *J. Chem. Soc. Faraday Trans.* **1990**, *86*, 1607-1614.

98. Wu, J.; Li, S.; Niu, J.; Fang, X. *Appl. Catal. A*, **1995**, *124*, 9-18.

99. Il'Chenko, N. I.; Golodets, G. I. *J. Catal.* **1975**, *39*, 57-72.

100. Singoredjo, L. S.; Korver, R. B.; Kapteijn, F. Moulijn, J. A. *Appl. Catal. B*, **1992**, *1*, 297-302.

101. Wollner, A.; Lange, F.; Schmetz, H.; Knozinger, H. *Appl. Catal. A*, **1993**, *94*, 181-203.

102. Craciun, R.; Dulamita, N. *Catal. Lett.* **1997**, *46(3,4)*, 229-234.

103. Akiyama, T.; Enomoto, Y.; Shibamoto, T. *J. Agric. Food Chem.* **1978**, *26(5)*, 1176-1179.

104. Markvart, M.; Pour, V. *Int. Chem. Eng.* **1975**, *15*, 546-551.

105. Kapteijn, F.; Singoredjo, L.; vanDriel, M.; Andreini, A.; Moulijn, J. A.; Ramis, G.; Busca, G. *J. Catal.* **1994**, *150*, 105-116.

106. Longya, X.; Quigxia, W.; Yide, X.; Jiashng, H. *Catal. Lett.* **1995**, *31*, 253-266.

107. Strohmeier, B. R.; Hercules, J. *J. Phys. Chem.* **1984**, *88*, 4922-4929.

108. Cavallaro, S.; Bertuccio, N.; Antonucci, P.; Giordano, N. *J. Catal.* **1982**, *73*, 337-348.

109. Kapteijn, F.; van Langeveld, D.; Moulijn, J. A.; Andreini, A.; Vuurman, M. A.; Turek, A. M.; Jehng, J. M.; Wachs, I. E. *J. Catal.* **1994**, *150*, 94-104.

110. McClune, W. F. *Powder diffraction file, Inorganic phases, International center for diffraction data*, Swarthmore, **1983**, p. 279, 599, 730, 731.

111. Baltanas, M. A.; Stiles, A. B. Katzer, J. R. *J. Catal.* **1984**, *88*, 362-373.

112. Abi-Aad, E.; Bennani, A.; Bonnelle, J. P.; Aboukais, A. *J. Chem. Soc. Faraday Trans.* **1995**, *91*, 99-104.

113. M. Shelef, L. P. Haack, R. E. Soltis, J. E. DeVries and E. M. Logothetis, *J. Catal.* **1992**, *137*, 114-126.

114. Ledford, J. S.; Kim, Y. M.; Houalla, M.; Proctor, A. Hercules, D. M. *Analyst*, **1992**, *117*, 323-327.

115. Ivanova, A. S.; Dzisco, V. A.; Moroz, E. M.; Nosckova, S. P. *Kinet. Katal.* **1986**, *27(2)*, 428-434.

116. Baltanas, M. A.; DeCaria, S. J.; Katzel, J. R.; Dybowski, C. *Acta Chim. Hung.* (Eng.) **1985**, *118(4)*, 285-295.

117. Imamura, S.; Shono, M.; Okamoto, A.; Ishida, S. *Appl. Catal A*, **1996**, *142*, 279-288.

CHAPTER 4

SYNTHETIC METHODS FOR PREPARATION OF

CeO_2-PROMOTED SiO_2 CATALYSTS

4.1 Introduction

Cerium oxide has been employed extensively as a catalyst or as a textural and structural promoter for supported metal or metal oxide catalysts [1-28]. Recently, in a review article Trovarelli [29] summarized many of the catalytic properties and characterization studies of CeO_2 reported during the last decades. Generally, the structural promotion effect was attributed to cerium's ability to form crystalline oxides with lattice defects which may act as catalytic active sites [3-4], whereas its textural promotion effect is given by the excellent thermal and mechanical resistance which CeO_2 confers to the catalysts [2-7]. Ce-based catalysts are commonly utilized in oxidation reactions; their use in automotive catalytic converters, for example, render them valuable catalysts [29]. Detailed information about studies on Ce-based catalysts was given in Chapter 3 (see 3.1 paragraph).

This part of the study is focused on the structural transformations of SiO_2-supported CeO_x species when various cerium precursors and thermal treatments were used for catalyst preparation. DRIFTS and cross polarization (CP) ^{29}Si MAS-NMR were used to obtain information about support - cerium precursor interactions. The crystalline nature and dispersion of CeO_2 on the SiO_2 support were investigated by transmission electron microscopy - energy dispersive X-ray analysis (TEM-EDX), XRD, and

temperature programmed reduction (TPR). Additional information about the bulk and surface structure of supported CeO_2 was provided by electron paramagnetic resonance (EPR) and X-ray photoelectron spectroscopy (XPS) analysis.

4.2 Experimental

Catalysts preparation. Catalysts were prepared by the impregnation of a SiO_2 support (surface area = $300m^2$/g) with Ce^{4+}-ammonium nitrate in water (Mallinckrodt Co) and Ce^{4+}-methoxyethoxide 18-20% in methoxyethanol (Gelest Co.) precursors. The support consists of finely ground (<230 mesh) silica-gel (Davison Chemical Co.), which was calcined in air at 500°C (800°C) for 24 h, prior to impregnation. Catalysts that originated from the Ce-nitrate precursor are designated as CeqN and those from Ce-alkoxide as CeqA, where q is the Ce/Si atomic ratio ($q = 8 \times 10^{-2}$). The actual cerium concentrations in the catalysts were confirmed by inductively coupled plasma (ICP) analysis. The results showed a ± 10% error when compared to cerium concentration calculated from the amount of precursor added during preparation. The impregnation techniques employed for catalysts preparation were: i) incipient wetness, using Ce^{4+}-nitrate (CeqN) and ii) "hot grafting" using the Ce^{4+}-methoxyethoxide solution (CeqA) monitored under inert (Ar) atmosphere with continuous mixing for 48 h, under reflux at 80-85°C. After impregnation, all catalysts samples were dried at 125°C for 16 h followed by calcination in air at 500°C or 800°C.

BET Surface Area. Surface area (S_a) measurements were performed using a Quanta-Chrome Quantasorb Jr. Sorption System. Approximately 0.1 g of catalyst was outgassed in N_2 at 165°C for 12h, prior to adsorption measurements. The measurements

were made using N_2 partial pressures in He of 0.05, 0.08, and 0.15 (N_2 surface area = 0.162 nm^2) at liquid N_2 temperature (77 K). The estimated error for S_a results is ± 5%.

Solid state ^{29}Si MAS-NMR. Solid state ^{29}Si MAS-NMR spectra were obtained at room temperature using a Varian VXR-400S spectrometer with an Oxford cryomagnet generating a magnetic field of 9.395 T and operated at a Sun workstation network with a V-NMR operating system Version 4.1. The Fourier transform of free induction decay (FID) was observed using a quadrature detection at 79.4559 MHz at a spinning rate of 4000 rot/min. The acquisition time was long enough to ensure full ^{29}Si nucleus relaxation for accurate quantitative data analysis. The cross polarization technique can be used to obtain a better resolution for the silica peaks. The technique was developed and used successfully to characterize a silica gel surface by Maciel and Sindorf [30]. Following their work, numerous studies have shown the reliability of this technique in studies on various type of silica [31-34]. The ^{29}Si-^1H cross polarization restricts detection to silicon nuclei that are positioned close to protons or near the surface [30]. Typical ^{29}Si resonance occurs when the magnetic moment and the spin of silica nucleus are antiparallel, resulting in a (-g) parameter. About 0.5 g catalyst powder was introduced into the spectrometer holder for analysis. The spectrometer was tuned at the minimum signal possible for both silica-29 and proton. Silica peaks were deconvoluted using the program from the V-NMR spectrometer workstation (for details about NMR analysis, please refer to Chapter 1).

DRIFTS analysis. Diffuse reflectance spectra were acquired using a Mattson-Galaxy FTIR-3020 instrument with a diffuse reflectance attachment from Spectra-Tech Inc. The catalyst powders (20-25 mg) were put into the sample holder and introduced

into the DRIFTS attachment. The spectra collected are in Kubelka-Munk units versus wavenumber. IR spectra were acquired with resolution of 4.0 cm^{-1} over a 400-4000 cm^{-1} wavenumber range. For details about DRIFTS analysis please refer to Chapter 1.

Transmission electron microscopy (TEM). The TEM bright field images, EDX, and electron diffraction patterns images were recorded with a Jeol 100CX II instrument equipped with an X-ray analyzer for EDX analysis, at accelerating voltages of 120V. Catalyst samples were deposited on a carbon-dusted copper grid coated with a holey film, and introduced into the analysis chamber on a beryllium grid holder. The catalyst above a hole of the holey film was chosen for analysis, in order to avoid interference from the film structure. EDX spectra were collected from the same spot where the TEM electron diffraction patterns have been recorded.

X-Ray Diffraction (XRD). X-ray powder diffraction patterns were obtained with a Rigaku XRD diffractometer employing Cu Kα radiation (λ = 1.541838 Å) and operated at 45 kV and 100 mA. Diffraction patterns were obtained using a scan rate of 0.5 deg/min with 1/2 mm slits. Powdered samples were mounted on glass slides by pressing the powder into an indentation on one side of the slide. The mean crystallite size ($\bar{d}$) of CeO$_2$ particles was determined from XRD line broadening measurements using the Scherrer equation (1-3) [35]. Semi-quantitative X-ray diffraction data were obtained by comparing CeO$_2$<111>/SiO$_2$ peak ratios measured for catalyst samples with those of CeO$_2$ and SiO$_2$ physical mixtures of known concentration. This method assumes that cerium addition does not disrupt the SiO$_2$ structure, and consequently, does not affect the intensity of the SiO$_2$ line. The error in this method was estimated to be ± 20%.

Temperature-programmed reduction (TPR). TPR profiles for the CeqN and CeqA catalysts were obtained using a classical U-shaped quartz reactor connected to a thermal conductivity detector (TCD) for H$_2$ consumption analysis. The temperatures were measured with a Ni-Cr-Ni thermoelement placed directly in the catalyst bed. A reducing agent mixture of 10% H$_2$ in N$_2$ was passed over 0.1 g catalyst powder, at 30 mL/min flow rate. The temperature interval considered for analysis is from 25°C to 950°C (10°C/min heating rate). The TPR profiles are presented as H$_2$ consumption (arbitrary units) versus temperature (°C).

Electron Paramagnetic Resonance (EPR). Powder catalyst samples were analyzed in quartz sample tubes at -160°C using a Varian E4 spectrometer. The magnetic field was set at 3200 Gauss with a modulation frequency of 100 kHz. The g-factor (g$_s$) for cerium samples (B$_s$) was determined by comparison with the field value at resonance for a reference (B$_{ref}$), in this case the diphenyl-picryl-hydrazyl radical (DPPH, g$_{ref}$ = 2.0036). The reference was placed together with the catalyst samples into the quartz tube for accurate g-value determinations. Accordingly, the value for g$_s$ was evaluated based on the relation (2) given below [36]:

$$g_s = g_{ref}\, B_{ref}/B_s \qquad\qquad (4\text{-}1)$$

X-ray photoelectron spectroscopy (XPS). Surface analyses of the catalyst samples were carried out using a Perkin-Elmer Physical Electronics XPS 5400 spectrometer equipped with a hemispherical analyzer. Instrument control, data collection and manipulation were performed with an Apollo 3500 workstation, running a PHI-XPS version 3.0 software. The standard Mg Kα X-ray source was used for all samples

analysis and was operated at 15 kV, 20 mA, and 300 W. The catalysts were mounted on sample stubs using double sided tape and placed into the analysis chamber for XPS analysis (base chamber pressure was 2×10^{-9} torr). The binding energies for catalyst samples were referenced to the Si_{2p} peak (103.4 eV). XPS binding energies were measured with a precision of ± 0.2 eV, or better. The reported XPS I_{Ce3d}/I_{Si2p} values are the average of three consecutive analyses.

4.3 Results and Discussion

Catalyst texture. BET measurements for the neat support and cerium catalysts (see in Table 4.1) indicate a decrease of surface area for the SiO_2 support from 300 m^2/g (precalcined at 500°C) to 210 m^2/g after calcination at 800°C. This process is attributed to the collapse of the silica porous structure at elevated temperature, process well known from the literature [37-38]. After cerium impregnation, the surface area of the CeqN and CeqA catalysts calcined at 500°C, remains unchanged, since CeO_2 is known to have no significant porosity which may influence the texture of the promoted catalyst unless a special preparation technique is employed [39]. For catalysts calcined at 800°C, a decrease in the surface area was observed; however, the magnitude of the decrease is very much attenuated due to the textural promoter effect of the CeO_2.

Table 4.1 BET, semi-quantitative XRD, and XPS analysis data for Ce-promoted SiO$_2$ catalysts

Catalysts	BET [m^2/g]	CeO$_2$ Size [nm]	% CeO$_2$ Crystalline	I$_{Ce3d}$/I$_{Si2p}$ X Intensity
SiO$_2$[b]	300	-	-	-
SiO$_2$[c]	210	-	-	-
CeqN[b]	303	9.9	89	0.4
CeqN[c]	268	10.0	97	0.2
CeqA[b]	300	2.5	29	6.7
CeqA[c]	272	2.8	43	4.6

a - the error in this method was estimated to be ± 20%; b - samples calcined at 500°C; c - samples calcined at 800°C.

Cerium precursor/SiO$_2$ support interaction. Differences in the chemical nature of the interaction between cerium precursors and SiO$_2$ support were used to explain why more CeO$_2$ crystalline phase was formed in the case of *Ce8N* catalysts than in the case of the *Ce8A* catalysts. For *Ce8N* catalysts, the weak physical interactions between cerium nitrate and silica support led after calcination at 500°C to an easy formation of large CeO$_2$ particles with a high degree of crystallinity. For *Ce8A* catalysts, covalent bonds between cerium alkoxide and surface hydroxyl groups from silica support led after calcination at 500°C to small CeO$_2$ crystallites and a low degree of crystallinity. To support these statements, diffuse reflectance infrared Fourier transform spectroscopy (DRIFTS) and ^{29}Si solid state nuclear magnetic resonance analysis were performed in order to understand the interaction between cerium precursors and SiO$_2$ support.
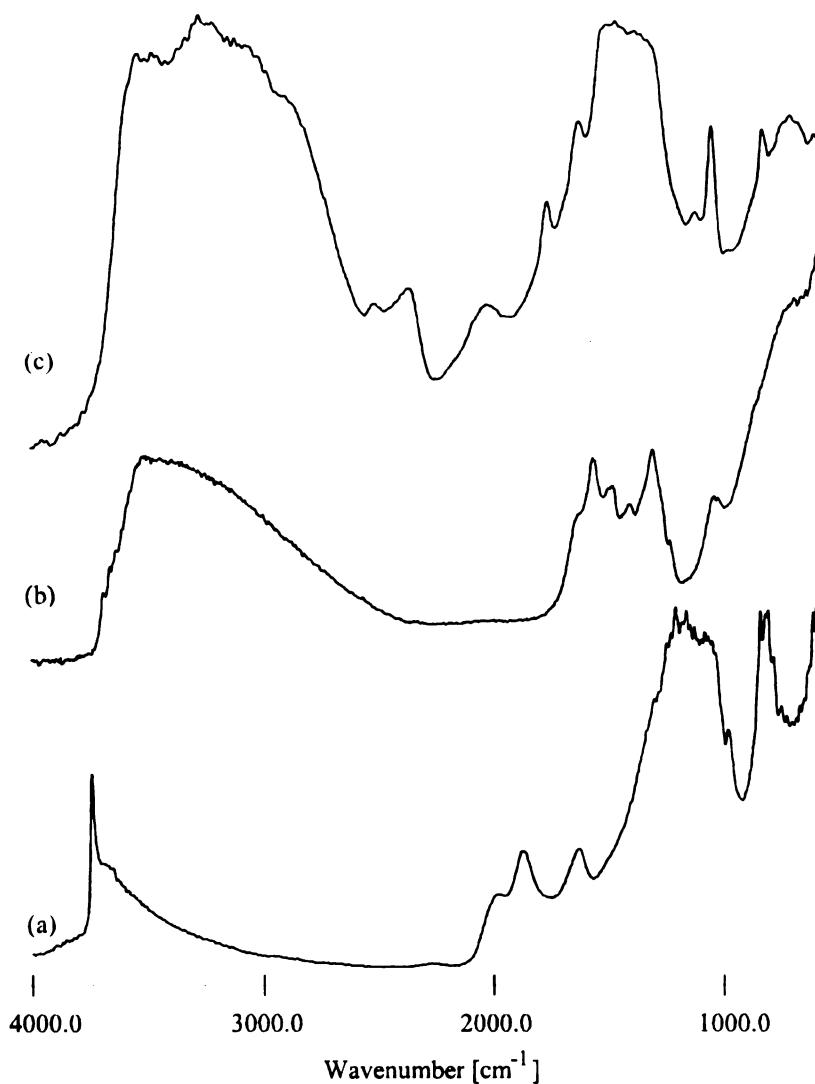
Figure 4.1 DRIFTS spectra of standard materials: a) SiO_2 support; b) CeO_2;
c) $Ce(OH)_4$.

DRIFTS spectra of SiO_2 (Figure 4.1 a), CeO_2 (Figure 4.1 b) and $Ce(OH)_4$ (Figure

4.1 c) are presented as reference for interpretation of the DRIFTS spectra obtained for the

CeO_2/SiO_2 catalysts prepared by grafting and incipient wetness impregnation.

Table 4.2. Tentative infrared bands assignments for cerium treated SiO_2 catalysts

Ord #	Wavenumber [cm^{-1}]	IR Band Assignments	References
1	3740	free -OH stretch on SiO_2	42, 43
2	3700-3000	-OH stretch hydrogen bonded	40, 42, 43
3	3540	-OH stretch hydrogen bonded from $Ce(OH)_4$	41
4	2986	C-H stretch from $-CH_2-$ (R)	40, 41
5	2928, 2830	C-H stretch from CH_3- (R)	40, 41
6	1638	H_2O adsorbed on SiO_2 surface	40, 41
7	1514	-OH bend (in plane)	44
8	1473	-OH bend	44
9	1456	C-H bend from -R	40, 41
10	1382	O-C-O stretch	44
11	1292, 1076	C-O stretch	40, 44
12	1110-1000	Si-O-Si stretch	42, 43
13	970-920	Si-O-R stretch	42, 43
14	910-830	Si-OH stretch	42, 43
15	853	Si-O-Si bend	42-43
16	811	-NO stretch from Ce $(NH_4)_2(NO_3)_4$	40, 41
17	746	-NO bend from $Ce(NH_4)_2(NO_3)_4$	40, 41

The tentative bands assignments are listed in Table 4.1. Characteristic for the silica spectrum (a) is the presence of the 3740 cm^{-1} band, which is attributed to the free hydroxyl groups present on the surface [42-43]. The other bands observed in the spectrum are due to the residual molecules of CO_2 and H_2O (1638 cm^{-1}) adsorbed on the

silica surface, and the bands around 1200-1000 cm^{-1} are attributed to Si-O stretch and bend from silica [44]. Due to the sensitivity of the DRIFTS analysis, several well defined bands for CeO_2 (Figure 4.1 b) were observed which are otherwise hard to see using simple FTIR analysis. As in the case of the silica support (a), the free and coupled hydroxyl groups from the surface, can be easily distinguished. The bands observed at 1556 cm^{-1}, 1473 cm^{-1}, 1299 cm^{-1}, and 1034 cm^{-1} were attributed in a recent study made by Verduraz *et al.* [44], to the carbonate and carboxylate species present on the CeO_2 surface. The band at 1556 cm^{-1} corresponds to a carboxylate species, 1473 cm^{-1} and 1299 cm^{-1} to a bidentate carbonate and 1034 cm^{-1} to a monodentate carbonate surface species. The $Ce(OH)_4$ spectrum shown in Figure 4.1 c includes a broad band characteristic of the OH stretch (3500-3000 cm^{-1}) involved in intra- or intermolecular hydrogen bonds, more intense bands characteristic of CO_2 and H_2O, bands characteristic of carboxyl or carbonyl surface species and bands characteristic of deformation of O-H bond (the broad band between 1500 - 1200 cm^{-1}) [44-47].

Figure 4.2 shows the DRIFTS spectra of the CeqN catalysts, respectively, dried at 120°C (b) and calcined at 500°C (c) for comparison with the spectrum of neat SiO_2 (a), respectively. The spectrum from Figure 4.2 b reveals the formation of $Ce(OH)_4$ species on SiO_2 after drying the catalyst at 120°C. The process may be favored by the weak acidity of the silica surface, which favors the formation of hydrated particles from Ce^{4+}-nitrate solution. Simple water solvation and drying of cerium nitrate compounds led to identical DRIFTS spectra as the starting compounds. Together with the formation of the $Ce(OH)_4$ on the support, the silica band at 3690 cm^{-1} corresponding to the free hydroxyl

groups disappears and a broad band around 3500-3000 cm⁻¹ is observed, corresponding to

hydrogen bonded hydroxyl groups. This fact suggests that the interaction between the

cerium precursor and silica support has only a physical nature, e.g. dipole-dipole

interactions and hydrogen bonds.

(c)

(b)

(a)

4000.0	3000.0	2000.0	1000.0

Wavenumber [cm⁻¹]
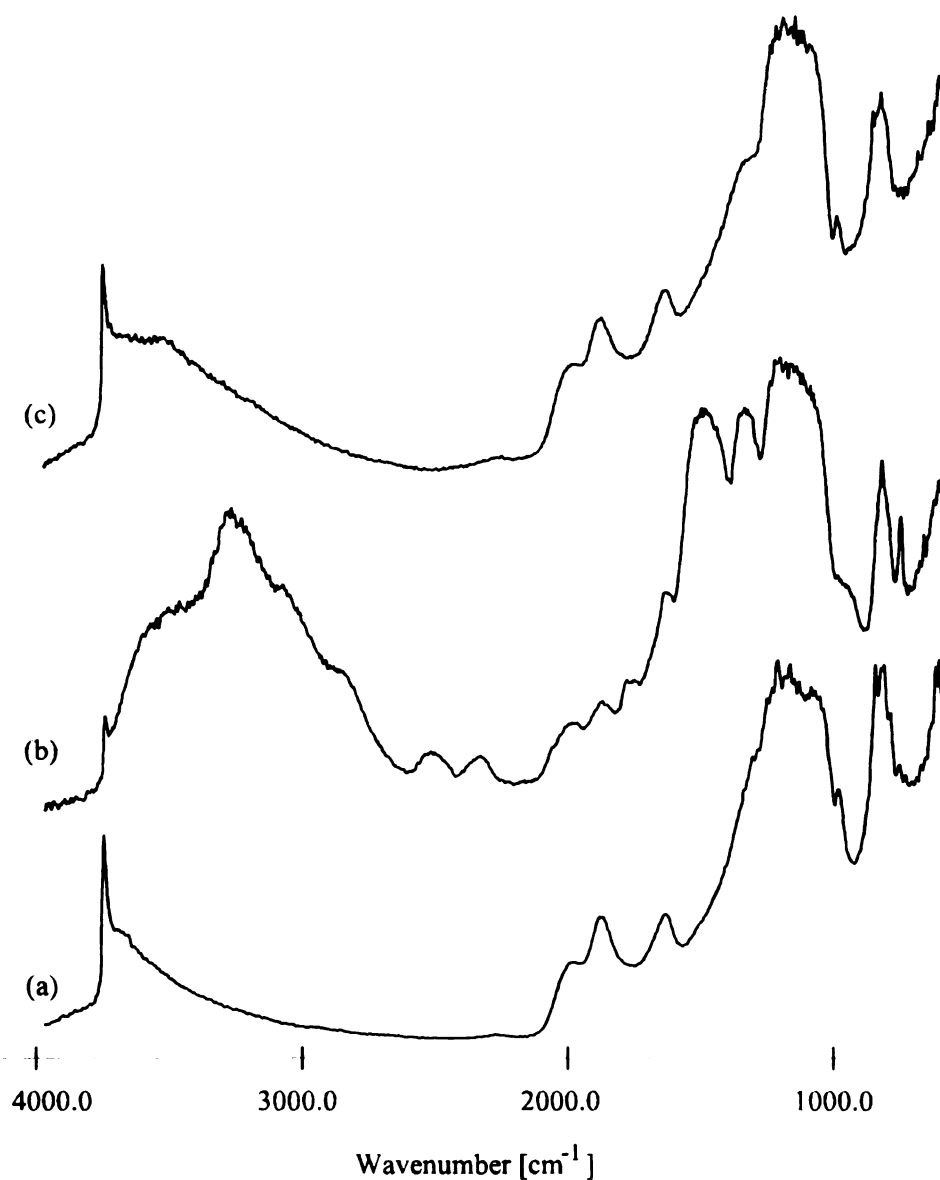
Figure 4.2 DRIFTS spectra of CeqN catalysts: a) SiO$_2$ support; b) CeqN catalyst dried at 125°C; c) CeqN calcined at 500°C.

After calcination at 500°C (Figures 4.2 c), the IR spectrum of the catalyst became similar to the spectrum of the pure silica support. The IR band at 3740 cm^{-1} corresponding to free surface hydroxyl groups is almost completely regenerated. Some remaining bands from bending -OH groups are still observable at 1520 cm^{-1} and 1100 cm^{-1}.

Figure 4.3 shows the DRIFTS spectra for the CeqA catalysts acquired during impregnation and thermal treatment. The grafting process involves a chemical interaction (covalent bond) between the precursor and support. The interaction of the cerium alkoxide with the support may take place either through a reaction with the hydroxyl groups involved in intramolecular hydrogen bonds or reaction with the free hydroxyl groups from the surface leading to the formation of Si-O-Ce-Alkoxide bonds [41, 48]. If the Ce-OH phase is formed in the solution, the precursor-support interaction could be an intermolecular interaction through hydrogen bonds. After grafting impregnation DRIFTS spectra shown in Figure 4.3 b-d indicate the disappearance of the band at 3740 cm^{-1} characteristic of the free hydroxyl groups from the SiO$_2$ surface. The presence of the IR bands at 2837 cm^{-1} characteristic of C-H stretching from cerium alkoxide are clearly observed for the grafted (Figure 4.3 b), dried (Figure 4.3 c) and calcined at 200°C (Figure 4.3 d), when all the solvent, water or other physisorbed compounds are removed from the silica surface. This observation supports the idea of a covalent bond interaction between the cerium alkoxide and silica surface. In addition, no Ce(OH)$_4$ phase formation was observed during grafting, as the DRIFTS spectrum of the dried catalyst indicates.

After calcination, the DRIFTS spectra of the catalyst indicate the regeneration of the band corresponding to the free hydroxyl group from the support surface (1740 cm^{-1}

band) and the band which can be assigned to a surface carboxylate species formed on

CeO_2 (1523 cm^{-1}) [44, 47].
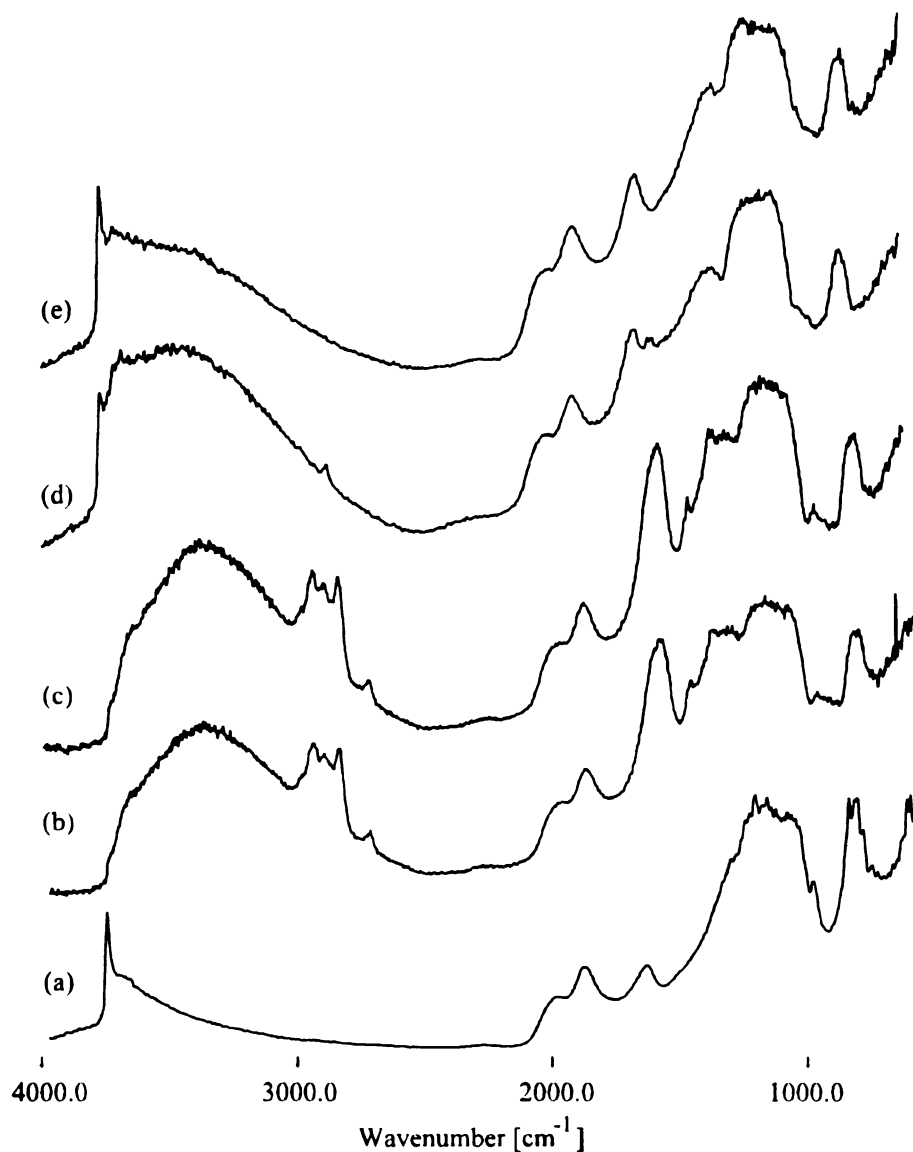
Figure 4.3 DRIFTS spectra of CeqA catalysts: a) SiO_2 support; b) CeqA catalyst dried at 25°C; c) CeqA dried at 125°C; d) CeqA calcined at 200°C; e) CeqA calcined at 300°C; f) CeqA calcined at 500°C.

Cerium-oxygen bands, which appear in the 500-250 cm^{-1} region, are hard to be observed due to the strong absorption bands of the SiO_2 support in this region [41].

^{29}Si solid state NMR spectra and the deconvolution of the peaks into the main components for the neat SiO$_2$, CeqN, and CeqA catalysts after impregnation with the different cerium precursors and dried at 125°C, are presented in Figure 4.4 a-c. Figure 4a', 4b' and 4c' show the deconvolution result spectra for the CeqA, CeqN, and SiO$_2$ catalysts. Various types of silica from the catalyst samples were identified based on chemical shift [in ppm] and assignments from previous work [31, 49-51]. The chemical shifts at which silicon atoms show resonance are in the range from -85 to -110 ppm. Sheme 4.1 presents the silicon configuration and the corresponding ^{29}Si NMR chemical shift observed, reported in the literature [31-33, 51].

Scheme 4.1 Silica structures and the corresponding ^{29}Si NMR shifts [31-33]

(A)

$\delta = -108.7$ ppm

(B)

$\delta = -100.3$ ppm
Trifunctional branching

(C)

$\delta = -95.6$ ppm
Middle branching

(D)

$\delta = -88.5$ ppm
End Branching

(E)

$\delta = -76.0$ ppm
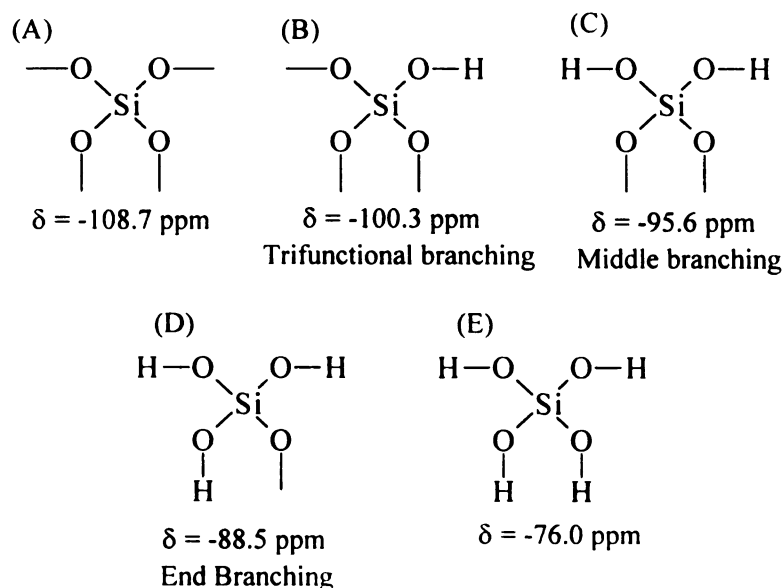
In each spectrum shown in Figure 4.4, silica shows characteristic peaks at -108.3 ppm (A), -100.7 ppm (B), -95.6 ppm (C), and -88.5 ppm (D) corresponding to silicon atoms with the configurations presented in Scheme 4.1.
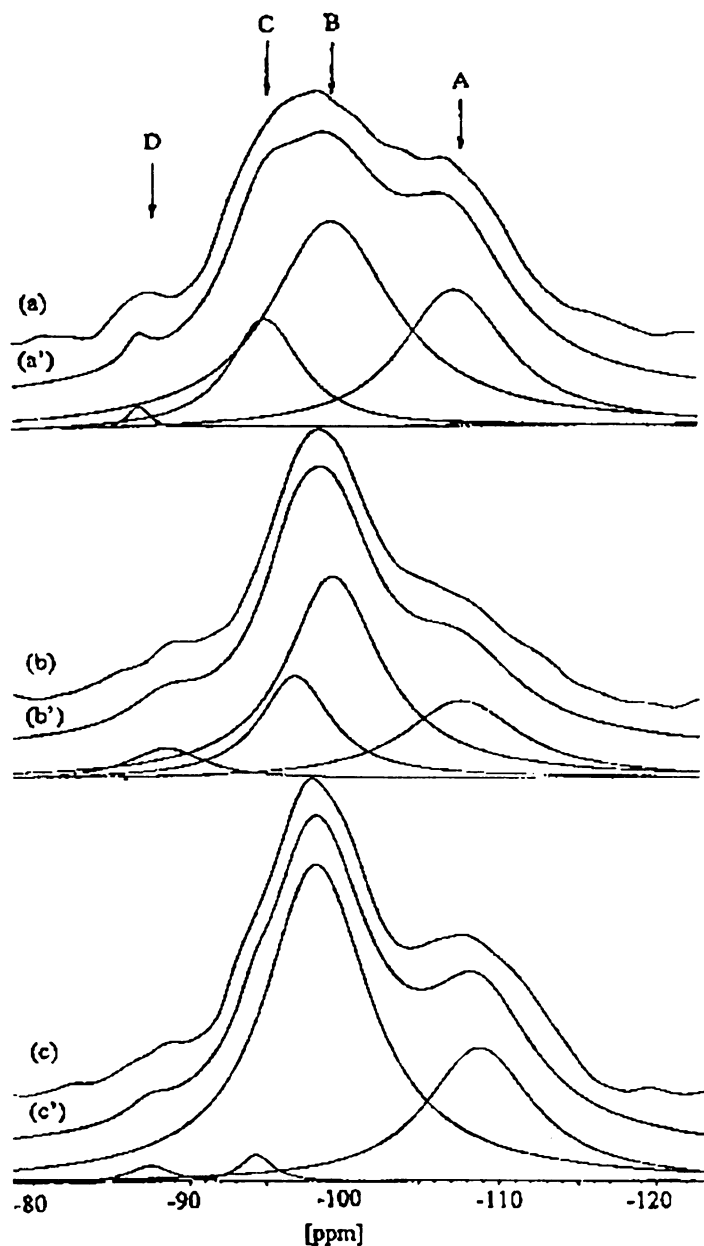
Figure 4.4 ^{29}Si NMR spectra of the catalysts dried at 125°C: a) CeqA; b) CeqN; c) SiO$_2$ in comparison with the deconvoluted spectra for each samples (a', b' and c')

Table 4.3 presented below, shows the ratio values of silica peaks from B, C, and

D, relative to peak A, calculated on the basis of deconvoluted peak area of each silica

peak.

Table 4.3 ^{29}Si NMR peak intensity ratios and XPS I_{La3d}/I_{Si2p} ratio for silica in B, C, and D configuration relative to A (see Scheme 4. 1)

Catalysts	I_{Ce3d}/I_{Si2p} XPS Intensity	^{29}Si NMR Peak Ratio		
		B/A	C/A	D/A
SiO$_2$	-	2.43	0.07	0.05
CeqN dried at 125°C	7.9	2.27	0.87	0.27
CeqA dried at 125°C	1.2	1.84	0.57	0.04

For the CeqN catalyst dried at 125°C, the B/A, C/A and D/A have very close

values with those obtained in the case of the neat SiO$_2$ support (ex. 2.27 compared with

2.43). Consequently, no chemical interaction occurred between the CeqN precursor and

the support during the impregnation and drying processes. In the case of the CeqA dried

catalyst, the B/A value (1.84) is very different from that obtained for SiO$_2$. There is less

change in the case of the C/A and no significant change in the D/A values. This

observation can be explained by considering that after impregnation with Ce-Alk solution

and drying, cerium alkoxide is grafted on silica and many of the surface hydroxyl groups

(trifunctional silica groups, Scheme 1B) are bonded to the precursor, as shown in the

reaction (4-3):

$$\text{Support-OH} + \text{Ce-(OR)}_4 \quad \xrightarrow[\text{reflux}]{80\text{-}85\ ^{\circ}\text{C}} \quad \text{Support - O - Ce-(OR)}_3 + \text{R-OH} \qquad (4\text{-}3)$$

where R = -O-CH$_2$-CH$_2$-O-CH$_3$.

After calcination in air at 500°C, the alkoxide part is removed from the CeqA dried catalyst, while in the case of CeqN dried catalyst only the water has been removed with formation of CeO$_2$. The S/N ratio of the NMR spectra and the resolution decreases as the proton abundance near silica atoms decreases. As a consequence, for catalysts calcined at 500°C and 800°C the quality of the spectra is not sufficient for a proper interpretation. The low S/N ratio observed for the spectrum of SiO$_2$ calcined at 800°C is due to the lower concentration hydroxyl groups (mostly free hydroxyl groups, so low proton concentration) from dehydration process which lead to a lower ^{29}Si signal enhancement by proton decoupling. The ^{29}Si spectra for CeqN and CeqA calcined at 500°C and 800°C (not shown) look similar with those obtained for SiO$_2$ support, indicating no clear chemical interaction between cerium oxide and silica. The appearance of peak E at -76.0 ppm for both types of catalysts indicates a reorganization in the silica structure probably with participation of the cerium oxide formed on the SiO$_2$ surface. The formation of Ce-Si can be excluded because the chemical shifts observed is these type of interaction are very large (> 100 ppm) [51]. For both type of catalysts, calcination at 500°C regenerates the surface free hydroxyl groups from SiO$_2$, phenomena observed by DRIFTS as well.

CeO$_2$ crystallinity and dispersion. Information about the crystallinity of CeO$_2$ deposited on SiO$_2$ support was obtained from TEM and XRD analyses.

a)
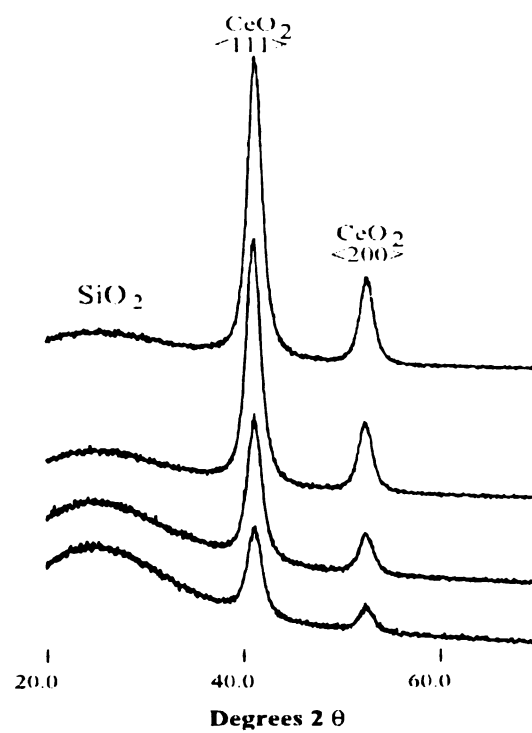
b)
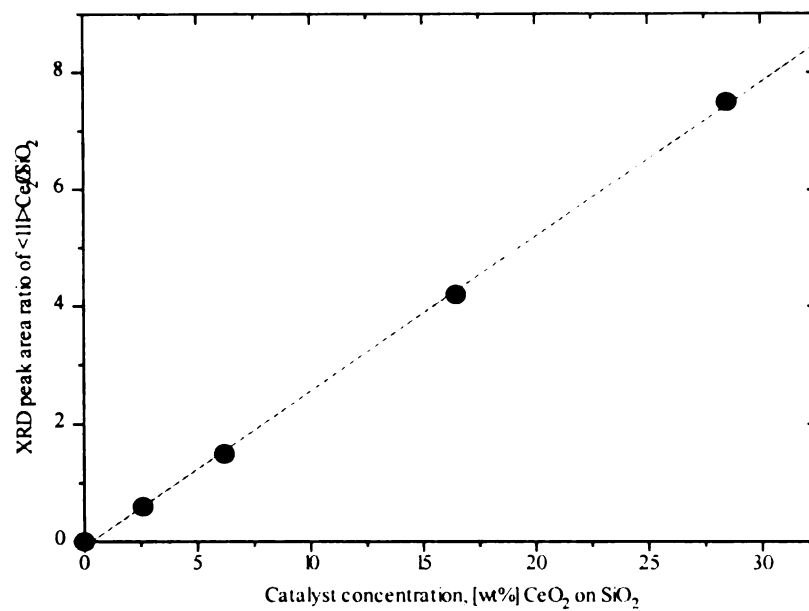
Figure 4.5   Semiquantitative XRD data: a) XRD pattern of CeO_2/SiO_2 physical mixture with different CeO_2 loading; b) corresponding calibration curve.

The TEM electron diffraction patterns for CeqN and CeqA catalysts were obtained at a M = 83,000 (M = magnification). In the case of CeqN catalyst, the electron diffraction micrograph shows the presence of crystalline material in the sample, containing diffraction patterns which can be attributed to crystalline CeO_2 formed on SiO_2 support after calcination. X-ray analysis performed on the same spot confirms the presence of Ce and Si as the main elements in the sample. The electron diffraction image obtained in the case of CeqA catalysts shows only diffuse rings with no clear diffraction patterns, presumably due to amorphous materials. The amorphous phase observed in this electron diffraction pattern corresponds to both SiO_2 and CeO_2 material. EDX analysis confirmed the presence of cerium from amorphous CeO_2 formed on the CeqA catalysts.

The results from semiquantitative analysis were presented in Table 4.1. These data were evaluated based on results from XRD analysis of CeO_2/SiO_2 physical mixture, with various cerium loading. The XRD patterns for the physical mixture samples are presented in Figure 4.5 a. The Ce<111> (2θ = 28.5°) have been chosen for our calculations. The intensity for the SiO_2 peak was estimated by deconvolution of the XRD pattern. The calibration curve obtained is presented in Figure 4.5 b (standard deviation for each point was evaluated at 5%). A good linearity was obtained for the cerium loading (CeO_2 crystalline %) versus Ce<111>/SiO_2 XRD intensity ratio. As a consequence, the evaluation of CeO_2 crystalline phase for the CeqN and CeqA catalysts can be considered accurate. Figure 4.6 presents the X-ray diffraction patterns of the SiO_2 support (Figure 4.6 a) in comparison with those obtained for the CeqN (Figure 4.6 b and 4.6 c) and CeqA catalysts (Figure 4.6 d and 4.6 e). Diffraction patterns specific to CeO_2

crystalline phase [52] can be identified in both Ce*q*A and Ce*q*N catalyst samples. Particle

size evaluation and semiquantitative XRD analysis for the Ce*q*N and Ce*q*A catalysts are

reported in Table 4.1 (columns 3 and 4, respectively).
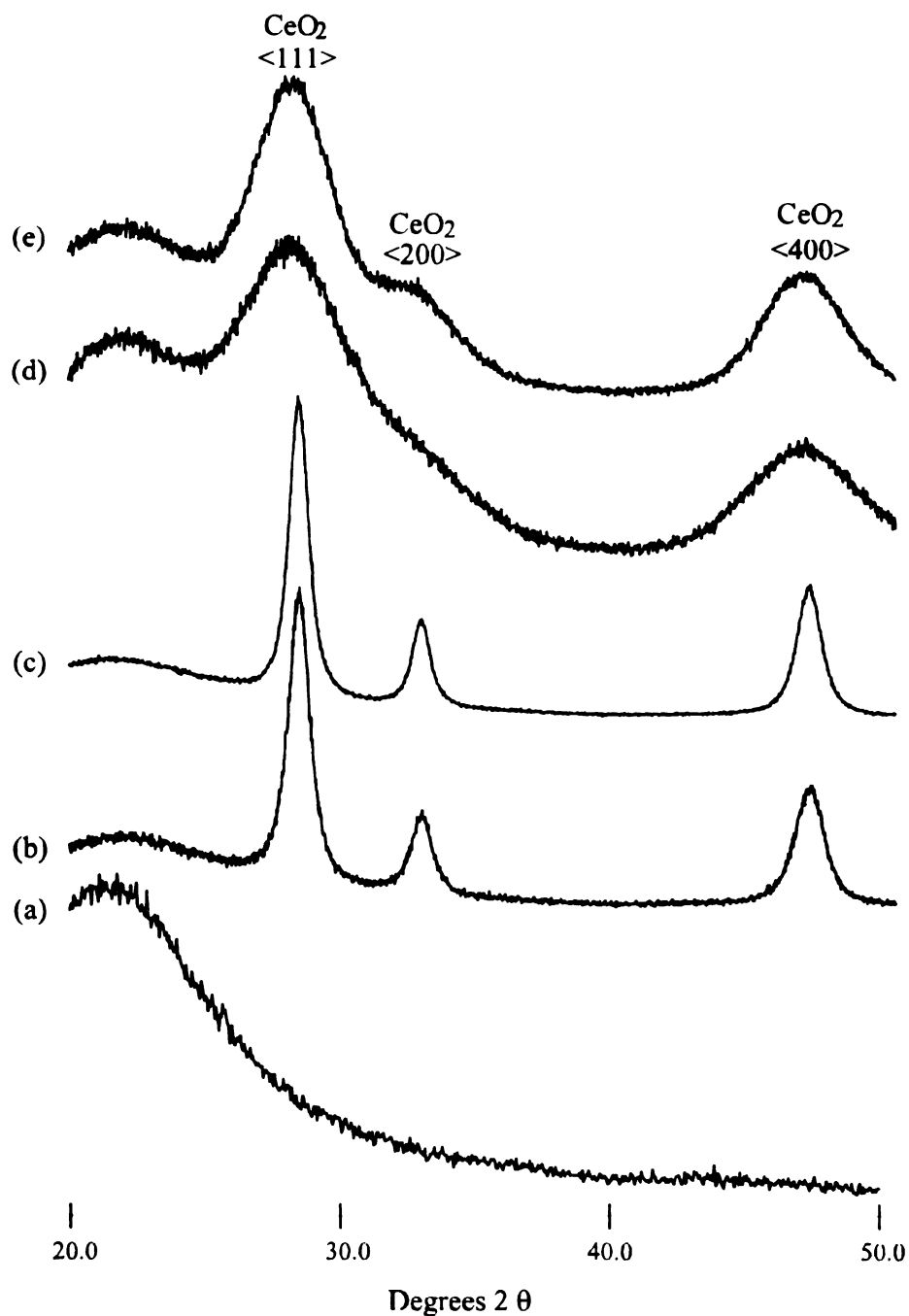
Figure 4.6 XRD patterns of: a) SiO_2; b) Ce*q*N calcined at 500°C; c) Ce*q*N calcined at 800°C; d) Ce*q*A calcined at 500°C; e) Ce*q*A calcined at 800°C.

The CeO_2 particle size for cerium supported catalysts, evaluated from line broadening calculations, were found to be larger for CeqN than for CeqA catalysts. This fact was attributed to the difference in the catalyst impregnation method. As observed from the impregnation study (DRIFTS and ^{29}Si NMR), the grafting method allows a stronger interaction between precursor and support, as compared to the incipient wetness method, where the interaction has a physical nature (hydrogen bonding or dipol interaction) [37-38]. A crystalline CeO_2 phase is formed during calcination at high temperatures (>400°C), so this process is slowed down in the case of CeqA catalyst by the strong interaction between the Ce-methoxyethoxide with SiO_2 support, affecting the grows of CeO_2 crystalline particles.

The data from semiquantitative XRD analysis indicate the percentage of cerium present as crystalline CeO_2 in the catalyst. Crystalline CeO_2 accounts for most of the cerium (>90%) in the CeqN catalysts, but for less than 30% in the case of CeqA catalysts; consequently the rest of the cerium is present either as an amorphous phase or as small crystallites (see Table 4.1). Relating these results to those obtained from TEM electron diffraction, it can be stated that the rest of the cerium from CeqA catalysts is present as amorphous cerium oxide. Furthermore, simple calcination of cerium nitrate is known to lead to crystalline CeO_2, in agreement with the results observed for CeqN catalysts [21, 53]. For CeqA, the amorphous CeO_2 formation can be attributed to cerium alkoxide polymerization during the grafting impregnation process, which favors formation of amorphous and/or small CeO_2 particles after calcination. Previous studies have shown that only heating at temperatures higher than 600°C, under H_2 atmosphere, can lead to

formation of amorphous CeO_x/SiO_2 catalysts by partial reduction of Ce^{4+} from small

CeO_2 crystallites to Ce^{3+} [37, ,58, 59]. TPR profiles obtained for CeqN and CeqA

catalysts are presented in Figure 4.7.
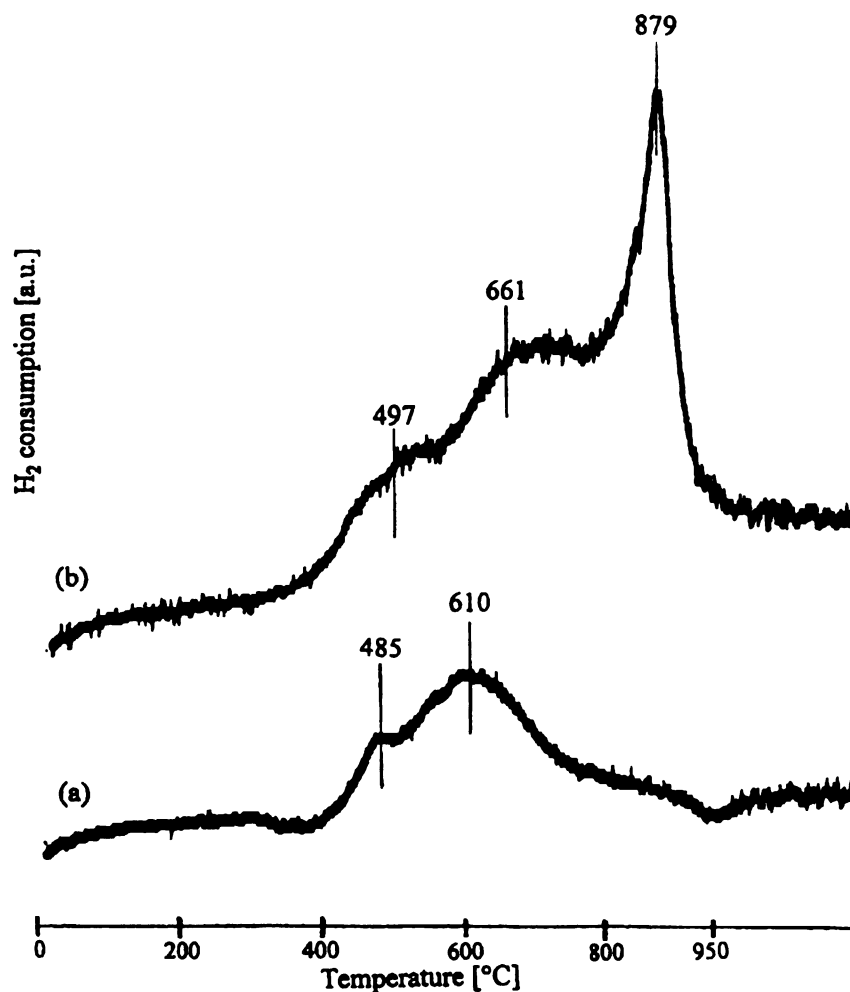
Figure 4.7 TPR profiles of: (a) CeqA and (b) CeqN catalysts calcined at 500°C

In the case of CeqA catalysts (Figure 4.7 a), the TPR profile indicates two major

peaks around 485°C and 610°C. It is known that for a low surface area neat CeO_2

sample, the TRP profile contains two major peaks, one at lower temperature (around

500°C), attributed to the reduction of surface oxygen from CeO_2 and one at higher temperature (around 800°C), attributed to the removal of bulk oxygen from CeO_2 structure [12]. The shape of the TPR profile is a function of temperature treatment (removing surface carbonates), CeO_2 surface area and particle size [39]. A decrease in the particle size of CeO_2 will result in a shift of the reduction peak maximum to lower temperatures. Based on the TPR profile observed in Figure 4.7 a which shows a maximum around 610°C, it can be concluded that CeqA catalysts contains small CeO_2 particles. In this case, the shifting of the reduction peak may be attributed to the presence of amorphous CeO_2, as well. The TPR of CeqN catalysts (Figure 4.7 b) shows a typical profile for CeO_2 similar with those reported in the literature [12, 39, 55]. The intense peak around 879°C from the TPR profile of CeqN catalysts indicates that most of the CeO_2 deposited on the SiO_2 support is in the form of large crystalline particles. The small changes in surface area observed after cerium impregnation, and the calcination to 500°C prior analysis (low surface carbonates content), led to negligible modifications in the TPR profiles of CeqN and CeqA catalysts.

XRD line broadening calculations showed formation of smaller CeO_2 particles on CeqA catalysts as compared with CeqN, indicating a better cerium dispersion on the SiO_2 support. The XPS I_{Ce3d}/I_{Si2p} intensity ratio can provide an additional rough estimation of the cerium dispersion, a large value being indicative of high dispersion [56]. For the dried (Table 4.3, column 2) and calcined (Table 4.1 column 5) CeqA catalysts, I_{Ce3d}/I_{Si2p} has a value around 7, lower in the case of the calcined to 800°C. The corresponding I_{Ce3d}/I_{Si2p} values for the CeqN catalysts are much lower (around 1). These XPS results are

in agreement with the dispersion data from XRD and TPR analyses, indicating a better

cerium dispersion in the case of CeqA catalysts in comparison with the CeqN catalysts.

XRD particle size, semiquantitative XRD and XPS analyses indicate that

calcination at 800°C led to lower cerium dispersion and higher CeO_2 crystallinity (see

Table 4.1). This fact suggests that the small crystallites formed on the silica surface are

mobile enough to get together and form large crystalline particles.

CeO_2 bulk and surface structure. EPR and XPS analysis were performed in order

to obtain additional information about the structure (cerium oxidation state) of cerium

deposited on the SiO_2 support after calcination at various temperatures. Figure 4.8 shows

the EPR spectrum of a CeO_2 standard material (Figure 4.8 a) in comparison with the EPR

spectra of CeqN (Figure 4.8 b and 4.8 c) and CeqA (Figure 4.8 d and 4.8 e) catalysts.

The EPR spectrum of CeO_2 (Figure 4.8 a) shows a peak at g = 1.952 ($g_\perp$), attributed in

the literature to Ce^{3+}-type defects present in a CeO_2 crystalline structure [57-61]. Non-

stoichiometric cerium oxide crystals formed during the calcination step, are most

probably responsible for the appearance of defects in the crystalline structure. Previously

obtained EPR spectra of CeO_2 showed two types of $g_{//}$ signals corresponding to two

different Ce^{3+} sites, form A ($g_{//}$ = 1.932), present only at low temperature, and form D ($g_{//}$

= 1.935), dominant after calcination at temperatures higher than 300°C [57-59].

Apparently, in the case of CeqN and CeqA catalysts calcined at 800°C, only cerium in

form A is present, due to the high temperature treatment (≥500°C) applied during the

preparation process.
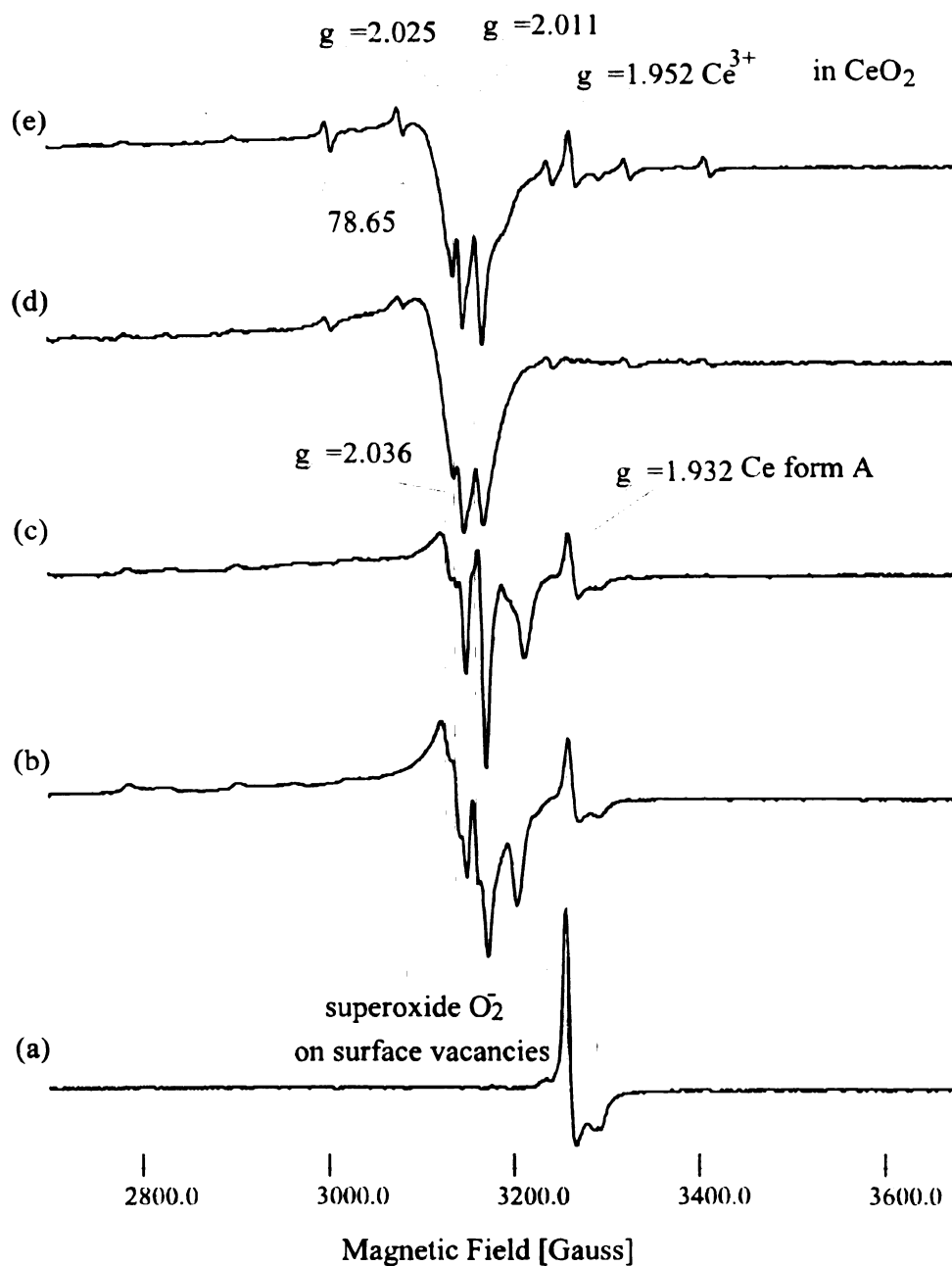
Figure 4.8 EPR spectra of: a) CeO_2; b) $CeqN$ calcined at 500°C; c) $CeqN$ calcined at 800°C; d) $CeqA$ calcined at 500°C; e) $CeqA$ calcined at 800°C.

The presence of EPR signals specific to bulk Ce^{3+} defects is associated with the signal

specific to O_2^- species (g = 2.011 and g = 2.036) from the CeO_2 crystals, however, the

intensity of both signals are reduced relative to the standard signals (Figure 4.8 a). The signals at $g_\perp = 2.011$ and $g_{//} = 2.036$ were attributed to O_2^- species bonded to surface Ce^{4+} ions from non-stoichiometric ceria [57-60]. At these g values, oxygen nuclei are located in the CeO_2 structure, equidistant from the surface. With higher temperature, other O_2^- species ($g_{//} = 2.025$) are formed in relation to the appearance of new vacancies or other defects into the cerium oxide structure [58]. The large percentage of crystalline CeO_2 phase formed in CeqN catalysts results in observation of more O_2^- species (Figure 4.8 b). A similar effect was observed for catalysts calcined at high temperature (Figure 4.8 c and 4.8 e). These types of oxygen species provide a catalyst with oxygen storage properties, capable to generate molecular oxygen involved into an oxidation processes. Another observation from Figure 4.8 concerns the hyperfine signals clearly observed for CeqA catalysts (Figure 4.8 d and 4e, $\Delta H = 78.65$ Gauss). These types of signals were attributed in the literature to a nuclear spin - electron spin interaction of a paramagnetic metal species, the signal magnitude being proportional with the metal loading and structure distortion in the metal structure. At this moment, no clear explanation can be offered to understand the appearance of these signals, further studies being necessary.

Figure 4.9 shows the XPS spectra for CeqN (Figure 4.9 a) and CeqA (Figure 4.9 b) catalysts, both calcined at 500°C, in comparison with the spectra for standard CeO_2 powder (Figure 4.9 c). The XPS Ce_{3d} spectrum is complicated due to hybridization of the Ce_{4f} with ligand orbitals and fractional occupancy of the valence 4f orbital [62-65].
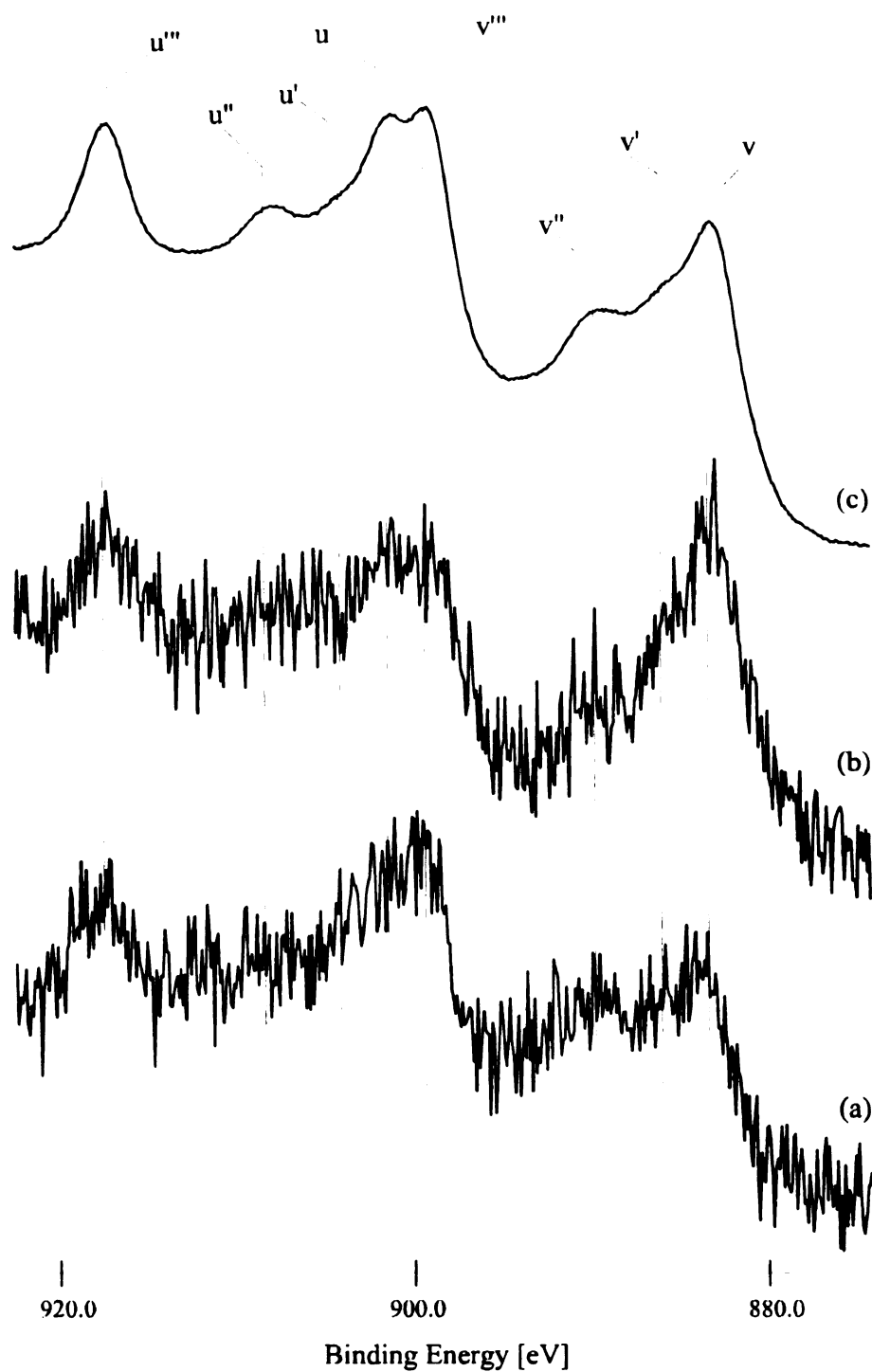
Figure 4.9 XPS spectra of: a) CeqN calcined at 500°C; b) CeqA calcined at 500°C; c) CeO$_2$.

The Ce$_{3d}$ spectrum measured for CeO$_2$ (Figure 4.9 c) contains three main 3d$_{5/2}$ features at

883.2 eV (v), 889.2 eV (v"), and 899.4 eV (v'"). The three main Ce3d$_{3/2}$ features appear

at 901.1 eV (u), 907.7 eV (u"), and 917.3 eV (u'"). The high binding energy doublet

v'''(u''') has been assigned to cerium with $4f^0$ orbital configuration. The v" and v (u" and

u) doublets are assigned to cerium with mixed $4f^1$ and $4f^2$ orbital configurations [62-64].

These states appear due to the core hole potential in the final state and the 4f

hybridization in the initial state [64-67]. The XPS Ce_{3d} spectra acquired for $CeqN$

(Figure 4.9 a) and $CeqA$ (Figure 4.9 b) catalysts are similar with that of CeO_2,

corresponding to cerium species with Ce^{4+} oxidation state. No surface Ce^{3+} was observed

by XPS analysis. The low S/N ratio of the XPS spectra for $CeqN$ and $CeqA$ catalysts are

due to the short scanning time needed to avoid cerium X-ray photoreduction, especially

of the amorphous CeO_x phase [36, 68-71].

A photoreduction study on the $CeqA$ catalysts by XPS was performed in order to

observed how easily Ce^{4+} is reduced to Ce^{3+} by X-ray during analysis (Figure 4.10). It is

known from the literature that cerium can be photoreduced during XPS analysis in high

vacuum due to intense heating of the sample surface, the presence of free electrons into

the chamber and variation in the crystallinity of the exposed particles [65-71]. For short

scanning time (Figure 4.10 a) the surface cerium phase is present as Ce^{4+}. As the

scanning time increases (Figure 4.10 b-d), the v'-peak intensity increases corresponding

to the appearance of surface Ce^{3+} species. Previous studies have shown that the

amorphous cerium phase is reduced more than the crystalline one. The results in Figure

4.9 indicate that cerium supported on SiO_2 ($CeqA$ which contained more amorphous

phase) is photoreduced readily.
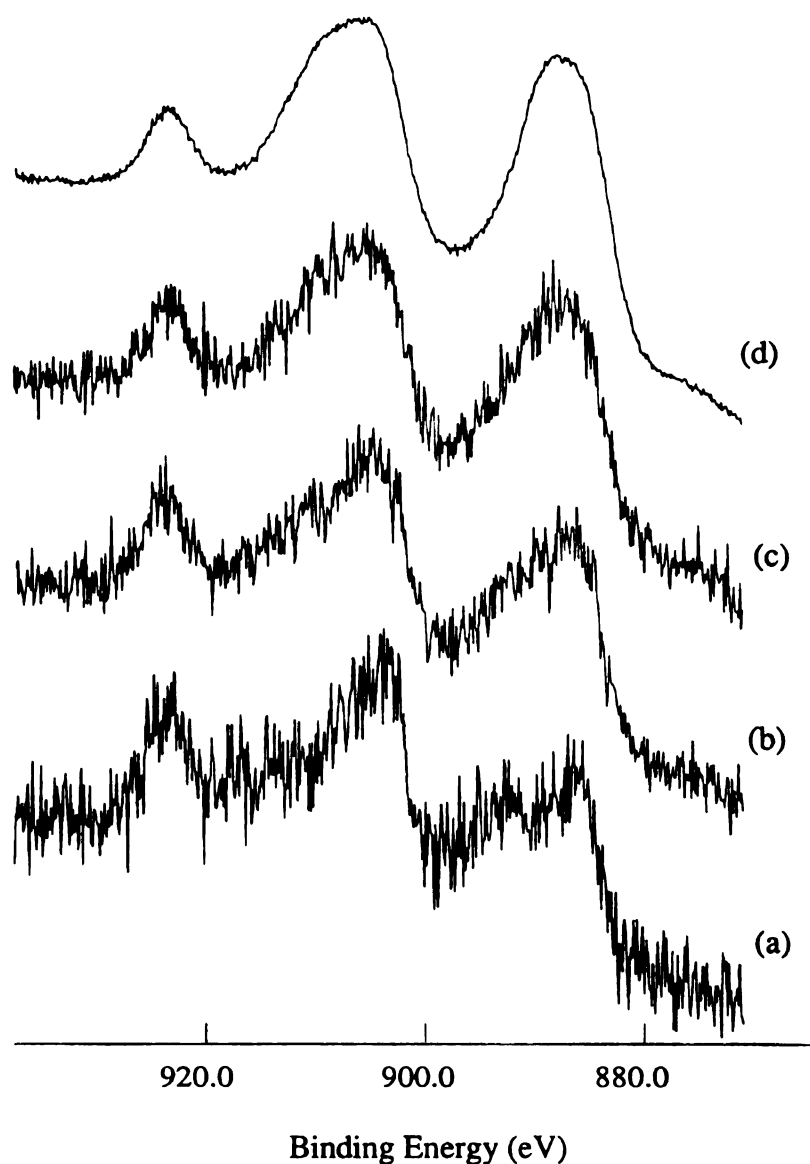
Figure 4.10 Cerium XPS photoreduction spectra for Ce*q*A catalyst calcined at 500°C after: a) 5 min.; b) 15 min.; c) 30 min.; d) 4 h of scanning.

The homogeneity of the catalysts was verified by comparing the XPS I_{Ce3d}/I_{Si2p} values from the ground and unground samples. XPS spectra acquired for Ce*q*N and Ce*q*A catalysts calcined at 800°C indicate that cerium is present as Ce^{4+} species (in CeO_2) and the X-ray photoreduction effect is very reduced due to the higher crystallinity of the cerium oxide phase.

4.4 Conclusions

Based on data obtained from DRIFTS analysis in correlation with those from ^{29}Si NMR, it can be concluded that Ce-nitrate precursor interacts with the support through intermolecular hydrogen bonds between surface hydroxyl groups from silica support and $Ce(OH)_4$ formed during the impregnation and drying of catalysts. Using the Ce-methoxyethoxide precursor, the silica support impregnation takes place through a strong grafting interaction between the surface hydroxyl groups from SiO_2 and Ce-Alk, with elimination of methoxyethanol (see reaction 4-3). After calcination of the catalysts at 500°C, structural modification of the silica support occurs with formation of more surface hydroxyl groups and lower surface area, as evidenced by BET measurements and ^{29}Si NMR. TEM-EDX analysis has provided information about the composition and crystallinity of the CeO_2/SiO_2 catalyst samples, calcined at 500°C. Electron diffraction patterns obtained by TEM have identified a crystalline CeO_2 phase in the CeqN catalysts and only amorphous phase in the CeqA catalysts. Cerium was positively identified by EDX analysis on the catalysts surface regardless of its crystalline structure. These observations are consistent with semiquantitative XRD analysis, which indicates that cerium is present in the CeqN catalysts mostly as crystalline CeO_2 (>90%), and in CeqA catalysts as mixed amorphous/crystalline CeO_2 (crystalline CeO_2 is less than 30%). Particle size evaluation from line broadening calculations indicate formation of larger CeO_2 crystallites on the SiO_2 support in the case of CeqN than for CeqA catalysts. Air calcination at 500°C of the grafted cerium from the silica support, led to an amorphous Ce^{4+} phase, while calcination at 800°C led to a higher degree of crystallinity and larger

CeO_2 particles. EPR spectra showed the presence of paramagnetic Ce^{3+} as defects in the CeO_2 crystalline structure of CeqN catalysts. No signals specific to Ce^{3+}-type species were found for CeqA catalysts. The large signal corresponding to O_2^- shows the presence of electrons capable to form O_2 molecules that further can be involved into a catalytic oxidation process. The small CeO_2 particle size shown by XRD, low temperature TPR profile, and relative high XPS I_{Ce3d}/I_{Si2p} intensity ratio indicate a better cerium dispersion on the SiO_2 support in the case of CeqA catalysts as compared with CeqN catalysts. Calcination at 800°C of CeqA catalysts led to formation Ce^{3+}-type defects in the CeO_2 crystalline structure. Finally, XPS analysis indicated only the presence of Ce^{4+}-species on the surface of CeqN and CeqA catalysts.

4.5 References

1. Barrault, J.; Guilleminot, A.; Achard, J. C.; Paul-Boncour, V.; Percheron, G. A.; *Appl. Catal.* **1986**, *21*, 307-312.
2. Fleisch, T. H.; Hicks, R. F.; Bell, A. T. *J. Catal.* **1984,** *87*, 398-413.
3. Reick, J. S.; Bell, A. T. *J. Catal.* **1985**, *96*, 88-105.
4. Miki, T.; Ogawa, T.; Haneda, M.; Kakuta, N.; Ueno, A.; Tateishi, S.; Matsuura, S.; Sato, M. *J. Chem. Phys.* **1990**, *94*, 6464-6467.
5. Diwel, A. F.; Rajaram, R. R.; Truex, T. J. *Catalysis and Automotive Pollution Control II*, Edit by Crucq, A. **1991**, Elsevier, Amsterdam, 139-152.
6. Pembo, J. M.; Lenzi, M.; Lenzi, J.; Lebugle, A. *Surf. Inter. Anal.* **1990**, *15(11)*, 663-668.
7. Yu-Yao, Y. F.; Kummer, J. T. *J. Catal.* **1987**, *106*, 307-312.
8. Chojnacki, T.; Krause, K.; Schmidt, L. D. *J. Catal.* **1991**, *128(1)*, 161-165.
9. Krause, K. R.; Schabes-Retchkiman, P.; Schmidt, L. D. *J. Catal.* **1992**, *134*, 204-219.
10. Schaper, H.; Doesburg, E. B. M.; VanReijen, L. L. *Appl. Catal.* **1983**, *7*, 211-220.
11. Oudet, F.; Courtine, P.; Vejux, A. J. *J. Catal.* **1988**, *114*, 112-118.
12. Yao, H. C.; Yu-Yao, Y. F. *J. Catal.* **1984**, *86*, 254-265.
13. Yang, J. K.; Swartz, W. E. *Spectrosc. Lett.* **1984**, *17(6&7)*, 331-337.
14. Gaugin, R.; Graulier, M.; Papee, D. *Adv. Chem. Ser.* **1975**, *143*, 147-149.
15. Yamaguchi, T.; Ikeda, N.; Hattony, H.; Tanabe, K. *J. Catal.* **1981**, *67*, 324-330.
16. Raen, S.; Braten, N. A.; Grepstad, J. K.; Qui, S. L. *Phys. Scr.* **1990**, *41(6)*, 1001-1002.
17. Nunan, J.; G.; Robota, H. J.; Cohn, M. J.; Bradley, S. A. in *Catalysis and Automotive Pollution Control II*, Edit by Crucq, A. Elsevier, Amsterdam, **1991**, 21-230.
18. Rodriguez, R. I.; Guerrero, R. A.; Fierro, J. L. G. *Appl. Surf. Sci.* **1989**, *40(3)*, 239-241.
19. Silver, R. G.; Summers, J. C.; Williamson, W. B. in *Catalysis and Automotive Pollution Control II*, Edit by Crucq, A. Elsevier, Amsterdam, **1991**, 167-180.
20. LeNormand, F.; Hilaire, L.; Kili, K.; Krill, G.; Maire, G. *J. Phys. Chem.* **1988**, *92*, 2561-2568.
21. Shyu, J. Z.; Otto, K.; Watkins, W. L. H.; Graham, G. W.; Belitz, R. K.; Gandhi, H. S. *J. Catal.* **1988**, *114*, 23-33.
22. Graham; G. W.; Jen, H.-W.; McCabe, R. W. *Catal. Lett.* **1997,** *44*, 185.
23. Haneda, M.; Mizushima, T.; Kakuta, N.; Ueno, A.; Sato, Y.; Matsuura, S.; Kasahara, K.; Sato, M. *Bull. Chem. Soc. Jpn.* **1993**, *66*, 1279-1288.
24. Mizukami, F.; Maeda, K.; Watanabe, M.; Masuda, K.; Sano, T.; Kuno, K. in *Catalysis and Automotive Pollution Control II,* Edit by Crucq, A. **1991**, Elsevier, Amsterdam, 557-568.
25. Leclercq, G.; Danthy, C.; Mabilon, G.; Leclercq, L. in *Catalysis and Automotive Pollution Control II*, Edit by Crucq, A. **1991**, Elsevier, Amsterdam, 181-194.
26. Weibel, M.; Garin, F.; Bernhardt, P.; Maire, G.; Prigent, M. in *Catalysis and Automotive Pollution Control II*, Edit by Crucq, A. **1991**, Elsevier, Amsterdam,

95-205.

27. Munuera, G.; Fernandez, A.; Gonzalez-Elipe, A. R. in *Catalysis and Automotive Pollution Control II*, Edit by Crucq, A. **1991**, Elsevier, Amsterdam, 207-219.

28. Zhou, Y.; Nakashima, M.; White, J. M. *J. Phys. Chem.* **1988**, *92*, 812-818.

29. Trovarelli, A. *Catal Rev.* **1996**, *38*, 439-520.

30. Maciel, G. E.; Sindorf, D. W. *J. Am. Chem. Soc.* **1980**, *102*, 7607-7608.

31. Rocha, J.; Klinowski, J. *Phys. Chem. Minerals*, **1990**, *17*, 179-186.

32. Harris, R. K.; Leach, M. J.; Thompson, D. P. *Chem. Mat.* **1989**, *1*, 336-338

33. Sato, S.; Maciel, G. E. *J. Molec. Catal: A*, **1995**, *101*, 153-161.

34. Chuang, I. S.; Kinney, D. R.; Bronnimann, C. E.; Zeigler, R. C.; Maciel, G. E. *J. Phys. Chem.* **1992**, *96*, 4027-4034.

35. Klug, H.P.; Alexander, L.E. *X-ray Diffraction Procedures for Polycrystalline and Amorphous Materials,* 1-st Ed. Wiley, New York, **1954**.

36. Che, M.; Giamello, E. in *Studies in Surface Science and Catalysis* by Delmon, B. and Yates, J. T. Vol. 57, Elsevier, **1990**, p. B265-B283.

37. Kepinski, L.; Wolcyrz, M. *Catal. Lett.* **1992**, *15*, 329-337.

38. Bensalem, A.; Bozon-Verduraz, F.; Delamar, M.; Bugli, G. *Appl. Catal.* **1995**, *121*, 81-93.

39. Bruce, L. A.; Hoang, M.; Hughes, A. E.; Turney, W. *Appl. Catal.* **1996**, *134*, 151-362.

40. Craciun, R. Master Thesis Dissertation, Michigan State University, East Lansing, MI, USA, **1996.**

41. Nakamoto, K. in *Infrared and Raman Spectra of Inorganic and Coordination Compounds*, 4-th Ed. Wiley, New York, **1986**, p231, p384.

42. Wovchko, E. A.; Camp, J. C.; Glass, J. A.; Jr.; Yates, J. T. Jr. *Langmuir*, **1995**, *11*, 2592-2599.

43. Matsumura, Y.; Moffat, J. B. *J. Chem. Soc. Faraday Trans.* **1994**, *90(8)*, 1177-1182.

44. Verduraz, F. B.; Bensalem, A. *J. Chem. Soc. Faraday Trans.* **1994**, *90(4)*, 653-657.

45. Waltenburg, H. H.; Yates, Jr. J. T. *Chem, Rev.* **1995**, *95*, 1589-1673.

46. Morrow, B. A.; McFarlan, A. J. *J. Phys. Chem.* **1992**, *96*, 1395-1400.

47. Binet, C.; Badri, A.; Kizling, M. B.; Lavalley, J. C. *J. Chem. Soc. Faraday Trans.* **1994**, *90*, 1023-1028.

48. Nedez, C.; Choplin, A.; Basset, J. M. *Inorg. Chem.* **1994**, *33*, 1094-1098.

49. Reven, L. *J. Molec. Catal.*, **1994**, *86*, 447-477.

50. Sanz, J.; Madani, A.; Serratosa, J. M.; Moya, J. S.; Aza, S. *J. Am. Ceram. Soc.* **1988**, *71(10)*, C-418-C421.

51. Diehl, P.; Fluck, E.; Kostfeld, R. in *NMR Oxygen-17 and Silicon-29,* Springer-Verlag Inc. **1981**, p 65-150.

52. McClune, W. F. *Powder diffraction file, Inorganic phases, International center for diffraction data*, Swarthmore, **1983,** 730, 731.

53. Kifenski, J.; Baiker, A.; Glinski, M.; Dollenmeier, P.; Wokaun, A. *J. Catal.* **1986**, *101*, 1-11.

54. Nabavi, M.; Spalla, O.; Cabane, B. *J. Colloid Interface Sci.* **1993**, *160*, 459-471.

55.   Laachir, A.; Perrichon, V.; Badri, A.; Lamotte, J.; Catherine, E.; Lavalley, J. C.; ElFallah, J.; Hilaire, L.; le Normand, F.; Quemere, E.; Sauvion, G. N.; Touret, O. *J. Chem. Soc. Faraday Trans.* **1991**, *87(10)*, 1601-1609.

56.   Niemantsverdriet, J. W. *Spectroscopy in Catalysis*, **1993**, VCH Weinheim, p 51-55.

57.   Che, M.; Kibblewhite, J. F. J.; Tench, A. J. *J. Chem. Soc. Faraday Trans.* **1973**, *69*, 857-863.

58.   Zhang, X.; Klabunde, K. J. *Inorg. Chem.* **1992**, *31*, 1706-1709.

59.   Abi-Aad, E.; Bechara, R.; Grimblot, J.; Aboukais, A.; *Chem. Mater.* **1993**, *5*, 793-797.

60.   Abi-Aad, E.; Bennani, A.; Bonnelle, J. P.; Aboukais, A. *J. Chem. Soc. Faraday Trans.* **1995**, *91*, 99-104.

61.   Kaufherr, N.; Mendelovici, L.; Steinberg, M.; *J. Less Common Metals*, **1985**, *107*, 281-289.

62.   Wuilloud, E.; Delley, B.; Schneider, W. D.; Baer, Y. *Phys. Rev. Lett.* **1984**, 53(2), 202-205.

63.   Fujimori, A. *Phys. Rev. B.* **1984**, *28*, 2281-2283.

64.   Wuilloud, E.; Delley, B.; Schnieder, W. D.; Baer, Y. *Phys. Rev. Lett.* **1984**, *53(26)*, 2519.

65.   Jo, J.; Kotani, A. *Phys. Scrp.* **1987**, *35*, 570-575.

66.   Praline, G.; Koel, B. E.; Hance, R. L.; Lee, H. I.; White, J. M. *J. Electron Spec. Relat. Phenom.* **1980**, *21*, 17-46.

67.   El Fallah, J.; Hilaire, L.; Romeo, M.; LeNormand, F.; *J. Electron Spectrosc. Rel. Phenom.* **1995**, *73*, 89-94.

68.   Daucher, A.; Hilaire, L.; LeNormand, F.; Muller, W.; Maire, G.; Vasquez, A.; *Surf. Interface Anal.* **1990**, *16*, 341-345.

69.   Paparazzo, E. *Surf. Sci.* **1990**, *234*, L253.

70.   Paparazzo, E.; Ingo, G. M.; Zacchetti, N. J. *J. Vac. Sci. Technol. A*, **1991**, *9*, 1416.

71.   Park, W. P.; Ledford, L. S. *Langmuir*, **1996**, *12*, 1794-1799.

CHAPTER 5

CHARACTERIZATION OF UNPROMOTED AND CeO_2 PROMOTED

MnO_x/SiO_2 CATALYSTS

5.1 Introduction

Supported MnO_x and rare earth oxide catalysts have been successfully utilized in

oxidative dehydrogenation reactions [1-4]. Previous studies on structural characterization

and activity measurements of MnO_x have emphasized catalysts in which $\gamma-Al_2O_3$ was

used as support [5-9]. The activity of transition metal oxide catalysts can be modified by

addition of lanthanide oxides which can act as textural and/or structural promoters [10-

15]. Previous studies have shown that rare earth oxide promoted $MnO_x/\gamma-Al_2O_3$ catalysts

behave as materials with high oxygen storage capabilities, showing excellent catalytic

activity in oxidation reactions [8, 13-19]. Cerium oxide (CeO_2) is known to be effective

as a promoter by increasing thermal resistance (inhibits the loss of the support surface

area), dispersion, and the stability of the transition metals used as active catalyst

components [11-15]. The structure of unpromoted and CeO_2-promoted MnO_x/SiO_2

catalysts is strongly dependent on preparation method, the chemical nature of precursors

used, and Mn/Si and Ce/Si ratio and loading [7-17, 20].

The purpose of this research was to examine the influence of Mn-loading,

calcination temperature, and the presence of CeO_2 promoter on the SiO_2 supported MnO_x

catalysts. Catalytic activity and selectivity at different temperature, will be summarized and presented in correlation with the catalysts' structures.

a) Methyl lactate catalytic oxidative dehydrogenation reaction

Methyl-Lactate   Methyl-Pyruvate
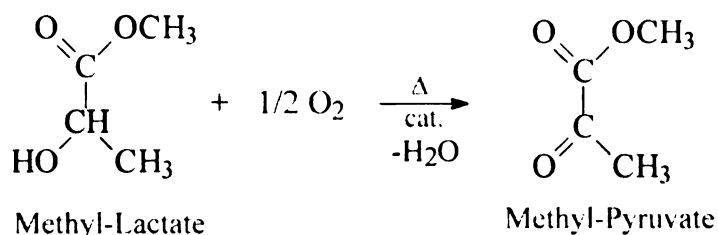
b) 2,3-Pentanedione condensation reaction with ethylenediamine

2,3-Pentanedione   Ethylene-diamine   2-Ethyl-3-Methyl
Dihydro-Pyrazine
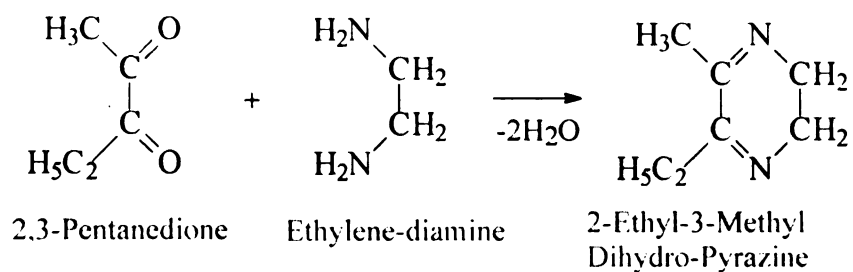
c) Dihydro-pyrazine oxidative dehydrogenation to pyrazine

2-Ethyl-3-Methyl
Dihydro-Pyrazine   2-Ethyl-3-Methyl
Pyrazine
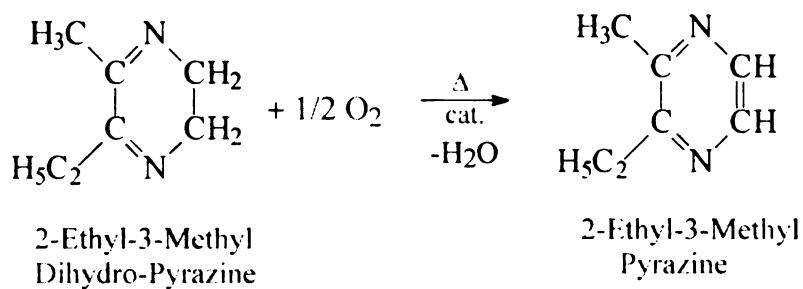
Figure 5.1 Oxidative dehydrogenation processes considered as probe reactions for unpromoted and CeO_2-promoted MnO_x/SiO_2 catalysts

X-ray diffraction (XRD), temperature programmed reduction (TPR), electron paramagnetic spectroscopy (EPR) and X-ray photoelectron spectroscopy (XPS) analyses were used to obtain information about the bulk and surface structure, and to characterize

the fresh and used, unpromoted and CeO_2-promoted MnO_x/SiO_2 catalysts. Reactions used for catalyst testing are presented in Figure 5.1. Catalytic activity data for the catalysts used in oxidative dehydrogenation of methyl lactate (ML) to methyl pyruvate (MP, Figure 5.1 a), and 2-ethyl-3-methyl-dihydropyrazine (23HPy, obtained from 23P and ethylenediamine, Figure 5.1 b) to 2-ethyl-3-methyl-pyrazine (23Py, Figure 5.1 c) are reported in correlation with their bulk and surface structure. Previously, MnO_2 was successfully used in dihydropyrazine dehydrogenation reactions (with high yield and selectivity) but in a discontinuous (batch) process [21]. Oxidative dehydrogenations of lactic acid to pyruvic acid [22] or of ethyl lactate to ethyl pyruvate [23-25] were performed with high yields and selectivity in the presence of Fe/P based catalysts. Providing the activity of MnO_x-based catalysts in oxidation reaction, ML to MP has been used as a probe reaction in this study, as well.

Experimental

Catalysts preparation. The pure SiO_2 support was prepared from silica-gel (Davison Chemical Co.) which was finely grounded (< 230 mesh) and calcined in air at 500°C for 24h, prior to impregnation (300 m^2/g). Pure SiO_2 and CeO_2-promoted SiO_2 (CeqA and CeqN, see Chapter 4) were used as supports for Mn-based catalysts. Aqueous $Mn(NO_3)_2 \times 6H_2O$ (Aldrich) was used to prepare MnO_x/SiO_2 (with Mn/Si atomic ratio $y =$ 0.5-14×10^{-2}) and $MnO_x/CeO_2/SiO_2$ ($y = 10\times10^{-2}$) catalysts. Catalysts with various Mn/Si atomic ratios (y) were designated as MnynT, followed by the calcination temperature (T) used during preparation.

Table 5.1 The list of the unpromoted and CeO_2-promoted MnO_x/SiO_2 catalysts together with the designated symbols used in this study.

Ord. #	Catalyst Symbols	Description of the catalysts: Mn/Si and Ce/Si atomic ratio, calcination temperature, presence of CeO_2 promoter
1	SiO_2	Pure SiO_2 support from silicagel, calcined at 500°C
2	Mn005n500	MnO_x/SiO_2 catalyst, with Mn/Si = 0.005, calcined at 500°C
3	Mn02n500	MnO_x/SiO_2 catalyst, with Mn/Si = 0.02, calcined at 500°C
4	Mn06n500	MnO_x/SiO_2 catalyst, with Mn/Si = 0.06, calcined at 500°C
5	Mn10n300	MnO_x/SiO_2 catalyst, with Mn/Si = 0.10, calcined at 300°C
6	Mn10n400	MnO_x/SiO_2 catalyst, with Mn/Si = 0.10, calcined at 400°C
7	Mn10n500	MnO_x/SiO_2 catalyst, with Mn/Si = 0.10, calcined at 500°C
8	Mn10n575	MnO_x/SiO_2 catalyst, with Mn/Si = 0.10, calcined at 575°C
9	Mn10n650	MnO_x/SiO_2 catalyst, with Mn/Si = 0.10, calcined at 650°C
10	Mn10n750	MnO_x/SiO_2 catalyst, with Mn/Si = 0.10, calcined at 750°C
11	Mn10n500	MnO_x/SiO_2 catalyst, with Mn/Si = 0.10, calcined at 500°C
12	CeqA	CeO_2-promoted SiO_2 support with Ce/Si = 0.08, calcined at 500°C, using a Ce-alkoxide promoter
13	Mn10sicea	Mixed Mn-Ce/SiO_2 catalyst with Mn/Si = 0.10, on CeqA support, calcined at 500°C
14	CeqN	CeO_2-promoted SiO_2 support with Ce/Si = 0.08, calcined at 500°C, using a Ce-nitrate promoter
15	Mn10sicen	Mixed Mn-Ce/SiO_2 catalyst with Mn/Si = 0.10, on CeqN support, calcined at 500°C

The Mn-based catalysts prepared in this study were obtained by incipient wetness impregnation with aqueous precursor solutions. The CeO_2-promoted MnO_x/SiO_2 catalysts were prepared by sequential impregnation (first cerium followed by manganese). All samples were dried at 125°C and calcined for 16 h in air at 500°C after each

impregnation step, prior their use in the oxidative dehydrogenation processes of ML to MP and of 23HPy to 23Py.

X-Ray Diffraction (XRD). X-ray powder diffraction patterns were obtained with a Rigaku XRD diffractometer employing Cu Kα radiation (λ = 1.541838 Å) and operated at 45 kV and 100 mA. Diffraction patterns were obtained using a scan rate of 0.5 deg/min with 1/2 mm slits. Powdered samples were mounted on glass slides by pressing the powder into an indentation on one side of the slide. The mean crystallite size ($\bar{d}$) of MnOx particles was determined from XRD line broadening measurements using the Scherrer equation (1-11, Chapter 1). Semi-quantitative X-ray diffraction data for evaluation of the MnO_2/Mn_2O_3 ratio were obtained by comparing MnO_2 <110> and Mn_2O_3 <222> peak ratios calculated for each catalyst sample (see details in Chapter 1)

Temperature-programmed reduction (TPR). A common technique used today to characterize the redox properties of an active phase from a catalysts is temperature programmed reduction. The technique uses a nitrogen-hydrogen reducing mixture which flows at various temperatures over the catalyst sample, connected to a thermal conductivity detector (TCD) recording the amount of H_2 evolving from the sample and compared with the initial feed. Due to reducing processes, hydrogen is consumed by the sample. The total uptake during a TPR analysis and the position of the reduction maxima as a function of temperature represent a real fingerprint of the catalyst sample [26]. The reduction of the supported metal oxides may be slowed down or promoted by their dispersion on inert porous materials such as Al_2O_3, SiO_2 or TiO_2 and is a function of the metal oxide-support interaction. The surface of the metal oxide is reduced much easier

than the bulk phase. Characteristics such as catalyst sensitivity to reduction, autocatalytic effect, structure, porosity, and dispersion influence significantly the position of the maxima from a TPR profile. Any factors which limit or favor the H_2 adsorption on the catalyst sample surface should be accounted in order to correctly interpret the TPR profile. The presence of any impurities or small molecules adsorbed on the surface capable to consume H_2 such as CO, C, various carbonate-like species, hydrocarbon residue, nitrate-like species etc., will influence the results and interfere with the real reduction activity of the sample [28].

Figure 5.2 show a laboratory setup for a classical TPR experiment. At the beginning of the TPR experiment, the gas flows over a catalyst (accurately weighted) at a temperature low enough to prevent reduction. The temperature on the catalyst is then increased with a linear rate and the rate of the reaction is monitored by measuring concentration or pressure changes in the gas phase or weight of the catalyst. The reducing gas used in the TPR experiments is usually a mixture of N_2/H_2. The experimental setup can be used for temperature programmed oxidation (TPO) as well, by replacing the reducing gas with air [27].

Generally, TPR is considered to be a very sensitive technique which is independent of any specific catalyst properties. The method has been applied to the study of many supported catalyst systems. It was therefor considered to be a proper and useful technique for the study of the $MnO_x/CeO_2/SiO_2$ system.
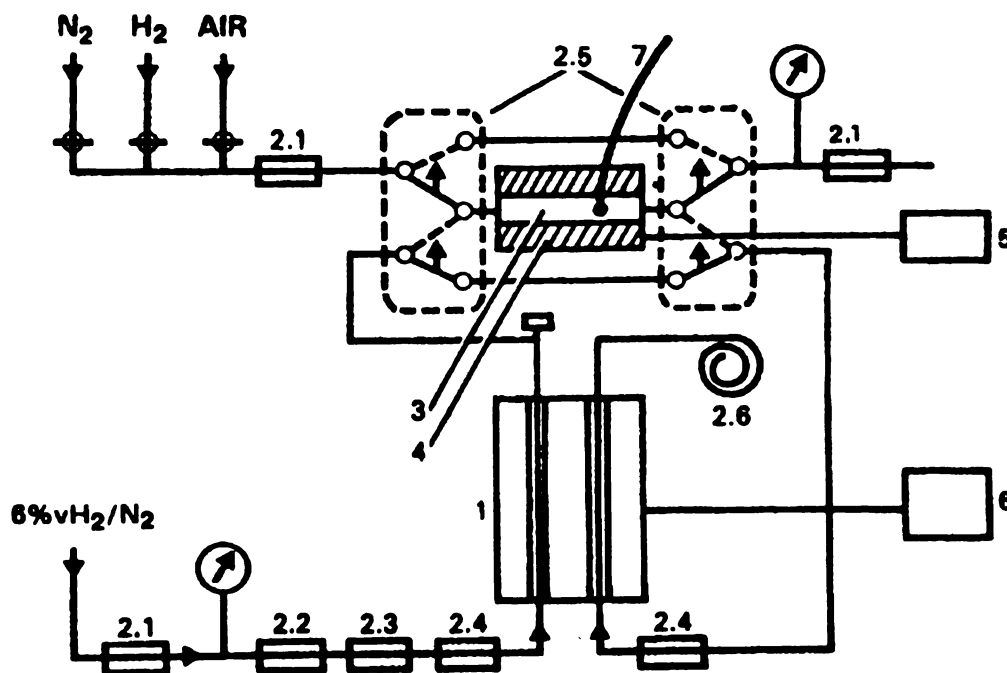
Figure 5.2 Laboratory setup for a TPR experiment: 1 - thermal conductivity cell; 2.1 - reduction valve; 2.2 - M/Al₂O₃ catalyst; 2.3 - molecular sieves; 2.4 - Dewar trap (193 K); 2.5 - gas flow switch; 2.6 - brake capillary; 3 - reactor; 4 - furnace; 5 - temperature programmer; 6 - chart recorder; 7 - thermocouple [27].

TPR profiles for the CeqN and CeqA catalysts were obtained using a classical U-shaped quartz reactor connected to a thermal conductivity detector (TCD) for H$_2$ consumption analysis. The temperatures were measured with a Ni-Cr-Ni thermoelement placed directly in the catalyst bed. A reducing agent mixture of 10% H$_2$ in N$_2$ was passed over 0.1 g catalyst powder, at 30 mL/min flow rate. The temperature interval considered for analysis is from 25°C to 950°C (10°C/min heating rate). The TPR profiles are reported as H$_2$ consumption (arbitrary units) versus temperature [°C].

Electron Paramagnetic Resonance (EPR). EPR is a spectroscopic technique well suited to study paramagnetic solid materials as well as paramagnetic species adsorbed on

solid surfaces. Surface defects, paramagnetic metal oxides supported on high surface area materials, adsorbed atoms, molecules or ions which, in many cases, may be intermediates of a catalytic reaction, are several classes of species observable by EPR spectroscopy, and may provide useful insights about a heterogeneous catalysis process. The sensitivity of the technique allows the study of very low concentrations of active species. A limitation as well as an advantage of EPR is that the technique does not detect diamagnetic species. The oxidation state of a transition metal, crystalline defects, and coordination with neighboring atoms are just some of the data which can be obtained from EPR spectra of solid catalyst materials.

The principle of EPR spectroscopy is based on the Zeeman effect observed for paramagnetic species (the presence of a unpaired electron with 1/2 spin). Placed into a magnetic field, the energy level of the free electron splits in two levels, as shown in Figure 5.3. At thermal equilibrium, the spin population of the level is given by the Maxwell-Boltzmann law (5-1):

$$n_1/n_2 = \exp(-\Delta E/kT) \qquad (5\text{-}1)$$

where n_1 and n_2 are the spin populations characterized by the M_s values of $=1/2$ and $-1/2$, respectively. At 77K, in a field of about 300 Gauss, n_1 and n_2 differ by less than 0.005 [29]. The transition between the two Zeeman levels can be induced by suitable electromagnetic radiation which is able to provide the required energy gap to fulfill the resonance condition (5-2):

$$h\upsilon = g_e\mu_B B \qquad (5\text{-}2)$$

where h = Plank constant, g_e = giromagnetic factor of an electron; μ_B = 9.27×10^{-21} erg/gauss = Bohr magneton, B = magnetic flux (in tesla), and υ = flux frequency.
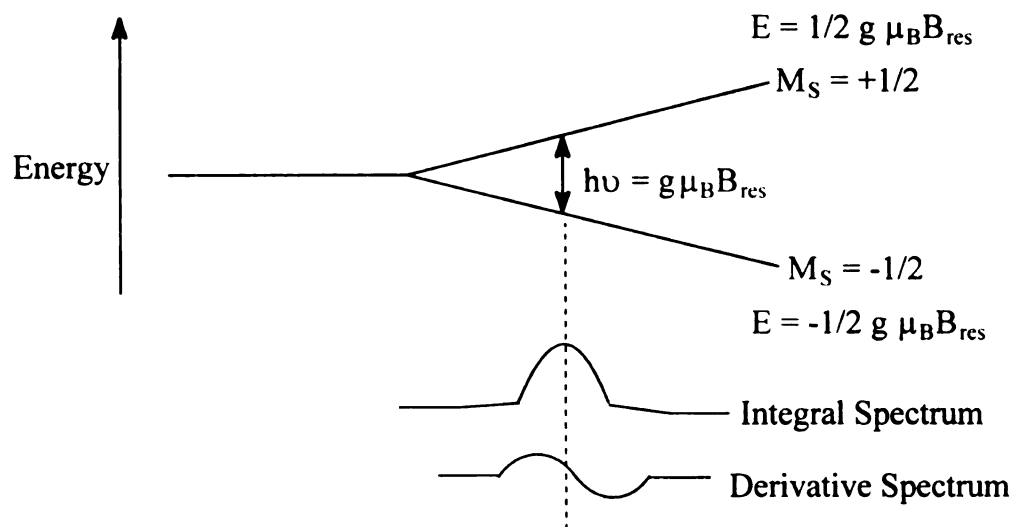
Figure 5.3 The Zeeman energy levels of a free electron placed into an external magnetic field [29].

At about 2.8 MHz/Gauss value for the magnetic field applied on a paramagnetic system, resonant transitions can take place. The typical radiation, employed in EPR spectroscopy is in the microwave region. The energy absorption necessary to promote electrons from a lower to a upper energy level is called a resonance signal, and at this moment n_1 and n_2 equalizes if the absorption reaches saturation. When the electron from the upper level emits the $h\upsilon$ energy, it can return to the lower level and satisfy the Maxwell-Bolzmann law. The energy can be dissipated to the lattice (T_1, spin-lattice relaxation) or it can be exchange with other neighbor spins (T_2, spin-spin relaxation). EPR experiments are typically performed under liquid N_2 (77K) or He (4.2K) due to the temperature dependence of relaxation time (T_1). If T_1 is too long, electrons do not have

time to return to the initial energy level, so the intensity of the signal decreases and is no longer proportional to the spin number present in the sample (saturation effect). The typical shape of an EPR signal is Gaussian or Lorentzian, and it can be represented either as an integral or as an derivative signal (see Figure 5.3) [29]. The g value from a real sample is usually slightly different from the g_e, but to extract chemical information this value should be very accurately determined. The absolute value of g can be evaluated either by independent B and υ measurements or computer simulation. Equation 5-3 shows the relationship between g, B and υ.

$$g = h\upsilon/\mu_B B \qquad (5-3)$$

where h = Plank constant, $\mu_B = 9.27 \times 10^{-21}$ erg/gauss = Bohr magneton, B = magnetic flux (in tesla), and υ = flux frequency. In practice, the g value is often determined by comparing the field values at resonance for the sample with that from a reference such as diphenyl-picryl-hydrazyl (DPPH), g = 2.0036, or Cr^{3+} in MgO matrix, g = 1.9797. Relation 4-1 (see Chapter 4) gives the equation for the evaluation of g. The surface of a catalyst containing a paramagnetic species can be studied by analyzing the g value. This value may provide the structural information for the supported metal oxides (lattice parameters, octahedral distortion, etc.) [30]. Information about the structure of a catalyst using EPR can be obtained by indirect study of paramagnetic gas-probe molecules such as NO [31], $^{18}O_2$ [32], or $C^{18}O$ [33] adsorbed on the surface. Data derived from EPR spectra can provide information about the surface crystal field, the redox properties of the surface, the identification of catalytically active sites, the surface morphology, the mobility of adsorbed species and the coordination chemistry of surface metal ions [29].

In this study, the $MnO_x/CeO_2/SiO_2$ powder catalyst samples were analyzed in quartz sample tubes at -160°C using a Varian E4 spectrometer. The magnetic field was set at 3200 Gauss with a modulation frequency of 100 kHz. The g-factor (g_s) for cerium samples (B_s) was determined by comparison with the field value at resonance for a reference (B_{ref}), in this case the DPPH radical (g_{ref} = 2.0036). The reference was placed together with the catalyst samples into the quartz tube for accurate g-value determinations. Accordingly, the value for g_s was evaluated based on relation 4-1.

X-ray photoelectron spectroscopy (XPS). The principle of XPS analysis is based on the photoelectric effect which implies emission of electrons with a given kinetic energy from a surface (sample) when irradiated with an electromagnetic flux (for ex. light or X-ray). The number of photoelectrons depends on the intensity and energy of the light. Figure 5.4 shows schematically the photoelectric process together with the Auger process which follows [34].

The ejected photoelectron (core electrons) contains information about the surface configuration due to the fact that its kinetic energy is specific to the electronic level and the type of element from which originated and is proportional with the energy ($h\upsilon$) of the irradiating light.

Only the surface electrons (first 10-50 Å), unaltered by inelastic collisions with other particles during ejection are information carriers. Relation 5-4 defines the kinetic energy of a core or valence electron ejected from given sample:

$$KE = h\upsilon - BE - \varphi \qquad (5-4)$$

where KE = kinetic energy; BE = binding energy of the photoelectron; h = Plank

constant; υ = frequency of the exciting radiation; φ = spectrometer work function.
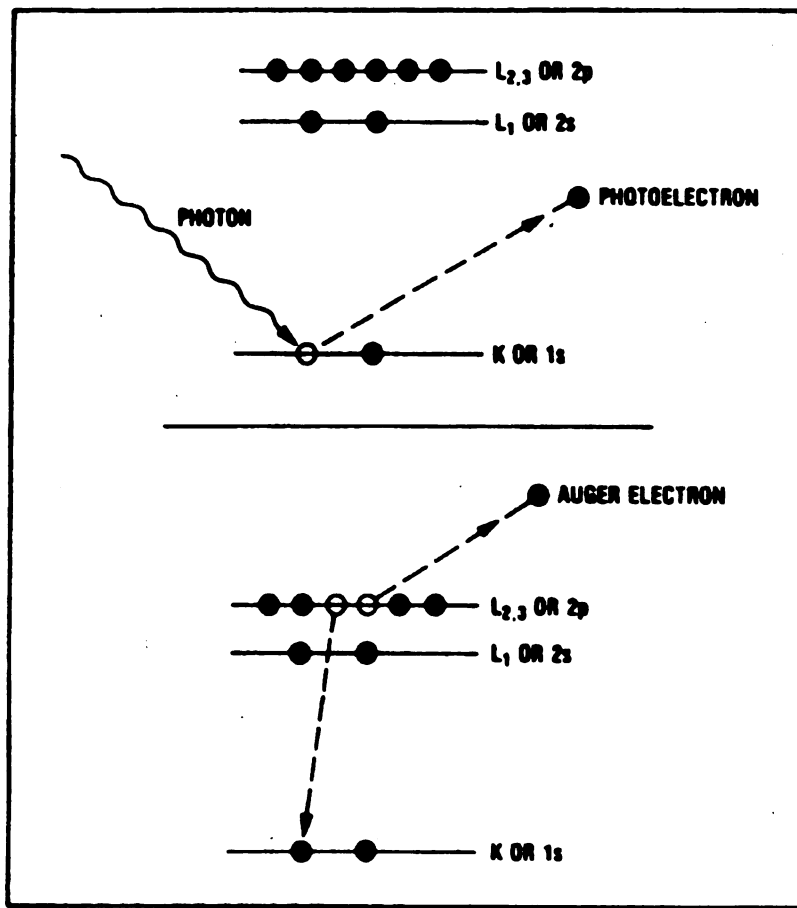
Figure 5.4 Schematically representation of the photoelectric effect [34]

The sources most common used for photoexcitation are X-ray sources, either Mg Kα

(1253.6 eV) or Al Kα (1486.3 eV). The technique was developed in the 1950's by

Siegbahn, but the first commercial instrument was available only after 1970. XPS

analysis provides information about the surface structure (elemental composition, metal's

oxidation state) and in some cases can evaluate the dispersion of one phase over another

[35]. Mn and Ce surface concentrations were evaluated from the intensity of the Ce_{3d} and Mn_{2p} peaks relative to the Si_{2p} peak, after area correction with the atomic sensitivity (ASF, [34]) factors for each atom detected at the catalyst surface.

The model proposed by Kerkhof and Moulijn [36] has been used to evaluate the theoretical monolayer dispersion of MnO_x from the XPS I_{Mn2p}/I_{Si2p} intensity ratio. In this model, a supported catalyst is considered to be a stack of sheets of supported material, with cubic crystals representing supported particles. Figure 5.2 illustrates schematically the proposed stratified model. The electrons ejected from the surface are considered to have a perpendicular trajectory to the surface (support sheets) and that a Lambert-Beer type law is valid. The XPS intensity ratio, I_p/I_s [p = promoter (Mn); s = support (Si)], assumes an exponential attenuation of the electrons escape depth in the particle and support and is described by the relation presented in Figure 5.2 , below the catalyst model [36]. The photoelectron cross sections for Mn, Ce, and Si were taken from tables reported in the literature [37]. The escape depths of the Mn_{2p} electrons were calculated using the relations develop by Penn for quantitative XPS analysis [38]. The surface coverage factor was calculated by considering that manganese is deposited on a high surface area SiO_2 (S_o =300m^2/g and ρ = 2400 kg/m^3).

.
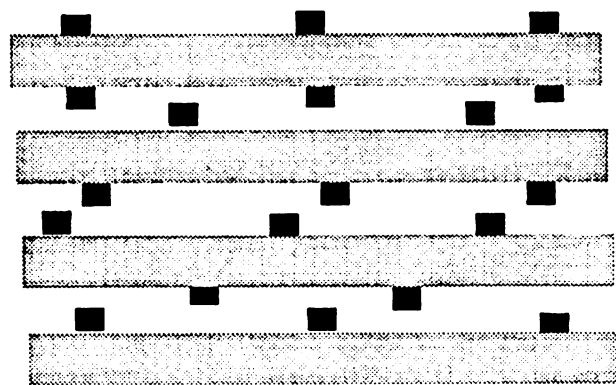
$$I_{exp} = \frac{I_{pr}}{I_{sup}} = (\frac{pr}{sup})\frac{\sigma_{pr}\beta_1(1+e^{-\beta_2})D_{(\epsilon_{pr})}}{\sigma_{sup}2(1-e^{-\beta_2})D_{(\epsilon_{sup})}}$$

Figure 5.5 Schematically representation of the Kerkhof-Moulijn model for a supported catalyst surface: $I_{p,s}$ = XPS intensity; $D_{(\epsilon p,s)}$ = detector efficiency; (p/s) = atomic ratio; $\sigma_{p,s}$ = photoelectron cross section; $\beta = t/\lambda$, λ = escape depth factor (t = $2/\rho S_o$, where ρ = density, and S_o surface are of the support) [36].

XPS data were obtained using a Perkin-Elmer Surface Science instrument equipped with a magnesium anode (1253.6 eV) operated at 300W (15 kV, 20 mA) and a hemispherical analyzer operated with a pass energy of 50 eV. Spectra were collected using a PC137 board interfaced to a Zeos 386SX computer. The instrument typically operates at pressures below 1 x 10^{-8} torr in the analysis chamber. Samples were analyzed as powders dusted onto double-sided sticky tape. Binding energies for the catalyst samples were referenced to the Si_{2p} peak (103.4 eV) and C_{1s} (285.4 eV). XPS binding energies were measured with a precision of $\pm$ 0.2 eV or better.

Activity measurements. As mentioned above, oxidative dehydrogenation of ML

to MP (Figure 5.1 a), and 23HPy to 23Py were used as probe reactions for catalysts

testing. The reactions were performed in a vertical, fixed-bed Pyrex reactor equipped

with a heating system capable of controlling the temperature with ±1°C accuracy. The

reactions were run at various temperatures (200°C for 23HPy to 23Py and 260°C for ML

to MP) maintaining (as much as possible) all other conditions constant: ML (23HPy)

flow rate = 0.13 mL/min, air flow rate = 42 ml/min, atmospheric pressure, residence time

= 15 s. Typically, products are collected for 20 min during steady-state operation of the

reactor. The reaction products exit the bottom of the reactor and are condensed in a

cooling flask using an ice-bath. The volume of the liquid product and the flow rate of the

gas product are measured during operation in order to compute a mass balance. The

outlet of the reactor was connected to a Riken infrared CO_2 gas analyzer which measured

the amount produced in the reaction. Product analyses in ML oxidation was performed

using a Varian 3700 gas chromatograph equipped with FID detector and a Supelco

packed column (4% carbovax/carbopack B-DA). Good reproducibility of reactant and

product analysis was achieved by direct on-column injection into the column of 1 μl

condensed product solution mixed with the internal standard. A response factor was

determined for each component observed in the product mixture using isopropanol as

internal standard. For 23HPy oxidative dehydrogenation reaction, the reactants and

products were analyzed using a Varian 3300 gas chromatograph equipped with a TCD

detector and a capillary column (Supelco SPB-1). The internal standard used in this case

was hexanol. ML and 23HPy conversions and selectivities in MP and 23Py, respectively, were reported in wt.% relative to the theoretical yields based on converted reactants.

Results and Discussions

Unpromoted fresh MnO_x/SiO_2 Catalysts. In the case of unpromoted MnO_x/SiO_2 catalysts, calcined at 500 °C and with y varying from 0.5 to 14, different XRD patterns were observed. Figure 5.6 shows the XRD pattern observed for the Mnyn catalysts.

For low manganese loading (y = 005, Figure 5.6 e) no pattern specific to a crystalline MnO_x phase was observed; for $02 \leq y \leq 10$, (Figure 5.6 c-d) only the MnO_2 crystalline phase was identified; when $y \geq 10$ (Figure 5.6 a-b) mixed XRD patterns indicative of MnO_2 and Mn_2O_3 crystalline phases was identified [40]. Based on the diffraction patterns observed and presented in Figure 5.6, the crystalline particle sizes of the MnO_2 and Mn_2O_3 were evaluated from line broadening calculations. The results are presented in Table 5.2 together with BET and XPS surface concentration data.

As observed from Table 5.2, column 2, the surface area of the Mnyn500 catalysts does not change significantly after manganese impregnation due to the fact that MnO_x formed after calcination is not a porous material which may affect the catalyst texture. The small differences observed are due to the variation in the catalyst weight considered for calculation as a function of Mn loading.
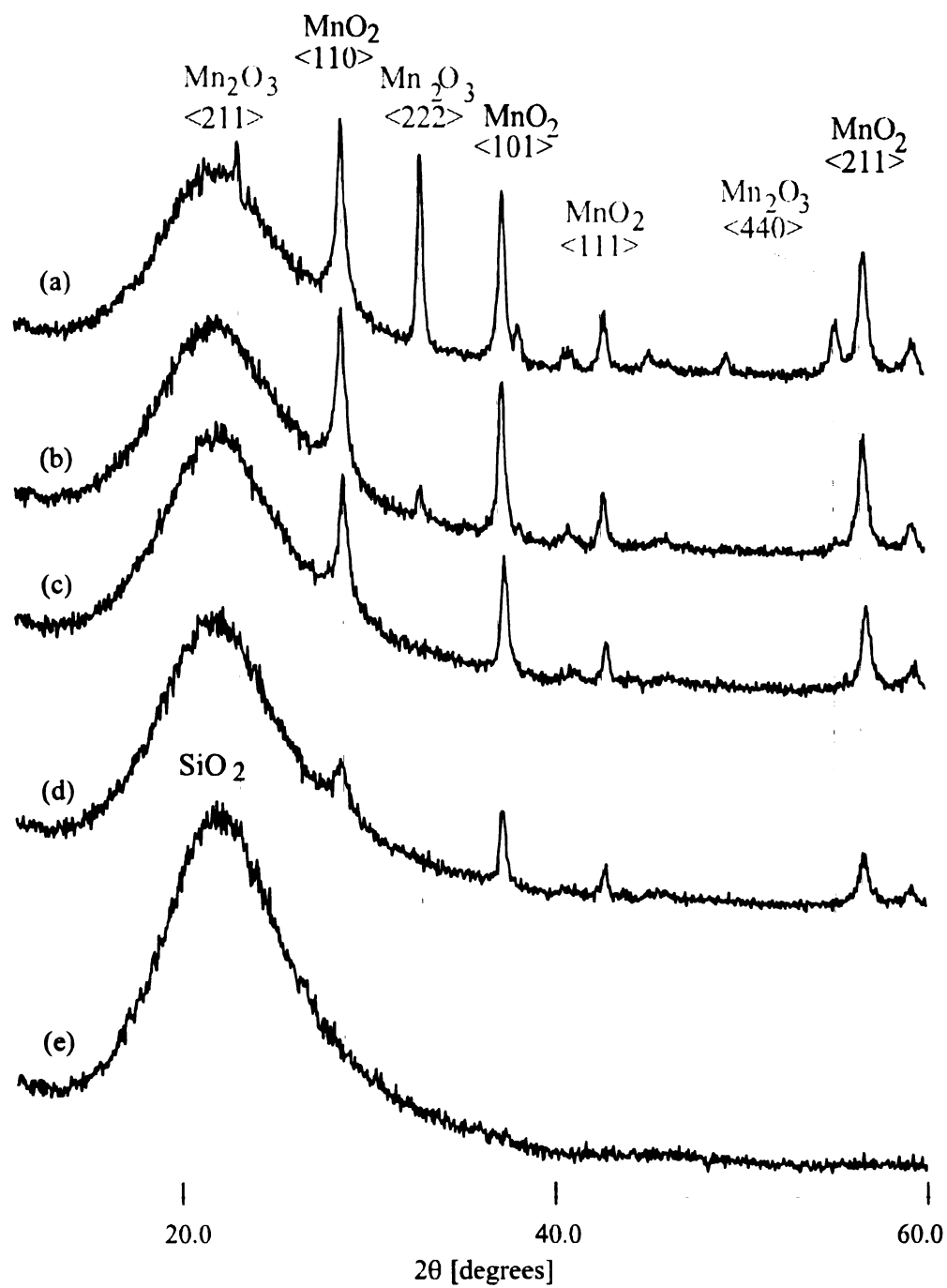
Figure 5.6 XRD pattern for Mnyn catalysts calcined at 500°C: a) Mn14n500; b) Mn10n500; c) Mn06n500; d) Mn02n500; e) Mn005n500.

In Table 5.2, columns 3 and 4 present the crystalline particle size values ($\bar{d}$) for

the MnO_2 and Mn_2O_3 species, and column 4 shows the MnO_2/Mn_2O_3 ratio. As observed,

at low loading ($y < 10$) the dominant species on the catalyst is MnO_2.

Table 5.2 XRD and XPS MnO_x dispersion data and MnO_2/Mn_2O_3 ratio evaluated from diffraction patterns for $Mnyn500$ catalysts ($y = 0.5\text{-}14 = Mn/Si$ atomic ratio)

Catalyst	Surface Area [m²/g]	$\bar{d}$ [nm] β-MnO₂	$\bar{d}$ [nm] α-Mn₂O₃	R[a]	[c]XPS I_{Mn2p}/I_{Si2p} corrected
Mn005n	282	b	b	---	0.15
Mn02n	275	11.6	b	1	0.35
Mn06n	257	15.5	b	1	0.98
Mn10n	255	16.5	23.7	0.89	1.08
Mn14n	255	16.8	25.5	0.59	1.09

a - R = A(<110>MnO_2)/[A(<110>MnO_2) + A(<222>Mn_2O_3)]; b - no XRD pattern observed; c - evaluation of XPS I_{Mn2p}/I_{Si2p} ratio based on corrected area using the atomic sensitivity factor (ASF) of Mn and Si specific to the instrument

The particle size of MnO_2 increases with the increase of the Mn loading (11.6 nm to 16.8

nm). At high Mn loading ($y \geq 0.1$), the presence of Mn_2O_3 species becomes significant,

and at $y = 14$, the ratio between the two manganese oxide species approaches 1/2. The

particle size for Mn_2O_3 crystallites is around 24 nm, much larger than that for MnO_2.

This observation can be attributed to the fact that at low loading, after impregnation with

$Mn(NO_3)_2$ precursor, manganese as Mn^{2+} is well dispersed on the SiO_2 support and

accessible to the oxygen from air. Thus, during calcination Mn^{2+} is oxidized easily to

Mn^{4+} and forms small crystalline MnO_2 particles.

(a)
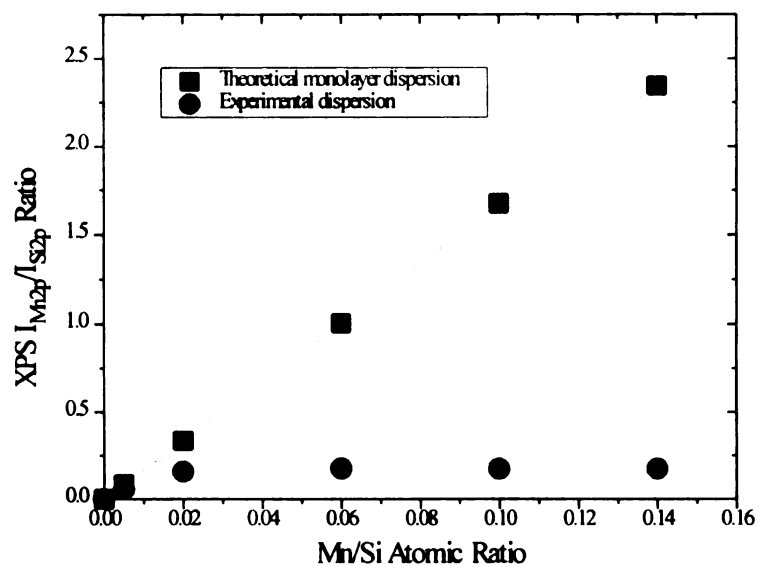
(b)

Figure 5.7 Mn monolayer dispersion (squares) evaluated from Kerkhof and Moulijn model in comparison with the experimental value (rhombus) for: a) Mnyn catalysts; b) Mn10n calcined at various temperatures

At high Mn loadings, after impregnation, manganese is probably forming large clusters which are less permeable to oxygen and as a consequence the oxidation process during air calcination occurs only to Mn_2O_3 which is present on SiO_2 surface as large crystallites.
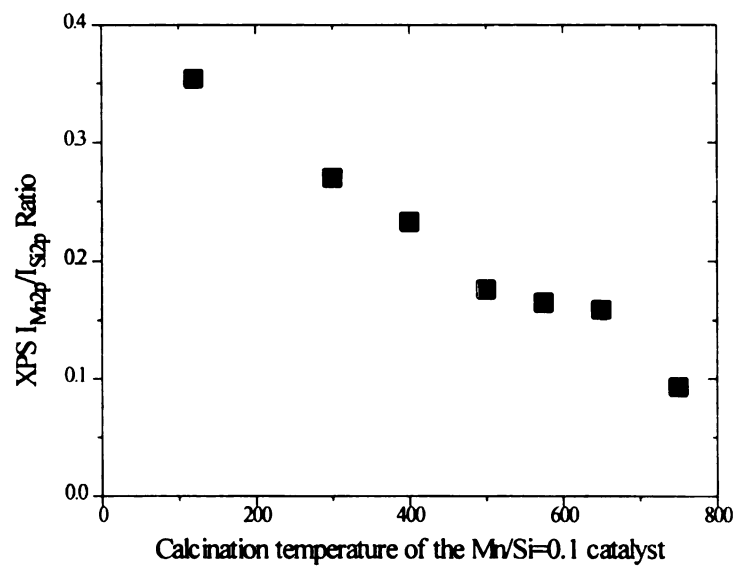
XPS I_{Mn2p}/I_{Si2p} ratio based the corrected areas for Mn_{2p} and Si_{2p} using the ASF values specific to Mn and Si atoms (Table 5.2, column 5) indicates, an expected increase with the Mn loadings leveling out at y values above 0.06. Based on this observation, it can be concluded that Mn dispresion is decreasing with increasing the MnO_x concentration. A more accurate estimation of the Mn dispersion is possible considering the Kerkhof and Moulijn model [36], described in the experimental section.

Figure 5.7 a shows the Mn monolayer dispersion used as a reference in comparison with the dispersion values expressed by the XPS I_{Mn2p}/I_{Si2p} ratio. The experimental values follow the theoretical monolayer dispersion only for the Mn005n500 and Mn02n500 catalysts (low Mn loadings). For catalysts with higher Mn loading ($y \geq$ 06), the experimental value is situated far from the Mn monolayer dispersion. The XPS dispersion results are consistent with the data obtained from XRD line broadening calculations which indicated MnO_2 (Mn_2O_3) crystalline particles larger than 15 nm for catalyst with Mn loading greater than $y = 06$, which clearly indicates a low manganese dispersion. The value of binding energy of the $M_{2p3/2}$ XPS peak lies around 642.2 eV, which is attributed to $Mn^{4+}O_2$ [9, 34]. The peak at 642.2 becomes more and more asymmetric as the Mn loading increases, corresponding to the appearance of a peak specific to Mn^{3+} and Mn^{2+} species, which have a binding energy for $Mn_{2p3/2}$ at around 640.8 eV [9, 34]. For a better correlation between the binding energies specific to various

type of MnO_x species, XPS analysis of standard compounds were performed and used for comparison (see Figure 5.8 a-d).
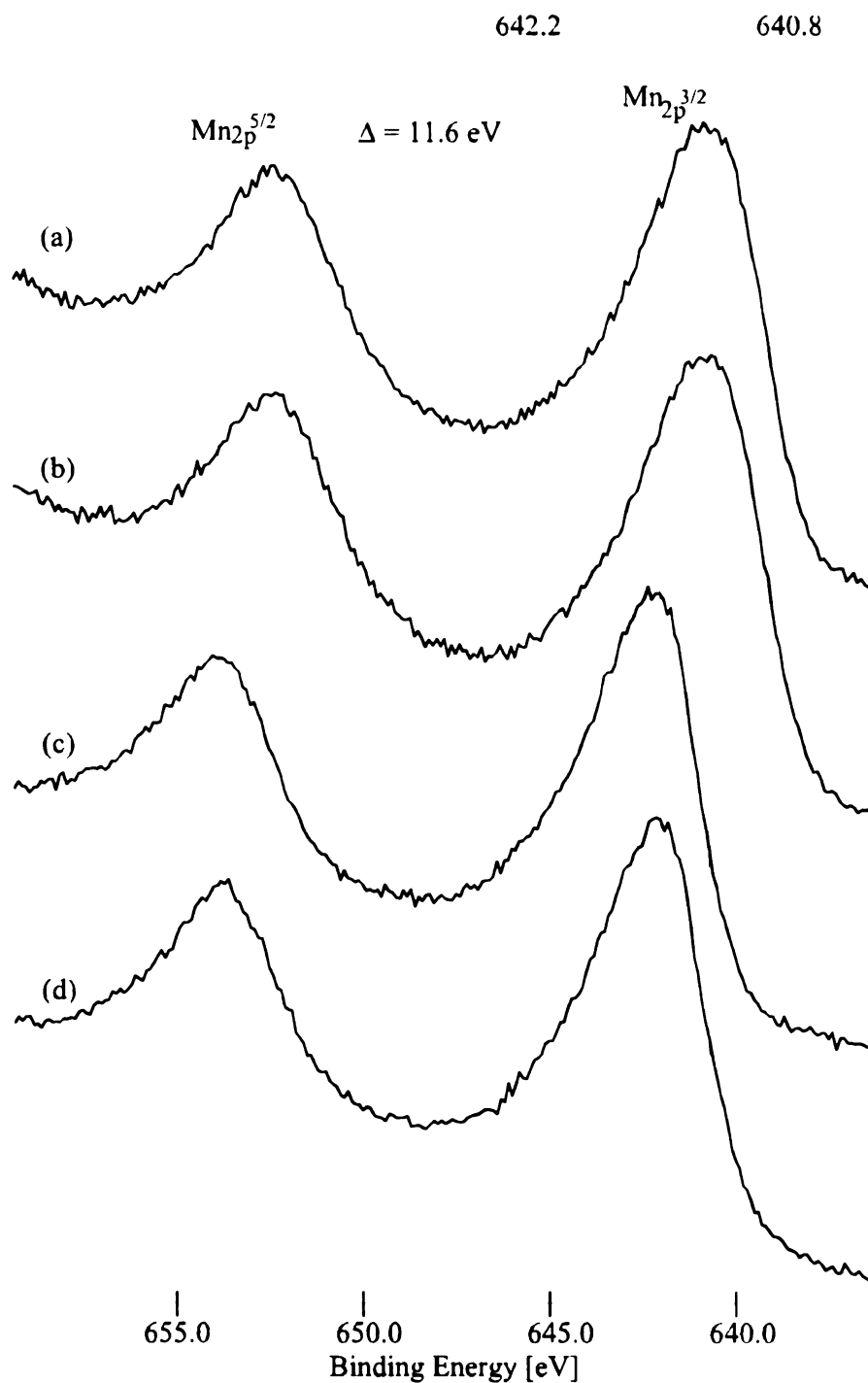
Figure 5.8 Mn_{2p} XPS spectra for Mn-standard compounds: a) pure Mn_2O_3; b) Mn_2O_3 obtained from calcination of $Mn(NO_3)_2$ at 750°C; c) pure MnO_2; d) MnO_2 obtained from calcination of $Mn(NO_3)_2$ at 300°C.

XPS and XRD results can be well correlated with the TPR results obtained for the

Mnyn catalysts and presented in Figure 5.9.
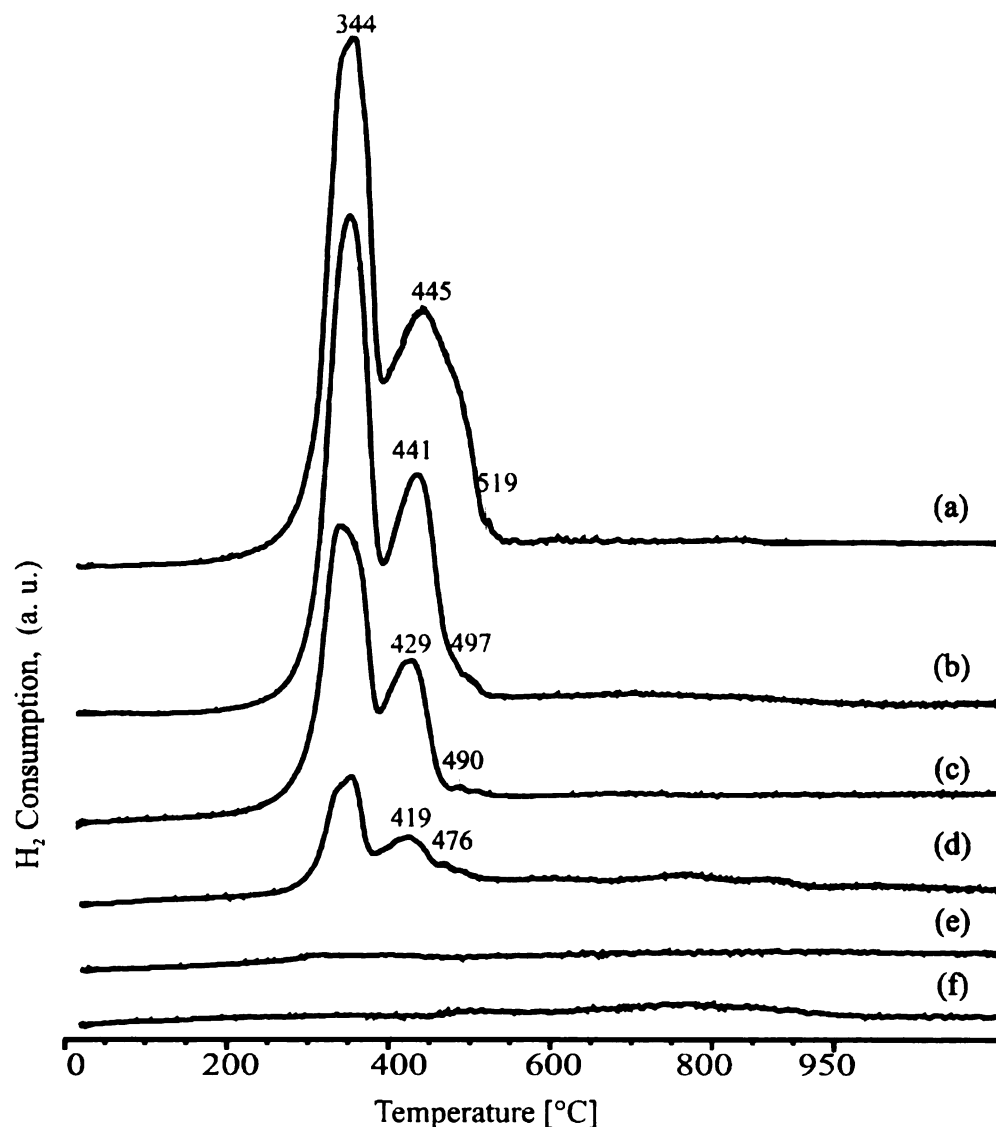
Figure 5.9 TPR profiles for the Mnyn catalysts calcined at 500°C: a) Mn14n500;
b) Mn10n500; c) Mn06n500; d) Mn02n500; e) Mn005n500; f) pure SiO_2.

The TPR profiles of the Mnyn500 catalysts are similar with that observed for the

unsupported MnO_2, exhibiting two major peaks at 344°C and at 445°C. This indicates

that MnO_2 is physically deposited on the SiO_2 support without a strong chemical

interaction. In the literature, the two peaks were attributed to the two-steps reduction process of the MnO_2 or MnO_2/Mn_2O_3 mixture, first to Mn_3O_4 and then to MnO species [9]. The small shifts in the peak position observed as the Mn/Si ratio increases can be attributed to the difference in the particles size of the supported MnO_2. It is known that a higher reduction temperature corresponds to bulk phase reduction whereas a lower reduction temperature is required for dispersed phase [27-28]. As a consequence of the increased MnO_x particle size with Mn loading, the reduction temperature varies from 419°C for the Mn02n catalyst (small MnO_x particles) to 445°C for the Mn14n catalyst (large MnO_x particles). The relative intensities of TPR peaks vary with the Mn-loading, too, the H_2 consumption being proportional with the manganese available for reduction on the catalysts.

The effect of the calcination temperature on the structure of the unpromoted MnO_x/SiO_2 catalysts used during the preparation process was studied as well. The XRD spectra obtained from the analysis of Mn10n catalysts calcined at various temperature (in the 125°-750°C range) are presented in Figure 5.10. These data indicate a variation in the MnO_2/Mn_2O_3 ratios, with MnO_2 dominant at low temperature and Mn_2O_3 at temperature above 600°C, consistent with previous findings [7,9]. In the 400°-600°C domain, mixed XRD patterns specific to bath MnO_2 and Mn_2O_3 species are observable. As observed in Table 5.3, column 4, the R_a value is close to 1 for catalyst dried at 125°C or calcined at temperatures below 400°C, decreases as calcination temperature is raised and reach 0 at temperatures above 600°C.

Figure 5.10   XRD patterns for Mn10n catalysts calcined at various temperatures:
a) Mn10n750; b) Mn10n650; c) Mn10n575; d) Mn10n500; e) Mn10n400; f) Mn10n300;
Mn10n125.

As observed from the data presented in Table 5.3 column 2 and 3, the particle size

($\bar{d}$) evaluated from XRD line broadening using MnO_2 <110> and Mn_2O_3 <222>

diffraction peaks increased with calcination temperature.

Table 5.3 XRD particle size evaluated from line broadening calculations for β-MnO_2 and α-Mn_2O_3 species on Mn/Si = 0.10 (atomic ratio) catalyst calcined at various temperatures (125°-750°C temperature domain)

Catalyst	$\bar{d}$ [nm] β-MnO_2	$\bar{d}$ [nm] α–Mn_2O_3	R^a	^{c}XPS I_{Mn2p}/I_{Si2p} corrected
Mn1si125	15.1	b	1	2.08
Mn1si300	15.4	b	1	1.67
Mn1si400	16.2	12.1	0.97	1.37
Mn1si500	16.5	23.7	0.89	1.08
Mn1si575	17.5	25.3	0.33	0.9
Mn1si650	b	26.0	0	0.98
Mn1si750	b	29.4	0	0.75

a - $R = A(<110>MnO_2)/[A(<110>MnO_2) + A(<222>Mn_2O_3)]$; b - no XRD pattern observed; c - evaluation of XPS I_{Mn2p}/I_{Si2p} ratio based on corrected area using the atomic sensitivity factor of Mn and Si specific to the instrument

This fact can be attributed to the mobility of small MnO_2 crystallites formed and well

dispersed on the silica surface during calcination allowing them to get together and form

large crystalline particles, at high temperatures. Again, the Mn_2O_3 crystalline particles

are larger that those observed for MnO_2. The Mn dispersion evaluated from XPS surface

concentration indicates a decrease in Mn surface coverage with increasing calcination

temperature. This observation is consistent with that from the XRD line broadening

calculations which indicate an increase in MnO_x particle size with increased calcination temperature. As observed from Figure 5.7 b, the XPS I_{Mn2p}/I_{Si2p} ratio shows a steady decrease with the increase in the calcination temperature of the catalyst.

An analysis of the Mn oxidation state using XPS data, is presented in Figure 5.11. The S/N decreases with increasing calcination temperature. The XPS spectra from Figure 5.11 a-b show a symmetric peak at 640.8 eV indicating the presence of manganese as Mn^{3+} or Mn^{2+} species whereas the spectra from Figure 5.11 e-g show a symmetric peak at 642.2 eV corresponding to manganese as Mn^{4+}- type of species. These data are consistent with the XRD data which pointed to Mn_2O_3 formation at high temperatures and MnO_2 formation at low temperatures. The XPS spectra from Figure 5.11 c-d, show the presence of mixed Mn^{4+}/Mn^{3+} type of species (with the maximum at 640.8 eV and a shoulder at 642.2 eV) on the surface of the catalysts. Additional information was obtained from TPR analysis of the Mn10n catalyst calcined at various temperatures (Figure 5.12 a-d). As observed from Figure 5.12 a, calcination to high temperature (750°C) led to an attenuation of the reduction peaks at 344°C and 445°C and the appearance of a strong peak at 519°C. The new peak can be attributed to the reduction of the Mn_3O_4 phase to MnO. Thus, high temperature calcination of the Mn10n catalysts led to formation of a stable Mn_3O_4 phase. Some of the Mn_2O_3 phase is still present. The presence of three clear peaks in the TPR profile of the sample calcined at 575°C is indicative of the existence of all three MnO_x phases on the catalyst surface.

$\Delta = 11.6\ eV$ 642.2 640.8

(a)

(b)

(c)

(d)

(e)

(f)

(g)

| | | | |
655.0 650.0 645.0 640.0

Binding Energy [eV]

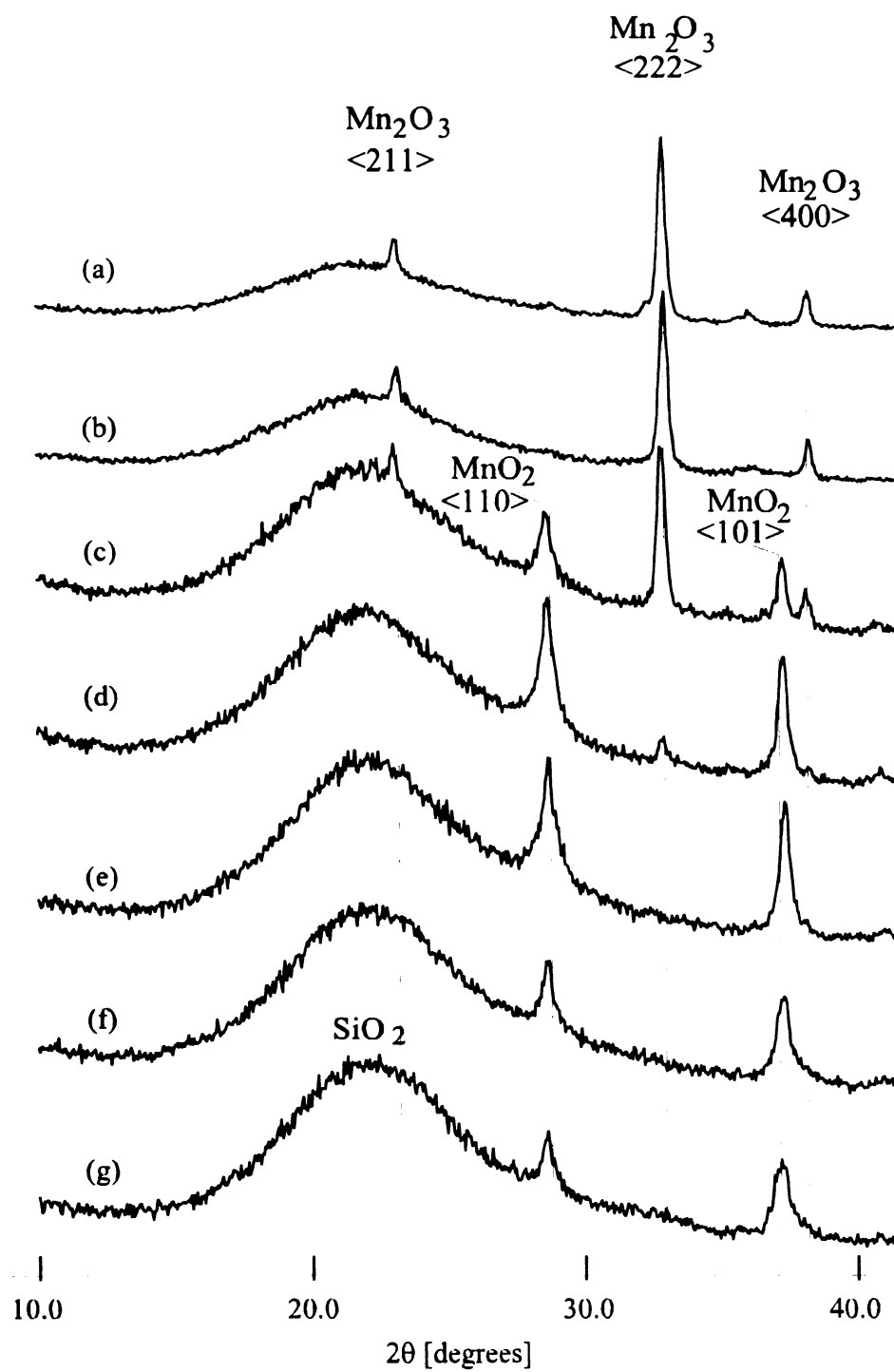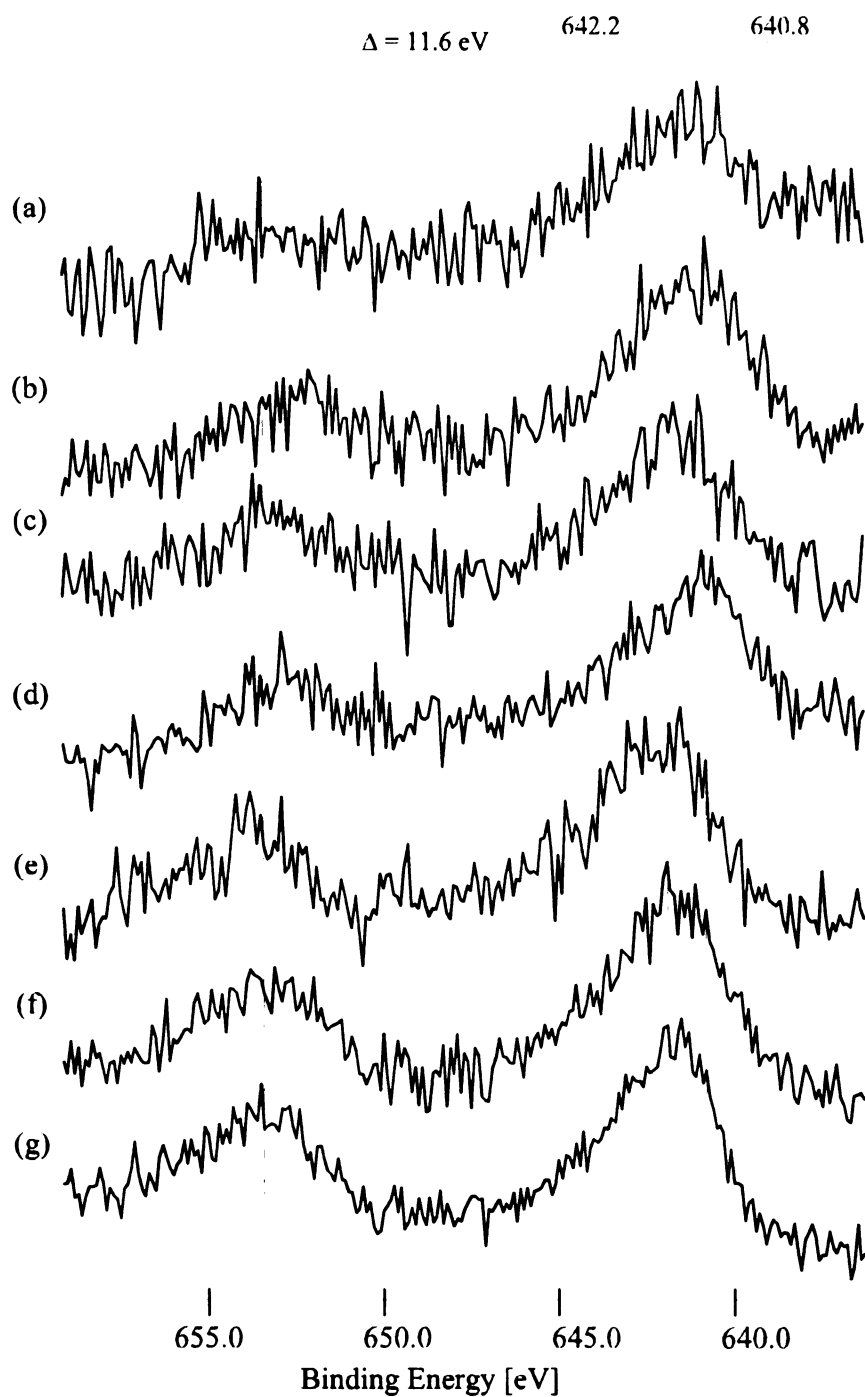Figure 5.11 Mn$_{2p}$ XPS spectra for Mn10n catalysts calcined to various temperatures: a) Mn10n750; b) Mn10n650; c) Mn10n575; d) Mn10n500; e) Mn10n400; f) Mn10n300; g) Mn10n125.

Figure 5.12 TPR profiles of Mn10n catalysts calcined at various temperature during preparation: a) Mn10n750; b) Mn10n575; c) Mn10n500; d) Mn10n300.

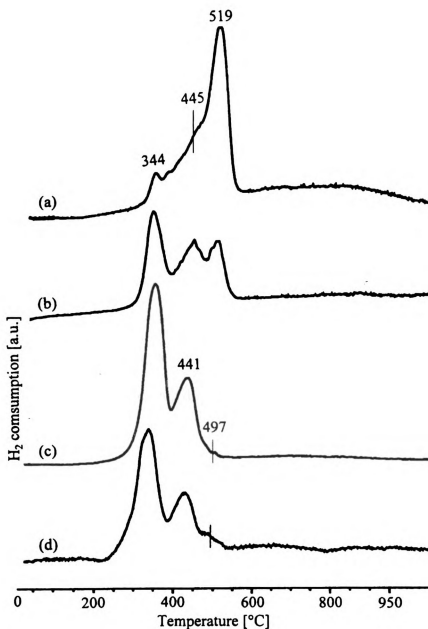The two clear peaks in the TPR profiles of samples calcined at low temperature, indicate the presence of a MnO_2 phase on the catalyst. The two peaks correspond to the two steps reduction of MnO_2 (MnO_2 to Mn_2O_3, and Mn_2O_3 to MnO, respectively).

CeO₂ promoted MnOₓ/SiO₂ catalysts. Information about the crystalline phases formed on the CeO_2-promoted catalysts was obtained from the XRD spectra presented in Figure 5.13. For the two types of CeO_2-supported MnO_x/SiO_2 catalysts (Mn10ncea and Mn10ncen), only diffuse XRD patterns specific to a MnO_x crystalline phase were observed. This fact can be attributed either to the formation of small MnO_x particles or to an amorphous manganese phase from the CeO_2-promoted SiO_2 catalysts calcined at 500°C. It seems that the presence of cerium favors high MnO_x dispersion on the SiO_2 support. Analyzing the positions of the diffuse XRD peaks other than those specific to CeO_2, the most probable manganese species formed is MnO_2. The particle sizes of MnO_x evaluated from line broadening calculations are presented in Table 5.4, together with BET surface area and XPS dispersion data for supported MnO_x.

Table 5.4 MnO_x particle size evaluated from XRD line broadening calculations, XPS surface concentration, and Mn dispersion data for unpromoted and CeO_2-promoted MnO_x/SiO_2 catalysts

Catalyst	Surf. Area [m²/g]	d̄ [nm] MnO₂	Mn₂p₃/₂ BEᵃ [eV]	ᵇXPS I_Mn2p/I_Si2p corrected	I_Mn2p/I_Si2p Experim.ᶜ
Mn10n500	255	16.5	642.5(640.8)	1.08	0.176
Mn10sicea	225	6.7	642.3	1.77	0.286
Mn10sicen	230	13.8	642.2	1.13	0.192

a - BE = binding energy; b - evaluation of XPS I_{Mn2p}/I_{Si2p} ratio based on corrected area using the atomic sensitivity factor of Mn and Si specific to the instrument; c - for y = 10, theoretical monolayer XPS I_{Mn2p}/I_{Si2p} = 1.67, (based on Kerkhof-Moulijn model)
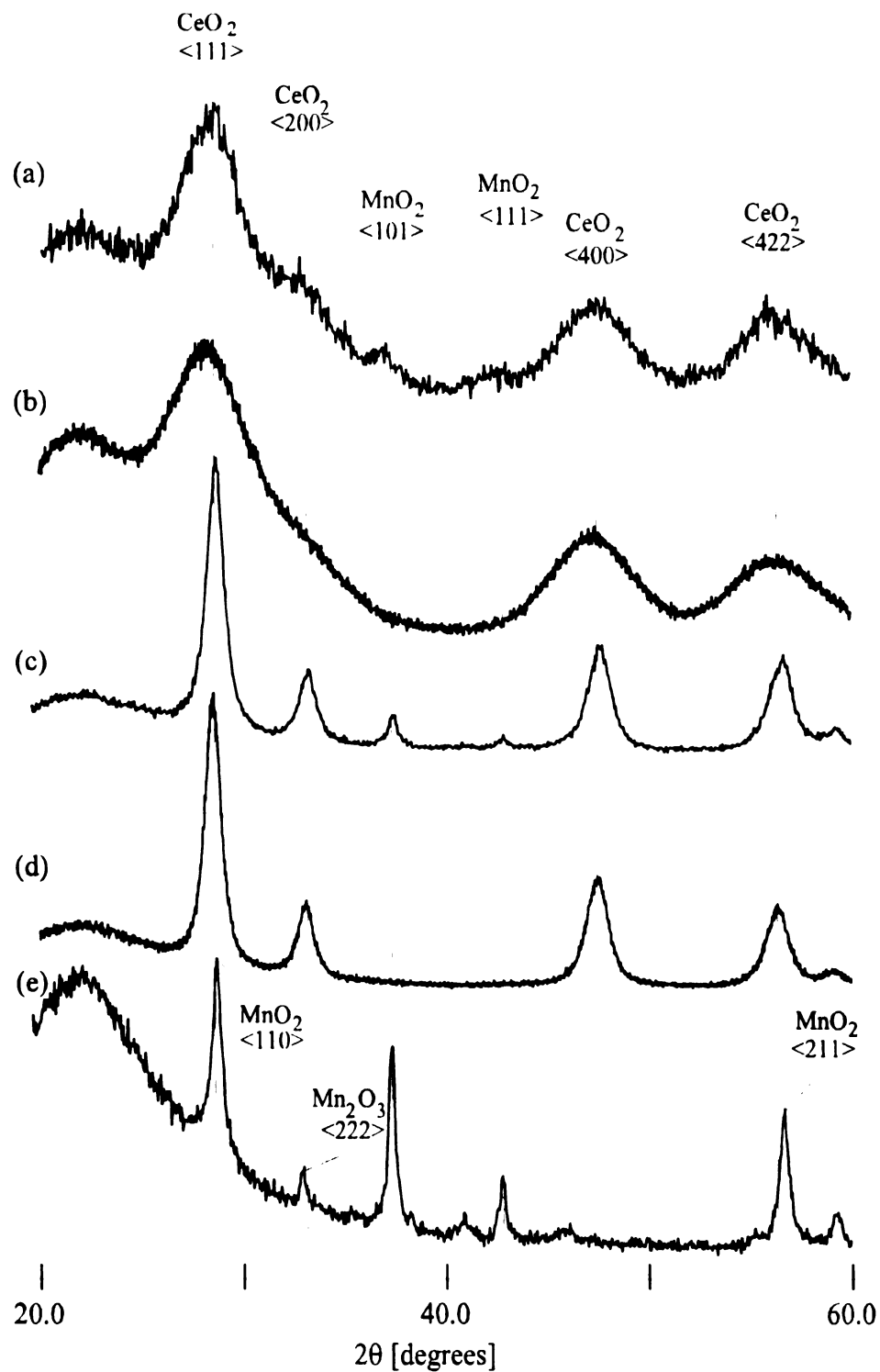
Figure 5.13   XRD patterns of unpromoted and CeO₂-promoted MnOₓ/SiO₂ catalyst (y = 10) calcined at 500°C: a) Mn10ncea; b) CeqA; c) Mn10ncen; d) CeqN; e) Mn10n500.

As mentioned above, calcination of the catalyst to 500°C in air led to the formation of a mixed MnO_2-Mn_2O_3 phase on the SiO_2 support, with crystalline particles around 16 nm for MnO_2 and 25 nm for Mn_2O_3. For the fresh unpromoted catalyst (Table 5.4, column 4), the Mn_{2p} XPS spectrum shows that Mn is present as mixed Mn^{3+}/Mn^{4+} with an asymmetric profile which can be related to a mixed Mn_{2p} spectrum from MnO_2 (Figure 5.8 c) and Mn_2O_3 (Figure 5.8 a). However, the peak is shifted more toward the BE of Mn^{4+} species (642.5 eV), indicating a higher MnO_2 content. This observation is in good agreement with the XRD data for Mn10n500 catalysts (see Figure 5.10 and Table 5.2) which show diffraction patterns specific to MnO_2 and Mn_2O_3 species, with R = 0.89.

Evaluation of the MnO_2 crystalline particle size ($\bar{d}$) from the patterns observed in the XRD spectra of the CeO_2-promoted catalyst led to values of 6.7 nm for Mn10ncea catalyst and 13.8 nm for the Mn10ncen catalyst, significantly lower than in the case of unpromoted Mn10n500 catalyst. This fact may be attributed to the interaction of the CeO_2 promoter with Mn during impregnation which precludes formation of large MnO_2 crystallites. The fact that Mn is present on the CeO_2 promoted catalysts just as MnO_2 can be explained by the better Mn dispersion and consequently to the better contact with the oxygen from air during calcination which allowed the oxidation process to occur to the highest oxidation state of the Mn (4+). For the cerium promoted catalyst, the XPS spectra of the $Mn_{2p3/2}$ shows symmetric peaks with binding energy located at 642.2 eV (see Table 5.4, column 4), characteristic of Mn^{4+}. XPS dispersion data presented in Table 5.4, columns 5 and 6, confirms the better Mn dispersion on the promoted catalysts, the I_{Mn2p}/I_{Si2p} = 0.286 for Mn10ncea catalyst, double value in comparison with that for

Mn10n500 catalyst. From XPS data, the difference in Mn dispersion between the Mn10ncen and Mn10n500 samples is not significant.

Additional information about the cerium promoted catalysts were obtained from TPR data. Figure 5.14 presents the TPR profiles for the unpromoted (5.14 a) and CeO_2-promoted catalyst (5.14 b-c) in comparison with the profiles for the Mn-free CeO_2-promoted SiO_2 (5.14 d-e). The TPR profile of the Mn10n500 contains two peaks and corresponds to the two step reduction of MnO_2 (see explanations above). The profiles for the CeO_2-promoted SiO_2 catalysts were explained elsewhere (see Chapter 4). These TPR data are presented in Figure 5.14 as references. The TPR profiles of the Mn10ncea (Figure 5.14 b) and Mn10ncen (Figure 5.14 c) are very different from the reference profiles, though they both show peaks for the reduction of the two metal oxides (Mn and Ce) present on the catalysts. One of the main differences is the position of the peak corresponding to the MnO_2 reduction to Mn_2O_3, which is shifted to 314°C, lower than that observed for the unpromoted catalyst. Shifts in the peaks of the TPR profiles from the value observed for pure materials have been reported in the literature for MnO_x species and attributed either to the formation of mixed oxides when more than one metal was present on the catalyst surface [42] or to a catalytic effect of the second metal (Pt or Pd) over the oxidation of Mn [43]. In other cases, these types of shifts in the TPR profile were related to a chemical interaction with the support or to smaller particle size [27-28]. Consequently, the shift of the peak at 314°C may be due to smaller MnO_2 particles and probably to an interaction between Ce and Mn. There is no shift in the second peak at

441°C. A new clear peak can be observed at 497°C for Mn10ncen catalyst. This peak

overlaps with that from cerium, in the case of the TPR profile for the Mn10ncea catalyst.
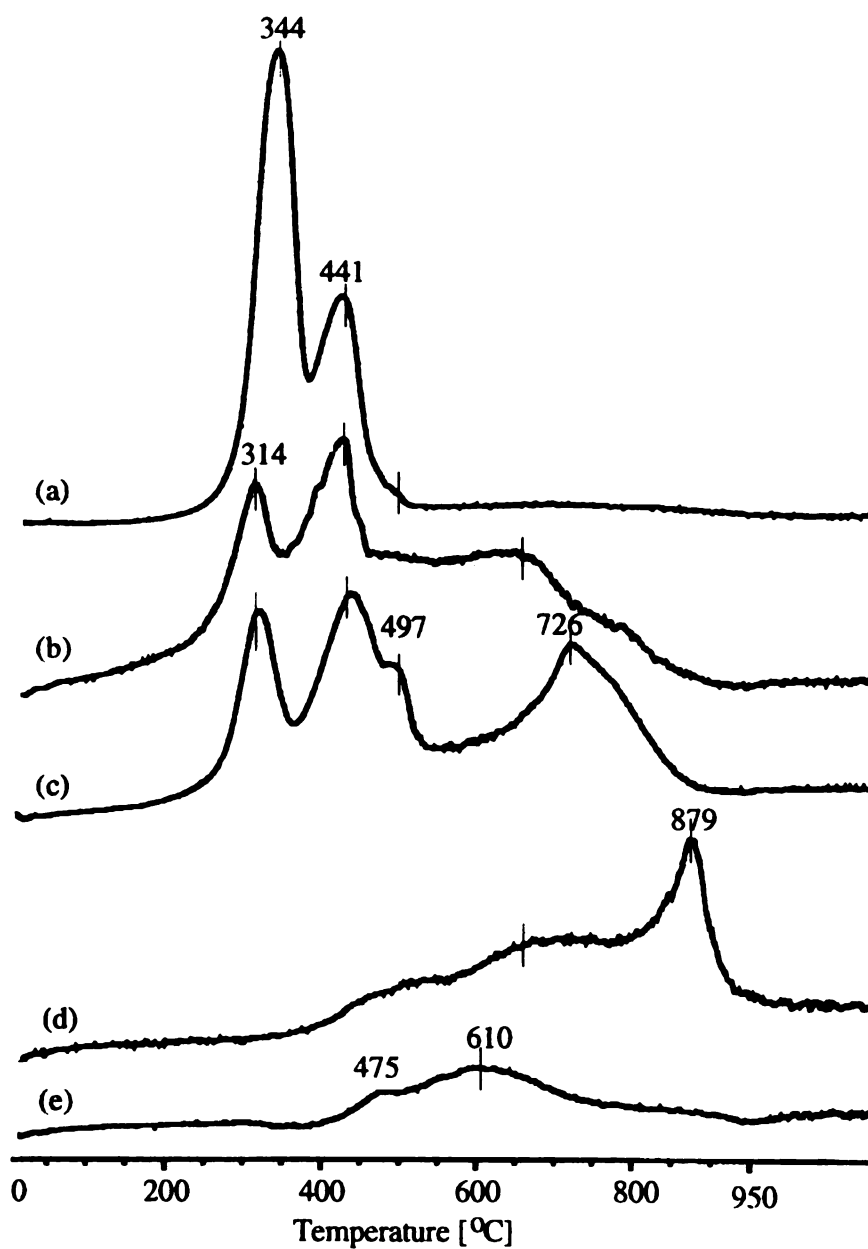

Figure 5.14 TPR profile of the unpromoted and CeO₂ promoted MnOₓ/SiO₂ and SiO₂ catalysts: a) Mn10n500; b) Mn10ncea; c) Mn10ncen; d) CeqN; e) CeqA.

This peak overlaps with that from cerium, in the case of the TPR profile for the Mn10ncea catalyst. It was found that for catalysts calcined at high temperature ($\geq 575°C$), a peak at 519°C is related to the reduction of Mn_3O_4 to MnO. Thus, the assignment of the peak at 497°C for the Mn10ncea and Mn10ncen catalysts should be the same, but considering the shift due to Ce-Mn interaction. A similar shift was observed for the bulk cerium reduction peak at 879°C which appeared in the Mn10ncen catalyst at 726°C. There is no clear shift in the case of the cerium peak at around 610°C for the Mn10ncea catalyst.

More information about the possible Mn-Ce interaction from the CeO_2 promoted MnO_x/SiO_2 catalyst was obtained from EPR data. EPR spectra of the cerium-promoted catalysts are presented in Figure 5.15 a-d. Cerium-promoted SiO_2 catalysts prepared from Ce^{4+}-nitrate ($CeqN$, Figure 5.15 d) showed the presence of Ce^{3+} ions as well as paramagnetic oxygen species (O_2^- or O^-) stabilized in the CeO_2 lattice formed on the SiO_2 surface. In contrast, when Ce^{4+}-methoxyethoxide ($CeqA$, Figure 5.15 b) was used as precursor, only the surface superoxide oxygen resonances were observed. Detailed explanations about the EPR spectra interpretation for the $CeqA(N)$ catalysts were given in Chapter 4. The presence of manganese on the catalyst surface (Mn10ncea, Figure 5.15 a) led to a signal containing six hyperfine peaks (noted on in Figure 5.15 a, from 1 to 6). Similar EPR spectra were reported in the literature for unsupported Mn/Ce mixed oxides and attributed to the manganese nucleus ($I = 5/2$ for ^{55}Mn) interaction with the $Mn^{2+}(Mn^{4+})$ spin, from ions located in sites with distorted octahedral symmetry or to Mn-dimmers from the mixed oxide [44-48]. Considering the fact that XRD data show small

MnO_2 crystallites on the Mn10ncea catalyst and the $Mn_{2p3/2}$ XPS binding energy is situated at 642.3 eV (specific to a Mn^{4+} species), the mixed $MnCeO_x$ species likely contain Mn^{4+} rather that Mn^{2+} ions incorporated into the mixed crystals.
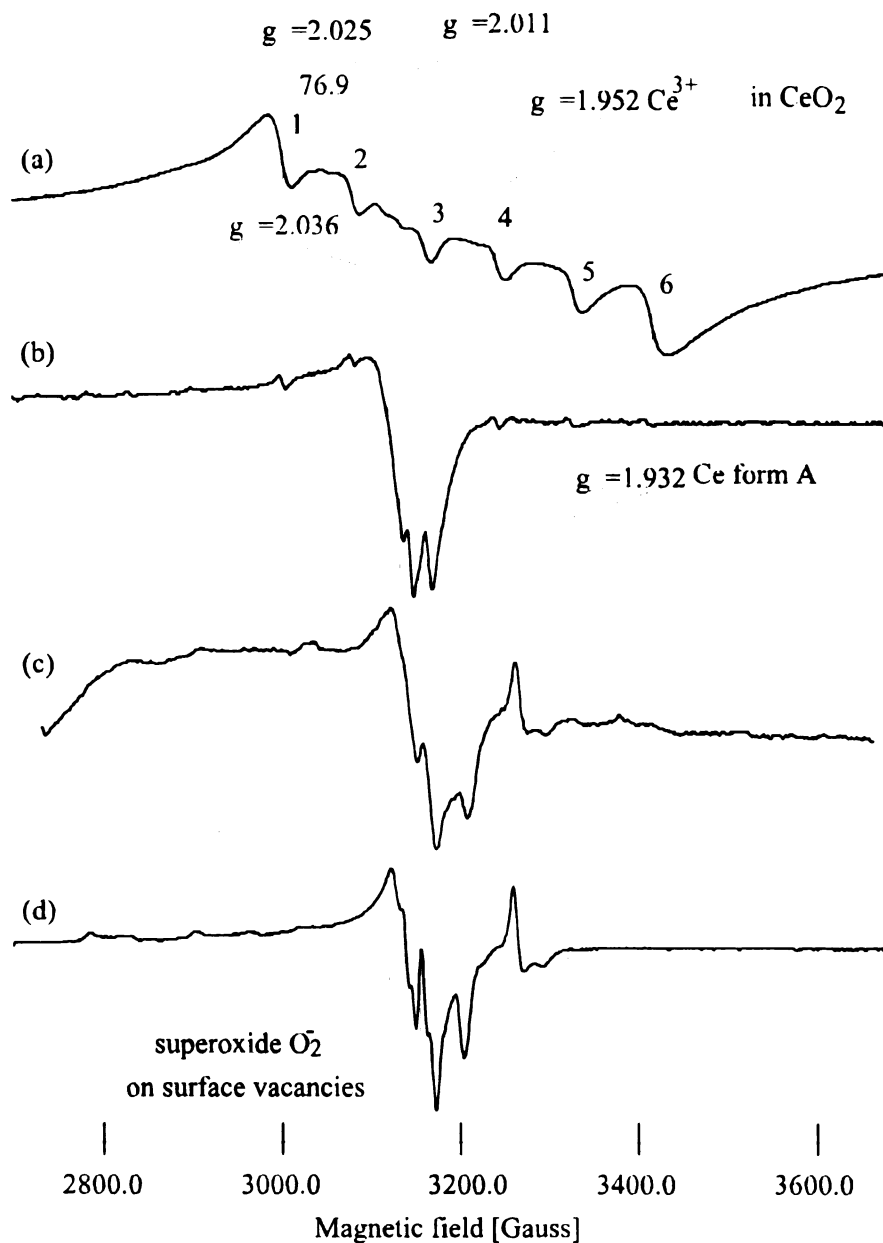

Figure 5.15   EPR spectra for the CeO_2-promoted MnO_x/SiO_2 catalysts: a) Mn10ncea; b) CeqA; c) Mn10ncen; d) CeqN.

If Mn^{2+} species are present in the catalyst structure, they would be located in the bulk part of the crystal lattice. The EPR spectrum of the Mn10ncea catalyst indicates an attenuation of the signals characteristic to oxygen from surface superoxides (O_2^-). No Ce^{3+} defects were observed in the Mn10ncea catalyst, consistent with XPS data which indicated the presence of cerium on the surface as Ce^{4+}. It appears that the amorphous CeO_2 formed on the CeqA promoted catalyst is more reactive in solid state reactions with Mn, favoring the formation of the Mn/Ce mixed crystal. The formation of the mixed Mn/Ce oxide is not observed in the case of the Mn10ncen catalyst. As observed in Figure 5.15 c, the EPR spectrum of the Mn10ncen sample looks like that of the CeqN support. The EPR spectrum of a physical mixture of the CeqN and MnO_2 sample looks similar to the spectrum obtained for Mn10ncen catalyst. From these data it seems that in the case of Mn10ncen catalyst, MnO_2 and CeO_2 crystals exist mostly separately on the SiO_2 support. The formation process of mixed Mn/Ce oxide phase is significantly reduced. The low CeO_2 dispersion with large crystalline particles precludes a good interaction with MnO_2 formed on the SiO_2 surface during Mn10ncen catalyst preparation, leading to the formation of separate MnO_2 and CeO_2 crystalline phases. The EPR spectrum of Mn10ncen catalyst (Figure 5.14 c) still shows the presence of Ce^{3+} ($g_\perp$ = 1.952) lattice defects from the CeO_2 crystalline structure as well as the surface superoxide oxygen species O_2^- ($g_{//}$ = 2.025 and $g_\perp$ = 2.011). These data are consistent with that obtain from XRD analysis for the Mn10ncen catalyst which indicated MnO_2 crystalline particles with $\bar{d}$ = 13.8 nm (low MnO_x dispersion, see Table 5.3).

Based on all the bulk and surface characterization data presented in Chapter 4

about the preparation of the CeO_2-promoted SiO_2 supports and in this chapter about the

unpromoted and CeO_2-promoted MnO_x/SiO_2 catalysts, the variation in their structures

can be schematically summarized as follow (see Figure 5.16).

(a) Ce8N Catalyt

(b) Ce8A Catalyst
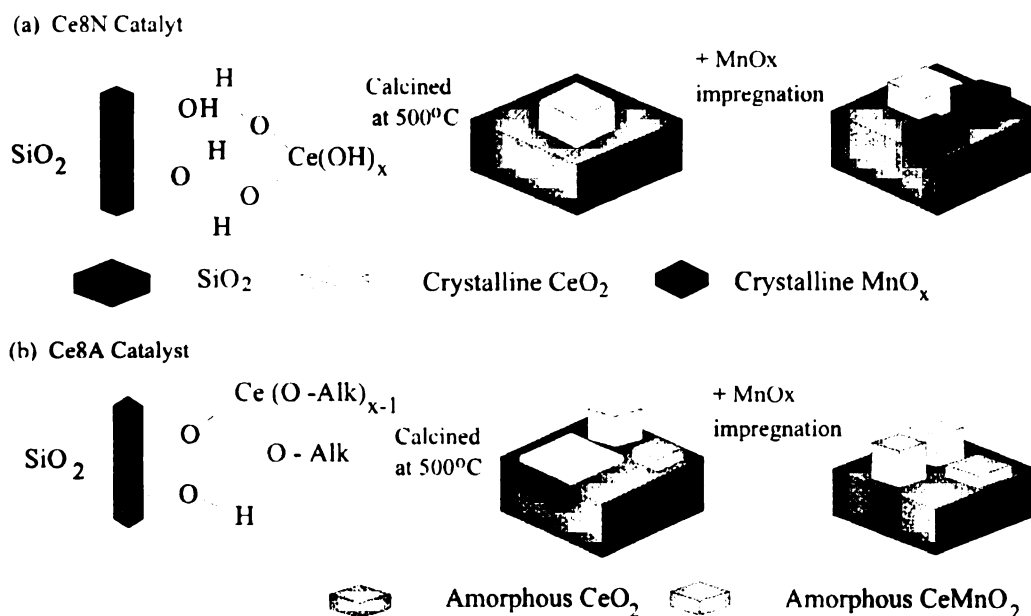
Figure 5.16   Schematic representation of unpromoted and CeO_2 promoted MnO_x/SiO_2 catalysts.

From Figure 5.16 it can be concluded that the impregnation method used to

prepare the CeO_2-promoted catalysts strongly affects the MnO_x/SiO_2 catalysts' structures.

The interaction of the support with the cerium precursor determined a significant change

in CeO_2 promoter structure with consequences on the next step of the catalyst

preparation.   All the results obtained in this study are easily reproducible.   The

modifications in the catalysts' structures observed during preparation can be accurately

monitored by controlling the preparation parameters (precursor concentrations, temperature, impregnation technique, etc).

Catalyst activity. Table 5.5 present the catalytic activity data in terms of reactant conversion and selectivity, for the unpromoted and CeO_2-promoted MnO_x/SiO_2 catalysts for the oxidative dehydrogenation of ML at 200°C and 23HPy at 260°C, respectively.

Table 5.5 Conversions and selectivities for ML and 23HPy catalytic oxidative dehydrogenation on unpromoted and CeO_2-promoted catalysts

Ord. #	Catalyst	Dihydro-Pyrazine at 200°C [%]		Methyl Lactate at 260°C [%]	
		conversion	selectivity	conversion	selectivity
1	SiO_2	100	35.5	37.7	12.6
2	Mn10n400	97.9	61.9	42.1	10.3
3	Mn10n500	98.1	51.3	33.5	16.7
4	Mn10n750	82.8(100)	66.9(55.4)	31.4	15.6
5	Mn14n500	98.9	65.4	36.8	13.6
6	CeqA	100	2.4	48.1	7.3
7	Mn1sicea	85.5(100)	48.7(41.6)	43.8	5.4
8	CeqN	100	5.6	25.4(35)	29.9(21.7)
9	Mn1sicen	93(100)	52(48.4)	35.2	21.9

As observed from Table 5.5, column 2, the conversion at 200°C of 23HPy by oxidative dehydrogenation to 23Py reaches 98 % with selectivity as high as 62 %. Temperature plays an important role in the conversion value. Tests reactions performed at low temperatures (130°C and 150°C) indicate conversions of only 3-5%. No 23Py product was detected at these low temperatures. It seems that the catalysts start to

function only at temperatures above 160°C. At temperatures above 200°C, most of the reactant or formed products are burned or converted to CO, CO_2 and H_2O. To properly compare selectivities for various catalysts, the values considered should correspond to a same conversion. In parenthesis are presented the calculated selectivity values at full conversion (100%) for the tested catalysts. Catalysts with higher concentrations of Mn (Mn14n500) and the MnO_2 (Mn10n400) proved to be more active catalysts than those with Mn_2O_3 phase for the oxidative dehydrogenation of 23HPy to 23Py. Consequently, the Mn10n400 with higher MnO_2 content was found to be the most active in 23Py formation (conversion of 98% with 62% selectivity). Catalysts with higher Mn loading show higher catalytic activity. The catalysts calcined to higher temperatures or those with a higher Mn_2O_3 concentration show lower conversions and selectivities. It was found that feeding only the product (23Py) at 200°C, around 16% of the amount passing through the reactor have been burned. Consequently, the selectivity in 23Py might be improved by optimizing the reaction temperature and thus, minimizing the 23Py burning process. In addition, it was observed that lowering the concentration of the 23HPy in the ethanol from the reaction feed decreases the burning or side reaction processes. These observations are in good correlation with other studies implying large organic molecules oxidative dehydrogenation which indicated that low concentrated feed (maximum 10%) led to high conversion and selectivity in the desired product [22-24]. On the other hand, it appears that the Ce-promoted catalysts are more active toward total oxidation than selective oxidation, a large quantity of carbon deposition being observed.

In the case of ML to MP oxidative dehydrogenation, the Mn10ncea catalyst (in which $MnCeO_x$ mixed oxide species formation was observed, Mn making less accessible for the catalysis process) shows low activity. In the case of Mn10ncen catalyst in which MnO_2 deposits are observed to be separated from CeO_2 (like a physical mixture) higher activity is found due to the doubled oxidation effect of the two active oxide species, MnO_2 and CeO_2, respectively, and to the presence of more surface superoxide species (O_2^-). Despite th relative good catalytic activity data for the CeO_2-promoted MnO_x/SiO_2 catalysts, the structural promotion effect is little observable in these test reactions except in the case of Mn10ncen catalyst used in ML oxidative dehydrogenation. Analysis of the used unpromoted and CeO_2 promoted MnO_x/SiO_2 catalyst may reveal if cerium can act as a textural promoter.

Used unpromoted and CeO₂-promoted catalysts. The used catalysts from ML oxidative dehydrogenation reaction were analyzed by XRD, TPR, and XPS. Diffraction patterns obtained for these catalysts are presented Figure 5. 17.

In the case of the used Mn10n500 catalyst, new patterns are observable (Figure 5.17 a) in comparison with the fresh catalyst (see Figure 5.6 b). These patterns were identified based on literature data and analysis of reference compounds, and thus, attributed to Mn_3O_4 ($MnO \times Mn_2O_3$) species formed during the catalytic process [40]. In the oxidation reaction, manganese oxide species act as oxygen donors, as a consequence MnO_2 acts as an oxidation agent, but is reduced to Mn_3O_4. On the used catalyst, MnO_2 can be regenerated by recalcination at 500°C in air. To further confirm the Mn transformation during the catalytic process, TPR analysis of the used catalyst was

undertaken and the result was compared with the fresh catalyst or standard material.

Figure 5.18 a shows the TPR profile of the used catalysts in comparison with a fresh

catalyst calcined at 650°C (Figure 5.18 b) and calcined at 500°C (Figure 5.18 c).
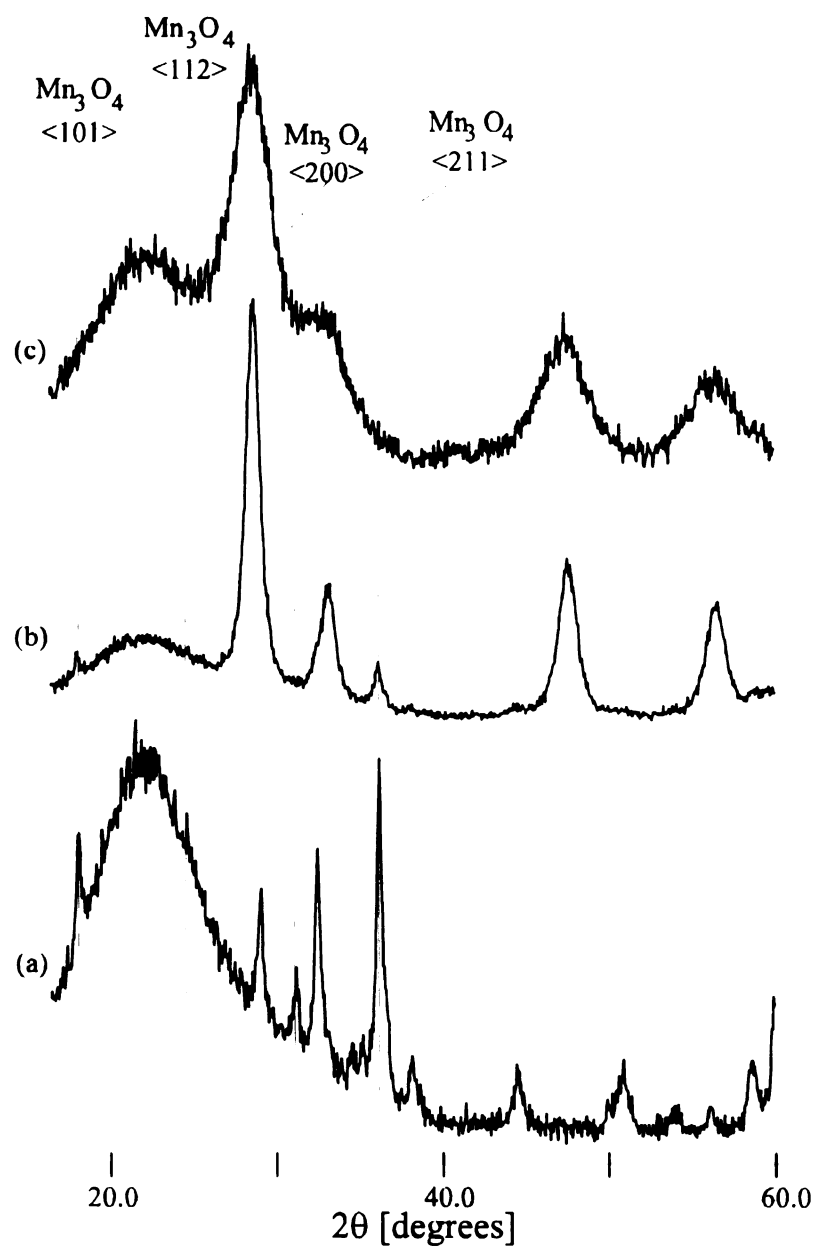
Figure 5. 17 XRD patterns of used unpromoted and CeO_2-promoted catalysts: a) Mn10n500; b) Mn10ncen; c) Mn10ncea.

It is known from the previous data (see Figure 5.11) that the TPR profiles of the Mnyn500 catalysts are modified with calcination temperature due to the change in the oxidation state of manganese. Supported MnO$_x$ show a TPR profile similar with that of the unsupported MnO$_x$, reported in the literature [9]. During the reduction process, Mn$_3$O$_4$ and MnO phases are formed. As mentioned above, the peaks at 344°C and 441°C were attributed to the reduction of the mixed MnO$_2$/Mn$_2$O$_3$ phase to Mn$_3$O$_4$ in a first step followed by the complete reduction of Mn$_3$O$_4$ to MnO (Figure 5.11 b).

Figure 5.18 TPR profiles of the fresh and used unpromoted MnO$_x$/SiO$_2$ catalysts: a) used Mn10n500; b) fresh Mn10n650; c) fresh Mn10n500.

When the sample is calcined at 650°C, most of the manganese is in the form of Mn_2O_3 with highly crystalline particles. Consequently, the main peak in the TPR profile is situated at 519°C, hig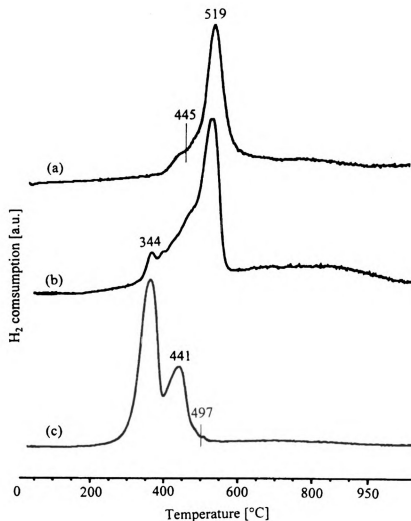her than in the case of smaller Mn_2O_3 particles (441°C). The small shoulders at 344°C and 445°C correspond to traces of small crystalline particles of MnO_2 and Mn_2O_3. The TPR profile for the used Mn10n500 catalyst (Figure 5.18 a) is similar with that for the Mn10n650 catalyst. In this case, the peak from around 519°C can be attributed to the reduction of Mn_3O_4 to MnO. The TPR profile for the used Mn10n500 catalyst does not show the peak at 344°C corresponding to MnO_2 butretains that at 445°C corresponding to traces amount of Mn_2O_3. These data are consistent with those observed in the XRD spectrum presented in Figure 5.13 e, for used Mn10n500 catalyst, which indicates patterns specific to Mn_2O_3 and Mn_3O_4 phases.

The XRD spectra of the used CeO_2-promoted MnO_x/SiO_2 catalysts are presented in Figure 5.17 b and 5.17 c. Compared with the fresh catalysts (see Figure 5.13 a, c), the XRD patterns of the used catalysts remain essentially unchanged. Low intensity XRD patterns specific to Mn_3O_4 species are observed in the case of Mn10ncen catalyst (Figure 5.17 b) but they are not found in the XRD patterns of the Mn10ncea catalyst (Figure 5.17 c). It appears that the presence of the CeO_2 promoter affects the resistance of MnO_2 to reduction during the catalytic process, providing oxygen to manganese and maintaining its oxidation state unchanged. On the other hand, the CeO_2 promoter can also play an important role in oxygen mobility on oxidation catalysts, by participating into an oxygen exchange process [27, 41]

The observations from TPR and XRD data are also in good agreement with the

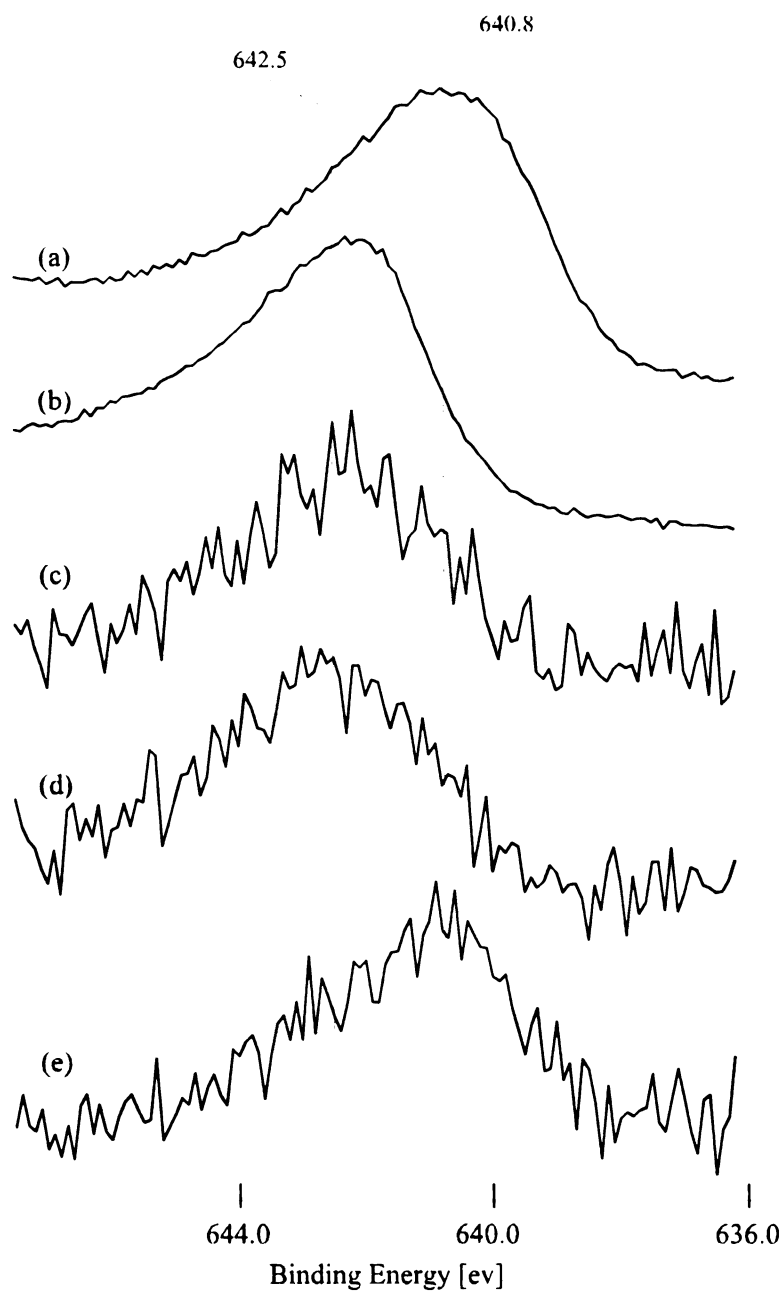XPS data presented in Figure 5.19 c-e.

Figure 5.19 $Mn_{2p3/2}$ XPS spectra of the used unpromoted and CeO_2-promoted catalysts in comparison with standard MnO_x materials: a) Mn_2O_3 (Mn_3O_4); b) MnO_2; c) Mn10ncea; d) Mn10ncen; e) Mn10n500.

The $Mn_{2p3/2}$ XPS spectrum for used Mn10n500 catalyst clearly shows a shift in the binding energy of $Mn_{2p3/2}$ peak at 642.5 eV observed in the fresh catalyst (see Figure 5.19 e) characteristic to Mn^{4+} species toward a binding energy of 640.8 eV characteristic to Mn^{3+}/Mn^{2+} [34]. It is hard to identify a signal specific to the Mn^{2+} species due to the overlap in binding energy value with Mn^{3+} species. Literature data show binding energy values for Mn_{2p} for Mn_3O_4 species in the 641.3 -641.4 eV range, and for Mn_2O_3 species in the 641.3-641.9 eV range [9, 34-35]. For the CeO_2 promoted catalysts, both Mn10ncen and Mn10acea, the binding energy of the $Mn_{2p3/2}$ peak is situated at 642.5 eV, specific to Mn^{4+} and similar with the fresh catalyst. The $Mn_{2p3/2}$ peak for the Mn10ncen catalyst shows a degree of asymmetry which might be an indication of the presence of Mn^{3+}/Mn^{2+} species. Due to the low S/N ratio, a clear deconvolution of the data was hard to obtain. Despite this inconvenience, this observation is consistent with that from XRD, which shows traces of XRD patterns specific to the Mn_3O_4 phase. The Mn_{2p} XPS spectra for used CeO_2-promoted MnO_x/SiO_2 catalyst, presented in Figure 5.19 c-d, shows a weak signal with the major peak located at BE = 642.5 eV corresponding to Mn^{4+} [22-25].

Conclusions

1) For the fresh catalyst, XRD and XPS analysis of the unpromoted catalyst calcined at 500°C have indicated that manganese was present mostly as crystalline MnO_2 and Mn_2O_3. The ratio between the two oxides and MnO_x particle size is a function of Mn loading and calcination temperature used during catalyst preparation.

2) The presence of CeO_2 favors the dispersion of manganese oxides deposited on SiO_2 support during calcination by forming mixed Mn-Ce oxides (no diffraction pattern

specific to MnO_x observed). The CeqA catalyst impregnated with Mn-nitrate clearly shows the formation of mixed $MnCeO_x$ species, a phenomenon which was not observed in the case of the CeqN catalyst. Manganese is present mostly as Mn^{4+}-species on the fresh $Mn/Ce/SiO_2$ catalyst.

3) Supported MnO_2 species proved to be more active catalysts than Mn_2O_3 for 23HPy oxidative dehydrogenation to 23Py. Consequently, the Mn14n500 with higher Mn loading and Mn10n400 with higher MnO_2 content was found to be the most active in 23Py formation. Catalysts with higher Mn loading show higher catalytic activity. The Ce-promoted catalysts are more active toward total oxidation than for selective oxidation. In the case of Mn10ncen catalyst in which MnO_x deposits are observed to be separated from CeO_2 (physical mixture) higher activity is seen due to the doubled oxidation effect of the two active oxide species, MnO_2 and CeO_2, respectively. The formation of mixed $MnCeO_x$ phase in the Mn10ncea catalyst, probably determined a poor catalytic activity in ML and 23HPy oxidative dehydrogenations.

4) Analysis of the used catalysts showed that the manganese oxidation state on unpromoted catalysts degenerates from Mn^{4+} to Mn^{2+}, leading to the formation of Mn_3O_4 species. Formation of Mn_3O_4 observed on the used catalyst might be responsible for decreasing the catalytic activity of the unpromoted MnO_x catalysts. The presence of CeO_2 on the MnO_x/SiO_2 catalysts precludes the formation of Mn_3O_4 during catalyst utilization. This effect is more evident in the case of CeqA-promoted catalyst. On the CeO_2-promoted MnO_x/SiO_2 catalyst, manganese remains dispersed with a structure similar to that in the fresh catalyst. However, in the case of the CeqN-promoted MnO_x/SiO_2 catalyst, small amounts of Mn_3O_4 are still observable. This difference was

attributed to the formation of "islands" of MnO_x and CeO_2, without a chemical interaction between then, which allows the formation Mn_3O_4 from MnO_2. Thus, CeO_2 acts as a textural rather than a structural promoter, helping to preserve the MnO_2 structure during an catalytic oxidative dehydrogenation process.

References

1. Cavani F.; Trifino, F. *Appl. Catal.* **1995**, *133*, 219.

2. Akiyama, T.; Enomoto, Y.; Shibamoto, T. *J. Agric. Food Chem.* **1978**, *26(5)*, 1176-1179.

3. Craciun, R. Masters Thesis, Michigan State University, East Lansing, USA, **1996**.

4. Sugiyama, S.; Sogabe, K.; Miyamoto, T.; Hayashi H.; Moffat, J. B. *Catal. Lett.* **1996**, *42*, 127-133.

5. Kim, J. J.; Weller, S. W. *Appl. Catal.* **1987**, *33*, 15.

6. Mooi, J.; Selwood, P. W.; *J. Am. Chem. Soc.* **1952**, *74*, 2461.

7. Strohmeier, B. R.; Hercules, D, M. *J. Phys. Chem.* **1984**, *88*, 4922.

8. Baltanas, M. A.; Stiles, A. B.; Katzer, J. R. *Appl. Catal.* **1986**, *28*, 13.

9. Kapteijn, F.; van Langeveld, D.; Moulijn, J. A.; Andreini, A.; Vuurman, M. A.; Turek, A. M.; Jehng, J. M.; Wachs, I. E. *J. Catal.* **1994**, *150*, 94-104.

10. Kieffer, R.; Kiennemann, A.; Rodriguez, M.; Bernal, S.; Rodriguez-Izquirdo, J. M. *Appl. Catal.* **1988**, *42*, 77-89.

11. Usmen, R. K.; Graham, G. W.; Watkins, W. L. H.; McCabe, R. W. *Catal. Lett.* **1995**, *30*, 53.

12. Jun-Ying, Y.; Swartz, W. E. Jr. *Spectrsoc. Lett.* **1984**, *17*, 331.

13. Ledford, J. S.; Houalla, M.; Proctor A.; Hercules, D. M. *J. Phys. Chem.* **1989**, *93* 6770.

14. Shelef, M.; Haack, L. P.; Soltis, R. E.; DeVries, J. E.; Logothetis, E. M. *J. Catal.* **1992**, *137*, 114.

15. Ledford, J.S.; Kim, Y. M.; Houalla, M.; Proctor, A; Hercules, D. M. *Analyst*, **1992**, *117*, 323.

16. Yamashita, T.; Vannice, A.; *J. Catal.* **1996**, *163*, 158.

17. Imamura, S.; Shono, M.; Okamoto, N.; Hamada, A.; Ishida, S. *Appl. Catal. A*, **1996**, *142*, 279.

18. Ivanova, A. S.; Dzisco, V. A.; Moroz, E. M.; Nosckova, S. P. *Kinet. Katal.* **1986**, *27(2)*, 285.

19. Baltanas, M. A.; DeCanio, S. J.; Katzer, J. R.; Dybowski, C. *Acta Chim. Hung.* **1986**, *118(4)*, 285.

20. Craciun, R.; Dulamita, N. *Catal. Lett.* **1997**, *46(3,4)*, 229-234.

21. Akiyama, T.; Enomoto Y.; Shibamoto, T. *J. Agric. Food Chem.* **1978**, *26(5)*, 1176-1179.

22. Ai, M.; Ohdan, K. *Appl. Catal. A*, **1997**, 150, 13-20.

23. Ai, M.; Ohdan, K. *Chem. Lett*, **1995**, 405.

24. Sugiyama, S.; Shigemoto, N.; Masaoka, N.; Suetoh, S.; Kawami, H.; Miyaura, K.; Hayashi, H.; *Bull. Chem. Soc. Jpn.* **1993**, *66(5)*, 1542-1547.

25. Pestman, R.; Koster, R. M.; van Duijne, A.; Pieterse, J. A. Z.; Ponec, V. *J. Catal.* **1997**, *168*, 265-272.

26. Zotin, F. M. Z.; Tournayan, L.; Varloud, J.; Perrichon, V.; Frety, R. *Appl. Catal. A*, **1993**, *98*, 99-114.

27. Hurst, N. W.; Gentry, S. J.; Jones, A. McNicol, B. D. *Catal. Rev.-Sci. Eng.* **1982**, *24(2)*, 233-309.

28.   Bruce, L. A.; Hoang, M.; Hughes, A. E.; Turney, W. *Appl. Catal.A,* **1996,** *134,* 151-362.

29.   Che, M.; Giamello, E. in *Spectroscopic Characterization of Heterogeneous Catalysts, Part B: Chemisorption of probe molecules,* Ed. Fierro, J. L. G. Elsevier, Amsterdam, **1990,** p. B265-B283.

30.   Soria, J.; Conesa, J. C.; Martinez-Arias, A.; Coronado, J. M. *Solid State Ionics,* **1993,** *63-65,* 755-761.

31.   Martinez-Arias, A.; Soria, J.; Conesa, J. C.; Seoane, X. L.; Arcoya, A.; Cataluna, R. *J. Chem. Soc. Faraday Trans.* **1995,** *91(11),* 1679-1687.

32.   Soria, J.; Martinez-Arias, A.; Conesa, J. C. *J. Chem. Soc. Faraday Trans.* **1995,** *91(11),* 1669-1678.

33.   Martinez-Arias, A.; Soria, J.; Conesa, J. C. *J. Catal.* **1997,** *168,* 364-373.

34.   Moulder, J. K.; Stickle, W. F.; Sobol P. E.; Bomben, K. D. *Handbook of X-ray photoelectron spectroscopy,* Perkin-Elmer Co. **1992,** p. 40-87.

35.   Barr, T. L. *Modern ESCA: the principles and practice of X-ray photoelectron spectroscopy,* CRC Press, Boca Raton, Florida, **1995.**

36.   Kerkhof, F. P. J. M.; Moulijn, J. A. *J. Phys. Chem.* **1979,** *83,* 1612-1619.

37.   Scofield, J. H. *J. Electron Spectrosc. Relat. Phenom.* **1976,** *8,* 129-137.

38.   Penn, D. R. *J. Electron Spectrosc. Relat. Phenom.* **1976,** *9,* 29-40.

39.   Gates, B. C. *Catalytic Chemistry,* Wiley&Sons, Inc. New York, **1992,** p 276-348.

40.   McClune, W. F. *Powder diffraction file, Inorganic phases, International center for diffraction data,* Swarthmore **1983,** p. 279, 599, 730, 731.

41.   Imamura, S.; Shono, M.; Okamoto, A.; Ishida, S. *Appl. Catal A,* **1996,** *142,* 279-288.

42.   Wollner, A.; Lange, F.; Schmetz, H.; Knozinger, H. *Appl. Catal. A,* **1993,** *94,* 181-203.

43.   Ruchenstein, E.; Pulvermacher, B.; *J. Catal.* **1973,** *29,* 224-245.

44.   Chan, S. I.; Fung, B. M.; Lutje, H. *J. Chem. Phys.* **1967,** *47,* 2121-2130.

45.   Breivagel, F. W.; Sarkissian, V. *J. Chem. Phys.* **1968,** *48,* 2442-2445.

46.   Schreurs, J. W. H. *J. Chem. Phys.* **1978,** 69, 2152-2155.

47.   Rubio, O. J. Munoz, P.; Boldu, O. J.; Chen, Y.; Abraham, M. M. *J. Chem. Phys.* **1979,** *70,* 633-638.

48.   Abi-Aad, E.; Bennani, A.; Bonnelle, J. P.; Aboukais, A. *J. Chem. Soc. Faraday Trans.* **1995,** *91,* 99-104.

CONCLUDING REMARKS

A combination of data regarding catalyst preparation, structural characterization, catalytic activity and mechanistic study related to catalytic conversion of lactic acid to various commodity and specialty chemicals have been presented in the above material. From these results, a set of concluding remarks can be defined:

1) The yield and selectivity of phosphate-catalyzed lactic acid conversion to 23P is a function of the sodium phosphate species from the Si/Al support; conversion up to 20% in lactic acid with selectivity of 30% in 23P was obtained on Na_3PO_4 supported on Si/Al catalyst; lower yields and selectivity in 23P were obtained in the case of NaH_2PO_4/Si/Al catalysts; this fact was attributed to acidity of the catalyst, reflected by high yield and selectivity in acetaldehyde; sodium polyphosphates species are formed on the catalysts surface often exposure to the reaction feed; ^{31}P-NMR relaxation time experiments help to differentiate various type of sodium phosphate species present on the Si/Al support and to evaluate the extent of sodium phosphate polymerization; regeneration of the active sodium phosphate species, by recalcination at 450°C can be done only partially;

2) DRIFT spectroscopy has identified the formation of sodium lactate on the catalyst surface; this intermediate may play an important role in the mechanism of catalytic lactic acid conversion to 23P;

3) The presence of $Ba(OH)_2$ on the SiO_2 surface may improve thermal resistance to the NaOH supported catalyst but affects negatively the selectivity of 23P formation from lactic acid;

4) A small decrease in the selectivity towards 23P with a corresponding slightly increase in the selectivity towards acetaldehyde is observed for the high surface area SiO_2 support in comparison to the low surface area, SiO_2; this was attributed to a higher surface acidity for the former support;

5) the yields and selectivities of lactic acid conversion toward 23P is a function of the loading and type of the alkali metal salt used to prepare the MOH supported catalysts; the yield and selectivity toward 23P increase in the order Ba < Na < K < Cs; optimized conditions (300°C, 0.5 MPa, 1-2 mmole MOH/g SiO_2, etc) and catalysts give 23P yields as high as 42% with selectivity up to 80%.

6) Based on experimental results such as D labeling experiments exchange, FTIR, D-NMR, GC-MS and VT-MS analyzed in the light of theoretical calculations, we have outlined and explored a detailed pathway for lactic acid condensation to 2,3-pentanedione. Lactate salts have been identified via DRIFTS on catalyst surfaces that have been exposed to lactic acid vapor. H/D exchange in the α-position of the lactic acid molecule has been observed, confirming the possibility of lactate enolization under these relative mild (buffered) conditions. This process leads to the key carbon nucleophile required for the condensation mechanism. Intermediate species with masses consistent with the proposed dimerization followed by loss of H_2O and CO_2 have been observed by VT-MS. PM3 and *ab initio* calculations, augmented by the SM3 solvation model, have

been used to evaluate energy variations and protonation state along the reaction sequence; for the condensed-phase situation, all energy changes were within accessible range at the reaction temperatures. The proposed pathway is energetically plausible and consistent with all observations.

7) Though specifically focused on the multistep mechanism of lactic acid condensation to 2,3-pentanedione, this work more generally illustrates the way in which theory and experiment can begin to dissect complex processes such as catalysis and condensed phase reactivity. Via such detailed mechanistic analyses of catalytic conversions, we hope to evolve toward a day when rational design will vastly accelerate discovery of novel catalysts and reaction paths.

8) The chemical reactivity of the precursor and impregnation technique used for preparation of a Ce-based SiO_2 promoted catalysts plays an important role to the its structure and catalytic activity. It was found that a $Ce(NO_3)_4(NH_4)_2$ precursor interacts with the support through intermolecular hydrogen bonds between surface hydroxyl groups from silica support and $Ce(OH)_4$ formed during the impregnation and drying of catalysts. Using the Ce-methoxyethoxide (Ce-alkoxide) precursor, the silica support impregnation takes place through a strong grafting interaction between the surface hydroxyl groups from SiO_2 and Ce-alkoxide, with elimination of methoxyethanol. After calcination of the catalysts at 500°C, diffraction methods (XRD, TEM) indicated that cerium is present in the Ce-nitrate derived catalysts mostly as large crystalline CeO_2 particles (>90%), and in Ce-alkoxide derived catalysts as mixed amorphous/crystalline, smaller size CeO_2 particles (crystalline CeO_2 is less than 30%). Air calcination at 500°C

of the grafted cerium from the silica support, led to an amorphous Ce^{4+} phase, while calcination at 800°C led to a higher degree of crystallinity and larger CeO_2 particles.

9) Unpromoted and CeO_2-promoted MnO_x/SiO_2 catalysts were prepared and characterized before and after their utilization in oxidative dehydrogenation processes. On the fresh unpromoted MnO_x/SiO_2 catalysts, manganese was present mostly as crystalline MnO_2 and Mn_2O_3. The ratio between the two oxides and MnO_x particle size is a function of Mn loading and calcination temperature used during catalyst preparation.

10) The presence of CeO_2 favors the dispersion of manganese oxides deposited on SiO_2 support during calcination by forming mixed Mn-Ce oxides (no diffraction pattern specific to MnO_x observed). The Ce-alkoxide derived SiO_2 support impregnated with Mn-nitrate shows formation of mixed $MnCeO_x$ species, a phenomenon which was not observed in the case of the Ce-nitrate derived silica. Manganese was present mostly as Mn^{4+}-species on the fresh $Mn/Ce/SiO_2$ catalyst.

11) Supported MnO_2 species proved to be more active catalysts than Mn_2O_3 for 2-ethyl-3-methyl-dihydropyrazine to 2-ethyl-3-methylpyrazine oxidative dehydrogenation. Catalysts with higher Mn loading show higher catalytic activity. The Ce-promoted catalysts are more active toward total oxidation than for selective oxidation. Unfortunately, in these test reactions the CeO_2 promotion effect was little observable, so CeO_2 has mostly a textural promoter effect.

12) Analysis of the used catalysts showed that the manganese oxidation state on unpromoted catalysts degenerates from Mn^{4+} to Mn^{2+}, leading to the formation of Mn_3O_4 species. Formation of Mn_3O_4 observed on the used catalyst might be responsible for

decreasing the catalytic activity of the unpromoted MnO_x catalysts. The presence of CeO_2 on the MnO_x/SiO_2 catalysts precludes the formation of Mn_3O_4 during catalyst utilization. This effect is more evident in the case of Ce-alkoxide derived catalyst. On the CeO_2-promoted MnO_x/SiO_2 catalyst, manganese remains dispersed with a structure similar to that in the fresh catalyst. However, in the case of the Ce-nitrate derived MnO_x/SiO_2 catalyst, small amounts of Mn_3O_4 are still observable.